Stability Analysis of Adaptation Process in FxLMS-Based Active Noise Control

Iman Tabatabaei Ardekani

Supervisor: Dr. Waleed H. Abdulla

A thesis submitted in partial fulfilment of the requirements for the degree of
Doctor of Philosophy in Electrical and Electronic Engineering,
The University of Auckland, New Zealand.

To my family.

Acknowledgements

First and foremost, I would like to express my sincere gratitude to *Dr. Waleed H. Abdulla*, who was my supervisor and mentor over the past 4 years. His time, expertise, support, guidance and encouragements have been invaluable and appreciated. Also, I would like to thank *A.P. Dr. Sing Kiong Nguang* who was my co-supervisor and guided me to conduct this research.

I would like to thank the examiners of this thesis, *Dr. Paul Teal* and *Professor Yoshinobu Kajikawa*, for their valuable comments, which definitely improved the quality of this work.

Last but not least, my deepest thanks to *my parents and family* for their continuous support throughout these years. Their understanding and support encouraged me to do my best in this Ph.D research. Also, my special thank goes to my friend, *Ramin Vali*, for sharing his expertise.

Abstract

This thesis is concerned with the *Filtered-x Least Mean Square* (FxLMS) adaptation algorithm and its applications in *Active Noise Control* (ANC). Generally, this algorithm is used in system identification problems in which a physical channel, called the *secondary path*, follows the adaptive filter. The FxLMS algorithm compensates for the secondary path effect by filtering the input signal (training data sequence) using an available estimate of the secondary path, called the *secondary path model*. However, this filtering causes the analytical model of the adaptation process to become highly complex. Because of this complexity, this model has to be simplified when it is desired to derive closed-form expressions for formulating different behaviours of the adaptation process. Usually, this simplification has been carried out by using unrealistic assumptions of pure delay secondary paths, broad-band acoustic noise, and perfect secondary path models.

The first contribution of this thesis is the derivation of *a set of closed-from mathematical expressions* for formulating behaviours of FxLMS-based ANC systems in steady-state and transient conditions. This derivation is carried out without using any simplifying assumption regarding the secondary path. Consequently, the obtained expressions extend the available knowledge on FxLMS-based ANC systems.

The second contribution is formulating *influences of acoustic noise band-width* on the newly-derived expressions. In the analysis of ANC systems with stochastic noise, it is usual to assume a broad-band acoustic noise with a flat frequency spectrum (which is usually referred to as a white signal), in order to avoid mathematical complexity. However, even if the acoustic noise has a flat spectrum over a wide frequency range, the signal picked up and fed to the ANC system is required to be processed with a sampling frequency higher than the maximum frequency of the acoustic noise. For this reason, a realistic noise signal can only have a flat spectrum over a limited band-width.

The third contribution is investigating *influences of secondary path models* on the newly-derived expressions. Usually, it is acceptable to assume a perfectly-accurate secondary path model; however, in order to generalise the obtained closed-form expressions, this assumption is also removed in this thesis. Consequently, the final closed-form expressions, proposed in this thesis, can apply to a relatively general case with an arbitrary secondary path, an acoustic noise with an arbitrary band-width, and an arbitrary (imperfect) secondary path model.

Another contribution of this thesis is determining trajectories of the poles of the FxLMS adaptation process in the z-plane. This investigation leads to find *the FxLMS adaptation process root locus*. It is shown that the dominant pole of this locus always locates on a certain branch with a typical trajectory

in the z-plane. A mechanism for localising this pole is then proposed in this thesis, resulting in a novel ANC algorithm, called the *Filtered Weight FxLMS*.

In addition to several numerical analyses and computer simulations, a *FPGA-based ANC setup*, developed for this research, is used to study the validity of the theoretical results obtained in this thesis. This setup is developed by using a *flexible FPGA programming structure* which can be used for the implementation of other ANC algorithms. Different experiments with this setup confirms the validity of the theoretical results proposed in this thesis.

Publications List

Most of the research results, obtained in this thesis, have been peer-reviewed and published in *11 different ISI journals and international conferences proceedings*. The list of these publications can be viewed in the following:

1. I. Tabatabaei Ardekani and W. H. Abdulla, "Effects of secondary path modelling error on performance of active noise control systems," *IEEE Transaction on Control Systems Technology,* Volume PP, Issue 99, 2011, Pages 1-11.

2. —, "On the stability of adaptation process in active noise control systems," *Journal of Acoustical Society of America*, Volume 129, Issue 1, January 2011, Pages 173-184.

3. —, "Filtered weight FxLMS adaptation algorithm: analysis, design and implementation," *International Journal of Adaptive Control and Signal Processing*, Volume 25, Issue 11, November 2011, Pages 1023–1037.

4. —, "On the convergence of real-time active noise control systems," *Signal Processing*, Volume 91, Issue 5, May 2011, Pages 1262-1274.

5. —, "Theoretical convergence analysis of FxLMS algorithm," *Signal Processing* , Volume 90, Issue 12, December 2010, Pages 3046–3055.

6. —, "FxLMS-based active noise control: a quick review," in Proceedings of 2011 Asia Pacific Signal and Information Processing Association Annual Conference (*APSIPA 2011*), Xi'an, China, 18-21 October 2012.

7. —, "Dominant pole localisation of FxLMS adaptation process in active noise control," in Proceedings of 2011 Asia Pacific Signal and Information Processing Association Annual Conference (*APSIPA 2011*), Xi'an, China, 18-21 October 2012.

8. —, "Study of convergence behaviour of real-time adaptive active noise control systems," in Proceedings of 2010 Asia Pacific Signal and Information Processing Association Annual Conference (*APSIPA 2010*), Biopolis, Singapore, 14-17 December 2010, Pages 534-537.

9. —, "Convergence analysis of active noise control systems using root locus theory," in Proceedings of 2010 Asia Pacific Signal and Information Processing Association Annual Conference (*APSIPA 2010*), Biopolis, Singapore, 14-17 December 2010, Pages 141-144.

10. —, “Allpass filtered reference LMS algorithm for adaptive feedback active noise control,” in Proceedings of 2009 Asia Pacific Signal and Information Processing Association Annual Conference (*APSIPA 2009*), Sapporo, Japan, October 4-7, 2009, Pages 859-865.

11. —, “A new subband algorithm for active attenuation of broadband noise,” in Proceedings of 2009 International Symposium on Active Control of Sound and Vibration *(ACTIVE 2009*), Ottawa, Canada, August 2009.

Contents

List of Figures

Chapter 1

Introduction

The traditional approach to acoustic noise control uses passive silencers to attenuate unwanted sound waves. These silencers are valued for their global noise attenuation; however, they are relatively bulky, costly and ineffective for low frequency noise. To overcome these problems, *Active Noise Control* (ANC), in which an electro-acoustic system is responsible to create a local silence zone, has received considerable interest.

The first patent on active noise control was granted to Paul Leug, in 1936 [1]. Figure 1.1 shows the drawings, which Leug appended to his patent, describing how two sinusoidal sound waves can cancel each other. For two decades this idea remained only a theory on paper until Olson used early analog electronic technology to invent the first ANC device, called the "electronic sound absorber" [2, 3]. By the end of the 1950's, several analog ANC devices were invented, including those patented by Fogel [4], Simshauser [5] and Bose. However, all of these analog ANC devices are not able to adapt to changing characteristics of the noise to be cancelled nor to changing environmental conditions. This is because adaptive signal processing techniques cannot be realised by using analog electronic technology. Only with the advent of digital technology did the realisation of adaptive ANC systems become possible. The theory of adaptive ANC, in which an adaptation algorithm automatically adjusts the ANC device, was established by Widrow in 1975 [6]; however the most significant progresses on this subject has been reported in the last two decades [7, 8].

In this chapter, the theory behind adaptive ANC is elaborated, followed by a literature review on signal processing techniques used in design and implementation of adaptive ANC devices. Shortcomings of available relevant work are discussed, based on which the main outstanding problems to be dealt with in this thesis are defined.

1.1 Physical Principles of Active Noise Control

This section introduces the acoustic wave propagation process and its properties. Based on the linearity of this process, the phenomenon of interference between sound waves, upon which the ANC theory is established, is then discussed.

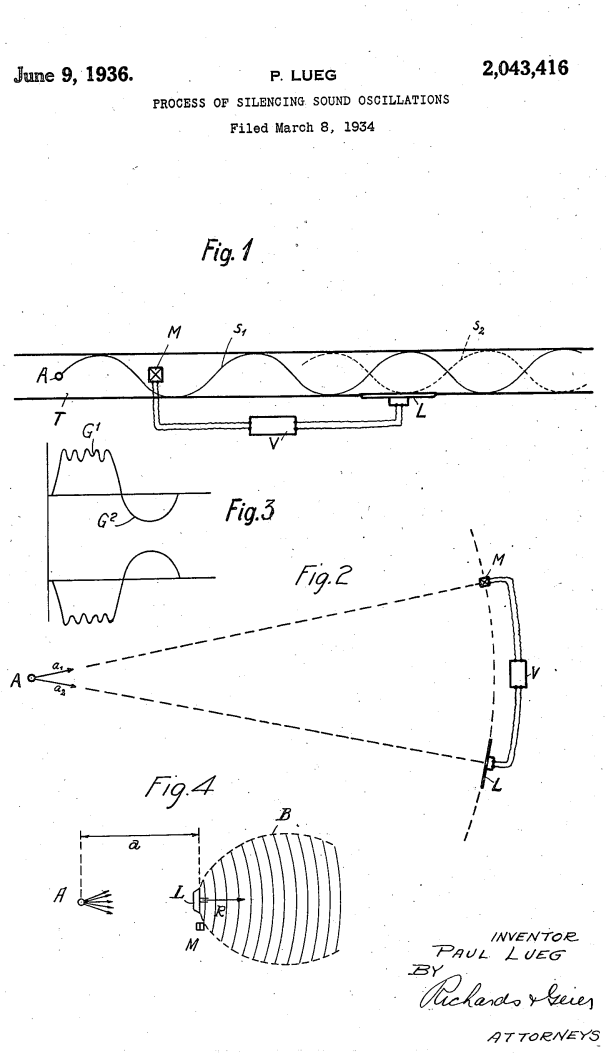

Figure 1.1: The drawings appended to the first patent on active noise control [1]

1.1.1 Acoustic Wave Propagation

Sound waves (also called "acoustic waves") are described by variations in the acoustic pressure through space and time. The acoustic pressure is defined as the local deviation from the ambient atmospheric pressure[1] caused by a sound wave. This scalar quantity, which can be directly measured using a microphone in air or a hydrophone in water, is the force (N) of sound on a surface area (m^2) perpendicular to the direction of the sound. The evolution of the acoustic pressure as a function of position and time can be described by the wave propagation equation in three-dimensional space [9]:

$$\nabla^2 p\left(x,y,z,t\right) - \frac{1}{c^2}\frac{\partial^2}{\partial t^2} p\left(x,y,z,t\right) = 0 \tag{1.1}$$

where $p\left(x,y,z,t\right)$ denotes the acoustic pressure at position (x,y,z) and continuous time t, operator ∇^2 is the Laplacian operator and constant c is the propagation speed of the sound in the ambient[2]. In [9], it

[1] Atmospheric pressure is the force per unit area exerted against a surface by the weight of air above that surface in the Earth's atmosphere.

[2] $c = 343 \frac{\mathrm{m}}{\mathrm{s}}$ in dry air at 20 °C

is shown that the propagation of a sound wave through the wave propagation process, given in Eq. (1.1), can be effectively modelled as a linear process.

1.1.2 Superposition Property

In system theory, the superposition property states that, for all linear systems, the net response at a given position and time caused by two or more sources is the algebraic sum of the responses, which would have been caused by each source acting individually. Therefore, based on the linearity of the acoustic wave propagation process, the net acoustic pressure at position (x, y, z) and (discrete) time index n caused by two or more sound sources, can be expressed as the algebraic sum of the acoustic pressures, caused by each sound source acting individually. Accordingly, in a general case with N sound sources, the net acoustic pressure at position (x, y, z) and time index n can be expressed as

$$p(x, y, z, n) = p_1(x, y, z, n) + ... + p_k(x, y, z, n) + ... + p_N(x, y, z, n) \tag{1.2}$$

where $p_k(x, y, z, n)$ denotes the acoustic pressure at position (x, y, z) and time index n, caused by the k-th sound source acting individually (for $k = 1, 2, \ldots, N$).

1.1.3 Acoustic Wave Interference

The phenomenon of interference between acoustic waves is based on the superposition property described above. For formulating this phenomenon, let us assume that there are only two sound sources in the ambient. In this case, Eq. (1.2) is simplified to

$$p(x, y, z, n) = p_1(x, y, z, n) + p_2(x, y, z, n) \tag{1.3}$$

which gives the acoustic pressure in three-dimensional space, while the existing sound waves interact with each other. The interaction of these two sound waves at a given point (x_0, y_0, z_0) and time index n, is called the *constructive interference* if the absolute value of $p(x_0, y_0, z_0, n)$ is equal or greater than the absolute values of $p_1(x_0, y_0, z_0, n)$ and $p_2(x_0, y_0, z_0, n)$. Otherwise, the interaction is called the *destructive interference*. This definition can be extended for a general case with an arbitrary number of sound sources. The phenomenon of destructive interference is the basis for the creation of a silence zone by ANC devices.

1.2 How to Create a Silence Zone

This section introduces the ANC physical mechanism by which a local silence zone can be created. Also, it is shown that this mechanism should be precisely driven by a digital electronic control system.

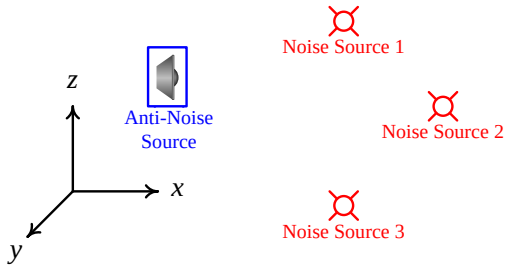

Figure 1.2: Location of noise and anti-noise sources in three dimensional space (single channel ANC)

1.2.1 ANC Physical Mechanism

In single channel ANC, there is a single control source, called the anti-noise source, dealing with a number of acoustic noise sources. This situation is illustrated in Figure 1.2 with the coordinate system used. For this general case, the net acoustic pressure at a given position and time can be mathematically described by using the superposition property:

$$p\left(x,y,z,n\right)=p_{d}\left(x,y,z,n\right)+p_{\tilde{d}}\left(x,y,z,n\right) \tag{1.4}$$

where $p_{d}\left(x,y,z,n\right)$ is the net acoustic pressure at position $\left(x,y,z\right)$ and time index n caused by all the existing noise sources, and $p_{\tilde{d}}\left(x,y,z,n\right)$ is the acoustic pressure at the same position and time caused by the anti-noise source acting individually. The unwanted acoustic pressure $p_{d}\left(x,y,z,n\right)$ itself can be described as the superposition of the acoustic pressures caused by the noise sources acting individually :

$$p_{d}\left(x,y,z,n\right)=p_{1}\left(x,y,z,n\right)+p_{2}\left(x,y,z,n\right)+p_{3}\left(x,y,z,n\right)+... \tag{1.5}$$

Now, let us define the following notations.

1. $Z_{s}\left(x_{s},y_{s},z_{s}\right)$ is the position of a desired silence zone in three-dimensional space.
2. $e_{ac}\left(n\right)$ is the net acoustic pressure at Z_{s} :

$$e_{ac}\left(n\right)\triangleq p\left(x_{s},y_{s},z_{s},n\right) \tag{1.6}$$

3. $d_{ac}\left(n\right)$ is the acoustic pressure at Z_{s} caused by all the existing noise sources:

$$d_{ac}\left(n\right)\triangleq p_{d}\left(x_{s},y_{s},z_{s},n\right) \tag{1.7}$$

4. $\tilde{d}_{ac}\left(n\right)$ is the acoustic pressure at Z_{s} caused by the anti-noise (control) source:

$$\widetilde{d}_{ac}\left(n\right)\triangleq p_{\tilde{d}}\left(x_{s},y_{s},z_{s},n\right) \tag{1.8}$$

Using the above notations, Eq. (1.4) can be re-expressed as

$$e_{ac}\left(n\right)=d_{ac}\left(n\right)+\widetilde{d}_{ac}\left(n\right) \tag{1.9}$$

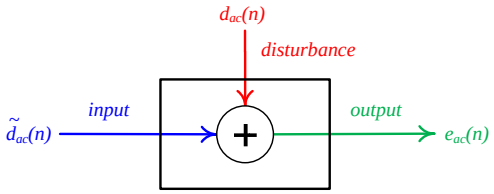

Figure 1.3: Physical mechanism of active noise control

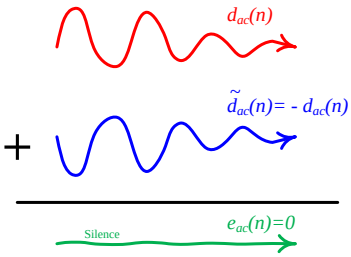

Figure 1.4: Physical concept of active noise control

Eq. (1.9) describes the physical mechanism which is responsible for ANC. The relation between the input and output of this mechanism is shown in Figure 1.3. According to this figure, the input of this mechanism is the control acoustic pressure at Z_s caused by the anti-noise source, the disturbance signal is the unwanted acoustic pressure at Z_s, and the output signal is the net acoustic pressure at Z_s. The ANC physical mechanism generates the output signal as the summation of the input and disturbance signals.

From Eq. (1.9), it can be shown that the net acoustic pressure at Z_s can be made zero if, and only if, the input and disturbance signals are equal in magnitude and opposite in phase:

$$e_{ac}(n) = 0 \Longleftrightarrow \widetilde{d}_{ac}(n) = -d_{ac}(n) \tag{1.10}$$

Therefore, by setting $\widetilde{d}_{ac}(n) = -d_{ac}(n)$, the ANC physical mechanism can create a silence zone at Z_s. This process is illustrated in Figure 1.4.

1.2.2 Digital Electronic Control System

Referring to Figure 1.5, it can be seen that the ANC physical mechanism can create a silence zone at a given position, if the loudspeaker acting as the anti-noise source is precisely driven to produce $\widetilde{d}_{ac}(n)$ exactly equal to $-d_{ac}(n)$. For this purpose, the ANC physical mechanism is usually associated with a digital electronic control system generating a *control signal* (or command signal) to drive the anti-noise source. This control system is usually referred to as the *ANC controller* and its combination with the loudspeaker acting as the anti-noise source, and with a number of microphones collecting information on the existing noise field is referred to as the *ANC system*.

A general ANC system is illustrated in Figure 1.6. As can be seen in this figure, one essential component of ANC systems is an *error microphone* measuring the net acoustic pressure at the desired silence zone: $e_{ac}(n)$. The response of this microphone, hereafter called the *error signal*, is directly used by the ANC controller as a feedback signal containing information on the performance of the ANC system.

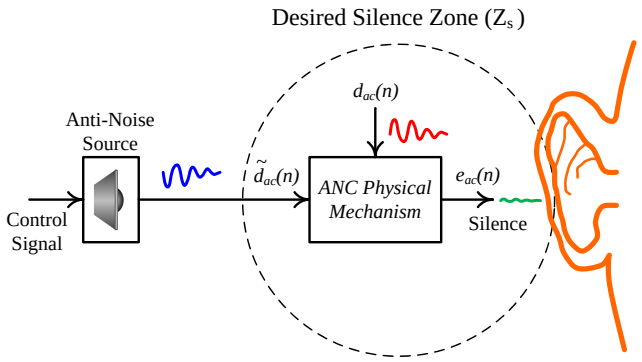

Figure 1.5: Creating a silence zone using the ANC physical mechanism

As illustrated in Figure 1.6, a digital ANC controller generates the control signal $y(n)$ in response to the input signal $x(n)$, called the *reference signal*. In order to generate an effective control signal, the controller requires the reference signal to contain enough information on the unwanted acoustic pressure. In other words, an ideal reference signal is identical to the unwanted acoustic pressure at Z_s: $d_{ac}(n)$. However, this signal cannot be measured during the operation of the anti-noise source. This is because $d_{ac}(n)$ is intended to be combined with the control acoustic pressure generated by the anti-noise source, $\widetilde{d}_{ac}(n)$. Here, it is useful to continue with an ideal case, where the ideal reference signal, as introduced above, is available:

$$x(n) = d_{ac}(n) \tag{1.11}$$

and where it is assumed that the waveform of the control acoustic pressure at Z_s is exactly equal to that of the control signal fed to the anti-noise source:

$$\widetilde{d}_{ac}(n) = y(n) \tag{1.12}$$

Now, by substituting Eqs. (1.11)-(1.12) into Eq. (1.10), the desired control signal, denoted by $y_o(n)$, is obtained as

$$y_o(n) = -x(n) \tag{1.13}$$

From Eq. (1.13), the impulse response of the desired ANC controller, $w_o(n)$ is obtained as

$$w_o(n) = -\delta(n) \tag{1.14}$$

where $\delta(t)$ denotes the Kronecker delta function. In practise, such a simple controller cannot perfectly create a silence zone at Z_s because of the existence of two constraints, the first of which is $\widetilde{d}_{ac}(n) \neq y(n)$ due to the existence of a physical Electra-acoustic channel between the output of the controller and Z_s (usually referred to as the secondary path) and the second of which is $x(n) \neq d_{ac}(n)$ due to the non-measurability of the ideal reference signal. These two constraints and the standard approaches used to deal with them are discussed in the following.

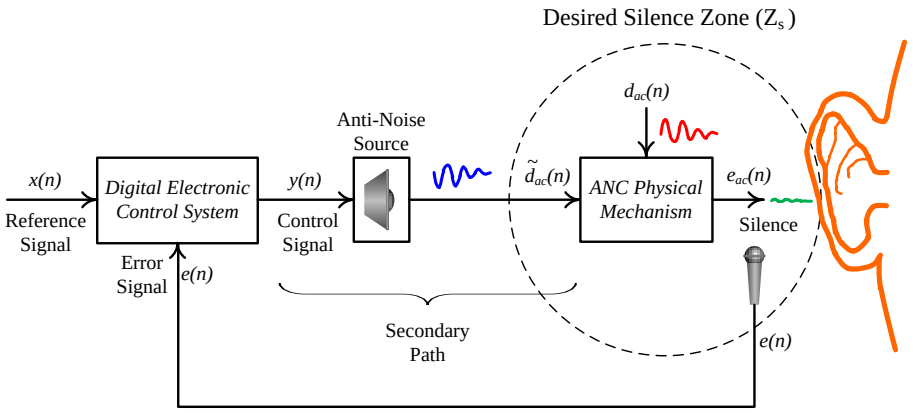

Figure 1.6: A general ANC system

1.2.2.1 Secondary Path Constraint

In practise, even if the ANC controller output $y\left(n\right)$ is identical to $-d_{ac}\left(n\right)$, the control acoustic pressure at Z_s, deviates from $-d_{ac}\left(n\right)$. Consequently, the net sound pressure at Z_s deviates from zero. This is because of the existence of an electro-acoustic channel, called the *secondary path*, between the ANC controller and Z_s. Assuming that $s\left(n\right)$ is the impulse response of the secondary path, the control acoustic pressure at Z_s can be expressed as

$$\widetilde{d}_{ac}\left(n\right) = s\left(n\right) * y\left(n\right) \tag{1.15}$$

where $*$ denotes the convolution operator. Therefore, for producing a control acoustic pressure equal to $\widetilde{d}_{ac}\left(n\right)$ at Z_s, the control signal driving the anti-noise source should be set to

$$y\left(n\right) = s^{-1}\left(n\right) * \widetilde{d}_{ac}\left(n\right). \tag{1.16}$$

From this result, it can be induced that only if the secondary path impulse response is known can the desired control signal $y\left(n\right)$ be estimated.

1.2.2.2 Reference Signal Measurement Constraint

As discussed, an ideal reference signal, to which the ANC controller can generate a perfect control signal in response, is equal to the unwanted acoustic pressure at Z_s. However, this acoustic pressure is not measurable because it is intended to be combined with the control acoustic pressure. Based on the structure upon which ANC devices deal with this constraint, these systems are classified into two major categories: feed-forward and feedback.

Feed-forward Structure:

Feed-forward ANC controllers have a long history in digital ANC. This dates back to Widrow's original work on adaptive ANC [6], in which an upstream microphone was used to give information about the

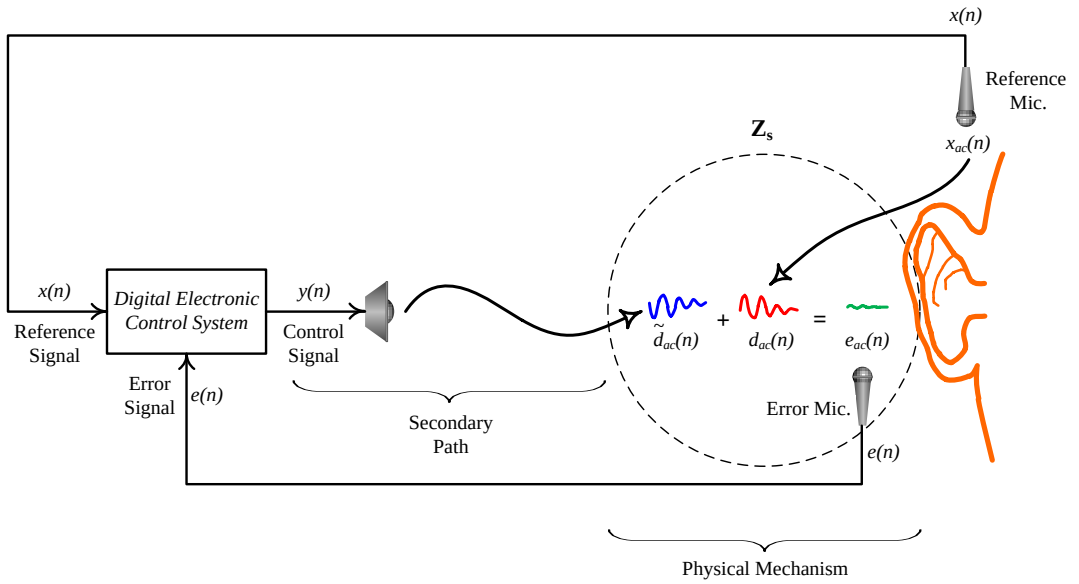

Figure 1.7: General diagram for feed-forward ANC

unwanted noise propagating down the system. However, most significant reports on feed-forward ANC were published in the 1980's, including those published by Morgan [10], Widrow [11], Burgess [12] and Warnaka [13].

Figure 1.7 shows the diagram of feed-forward ANC. As can be seen in this figure, a microphone, called the reference microphone, is located at a far position from Z_s, where the influence of the anti-noise source is not considerable. The response of this microphone is then fed to the controller as the reference signal $x\left(n\right)$. However, due to the existence of the distance between the reference microphone and Z_s the waveform of the measured signal $x\left(n\right)$ is different from that of $d_{ac}\left(n\right)$, which is the ideal reference signal. In the feed-forward structure, it is assumed that the ideal reference signal $d_{ac}\left(n\right)$ can be modelled as the response of a linear digital filter, called the *primary path*, to the measured reference signal $x\left(n\right)$:

$$d_{ac}\left(n\right) = p\left(n\right) * x\left(n\right), \tag{1.17}$$

where $p\left(n\right)$ is the impulse response of the primary path. Note that the primary path is an hypothetical signal path which is used for modelling the ideal reference signal, unlike the secondary path which is an actual signal path.

Feedback Structure:

As an alternative to the feed-forward structure, a feedback structure for ANC controllers was proposed by Eriksson in 1991 [14]. As illustrated in Figure 1.8, in this structure, $d_{ac}\left(n\right)$ is directly estimated by a feedback predictor from the measured error signal $e\left(n\right)$. Therefore, since the predicted $d_{ac}\left(n\right)$ is directly fed to the ANC controller, there is no signal path between $x\left(n\right)$ and $d_{ac}\left(n\right)$. In other words, the feedback structure is a special case of the feed-forward structure, in which the primary path is simply replaced by an identity system. The main advantage of this structure is that it does not require any refer-

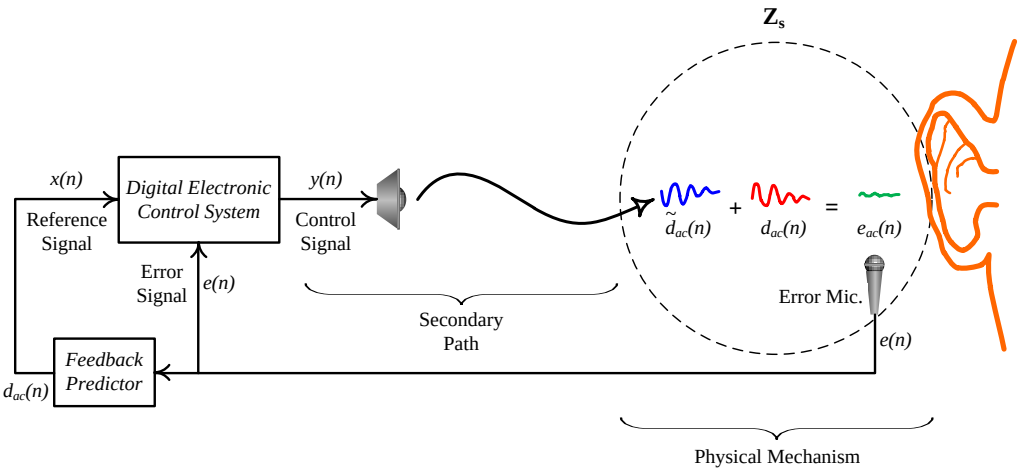

Figure 1.8: General diagram for feedback ANC

ence microphone; therefore, feedback ANC controllers are more compact and cost effective, compared to feed-forward ANC controllers. However, these controllers can attenuate only the predictable components of the unwanted noise. Furthermore, they are less robust than feed-forward ANC controllers. Due to these limitations, successful implementation of these controllers can be found only in specific applications such as personal hearing protection devices [15] and noise cancelling headphones [16–18].

Hybrid Feed-forward/Feedback Structure:

Hybrid ANC controllers are combined systems that derive the control signal from the outputs of both the reference and error microphone [19]. The feedback part of this structure controls the predictable component of the noise leaving the feed-forward part to concentrate on the other components of the noise. This structure results in a considerable overall performance improvement when compared to just a feed-forward or feedback system [20].

1.2.3 Adjustment of ANC Controller

Considering both the constraints, described in Section 1.2.2, the net acoustic pressure at the desired silence zone can be expressed by combining Eqs. (1.9), (1.15) and (1.17) as

$$e_{ac}(n) = p(n) * x(n) + s(n) * y(n) \tag{1.18}$$

Assuming that the error microphone has no effect on the signal waveform (or assuming that influences of this microphone is included in the primary and secondary paths), the response of the error microphone, which is called the error signal, can be expressed as

$$e(n) \approx e_{ac}(n). \tag{1.19}$$

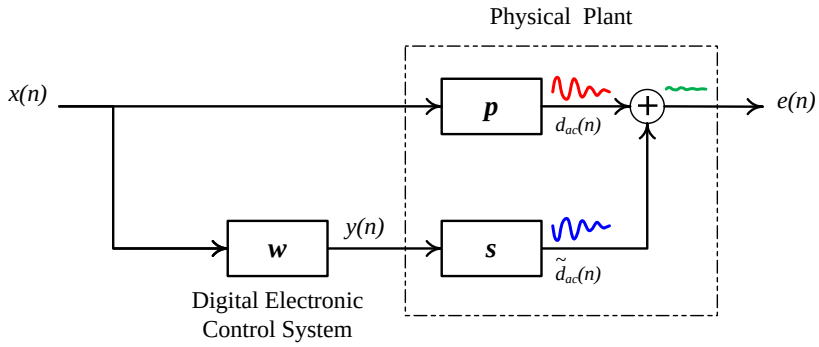

Figure 1.9: Functional block diagram for general ANC

Now, combining Eqs. (1.18) and (1.19) results in

$$e(n) = p(n) * x(n) + s(n) * y(n). \tag{1.20}$$

Eq. (1.20) represents a model in terms of electrical signals for the ANC physical mechanism. Considering that $y(n)$ is the response of the ANC controller to $x(n)$, the functional block diagram of this model can be drawn, as shown in Figure 1.9. In this diagram, blocks p, s and w represent the primary path, secondary path and ANC controller, respectively. Based on this block diagram, error signal $e(n)$ can be expressed as

$$e(n) = p(n) * x(n) + \{s(n) * w(n)\} * x(n), \tag{1.21}$$

where $w(n)$ is the impulse response of the ANC controller. By setting $e(n)$ to zero, the impulse response of the desired ANC controller, $w_o(n)$, can be obtained as

$$w_o(n) = -s^{-1}(n) * p(n) \tag{1.22}$$

Compared to Eq. (1.14) which describes an ideal ANC controller, Eq. (1.22) describes a more realistic ANC controller, considering both the secondary path and reference signal measurement constraints. However, since the impulse responses $p(n)$ and $s(n)$ are usually unknown, the desired ANC controller cannot be directly implemented. In this case, the role of Eq. (1.22) is reduced to a theoretical proof for the existence of the desired ANC controller.

1.3 Adaptive Active Noise Control

This section introduces adaptive ANC in which the desired ANC controller can be adaptively adjusted in a system identification framework without having the knowledge of the primary and secondary paths individually. Also, this section conducts a short review on available algorithms used in adaptive ANC.

1.3.1 Adaptive Identification of ANC Controller

According to Eq. (1.22), for realising the desired ANC controller, it is required to know the impulse responses of the primary and secondary paths, both of which are usually unknown time-varying electro-

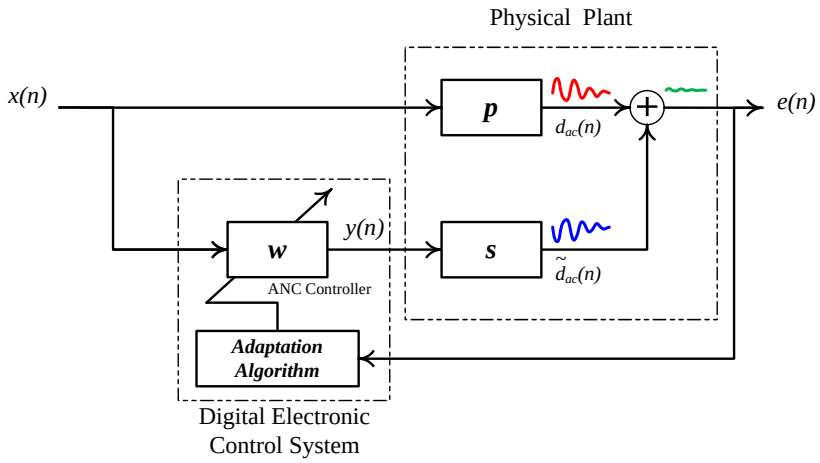

Figure 1.10: Functional block diagram for adaptive ANC

acoustic channels. To solve this problem, an adaptive scheme for ANC was proposed by Widrow in 1975 [6]. After publishing Widrow's original work, several researchers began working on this subject [10–13]. It was in 1981 that the first successful realisation of an adaptive ANC system for acoustic noise propagating in a duct was reported by Burgess [12].

In adaptive ANC, an identification (or adaptation) algorithm continually adjusts the ANC controller w in such a way that an error signal is progressively minimised, resulting in the gradual convergence of w to w_o. For the realisation of such an adaptive structure, the digital electronic control system should consist of two distinct parts (Figure 1.10):

1. A programmable digital filter, w acting as the ANC controller, and
2. An adaptation algorithm for the adjustment of the ANC controller.

Usually, the digital filter used as the ANC controller is an standard transversal filter; however, standard adaptation algorithms developed for the transversal filters e.g. Least Mean Square (LMS) or Recursive Least Square (RLS) cannot be used for the automatic adjustment of ANC controllers [8]. A relatively complete but not up-to-date review on adaptation algorithms used in ANC can be found in the book authored by Kuo [7]. A substantial number of other references are listed in this book. Also, the book authored by Elliott [8] provides detailed information on signal processing techniques used in adaptive ANC. In the next section, available ANC adaptation algorithms are briefly reviewed.

1.3.2 ANC Algorithms

In ANC systems, standard adaptation algorithms can not be used due to the existence of the secondary path. However, the influence of the secondary path on the performance of any standard adaptation algorithm can be compensated for if the reference signal is filtered using an estimate of the secondary path. This compensation mechanism results in a new range of adaptation algorithms referred to as *filtered-x adaptation algorithms*. The basic of which is the *Filtered-x Least Mean Square* (FxLMS) derived by

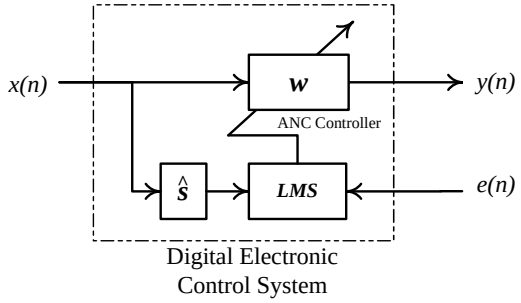

Figure 1.11: Block diagram of digital electronic control system in FxLMS-based ANC

Widrow in 1981 [11]. This algorithm is an LMS-type adaptation algorithm which can be used for the identification of an unknown system (e.g. a desired ANC controller) in the presence of a secondary path. The functional block diagram of an FxLMS algorithm adjusting an ANC controller is illustrated in Figure 1.11. In this figure $\hat{s}$ represents an estimate model of the secondary path. As can be seen, the reference signal is filtered by $\hat{s}$ before being used by the standard LMS algorithm. This is the only difference between the LMS and FxLMS algorithms, resulting in the compensation for the secondary path.

Other versions of the FxLMS such as Filtered-x Normalised LMS (FxNLMS) [13], Leaky FxLMS [21], Modified FxLMS (MFxLMS) [22, 23] etc [24, 25] were proposed to improve the performance of the original algorithm. However, the common problem with all of these algorithms is the slow convergence rate, specially when there is a large number of weights (which is usually the case). To overcome this problem, more complicated algorithms such as Filtered-x Recursive Least Square (FxRLS) [26, 27] or Filtered-x Affine Projection (FxAP) [28] can be used. These algorithms have faster convergence rate compared to the FxLMS; however they involve matrix computations and their real-time realisations may not be cost effective [29].

1.3.2.1 Frequency Domain ANC Algorithms

The above mentioned ANC algorithms suffer from either slow convergence rate or computational complexity. To overcome both of these problems, frequency domain algorithms can be used. The first frequency domain system identification framework was proposed in the 1970's [30] and the first frequency domain ANC algorithm was developed in 1992 [31]. In this algorithm, the reference and error signals are first stored in buffers to form data blocks. These blocks are then transformed to frequency domain reference and error vectors by a Fast Fourier Transform (FFT). Elements of the frequency domain reference vector is multiplied by filter weights to generate the frequency-domain control vector. Then this vector is fed to an Inverse FFT (IFFT) to produce a block of control signal in the time domain. The filter weights, used in the generation of the control signal in the frequency domain, are updated by the complex FxLMS algorithm [32, 33]. This algorithm causes a time delay equal to the length of the FFT used between the input and output of the ANC controller. This problem is a shortcoming of frequency-domain ANC controllers, specially in controlling broad-band stochastic noise.

Table 1.1: Comparison of available structures and adaptation algorithms used in ANC

Algorithm(s)	Strengths	Weaknesses
FxLMS	Simple real-time realisation. Low computational complexity.	Slow convergence rate.
FxRLS or FxAP	Fast convergence. Low steady-state residual noise.	Huge computational complexity. Difficult real-time realisation.
Freq. Domain **FxLMS**	Low computational complexity. Fast convergence. Simple real-time realisation.	Only suitable for narrow-band noise.
Sub-band **FxLMS**	Low computational complexity. Fast convergence.	Only suitable for narrow-band noise.

1.3.2.2 Sub-Band ANC Algorithms

Another approach to overcome both the computational complexity and slow convergence rate problems associated with ANC algorithms, is based on using the sub-band system identification framework. This framework consists of a sub-band filter-bank structure and an adaptation algorithm for each filter of the filter-bank. Conventional sub-band adaptation algorithms introduce a delay into the signal path. This delay cannot be tolerable in ANC systems because these systems are very sensitive to any delay in the secondary path. To overcome this problem, Morgan proposed a delay-less sub-band system identification framework and its FxLMS-based adaptation algorithm in 1995 [34]. Later (in 2001), Park improved the performance of the Morgan's algorithm [35]. Recently, a number of different algorithms for adaptation of sub-band ANC controllers have been proposed [36–39].

In a typical sub-band ANC algorithm, the reference and error signals are divided into sub-bands and then an FxLMS algorithm adjusts a low order transversal filter for each sub-band in order to minimise the corresponding sub-band error signal. In order to avoid the sub-band processing delay, sub-band ANC controllers are not directly used for the generation of the control signals. From weights of sub-band controllers, a full-band transversal ANC controller is constructed. In this scheme, since low order adaptive filters are adjusted in parallel, the convergence rate is fast. Also, since the adaptation process is performed on low order sub-band transversal controllers, the total computational complexity is significantly reduced. The main drawback of sub-band ANC is its requirement of block processing. Hence, this scheme is only useful for low frequency noise but not very effective for broad-band noise.

1.4 FxLMS Adaptation Process

Table 1.1 summarises the strengths and drawbacks of different ANC algorithms. According to this table, most ANC algorithms rely on the FxLMS algorithm. For this reason, this algorithm is usually known as the basic ANC algorithm. This section discusses the performance of the adaptation process performed by the FxLMS algorithm (hereafter called *FxLMS adaptation process*). Also, this section briefly reviews the available studies on theoretical analysis of the FxLMS adaptation process.

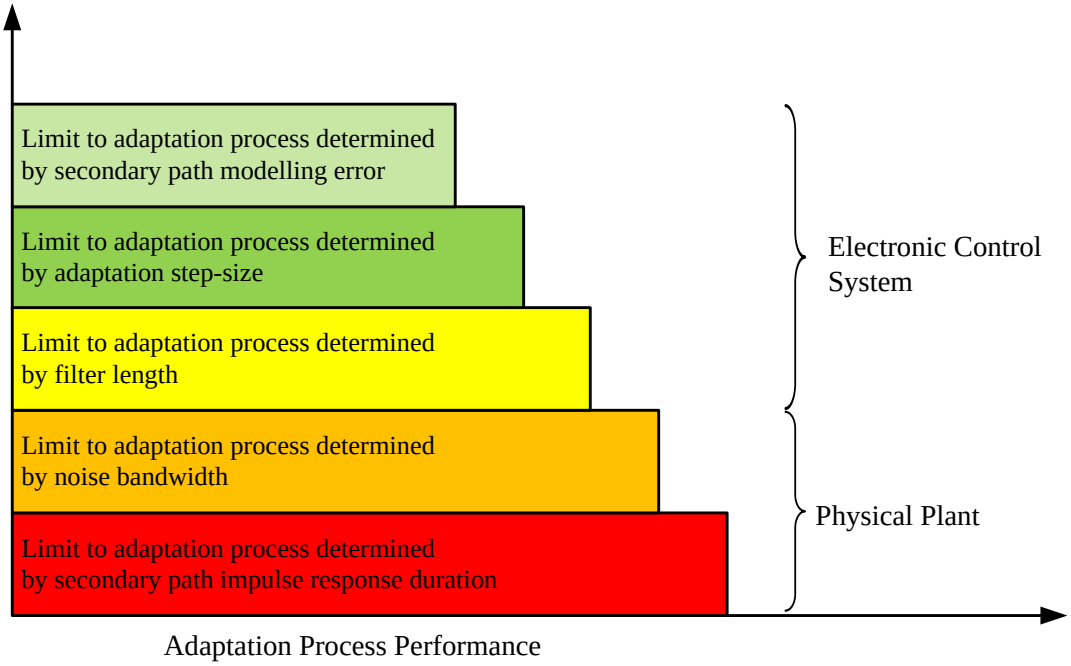

Figure 1.12: Performance hierarchy of FxLMS-based adaptation process

1.4.1 Performance of FxLMS Adaptation Process

The performance of the FxLMS adaptation process is limited by a number of related factors that must be addressed in the appropriate order. Referring to Figure 1.12, it can be seen that the absolute maximum level of performance is limited first by the characteristics of the physical plant to be controlled, including the secondary path impulse response and the acoustic noise band-width. This means that no matter how good is the electronic control system, the FxLMS will not function properly if the secondary path has a long impulse response and/or the acoustic noise has a wide band-width. After the physical plant characteristics, the design parameters of the electronic control system limit the maximum performance achievable. Among these parameters, the most important one is the length of the transversal filter used as the ANC controller. It should be noticed that although increasing the filter length improves the steady-state performance, it degrades the convergence rate of the FxLMS adaptation process. In addition to this trade-off, the filter length should be set considering the hardware resources available in the electronic control system.

After the filter length is set carefully, the maximum achievable performance is limited by a scalar parameter called the *adaptation step-size* (denoted by μ). In fact, the step-size is the only parameter in the original FxLMS algorithm which provides a control mechanism over the performance of the FxLMS adaptation process. The discussion on influences of this parameter is left to Section 1.4.2. According to Figure 1.12, the final factor limiting the performance of the FxLMS adaptation process is the accuracy of the secondary path model used in the algorithm. The discussion on this subject is left to Section 1.4.3.

1.4.2 Adaptation Step-Size

Analysing influences of the step-size μ on the FxLMS adaptation process is a complicated subject in adaptive signal processing. However, simplified theoretical analyses, simulation results and even experimental results show that these influences are similar to those derived for the LMS adaptation process. Hence, the rules governing influences of μ on the LMS adaptation process [40, 41] can be used as rules of thumb for the adjustment of μ in the FxLMS algorithm. These rules can be stated as follows.

1. There is an upper-bound for μ (denoted by μ_{max}) beyond which the process becomes unstable.
2. The convergence rate has a direct relationship with μ.
3. The steady-state performance has an indirect relationship with μ.

These rules provides a useful sense for setting the step-size; however, there are some ambiguities while using them. For example, the mathematical formulation for μ_{max}, which is available in ANC literature, has been derived only for a pure delay secondary path [7, 8] and the exact value of this bound is unknown for a realistic secondary path.

There have been several contributions in the performance analysis of the FxLMS adaptation process in terms of μ [42–49]. However, only a few have intended to find general closed-form expressions for μ_{max}, steady-state performance, and convergence speed of this process. Even if such expressions were derived, simplified cases with pure delay secondary paths were considered. This is mainly because of the mathematical complexity associated with the modelling of the FxLMS adaptation process.

Long summarised early work on the analysis of the FxLMS algorithm in [46, 47], while deriving closed-form expressions for μ_{max} and the steady-state performance. However, these expressions were derived only for pure delay secondary paths. In [48], Elliott derived another expression for μ_{max} which was very similar to the one previously derived by Long. The distinction between the two expressions was that Elliott derived his expression specifically for ANC applications. Hence, Elliott's expression for μ_{max} is very popular in ANC literature. In [49], Bjarnason conducted a comprehensive analysis on the FxLMS adaptation process. However, once he intended to derive closed-form expressions for μ_{max} and the steady-state performance, he had to simplify his formulations by assuming a pure delay secondary path. Also, Vicente derived another expression for μ_{max} when the acoustic noise is assumed to be sum of deterministic sinusoids [50].

All the aforementioned closed-form expressions for μ_{max} were derived for pure delay secondary paths. However, this assumption is not very realistic because usually an acoustic channel (which is the main part of the secondary path) has a long impulse response. Also, practical results show that the actual value of μ_{max} is different from those that have been proposed in available literature so far [51]. Xiao tried to compute μ_{max} for a realistic secondary path but, as he reported in [52], his theoretical results were not in a good agreement with the simulation results obtained.

1.4.3 Secondary Path Modelling Error

Due to mathematical difficulties, convergence analyses of adaptive ANC systems have been usually conducted without considering any secondary path modelling error (or by considering a perfect secondary path model). However, for some simplified cases, e.g. pure delay secondary paths or tonal noise, influences of this error on the FxLMS adaptation process have been studied [53–55]. All of these studies have shown that, for a particular special case, the FxLMS algorithm is very robust against the secondary path modelling error. It has to be noted that even for a perfect secondary path model, the analysis of the FxLMS adaptation process is an active area of research.

In [10], Morgan showed that for the trivial case when the secondary path model is an identity system, then this model does not cause the FxLMS adaptation process to become unstable if the phase difference between this model and the actual secondary path is below 90^o. Later, Boucher extends Morgan's 90^o condition for the case with pure delay secondary paths and tonal acoustic noise [56].

1.5 Thesis Contributions

The main contributions of this thesis can be summarised as follows.

- As discussed in Section 1.4, available mathematical expressions for formulating behaviours of FxLMS-based ANC systems can apply to only cases with pure delay secondary paths. However, a realistic secondary path is not a pure delay path. This is the first challenge which this thesis intends to deal with. In fact, it is desired to derive closed-form expressions for the step-size upper-bound, steady-state performance and convergence speed of FxLMS-based ANC systems without using any simplifying assumption regarding the secondary path.
- The second issue which this thesis is concerned with is to determine influences of the acoustic noise band-width on FxLMS-based ANC systems. These influences have been studied by different researchers; however, no theoretical and closed-form expressions describing them have been proposed so far.
- As a further step towards the generalisation of the theoretical results, this thesis aims at determining influences of secondary path modelling error on FxLMS-based ANC systems. This issue has been addressed by different researchers but it requires further investigation.
- While performing an analysis on FxLMS-based ANC systems, it is found that trajectories of the poles of the FxLMS adaptation process in the z-plane comply with certain rules. Also, it is found that the dominant pole is located on a particular trajectory. Based on this observation, this thesis develops a mechanism for localising the dominant pole of the FxLMS adaptation process.
- This thesis shows the validity of the obtained theoretical results by using an FPGA-based experimental setup developed for this research.
- 11 journal and conference publications are extracted from this thesis, a list of which is available in Page vii of the front matter.

1.6 Thesis Organisation

The remainder of this thesis is organised as shown in Figure 1.13 . Chapter 2 uses the available literature to formulate a theoretical frame-work for this research. Chapter 3 develops a novel theoretical model for describing behaviours of FxLMS-based ANC systems in general conditions. This chapter considers a realistic secondary path, an stochastic acoustic noise with an arbitrary band-width, and an arbitrary secondary path model. This means that this comprehensive model can precisely determine behaviours of practical FxLMS-based ANC systems. Chapter 4 simplifies this model by assuming a broad-band acoustic noise and a perfect secondary path model; however, without using any simplifying assumption regarding the physical secondary path. Based on the obtained model, this chapter derives closed-form expressions for the step-size upper-bound, steady-state performance and convergence speed of FxLMS-based ANC systems. The distinction between these expressions, and those previously derived, is that they can apply to any general secondary path while previously-derived expressions can apply to only pure delay secondary paths.

As another step towards the generalisation of the obtained theoretical results, Chapter 5 removes the constraints, caused by assuming a broad-band acoustic noise, from the theoretical results derived in Chapter 4. In fact, Chapter 5 extends the expressions derived in Chapter 4 to a more general case with a more realistic acoustic noise. This chapter continues by determining influences of the acoustic noise band-width on FxLMS-based ANC systems. Also, it is shown that the available expression for the step-size upper-bound with tonal acoustic noise, can be derived from a special case of the expressions developed in this chapter.

Chapter 6 removes the constraints, caused by assuming a perfect secondary path model, from the results obtained in Chapter 5. In fact, this chapter extends the expressions derived in Chapter 5 to the most general case in which the secondary path is a realistic acoustic channel, the acoustic noise is an stochastic signal with an arbitrary band-width, and the secondary path model is an arbitrary imperfect model .

Chapter 7 examines the validity of the theoretical results, obtained in Chapters 3-6, by using computer simulations. First, the validity of the model developed in Chapter 3 is shown. It is then shown that influences of the physical secondary path, acoustic noise band-width, and imperfect secondary path model on behaviours of FxLMS-based ANC systems can be accurately formulated by the expression given in Chapters 4-6.

Chapters 8 and 9 contain a different analysis of FxLMS-based ANC systems. In fact, Chapters 3-6 study FxLMS-based ANC systems to evaluate performance of these systems but Chapters 8 and 9 study these systems in view points of control engineering to develop a control mechanism over the FxLMS adaptation process dynamics. Another novel contribution of this thesis is that Chapter 8 analyses the FxLMS adaptation process using the root locus theory and determines the trajectories of the poles of this process in the z-plane (FxLMS root locus). The properties of the dominant root of this root locus are also determined. Chapter 9 uses the root locus analysis, performed in Chapter 8, to develop a mechanism for the localisation of the dominant root of the FxLMS adaptation process, leading to developing a new ANC algorithm which is called the Filtered-Weight FxLMS algorithm. This chapters ends by representing relevant simulation results.

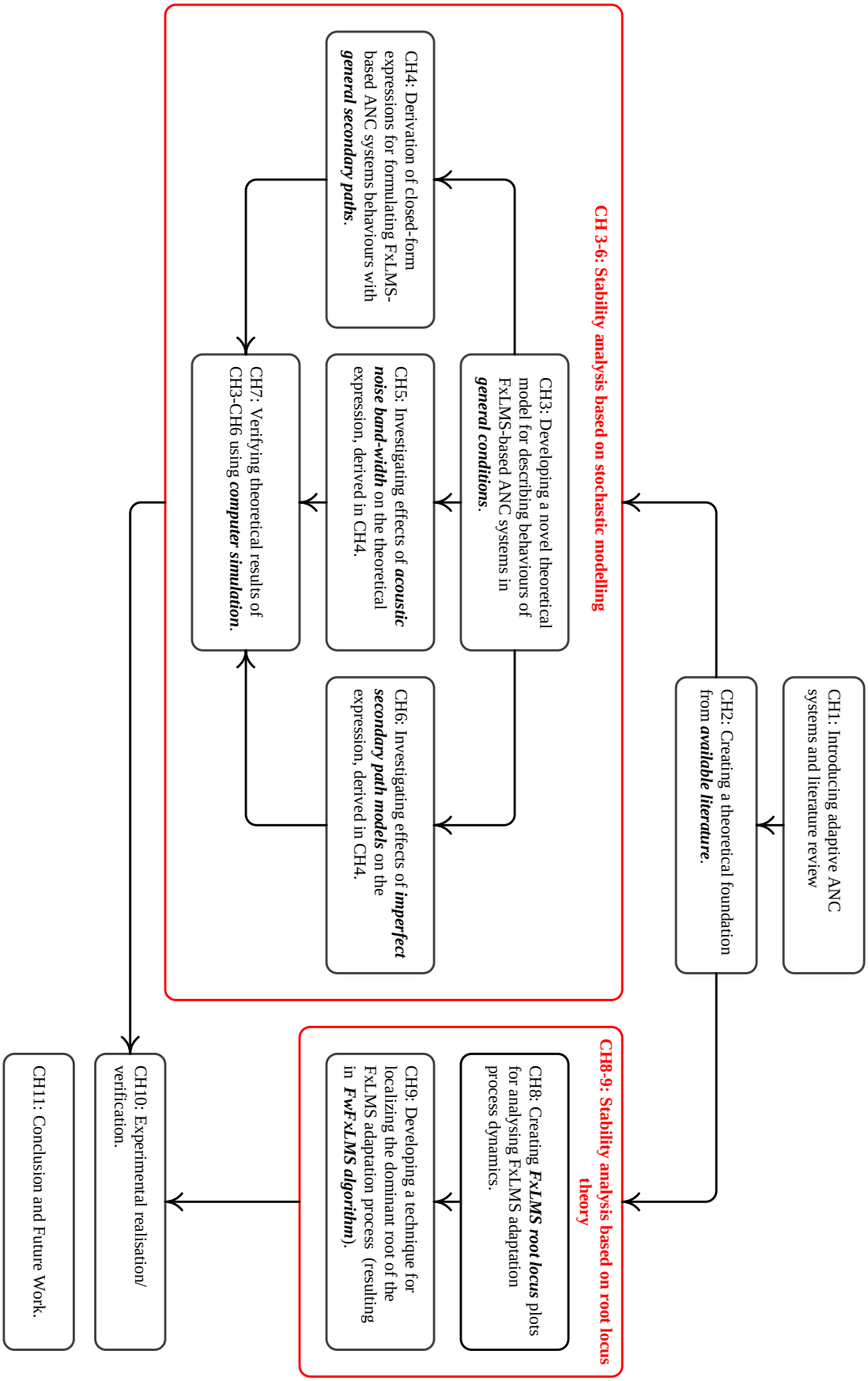

Figure 1.13: Thesis structure

Chapter 10 introduces the experimental setup used for the validation of the proposed theoretical results. Using this setup, it is shown that the theoretical expressions derived for the step-size upper-bound, steady-state performance and convergence speed of FxLMS-based ANC systems are valid in practise. Also, the proposed ANC algorithm, developed in Chapter 8, is implemented in the experimental setup. It is then shown that this algorithm is more efficient than the FxLMS algorithm. Finally, Chapter 11 gives concluding remarks and possible future work.

Chapter 2

Basic Principles of FxLMS Algorithm

This chapter uses the available literature to develop a mathematical foundation for the theoretical investigations to be conducted in the thesis. A typical single channel feed-forward ANC system that has a single control source, a single reference microphone and a single error microphone, is considered. This is because general techniques used for the design, analysis and implementation of this typical system, can apply to other varieties of ANC systems.

Section 2.1 introduces the single channel feed-forward ANC system. Section 2.2 derives the FxLMS algorithm as a gradient-based adaptation algorithm, which causes the residual acoustic noise at the desired silence zone to become minimal. Sections 2.3 defines the rotated vectors, based on which theoretical models for FxLMS-based ANC systems are developed. Sections 2.4 introduces some simplifying assumptions, which are commonly used in modelling and analysis of stochastic adaptation algorithms. Section 2.5 uses the definitions and assumptions, introduced in Sections 2.3 and 2.4, to formulate FxLMS-based ANC systems.

2.1 Single Channel Feed-forward ANC

The general block diagram of a single channel adaptive feed-forward ANC system is shown in Figure 2.1. In this figure, $d(n)$ is the noise signal (or unwanted acoustic pressure) at the desired silence zone, $x(n)$ is the reference signal, measured by the reference microphone, $y(n)$ is the anti-noise signal, generated by the ANC controller, and $e(n)$ is the residual acoustic noise, measured by the error microphone in the silence zone. Also, the primary and secondary paths are shown by linear systems p and s, respectively.

According to Figure 2.1, the acoustic noise $d(n)$ is assumed to be the response of the primary path p to the measured reference signal $x(n)$[1]. The acoustic signal $d(n)$ is combined with the (acoustic) anti-noise signal at the desired silence zone. As shown, the anti-noise signal is the actual response of the secondary path s to the control signal $y(n)$. The control signal is generated by an ANC controller w which has a transversal digital filter structure. This digital structure can be adjusted adaptively by using an adaptation algorithm (such as the FxLMS algorithm). In the following, different elements of the block diagram shown in Figure 2.1 are discussed in more detail.

[1] It is an assumption because p is a hypothetical system

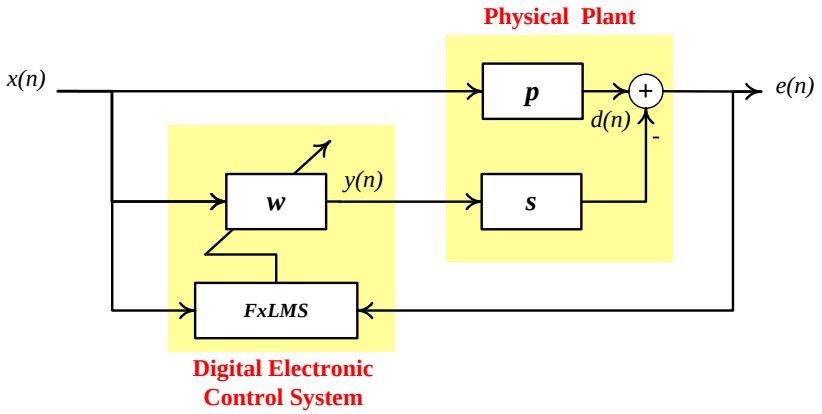

Figure 2.1: Functional block diagram of single channel adaptive feed-forward ANC

2.1.1 Control Signal

Assuming that the ANC controller w has a transversal structure of length L, the control signal $y(n)$, can be expressed as

$$y(n) = \mathbf{w}^T(n)\,\mathbf{x}(n) \tag{2.1}$$

where $\mathbf{x}(n)$, called the *tap reference vector*, is given by

$$\mathbf{x}(n) = \begin{bmatrix} x(n) & x(n-1) & \dots & x(n-L+1) \end{bmatrix}^T \tag{2.2}$$

and $\mathbf{w}(n)$, called the (adaptive) *weight vector*, is formed by filter parameters w_0, w_1, ...and w_{L-1} as

$$\mathbf{w}(n) = \begin{bmatrix} w_0(n) & w_1(n) & \dots & w_{L-1}(n) \end{bmatrix}^T \tag{2.3}$$

The FxLMS algorithm performs an adaptation process on $\mathbf{w}(n)$ in such a way that $y(n)$ causes the power of the residual acoustic noise $e(n)$ to be minimised. The derivation of this algorithm is left to Section 2.2.

2.1.2 Actual Secondary Path

A realistic secondary path can be represented by a Finite Impulse Response (FIR) system of length Q with an unknown impulse response in the form of

$$s(n) = \sum_{q=0}^{Q-1} s_q \delta(n-q) \tag{2.4}$$

where $\delta(n)$ is Kronecker delta function and s_q is the amplitude of the impulse response at time index q. Alternatively, this impulse response can be represented in the vector form of

$$\mathbf{s} \triangleq \begin{bmatrix} s_0 & s_1 & \dots & s_{Q-1} \end{bmatrix}^T \tag{2.5}$$

Note that the above formulation for the secondary path does not introduce any constraint because actual electro-acoustic channels usually have finite-duration impulse responses (FIR). However, even if a secondary path has an infinite impulse response, it can be represented by a FIR system of high order.

2.1.3 Secondary Path Model

As discussed in Chapter 1, the realisation of the FxLMS algorithm requires an estimate of the secondary path to be uploaded into the electronic control system. This estimate model, which is usually referred to as the *secondary path model*, can be obtained by using off-line secondary path identification techniques prior to the operation of the ANC system [7], or by using on-line techniques during the operation of the ANC system [57–60]. Since the actual secondary path is a FIR system, the secondary path model can be assumed to be another FIR system with the impulse response given by

$$\hat{s}\left(n\right) = \sum_{m=0}^{M-1} \hat{s}_m \delta\left(n-m\right) \tag{2.6}$$

where M is the length of the impulse response (usually $M < Q$) and scalar parameter $\hat{s}_m$ is the amplitude of the impulse response at time index m. Similar to the actual secondary path impulse response, $\hat{s}\left(n\right)$ can be represented by a $Q \times 1$ vector of

$$\hat{\mathbf{s}} \triangleq \left[\begin{array}{cccccc} \hat{s}_0 & \hat{s}_1 & \dots & \hat{s}_{M-1} & 0 & \dots \quad 0 \end{array} \right]^T \tag{2.7}$$

By using the definitions, given in Eqs. (2.5) and (2.7), it can be stated that when the secondary path model is perfect, vectors $\mathbf{s}$ and $\hat{\mathbf{s}}$ are equal: $\mathbf{s} = \hat{\mathbf{s}}$ and when the secondary path model is not perfect, these two vectors are not equal: $\mathbf{s} \neq \hat{\mathbf{s}}$.

2.2 Algorithm Derivation

This section drives the FxLMS algorithm as a gradient-based adaptation algorithm. It is shown that performing this algorithm on a transversal ANC controller causes the residual acoustic noise power to become minimal.

2.2.1 Modelling Residual Noise

Usually, the derivation of the FxLMS algorithm begins with developing a mathematical expression for the residual acoustic noise $e\left(n\right)$. This expression is then optimised with respect to $\mathbf{w}\left(n\right)$. For this purpose, by using Figure 2.1, $e\left(n\right)$ is initially expressed as

$$e\left(n\right) = d\left(n\right) - s\left(n\right) * y\left(n\right) \tag{2.8}$$

Now, substituting Eqs. (2.1) and (2.4) into (2.8) results in:

$$e(n) = d(n) - \sum_{q=0}^{Q-1} s_q \mathbf{w}^T(n-q)\,\mathbf{x}(n-q) \tag{2.9}$$

Eq. (2.9) gives an appropriate expression for $e(n)$, which can be used in the derivation of the FxLMS algorithm. In the following, this expression is used to minimise the power of $e(n)$ with respect to $\mathbf{w}(n)$.

2.2.2 Optimal ANC Controller

Here, the cost function $J(n)$ is defined as the power (or variance) of $e(n)$:

$$J(n) \triangleq E\left\{e^2(n)\right\} \tag{2.10}$$

where $E\{.\}$ denotes the *statistical expectation* operator. This cost function is usually referred to as the *Mean Square Error* (MSE) function. The *optimal weight vector* of an ANC controller, denoted by $\mathbf{w}_o(n)$, is the weight vector for which the MSE function is minimised. It can be shown that, for a stationary acoustic noise, the optimal weight vector is time-invariant [11]:

$$\forall n, \qquad \mathbf{w}_o(n) = \mathbf{w}_o \tag{2.11}$$

Accordingly, the optimal control signal, denoted by $y_o(n)$, can be expressed by setting $\mathbf{w}(n) = \mathbf{w}_o$ in Eq. (2.1) as

$$y_o(n) = y(n)|_{\mathbf{w}_o} = \mathbf{w}_o^T \mathbf{x}(n) \tag{2.12}$$

Similarly, the optimal residual acoustic noise, denoted by $e_o(n)$, can be expressed by setting $y(n) = y_o(n)$ in Eq. (2.9) as

$$e_o(n) = e(n)|_{y_o(n)} = d(n) - \mathbf{w}_o^T \sum_{q=0}^{Q-1} s_q \mathbf{x}(n-q) \tag{2.13}$$

This expression for $e_o(n)$ can be re-expressed in the form of

$$e_o(n) = d(n) - \mathbf{w}_o^T \mathbf{f}(n) \tag{2.14}$$

where $\mathbf{f}(n)$ is defined as

$$\mathbf{f}(n) \triangleq \sum_{q=0}^{Q-1} s_q \mathbf{x}(n-q) \tag{2.15}$$

Finally, the *minimal MSE*, denoted by J_o, can be obtained by setting $e(n) = e_o(n)$ in Eq. (2.10) as

$$J_o = E\left\{e_o^2(n)\right\} = \sigma_d^2 - 2\mathbf{w}_o^T E\left\{d(n)\,\mathbf{f}(n)\right\} + \mathbf{w}_o^T E\left\{\mathbf{f}(n)\,\mathbf{f}^T(n)\right\}\mathbf{w}_o \tag{2.16}$$

where $\sigma_d^2 = E\left\{d^2(n)\right\}$ is the power of the primary acoustic noise $d(n)$. Now, the cross-correlation vector $\mathbf{p}_f$ is defined as

$$\mathbf{p}_f \triangleq E\left\{\mathbf{f}(n)d(n)\right\} \tag{2.17}$$

Also, the auto-correlation matrix $\mathbf{R}_f$ is defined as

$$\mathbf{R}_f \triangleq E\left\{\mathbf{f}(n)\mathbf{f}^T(n)\right\} \tag{2.18}$$

By using these definitions, Eq. (2.16) can be re-expressed as

$$J_o = \sigma_d^2 - 2\mathbf{w}_o^T\mathbf{p}_f + \mathbf{w}_o^T\mathbf{R}_f\mathbf{w}_o \tag{2.19}$$

For a stationary acoustic noise, where $\mathbf{p}_f$ and $\mathbf{R}_f$ are constants, the minimal MSE is time-invariant, and, therefore, it can be represented by J_o. Also, since $\mathbf{w}_o$ minimises J_o, the following equation can be stated.

$$\nabla J_o|_{\mathbf{w}_o} = 0 \tag{2.20}$$

where ∇ is the *vector-gradient* operator. Now, combining Eqs. (2.19) and (2.20) results in

$$-2\mathbf{p}_f + 2\mathbf{R}_f\mathbf{w}_o = 0 \tag{2.21}$$

By solving this equation, the optimal weigh vector $\mathbf{w}_o$ can be obtained as

$$\mathbf{w}_o = \mathbf{R}_f^{-1}\mathbf{p}_f \tag{2.22}$$

Finally, combining Eqs. (2.19) and (2.22), the optimal MSE is obtained as

$$J_o = \sigma_d^2 - \mathbf{p}_f^T\mathbf{R}_f^{-1}\mathbf{p}_f \tag{2.23}$$

In signal processing, the optimal weight vector, given in Eq. (2.22), is usually referred to as the *Wiener-Hopf optimal filter*. Also, the value of J_o is referred to as the minimum achievable MSE function. In ANC literature, J_o can be interpreted as the minimum achievable residual acoustic noise power. Note that J_o is only a function of acoustic noise statistics and impulse responses of primary and secondary paths. In other words, J_o is independent of instantaneous values of the acoustic noise and operational parameters of the FxLMS algorithms (e.g. step-size and secondary path model).

2.2.3 Gradient-Based Optimisation

The optimal weight vector, given in Eq. (2.22), can be directly calculated from $\mathbf{R}_f$ and $\mathbf{p}_f$; however, estimation of $\mathbf{R}_f$ and $\mathbf{p}_f$ requires a considerable amount of computation. Another approach to determining the optimal weight vector is based on using the *steepest-descent method* [61]. According to this method, if the weight vector $\mathbf{w}(n)$ is updated by the following equation, then it is bound to move towards the optimal solution given in Eq. (2.22).

$$\mathbf{w}(n+1) = \mathbf{w}(n) - \frac{1}{2}\mu\nabla J(n) \tag{2.24}$$

where scalar parameter μ is the *adaptation step-size*. For the realisation of this equation, it is required to estimate $\nabla J(n)$ in terms of available parameters and signals so that it can be computed. For this purpose, the following approximation should be made [11].

$$\nabla J(n) \quad = \nabla E\left\{e^2(n)\right\} = E\left\{\nabla e^2(n)\right\} \simeq \quad \nabla e^2(n) = 2e(n)\nabla e(n) \tag{2.25}$$

According to Eq. (2.25), the computation of $\nabla J(n)$ requires an estimation for $\nabla e(n)$. By differentiating Eq. (2.9), $\nabla e(n)$ can be expressed as

$$\nabla e(n) = \frac{\partial e(n)}{\partial \mathbf{w}(n)} = -\sum_{q=0}^{Q-1} s_q \frac{\partial \mathbf{w}^T(n-q)}{\partial \mathbf{w}(n)} \mathbf{x}(n-q) \tag{2.26}$$

When the adaptation process is slow, it can be assumed that

$$\mathbf{w}(n) \approx \mathbf{w}(n-1) \approx \cdots \approx \mathbf{w}(n-Q+1) \tag{2.27}$$

Substituting this approximation into Eq. (2.26) results in

$$\nabla e(n) = -\sum_{q=0}^{Q-1} s_q \mathbf{x}(n-q) \tag{2.28}$$

From Eqs. (2.15) and (2.28), it can be shown that

$$\nabla e(n) = -\mathbf{f}(n) \tag{2.29}$$

Subsequently, combining Eqs. (2.25) and (2.29) results in

$$\nabla J(n) = -2e(n)\mathbf{f}(n) \tag{2.30}$$

Now, the FxLMS update equation can be obtained by substituting Eq. (2.30) into (2.24) as

$$\mathbf{w}(n+1) = \mathbf{w}(n) + \mu e(n)\mathbf{f}(n) \tag{2.31}$$

In practise, $\mathbf{f}(n)$ is not physically available, therefore, the implementation of Eq. (2.31) requires an estimate of $\mathbf{f}(n)$. This estimate can be obtained by filtering $\mathbf{x}(n)$ using the available estimate of the secondary path, given in Eq. (2.6). Therefore, the estimate of $\mathbf{f}(n)$, denoted by $\hat{\mathbf{f}}(n)$, can be obtained by

$$\hat{\mathbf{f}}(n) = \sum_{m=0}^{M-1} \hat{s}_m \mathbf{x}(n-m) \tag{2.32}$$

Usually, $\hat{\mathbf{f}}(n)$ is called the *filtered reference vector*. Now, by replacing $\mathbf{f}(n)$ with $\hat{\mathbf{f}}(n)$ in Eq. (2.30), $\nabla J(n)$ is approximated by

$$\nabla J(n) \approx -2e(n)\hat{\mathbf{f}}(n) \tag{2.33}$$

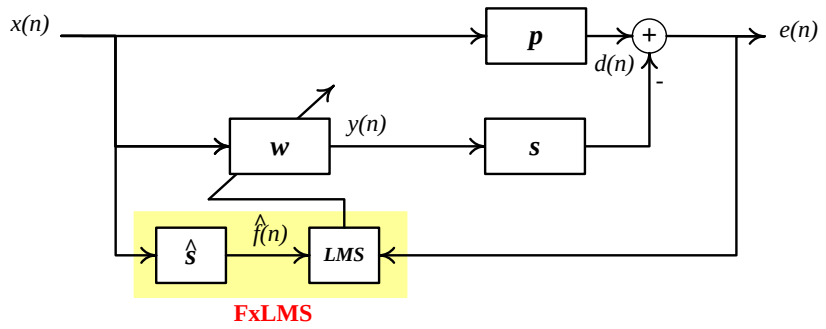

Figure 2.2: Functional block diagram of FxLMS-based ANC

Also, the updating equation, given in Eq. (2.24), becomes

$$\mathbf{w}\left(n+1\right)=\mathbf{w}\left(n\right)+\mu e\left(n\right)\hat{\mathbf{f}}\left(n\right) \tag{2.34}$$

Eq. (2.34) can be implemented using available signals and parameters. As shown in Figure 2.2, $\hat{\mathbf{f}}\left(n\right)$ can be obtained by filtering the reference signal and buffering the obtained values as

$$\hat{\mathbf{f}}\left(n\right)=\left[\begin{array}{cccc}\hat{f}\left(n\right) & \hat{f}\left(n-1\right) & \ldots & \hat{f}\left(n-L+1\right)\end{array}\right]^{T} \tag{2.35}$$

where $\hat{f}\left(n\right)$ is the *filtered-reference signal* given by

$$\hat{f}\left(n\right)=\sum_{m=0}^{M-1}\hat{s}_{m}x\left(n-m\right) \tag{2.36}$$

Eqs. (2.34)-(2.36) give a formulation for the FxLMS algorithm, which can be implemented practically.

2.3 Rotated Vectors

In the analysis of a gradient-based adaptation algorithm, it is more convenient to use the rotated reference vector and rotated weight misalignment vector, instead of the original reference and weight vectors [61]. This is because the auto-correlation matrix of the rotated reference vector is diagonal, and the equilibrium point of the rotated weight misalignment vector is the origin, rather than the Wiener-Hopf solution. In this section, these rotated vectors are introduced.

2.3.1 Auto-Correlation Matrix

The *Auto-Correlation Matrix* (ACM) of the reference vector is defined as

$$\mathbf{R}\triangleq E\left\{\mathbf{x}\left(n\right)\mathbf{x}^{T}\left(n\right)\right\} \tag{2.37}$$

Since $\mathbf{R}$ is a Toeplitz matrix, it can be diagonalised as

$$\mathbf{R}=\mathbf{F}\mathbf{\Lambda}\mathbf{F}^{T} \tag{2.38}$$

where square matrix $\mathbf{F}$ is the modal matrix, formed by the Eigenvectors of $\mathbf{R}$:

$$\mathbf{F} = \begin{bmatrix} \mathbf{F}_0 & \mathbf{F}_1 & \dots & \mathbf{F}_{L-1} \end{bmatrix} \tag{2.39}$$

and diagonal matrix $\mathbf{\Lambda}$ is formed by the Eigenvalues of $\mathbf{R}$:

$$\mathbf{\Lambda} = \begin{bmatrix} \lambda_0 & 0 & \dots & 0 \\ 0 & \lambda_1 & \ddots & \vdots \\ \vdots & \ddots & \ddots & 0 \\ 0 & \dots & 0 & \lambda_{L-1} \end{bmatrix} \tag{2.40}$$

In Eqs. (2.39) and (2.40), $\mathbf{F}_0, \mathbf{F}_1, \dots, \mathbf{F}_{L-1}$ are Eigenvectors and $\lambda_0, \lambda_1, \dots, \lambda_{L-1}$ are Eigenvalues of the ACM matrix $\mathbf{R}$. The inverse of any modal matrix is equal to its transpose; thus:

$$\mathbf{F}^T\mathbf{F} = \mathbf{I} \tag{2.41}$$

In this case, from Eqs. (2.38) and (2.41) it can be shown that

$$\mathbf{F}^T\mathbf{R}\mathbf{F} = \mathbf{\Lambda} \tag{2.42}$$

Eqs. (2.41) and (2.42) are widely used in the next chapters.

2.3.2 Rotated Reference Vector

Using the modal matrix $\mathbf{F}$ as a rotation matrix, the *rotated reference vector* is defined as:

$$\mathbf{z}(n) \triangleq \mathbf{F}^T\mathbf{x}(n) \tag{2.43}$$

This vector can be expressed in the form of

$$\mathbf{z}(n) = \begin{bmatrix} z_0(n) & z_1(n) & \dots & z_{L-1}(n) \end{bmatrix}^T \tag{2.44}$$

From Eq. (2.43), it can be shown that the l-th element of $\mathbf{z}(n)$ can be computed as

$$z_l(n) = \mathbf{F}_l^T\mathbf{x}(n), \qquad l = 0, 1, \dots, L-1 \tag{2.45}$$

where vector $\mathbf{F}_l$ is the l-th column of matrix $\mathbf{F}$.

2.3.3 Rotated Weight Misalignment Vector

The *weight misalignment vector* at time n, denoted by $\mathbf{v}(n)$, is defined as the difference between the weight vector at time n and the optimal weight vector:

$$\mathbf{v}(n) \triangleq \mathbf{w}(n) - \mathbf{w}_o, \tag{2.46}$$

Also, the rotated weight misalignment vector is defined as

$$\mathbf{c}(n) \triangleq \mathbf{F}^T \mathbf{v}(n) = \mathbf{F}^T (\mathbf{w}(n) - \mathbf{w}_o). \tag{2.47}$$

This vector can be also represented in the form of

$$\mathbf{c}(n) = \begin{bmatrix} c_0(n) & c_1(n) & \dots & c_{L-1}(n) \end{bmatrix}^T. \tag{2.48}$$

where $c_l(n)$ is computed as

$$c_l(n) = \mathbf{F}_l^T (\mathbf{w}(n) - \mathbf{w}_o),, \qquad l = 0, 1, \dots, L-1. \tag{2.49}$$

As can be seen in Eq. (2.49), when $\mathbf{w}(n)$ converges to $\mathbf{w}_o$, the rotated weight misalignment vector converges to the origin. Due to this property, the analysis of the FxLMS algorithm using the rotated weight misalignment vector is more convenient.

2.4 Independence Assumptions

The analysis of gradient-based adaptation algorithms with stochastic reference signals is usually performed based on a set of simplifying assumptions, called the *independence assumptions*. These assumptions were proposed by Gardener in a signal processing context [62]; however, they have been widely used in analysing adaptive ANC systems. As Gardener stated in [62], "the independence assumptions apparently cannot be analytically justified for practical cases, but this is perhaps the best that can be done from the pragmatic point of view of obtaining a good trade-off between model realism and model tractability".

In the following, these assumptions are discussed and formulated in detail. Later, the validity of the theoretical results obtained by using these assumptions are verified in computer simulation and practise.

2.4.1 Primary Independence Assumption

The primary independence assumption states that, for a Gaussian reference signal, the sequence of reference vectors can be considered as an *independent identically distributed* (i.i.d) sequence with zero mean [62]. Accordingly, consecutive reference vectors are statistically independent. Based on this assumption, it can be shown that, for time indexes n_1 and n_2,

$$E\left\{\mathbf{x}(n_1)\mathbf{x}^T(n_2)\right\} = \begin{cases} \mathbf{R} & n_1 = n_2 \\ \mathbf{0} & n_1 \neq n_2 \end{cases} \tag{2.50}$$

where matrix $\mathbf{R}$ is given in Eq. (2.37). The above equality can be also re-expressed in the form of

$$E\left\{\mathbf{x}(n-m)\mathbf{x}^T(n-p)\right\} = \delta_{m,p}\mathbf{R} \qquad \forall n, m, p \in \mathbb{N} \tag{2.51}$$

Also, by using Eqs. (2.43) and (2.51), it can be shown that

$$E\left\{\mathbf{z}\left(n-m\right)\mathbf{z}^{T}\left(n-p\right)\right\}=\delta_{m,p}\mathbf{\Lambda}\qquad\forall n,m,p\in\mathbb{N},\tag{2.52}$$

Eq. (2.52) shows that consecutive rotated reference vectors are statistically independent and the ACM of these vector variables is the diagonal matrix $\mathbf{\Lambda}$.

2.4.2 Secondary Independence Assumption

According to the secondary independence assumption, for the problem of adaptive identification of an unknown system with finite impulse response (e.g. transversal ANC controllers), the optimal error (which is equivalent to $e_o\left(n\right)$ in ANC) is independent of the reference vector sequence [62]:

$$E\left\{e_o\left(n_1\right)\mathbf{x}\left(n_2\right)\right\}=E\left\{e_o\left(n_1\right)\right\}E\left\{\mathbf{x}\left(n_2\right)\right\}\tag{2.53}$$

Left multiplying both sides of this equality by $\mathbf{F}^T$ results in

$$E\left\{e_o\left(n_1\right)\mathbf{z}\left(n_2\right)\right\}=E\left\{e_o\left(n_1\right)\right\}E\left\{\mathbf{z}\left(n_2\right)\right\}\tag{2.54}$$

This equality shows that the optimal residual acoustic noise is also independent of the rotated reference vectors. Since the reference vector has zero mean, the following results can be obtained from Eqs. (2.53) and (2.54), respectively:

$$E\left\{e_o\left(n_1\right)\mathbf{x}\left(n_2\right)\right\}=\mathbf{0}\tag{2.55}$$

and

$$E\left\{e_o\left(n_1\right)\mathbf{z}\left(n_2\right)\right\}=\mathbf{0}\tag{2.56}$$

Therefore, the optimal residual acoustic noise is uncorrelated with both the reference and rotated reference vectors.

2.4.3 Independence of Weights and Reference Signal

Usually it is assumed that the weights of the ANC controller and samples of the reference signal are statistically independent [11, 63]. Based on this assumption, it can be shown that

$$E\left\{\mathbf{w}^{T}\left(n_1\right)\mathbf{x}\left(n_2\right)\right\}=E\left\{\mathbf{w}^{T}\left(n_1\right)\right\}E\left\{\mathbf{x}\left(n_2\right)\right\}\tag{2.57}$$

Also, from this equality, it can be shown that $\mathbf{c}\left(n\right)$ and $\mathbf{z}\left(n\right)$ are statistically independent. For proving this, both sides of Eq. (2.57), should be manipulated as

$$E\left\{\left[\mathbf{w}^{T}\left(n_1\right)-\mathbf{w}_o^{T}\right]\mathbf{x}\left(n_2\right)\right\}=E\left\{\mathbf{w}^{T}\left(n_1\right)\right\}E\left\{\mathbf{x}\left(n_2\right)\right\}-\mathbf{w}_o^{T}E\left\{\mathbf{x}\left(n_2\right)\right\}\tag{2.58}$$

The right side of this equality can be modified as

$$E\left\{\left[\mathbf{w}^{T}\left(n_1\right)-\mathbf{w}_o^{T}\right]\mathbf{x}\left(n_2\right)\right\}=\left(E\left\{\mathbf{w}^{T}\left(n_1\right)-\mathbf{w}_o^{T}\right\}\right)E\left\{\mathbf{x}\left(n_2\right)\right\}\tag{2.59}$$

Since $\mathbf{F}\mathbf{F}^T = \mathbf{I}$, Eq. (2.59) can be re-expressed as

$$E\left\{\left[\mathbf{w}^T(n_1) - \mathbf{w}_o^T\right]\mathbf{F}\mathbf{F}^T\mathbf{x}(n_2)\right\} = \left(E\left\{\mathbf{w}^T(n_1) - \mathbf{w}_o^T\right\}\mathbf{F}\right)E\left\{\mathbf{F}^T\mathbf{x}(n_2)\right\} \tag{2.60}$$

Finally, combining Eqs. (2.43), (2.47) and (2.61) results in

$$E\left\{\mathbf{c}^T(n_1)\,\mathbf{z}(n_2)\right\} = E\left\{\mathbf{c}^T(n_1)\right\}E\left\{\mathbf{z}(n_2)\right\} \tag{2.61}$$

This equality shows that the rotated weight misalignment vector $\mathbf{c}$ and rotated reference vector $\mathbf{z}$ are statistically independent. Note that for stationary acoustic noise $E\{\mathbf{x}(n)\} = E\{\mathbf{z}(n)\} = 0$.

2.5 Basic Model for FxLMS-Based ANC

This section expresses the FxLMS update equation and the residual acoustic noise in terms of rotated variables. The obtained expressions are used later in Chapters 3-6. Also, this section develops a dynamic model for the first-order moments of the adaptive weights in the FxLMS-based ANC systems. This dynamic model is the core of Chapters 8 and 9.

2.5.1 Alternative Expression for FxLMS Update Equation

In order to express the FxLMS update equation in terms of the rotated variables, Eq. (2.34) can be modified as follows.

$$\mathbf{F}^T\left[\mathbf{w}(n+1) - \mathbf{w}_o\right] \;=\; \mathbf{F}^T\left[\mathbf{w}(n) - \mathbf{w}_o\right] + \mu e(n)\mathbf{F}^T\hat{\mathbf{f}}(n) \tag{2.62}$$

Combining Eqs. (2.47) and (2.62) results in

$$\mathbf{c}(n+1) = \mathbf{c}(n) + \mu e(n)\mathbf{F}^{\mathbf{T}}\hat{\mathbf{f}}(n) \tag{2.63}$$

Now, the rotated filtered reference vector is defined as

$$\hat{\mathbf{g}}(n) = \mathbf{F}^{\mathbf{T}}\hat{\mathbf{f}}(n) \tag{2.64}$$

By using this definition, Eq. (2.63) can be re-expressed as

$$\mathbf{c}(n+1) = \mathbf{c}(n) + \mu e(n)\hat{\mathbf{g}}(n) \tag{2.65}$$

According to Eqs. (2.32), (2.43) and (2.64), vector $\hat{\mathbf{g}}(n)$ can be obtained by filtering $\mathbf{z}(n)$ using the available estimate of the secondary path:

$$\hat{\mathbf{g}}(n) = \sum_{m=0}^{M-1}\hat{s}_m\mathbf{z}(n-m), \tag{2.66}$$

Alternatively, $\hat{\mathbf{g}}(n)$ can be also represented in the form of

$$\hat{\mathbf{g}}(n) = \begin{bmatrix} \hat{g}_0(n) & \hat{g}_1(n) & \dots & \hat{g}_{L-1}(n) \end{bmatrix}^T, \tag{2.67}$$

where

$$\hat{g}_l(n) = \sum_{m=0}^{M-1} \hat{s}_m z_l(n-m). \tag{2.68}$$

Eqs. (2.65)-(2.68) describe the FxLMS update equation in terms of the rotated variables.

2.5.2 Alternative Expression for Residual Acoustic Noise

In order to develop an expression for the residual acoustic noise in terms of the rotated variables, Eq. (2.9) can be modified as follows.

$$\begin{aligned} e(n) &= d(n) - \sum_{q=0}^{Q-1} s_q \left[\mathbf{w}^T(n-q) - \mathbf{w}_o^T + \mathbf{w}_o^T\right] \mathbf{x}(n-q) \\ &= d(n) - \sum_{q=0}^{Q-1} s_q \mathbf{w}_o^T \mathbf{x}(n-q) - \sum_{q=0}^{Q-1} s_q \left[\mathbf{w}^T(n-q) - \mathbf{w}_o^T\right] \mathbf{F}\mathbf{F}^{\mathbf{T}}\mathbf{x}(n-q) \end{aligned} \tag{2.69}$$

As can be seen, $\mathbf{z}(n)$, $\mathbf{c}(n)$ and $\mathbf{f}(n)$ appear in the right side of Eq. (2.69); thus,

$$\begin{aligned} e(n) &= d(n) - \mathbf{w}_o^T \sum_{q=0}^{Q-1} s_q \mathbf{x}(n-q) - \sum_{q=0}^{Q-1} s_q \mathbf{c}^T(n-q)\mathbf{z}(n-q) \\ &= d(n) - \mathbf{w}_o^T \mathbf{f}(n) - \sum_{q=0}^{Q-1} s_q \mathbf{c}^T(n-q)\mathbf{z}(n-q). \end{aligned} \tag{2.70}$$

According to Eq. (2.14), the summation of the first two terms in Eq. (2.70) is equal to $e_o(t)$; therefore, Eq. (2.70) can be simplified to

$$e(n) = e_o(n) - \sum_{q=0}^{Q-1} s_q \mathbf{c}^T(n-q)\mathbf{z}(n-q). \tag{2.71}$$

or equivalently

$$e(n) = e_o(n) - \sum_{q=0}^{Q-1} s_q \mathbf{z}^T(n-q)\mathbf{c}(n-q). \tag{2.72}$$

This equation expresses the residual acoustic noise in terms of the rotated variables.

2.5.3 Dynamics of First-Order Moments

In [49], a dynamic model for the FxLMS adaptation process was derived. In the following, this model is derived and expressed in accordance with the terminology used in this thesis. For this purpose, Eqs.

(2.72) and (2.65) are initially combined as

$$\mathbf{c}\left(n+1\right)=\mathbf{c}\left(n\right)+\mu e_o\left(n\right)\hat{\mathbf{g}}\left(n\right)-\mu\sum_{q=0}^{Q-1}s_q\hat{\mathbf{g}}\left(n\right)\mathbf{z}^T\left(n-q\right)\mathbf{c}\left(n-q\right) \tag{2.73}$$

Combining Eqs. (2.66) and (2.73) results in

$$\mathbf{c}\left(n+1\right)=\mathbf{c}\left(n\right)+\mu e_o\left(n\right)\hat{\mathbf{g}}\left(n\right)-\mu\sum_{q=0}^{Q-1}\sum_{m=0}^{M-1}\hat{s}_m s_q\mathbf{z}\left(n-m\right)\mathbf{z}^T\left(n-q\right)\mathbf{c}\left(n-q\right) \tag{2.74}$$

Now, taking the statistical expectation form both sides of Eq. (2.74) results in

$$\bar{\mathbf{c}}\left(n+1\right)=\bar{\mathbf{c}}\left(n\right)+\mu E\left\{e_o\left(n\right)\hat{\mathbf{g}}\left(n\right)\right\}-\mu\sum_{q=0}^{Q-1}\sum_{m=0}^{M-1}\hat{s}_m s_q E\left\{\mathbf{z}\left(n-m\right)\mathbf{z}^T\left(n-q\right)\mathbf{c}\left(n-q\right)\right\} \tag{2.75}$$

where $\bar{\mathbf{c}}\left(n\right)$ is defined as the mean of the rotated weight misalignment vector:

$$\bar{\mathbf{c}}\left(n\right)\triangleq E\left\{\mathbf{c}\left(n\right)\right\} \tag{2.76}$$

$\bar{\mathbf{c}}\left(n\right)$ can be interpreted as the first-order moment of the adaptive weight vector. According to the secondary independence assumption, the optimal residual acoustic noise is uncorrelated with rotated reference vectors: $E\left\{e_o\left(n\right)\hat{\mathbf{g}}\left(n\right)\right\}=0$. Substituting this result into Eq. (2.75) results in

$$\bar{\mathbf{c}}\left(n+1\right)=\bar{\mathbf{c}}\left(n\right)-\mu\sum_{q=0}^{Q-1}\sum_{m=0}^{M-1}\hat{s}_m s_q E\left\{\mathbf{z}\left(n-m\right)\mathbf{z}^T\left(n-q\right)\mathbf{c}\left(n-q\right)\right\} \tag{2.77}$$

Since weights and reference signal are independent, Eq. (2.77) can be modified to

$$\bar{\mathbf{c}}\left(n+1\right)=\bar{\mathbf{c}}\left(n\right)-\mu\sum_{q=0}^{Q-1}\sum_{m=0}^{M-1}\hat{s}_m s_q E\left\{\mathbf{z}\left(n-m\right)\mathbf{z}^T\left(n-q\right)\right\}\bar{\mathbf{c}}\left(n-q\right) \tag{2.78}$$

Now, combining Eqs. (2.52) and (2.78) results in

$$\bar{\mathbf{c}}\left(n+1\right)=\bar{\mathbf{c}}\left(n\right)-\mu\sum_{q=0}^{Q-1}\sum_{m=0}^{M-1}\hat{s}_m s_q\delta_{m,q}\mathbf{\Lambda}\bar{\mathbf{c}}\left(n-q\right) \tag{2.79}$$

Assuming a perfect secondary path model ($\hat{\mathbf{s}}=\mathbf{s}$), Eq. (2.79) becomes

$$\bar{\mathbf{c}}\left(n+1\right)=\bar{\mathbf{c}}\left(n\right)-\mu\mathbf{\Lambda}\sum_{q=0}^{Q-1}s_q^2\bar{\mathbf{c}}\left(n-q\right) \tag{2.80}$$

Eq. (2.80) formulates a dynamic model for the first-order moments in FxLMS-based ANC systems. This model is used in Chapters 8 and 9.

Chapter 3

Stochastic Model for FxLMS-Based ANC

There are several contributions on theoretical modelling of FxLMS-based ANC systems [42–49]. However, when it is intended to derive elegant closed-form expressions for formulating stability or steady-state behaviours of these systems, a number of simplifying assumptions regarding the acoustic noise, the actual secondary path and its model have to be used.

This chapter develops a dynamic model for FxLMS-based ANC systems, considering a general stochastic acoustic noise and a general secondary path. Also, an arbitrary secondary path model, which is not necessarily a perfect model, is considered. The main distinction of the proposed model is its properties based on which closed-form expressions for formulating system behaviours can be derived, without using any simplifying assumptions regarding the acoustic noise, nor regarding the secondary path and its model. The derivation of these expressions are left to the next chapters.

3.1 MSE Function

This section derives an alternative expression for the MSE function. For this purpose, this function is initially expressed by combining Eqs. (2.10) and (2.71) as

$$\begin{aligned} J(n) &= E\left\{e_o^2(n)\right\} - 2\sum_{q=0}^{Q-1} s_q E\left\{\mathbf{c}^T(n-q)\,\mathbf{z}(n-q)\,e_o(n)\right\} \\ &\quad + \sum_{q,p=0}^{Q-1} s_q s_p E\left\{\mathbf{c}^T(n-q)\,\mathbf{z}(n-q)\,\mathbf{z}^T(n-p)\,\mathbf{c}(n-p)\right\} \end{aligned} \tag{3.1}$$

According to Eq. (2.16), the first term in Eq. (3.1) is equal to J_o. The second term is equal to zero because based on the independence assumptions, discussed in Chapter 2, the rotated reference vector $\mathbf{z}(n-q)$ is a zero mean vector and statistically independent of $e_o(n)$ and $\mathbf{c}(n)$. Therefore, Eq. (3.1) can be simplified to

$$J(n) = J_o + \sum_{q,p=0}^{Q-1} s_q s_p E\left\{\mathbf{c}^T(n-q)\,\mathbf{z}(n-q)\,\mathbf{z}^{\mathbf{T}}(n-p)\,\mathbf{c}(n-p)\right\} \tag{3.2}$$

Now, combining Eqs. (2.44), (2.48) and (3.2) results in

$$\begin{aligned} J(n) &= J_o + \sum_{q,p=0}^{Q-1} s_q s_p E\left\{\sum_{l=0}^{L-1} c_l(n-q)\, z_l(n-q) \sum_{k=0}^{L-1} z_k(n-p)\, c_k(n-p)\right\} \\ &= J_o + \sum_{q,p=0}^{Q-1}\sum_{l,k=0}^{L-1} s_q s_p E\left\{c_l(n-q)\, c_k(n-p)\, z_l(n-q)\, z_k(n-p)\right\} \end{aligned} \tag{3.3}$$

Since samples of the reference signal and adaptive weights are statistically independent (the third independence assumption), Eq. (3.3) can be simplified to

$$J(n) = J_o + \sum_{q,p=0}^{Q-1}\sum_{l,k=0}^{L-1} s_q s_p E\left\{z_l(n-q)\, z_k(n-p)\right\} E\left\{c_l(n-q)\, c_k(n-p)\right\} \tag{3.4}$$

Combining Eqs. (2.45) and (3.4) results in

$$J(n) = J_o + \sum_{q,p=0}^{Q-1}\sum_{l,k=0}^{L-1} s_q s_p E\left\{\mathbf{F}_l^T \mathbf{x}(n-q)\, \mathbf{F}_k^T \mathbf{x}(n-p)\right\} E\left\{c_l(n-q)\, c_k(n-p)\right\} \tag{3.5}$$

Since $\mathbf{F}_l$ and $\mathbf{F}_k$ are constant vectors, Eq. (3.5) can be simplified to

$$J(n) = J_o + \sum_{q,p=0}^{Q-1}\sum_{l,k=0}^{L-1} s_q s_p \mathbf{F}_l^T E\left\{\mathbf{x}(n-q)\, \mathbf{x}^T(n-p)\right\} \mathbf{F}_k E\left\{c_l(n-q)\, c_k(n-p)\right\} \tag{3.6}$$

Now, combining Eqs. (2.51) and (3.6) results in

$$J(n) = J_o + \sum_{q=0}^{Q-1}\sum_{l,k=0}^{L-1} s_q^2 \mathbf{F}_l^T \mathbf{R} \mathbf{F}_k E\left\{c_l(n-q)\, c_k(n-q)\right\} \tag{3.7}$$

On the other hand, from Eq. (2.42), it can be shown that

$$\mathbf{F}_l^T \mathbf{R} \mathbf{F}_k = \lambda_l \delta_{l,k} \tag{3.8}$$

Using this equality, Eq. (3.7) is simplified to

$$J(n) = J_o + \sum_{q=0}^{Q-1}\sum_{l=0}^{L-1} s_q^2 \lambda_l E\left\{c_l^2(n-q)\right\} \tag{3.9}$$

Finally, Eq. (3.9) can be expressed in the form of

$$J(n) = J_o + \sum_{q=0}^{Q-1} s_q^2 E\left\{\mathbf{c}^T(n-q)\, \mathbf{\Lambda} \mathbf{c}(n-q)\right\} \tag{3.10}$$

From Eq. (3.10), it can be seen that $J(n)$ is independent of instantaneous values of the acoustic noise. Also, it can be deduced that $J(n)$ is a positive scalar function of $\mathbf{c}(n)$.

3.2 Excess-MSE Function

Here, the *excess-MSE function* is defined as a dynamic measure, determining the deviation of the MSE function from its minimal level. Usually, the steady-state level of this function is referred to as the excess-MSE in ANC terminology. However, the excess-MSE function, which can be interpreted as the distance of the instantaneous residual noise power from the minimum achievable noise power, is considered in this thesis. Accordingly, stability behaviours of an ANC system can be studied by analysing the variation of the excess-MSE function during the operation of the adaptation algorithm on the ANC controller. For developing a dynamic model for the excess-MSE function, the MSE function is expressed as

$$J(n) = J_o + J_{ex}(n) \tag{3.11}$$

where J_o is the minimal MSE level and $J_{ex}(n)$ is the excess-MSE function. As can be seen in Eq. (3.11), the absolute value of $J_{ex}(n)$ determines how far the instantaneous residual noise power is from its minimal level. Obviously, since J_o is the minimal value of the positive definite function $J(n)$, $J_{ex}(n)$ is always a positive definite function of system variables:

$$\begin{aligned} \forall n,\ \min J(n) = J_o \quad &\Rightarrow \quad J(n) \geq J_o \Rightarrow J_o + J_{ex}(n) \geq J_o \\ &\Rightarrow \quad J_{ex}(n) \geq 0 \end{aligned} \tag{3.12}$$

Now, considering the expressions, given in Eqs. (3.10) and (3.11), $J_{ex}(n)$ can be formulated as

$$J_{ex}(n) \triangleq \sum_{q=0}^{Q-1} s_q^2 E\left\{\mathbf{c}^T(n-q)\,\mathbf{\Lambda c}(n-q)\right\} \tag{3.13}$$

Substituting Eqs. (2.40) and (2.48) into (3.13) results in

$$J_{ex}(n) = \sum_{q=0}^{Q-1}\sum_{l=0}^{L-1} \lambda_l s_q^2 E\left\{c_l^2(n-q)\right\} \tag{3.14}$$

which can be re-expressed as

$$J_{ex}(n) = \sum_{q=0}^{Q-1}\sum_{l=0}^{L-1} \lambda_l s_q^2 m_l(n-q) \tag{3.15}$$

where $m_0(n), m_1(n), \ldots, m_{L-1}(n)$ are the *second-order moments of the adaptive weights*:

$$m_l(n) \triangleq E\left\{c_l^2(n)\right\} \qquad l = 0, 1, \ldots, L-1 \tag{3.16}$$

Now, in order to investigate the variation of the excess-MSE function during the operation of the FxLMS algorithm, its time difference is defined as

$$\triangle J_{ex}(n) \triangleq J_{ex}(n+1) - J_{ex}(n) \tag{3.17}$$

By combining Eqs. (3.15) and (3.17), $\triangle J_{ex}(n)$ can be expressed as

$$\triangle J_{ex}(n) = \sum_{q=0}^{Q-1} \sum_{l=0}^{L-1} \lambda_l s_q^2 \triangle m_l(n-q) \tag{3.18}$$

where $\triangle m_l(n)$ is the time difference of the l-th second-order moment:

$$\triangle m_l(n) = m_l(n+1) - m_l(n), \qquad l = 0, 1, \ldots, L-1 \tag{3.19}$$

From Eq. (3.16), $\triangle m_l(n)$ can be expressed as

$$\triangle m_l(n) = E\left\{c_l^2(n+1)\right\} - E\left\{c_l^2(n)\right\} \tag{3.20}$$

On the other hand, from Eq. (2.65), it can be shown that

$$c_l(n+1) = c_l(n) + \mu \hat{g}_l(n) e(n) \tag{3.21}$$

By combining Eqs. (3.20) and (3.21), $\triangle m_l(n)$ is formulated by

$$\triangle m_l(n) = \mu^2 E\left\{\hat{g}_l^2(n) e^2(n)\right\} + 2\mu E\left\{c_l(n) \hat{g}_l(n) e(n)\right\} \tag{3.22}$$

On the other hand, from Eqs. (2.32), (2.45) and (2.68), it can be shown that

$$\hat{g}_l(n) = \mathbf{F}_l^T \hat{\mathbf{f}}(n) \tag{3.23}$$

By substituting the above expression for $\hat{g}_l(n)$ into Eq. (3.22), $\triangle m_l(n)$ is obtained as

$$\triangle m_l(n) = \mu^2 \mathbf{F}_l^T E\left\{\hat{\mathbf{f}}(n) \hat{\mathbf{f}}^T(n) e^2(n)\right\} \mathbf{F}_l + 2\mu \mathbf{F}_l^T E\left\{\hat{\mathbf{f}}(n) c_l(n) e(n)\right\} \tag{3.24}$$

This equation can be expressed as

$$\triangle m_l(n) = A_l(n) + B_l(n) \tag{3.25}$$

where scalar functions $A_l(n)$ and $B_l(n)$ are given by

$$A_l(n) = \mu^2 \mathbf{F}_l^T E\left\{\hat{\mathbf{f}}(n) \hat{\mathbf{f}}^T(n) e^2(n)\right\} \mathbf{F}_l \tag{3.26}$$

and,

$$B_l(n) = 2\mu \mathbf{F}_l^T E\left\{\hat{\mathbf{f}}(n) c_l(n) e(n)\right\} \tag{3.27}$$

The mathematical expressions, given in Eqs. (3.18) and (3.25)-(3.27), compose a stochastic dynamic model for the variation of the excess-MSE function during the operation of the FxLMS algorithm. The following two sections formulate scalar functions $A_l(n)$ and $B_l(n)$ and show that they are linear functions of the second-order moments $m_o(n), \ldots, m_{L-1}(n)$.

3.3 Variation of $A_l(n)$

Based on the third independence assumption, it can be shown that the reference vector $\mathbf{x}(n)$ is independent of the MSE function $J(n)$ [64]. Consequently, the filtered reference vector $\hat{\mathbf{f}}(n)$ is independent of $J(n)$. Accordingly, Eq. (3.26) can be simplified to

$$A_l(n) = \mu^2 \mathbf{F}_l^T E\left\{\hat{\mathbf{f}}(n)\,\hat{\mathbf{f}}^T(n)\right\}\mathbf{F}_l . J(n) \tag{3.28}$$

On the other hand, from Eqs. (2.32) and (2.51) , it can be shown that

$$\begin{aligned} E\left\{\hat{\mathbf{f}}(n)\,\hat{\mathbf{f}}^T(n)\right\} &= \sum_{q,p=0}^{M-1} \hat{s}_q \hat{s}_p E\left\{\mathbf{x}(n-q)\,\mathbf{x}^T(n-p)\right\} \\ &= \sum_{q=0}^{M-1} \hat{s}_q^2 \mathbf{R} \\ &= \|\hat{\mathbf{s}}\|^2 \mathbf{R} \end{aligned} \tag{3.29}$$

where $\|.\|$ denotes the Euclidean vector norm and vector $\hat{\mathbf{s}}$ is given in Eq. (2.7):

$$\|\hat{\mathbf{s}}\|^2 = \sum_{q=0}^{M-1} \hat{s}_q^2 = \sum_{q=0}^{Q-1} \hat{s}_q^2 \tag{3.30}$$

Now, by substituting Eq. (3.29) into (3.28), $A_l(n)$ is simplified to

$$A_l(n) = \mu^2 \|\hat{\mathbf{s}}\|^2 \mathbf{F}_l^T \mathbf{R} \mathbf{F}_l J(n) \tag{3.31}$$

From Eq. (2.42) , it can be shown that

$$\mathbf{F}_l^T \mathbf{R} \mathbf{F}_l = \lambda_l \tag{3.32}$$

Substituting this equality into Eq. (3.31) results in

$$A_l(n) = \mu^2 \lambda_l \|\hat{\mathbf{s}}\|^2 J(n) \tag{3.33}$$

Now, substituting Eq. (3.11) into Eq. (3.33) results in

$$A_l(n) = \mu^2 \lambda_l \|\hat{\mathbf{s}}\|^2 J_o + \mu^2 \lambda_l \|\hat{\mathbf{s}}\|^2 J_{ex}(n) \tag{3.34}$$

Finally, by using Eq. (3.15), Eq (3.34) can be expressed as

$$A_l(n) = \mu^2 \lambda_l \|\hat{\mathbf{s}}\|^2 J_o + \mu^2 \lambda_l \|\hat{\mathbf{s}}\|^2 \sum_{p=0}^{Q-1} \sum_{k=0}^{L-1} \lambda_k s_p^2 m_k(n-p) \tag{3.35}$$

Eq. (3.35) formulates $A_l(n)$ as a function of the second-order moments $m_o(n), \ldots, m_{L-1}(n)$.

3.4 Variation of $B_l(n)$

By substituting Eq. (2.71) into (3.27), $B_l(n)$ is expanded to

$$B_l(n) = 2\mu \mathbf{F}_l^T E\left\{\hat{\mathbf{f}}(n)\, c_l(n)\, e_o(n)\right\} - 2\mu \mathbf{F}_l^T \sum_{p=0}^{Q-1} s_p E\left\{c_l(n)\, \hat{\mathbf{f}}(n)\, \mathbf{c}^T(n-p)\, \mathbf{z}(n-p)\right\} \quad (3.36)$$

Considering the second and third independence assumptions, the first term in Eq. (3.36) is simplified to

$$2\mu \mathbf{F}_l^T E\left\{\hat{\mathbf{f}}(n)\, c_l(n)\, e_o(n)\right\} = 2\mu \mathbf{F}_l^T E\left\{\hat{\mathbf{f}}(n)\right\} E\left\{c_l(n)\, e_o(n)\right\} \quad (3.37)$$

Since the reference signal has zero mean, it can be shown that $E\{\hat{\mathbf{f}}(n)\} = \mathbf{0}$; therefore,

$$2\mu \mathbf{F}_l^T E\left\{\hat{\mathbf{f}}(n)\, c_l(n)\, e_o(n)\right\} = 0 \quad (3.38)$$

By substituting Eq. (3.38) into (3.36), $B_l(n)$ is simplified to

$$B_l(n) = -2\mu \mathbf{F}_l^T \sum_{p=0}^{Q-1} s_p E\left\{c_l(n)\, \hat{\mathbf{f}}(n)\, \mathbf{c}^T(n-p)\, \mathbf{z}(n-p)\right\} \quad (3.39)$$

Now, substituting Eq. (2.32) into (3.39) results in

$$\begin{aligned} B_l(n) &= -2\mu \mathbf{F}_l^T \sum_{p=0}^{Q-1} s_p E\left\{c_l(n)\left(\sum_{m=0}^{M-1} \hat{s}_m \mathbf{x}(n-m)\right) \mathbf{c}^T(n-p)\, \mathbf{z}(n-p)\right\} \\ &= -2\mu \mathbf{F}_l^T \sum_{p=0}^{Q-1}\sum_{m=0}^{M-1} s_p \hat{s}_m E\left\{c_l(n)\, \mathbf{x}(n-m)\, \mathbf{c}^T(n-p)\, \mathbf{z}(n-p)\right\} \end{aligned} \quad (3.40)$$

Substituting Eqs. (2.44) and (2.48) into (3.40) results in

$$\begin{aligned} B_l(n) &= -2\mu \mathbf{F}_l^T \sum_{p=0}^{Q-1}\sum_{m=0}^{M-1} s_p \hat{s}_m E\left\{c_l(n)\, \mathbf{x}(n-m) \sum_{i=0}^{L-1} c_i(n-p)\, z_i(n-p)\right\} \\ &= -2\mu \mathbf{F}_l^T \sum_{p=0}^{Q-1}\sum_{m=0}^{M-1}\sum_{i=0}^{L-1} s_p \hat{s}_m E\left\{c_l(n)\, c_i(n-p)\, \mathbf{x}(n-m)\, z_i(n-p)\right\} \end{aligned} \quad (3.41)$$

On the other hand, from Eq. (2.45), it can be shown that

$$z_i(n-p) = \mathbf{x}^T(n-p)\, \mathbf{F}_i \quad (3.42)$$

Combining Eqs. (3.41) and (3.42) results in

$$B_l(n) = -2\mu \mathbf{F}_l^T \sum_{p=0}^{Q-1}\sum_{m=0}^{M-1}\sum_{i=0}^{L-1} s_p \hat{s}_m E\left\{c_l(n)\, c_i(n-p)\, \mathbf{x}(n-m)\, \mathbf{x}^T(n-p)\right\} \mathbf{F}_i \quad (3.43)$$

Considering that adaptive weights and noise samples are statistically independent (third independence assumption), Eq. (3.43) can be simplified to

$$B_l(n) = -2\mu \mathbf{F}_l^T \sum_{p=0}^{Q-1} \sum_{m=0}^{M-1} \sum_{i=0}^{L-1} s_p \hat{s}_m E\left\{c_l(n) c_i(n-p)\right\} E\left\{\mathbf{x}(n-m) \mathbf{x}^T(n-p)\right\} \mathbf{F}_i \tag{3.44}$$

Now, substituting Eq. (2.51) into (3.44) results in

$$\begin{aligned} B_l(n) &= -2\mu \mathbf{F}_l^T \sum_{p=0}^{Q-1} \sum_{m=0}^{M-1} \sum_{i=0}^{L-1} s_p \hat{s}_m E\left\{c_l(n) c_i(n-p)\right\} \delta_{m,p} \mathbf{R}\mathbf{F}_i \\ &= -2\mu \sum_{p=0}^{Q-1} \sum_{i=0}^{L-1} s_p \hat{s}_p E\left\{c_l(n) c_i(n-p)\right\} \mathbf{F}_l^T \mathbf{R}\mathbf{F}_i \end{aligned} \tag{3.45}$$

Note that, according to Eq. (2.7), for $m > M-1$, $\hat{s}_m = 0$. On the other hand, Eq. (2.42) results in

$$\mathbf{F}_l^T \mathbf{R}\mathbf{F}_i = \lambda_l \delta_{l,i} \tag{3.46}$$

By using this equality, Eq.(3.45) is simplified to

$$\begin{aligned} B_l(n) &= -2\mu \sum_{p=0}^{Q-1} \sum_{i=0}^{L-1} s_p \hat{s}_p \lambda_l \delta_{l,i} E\left\{c_l(n) c_i(n-p)\right\} \\ &= -2\mu \lambda_l \sum_{p=0}^{Q-1} s_p \hat{s}_p E\left\{c_l(n) c_l(n-p)\right\} \end{aligned} \tag{3.47}$$

From the FxLMS update equation, given in Eq. (2.65), it can be shown that

$$\mathbf{c}(n) = \mathbf{c}(n-p) + \mu \sum_{k=1}^{p} \hat{\mathbf{g}}(n-k) e(n-k) \qquad p = 0, 1, \ldots, Q-1 \tag{3.48}$$

When the adaptation process is slow, Eq. (3.48) can be approximated by [1]

$$\mathbf{c}(n) \approx \mathbf{c}(n-p) + \mu p \hat{\mathbf{g}}(n-p) e(n-p) \qquad p = 0, 1, \ldots, Q-1 \tag{3.49}$$

Therefore, for the variation of the l-th adaptive weight, the following equation can be derived.

$$c_l(n) \approx c_l(n-p) + \mu p \hat{g}_l(n-p) e(n-p) \qquad p = 0, 1, \ldots, Q-1 \tag{3.50}$$

[1] For a slow adaptation process, it can be assumed that the variation of the gradient vector $\nabla J(n)$ is so slow that $\nabla J(n) \approx \ldots \approx \nabla J(n-p)$, for $p = 0, 1, \ldots, Q-1$. Therefore, by using the expression given for $\nabla J(n)$ in Eq. (2.33), it can be shown that $e(n)\hat{\mathbf{f}}(n) \approx \ldots \approx e(n-p)\hat{\mathbf{f}}(n-p)$. Subsequently, it can be shown that $e(n)\mathbf{F}^T\hat{\mathbf{f}}(n) \approx e(n-1)\mathbf{F}^T\hat{\mathbf{f}}(n-1) \approx \ldots \approx e(n-Q+1)\mathbf{F}^T\hat{\mathbf{f}}(n-Q+1)$, which is identical to $e(n)\hat{\mathbf{g}}(n) \approx \ldots \approx e(n-Q+1)\hat{\mathbf{g}}(n-Q+1)$. Therefore:

$$\sum_{k=1}^{p} \hat{\mathbf{g}}(n-k) e(n-k) \approx \mu p \hat{\mathbf{g}}(n-p) e(n-p)$$

Now, combining Eqs. (3.47) and (3.50) results in

$$\begin{aligned} B_l(n) &= -2\mu\lambda_l \sum_{p=0}^{Q-1} s_p \hat{s}_p E\left\{c_l^2(n-p)\right\} \\ &- 2\mu^2\lambda_l \sum_{p=0}^{Q-1} p s_p \hat{s}_p E\left\{c_l(n-p)\,\hat{g}_l(n-p)\,e(n-p)\right\} \end{aligned} \tag{3.51}$$

By using Eqs. (3.16), (3.23) and (3.27), Eq. (3.51) can be expressed as

$$B_l(n) = -2\mu\lambda_l \sum_{p=0}^{Q-1} s_p \hat{s}_p m_l(n-p) - \mu\lambda_l \sum_{p=0}^{Q-1} p s_p \hat{s}_p B_l(n-p) \tag{3.52}$$

By changing the index of the second summation in Eq. (3.52), $B_l(n)$ can be re-expressed as

$$B_l(n) = -2\mu\lambda_l \sum_{p=0}^{Q-1} s_p \hat{s}_p m_l(n-p) - \mu\lambda_l \sum_{r=0}^{Q-1} r s_r \hat{s}_r B_l(n-r) \tag{3.53}$$

The recursive equation, given in Eq. (3.53), can be expanded to

$$\begin{aligned} B_l(n) &= -2\mu\lambda_l \sum_{p=0}^{Q-1} s_p \hat{s}_p m_l(n-p) \\ &+ 2\mu^2\lambda_l^2 \sum_{p=0}^{Q-1} s_p \hat{s}_p \sum_{r=0}^{Q-1} r s_r \hat{s}_r m_l(n-p-r) \\ &- 2\mu^3\lambda_l^3 \sum_{p=0}^{Q-1} s_p \hat{s}_p \sum_{r=0}^{Q-1} r s_r \hat{s}_r \sum_{k=0}^{Q-1} k s_k \hat{s}_k m_l(n-p-r-k) \\ &\vdots \end{aligned} \tag{3.54}$$

For $\mu \ll 1$, Eq. (3.54) can be approximated by its two first terms as

$$B_l(n) \approx -2\mu\lambda_l \sum_{p=0}^{Q-1} s_p \hat{s}_p m_l(n-p) + 2\mu^2\lambda_l^2 \sum_{p,r=0}^{Q-1} r s_p \hat{s}_p s_r \hat{s}_r m_l(n-p-r) \tag{3.55}$$

Eq. (3.55) formulates $B_l(n)$ as a function of the second-order moments $m_o(n), \ldots, m_{L-1}(n)$.

3.5 Stochastic Model for Excess-MSE Function

Using the expressions, obtained in Sections 3.3 and 3.4, this section develops an stochastic model for the excess-MSE function. For this purpose, $\triangle m_l(n)$ is initially expressed by substituting Eqs. (3.35) and

(3.55) into Eq. (3.25) as

$$\begin{aligned}
\triangle m_l(n) &= \mu^2\lambda_l \|\hat{\mathbf{s}}\|^2 J_0 \\
&+ \mu^2\lambda_l \|\hat{\mathbf{s}}\|^2 \sum_{p=0}^{Q-1}\sum_{k=0}^{L-1} \lambda_k s_p^2 m_k(n-p) \\
&- 2\mu\lambda_l \sum_{p=0}^{Q-1} s_p\hat{s}_p m_l(n-p) \\
&+ 2\mu^2\lambda_l^2 \sum_{p,r=0}^{Q-1} r s_p\hat{s}_p s_r\hat{s}_r m_l(n-p-r)
\end{aligned} \tag{3.56}$$

Subsequently, substituting the above expression for $\triangle m_l(n)$ into Eq. (3.18) gives the following expression for $\triangle J_{ex}(n)$.

$$\begin{aligned}
\triangle J_{ex}(n) &= \mu^2 \|\hat{\mathbf{s}}\|^2 \sum_{q=0}^{Q-1}\sum_{l=0}^{L-1} \lambda_l^2 s_q^2 J_o \\
&+ \mu^2 \|\hat{\mathbf{s}}\|^2 \sum_{q,p=0}^{Q-1}\sum_{l,k=0}^{L-1} \lambda_l^2\lambda_k s_q^2 s_p^2 m_k(n-p-q) \\
&- 2\mu \sum_{q,p=0}^{Q-1}\sum_{l=0}^{L-1} \lambda_l^2 s_q^2 s_p\hat{s}_p m_l(n-p-q) \\
&+ 2\mu^2 \sum_{q,p,r=0}^{Q-1}\sum_{l=0}^{L-1} r\lambda_l^3 s_q^2 s_p\hat{s}_p s_r\hat{s}_r m_l(n-p-r-q)
\end{aligned} \tag{3.57}$$

Now, the RMS (Root Mean Square) value of the Eigenvalues is defined as

$$\lambda_{rms} = \sqrt{\frac{1}{L}\sum_{l=0}^{L-1}\lambda_l^2} \tag{3.58}$$

Using this definition, Eq. (3.57) can be simplified to

$$\begin{aligned}
\triangle J_{ex}(n) &= \mu^2 \|\hat{\mathbf{s}}\|^2 \|\mathbf{s}\|^2 \lambda_{rms}^2 L J_o \\
&+ \mu^2 \|\hat{\mathbf{s}}\|^2 L\lambda_{rms}^2 \sum_{q,p=0}^{Q-1}\sum_{k=0}^{L-1} \lambda_k s_q^2 s_p^2 m_k(n-p-q) \\
&- 2\mu \sum_{p,q=0}^{Q-1}\sum_{l=0}^{L-1} \lambda_l^2 s_q^2 s_p\hat{s}_p m_l(n-p-q) \\
&+ 2\mu^2 \sum_{q,p,r=0}^{Q-1}\sum_{l=0}^{L-1} r\lambda_l^3 s_q^2 s_p\hat{s}_p s_r\hat{s}_r m_l(n-p-r-q)
\end{aligned} \tag{3.59}$$

where $\|\mathbf{s}\|$ denotes the Euclidean norm of vector $\mathbf{s}$ as:

$$\|\mathbf{s}\|^2 = \sum_{q=0}^{Q-1} s_q^2 \tag{3.60}$$

In a slow adaptation process, the second-order moments are updated slowly so that:

$$m_l(n-p-r-q) \approx m_l(n-p-q), \qquad r = 0, 1, \ldots, L-1 \tag{3.61}$$

By using this assumption, Eq. (3.59) is simplified to

$$\begin{aligned}
\triangle J_{ex}(n) &= \mu^2 \|\hat{\mathbf{s}}\|^2 \|\mathbf{s}\|^2 \lambda_{rms}^2 L J_o \\
&+ \mu^2 \|\hat{\mathbf{s}}\|^2 L \lambda_{rms}^2 \sum_{q,p=0}^{Q-1} \sum_{k=0}^{L-1} \lambda_k s_q^2 s_p^2 m_k(n-p-q) \\
&- 2\mu \sum_{q,p=0}^{Q-1} \sum_{l=0}^{L-1} \lambda_l^2 s_q^2 s_p \hat{s}_p m_l(n-p-q) \\
&+ 2\mu^2 \left(\sum_{r=0}^{Q-1} r s_r \hat{s}_r \right) \sum_{q,p=0}^{Q-1} \sum_{l=0}^{L-1} \lambda_l^3 s_q^2 s_p \hat{s}_p m_l(n-p-q)
\end{aligned} \tag{3.62}$$

Now, by defining diagonal matrix $\mathbf{\Psi}$ as

$$\mathbf{\Psi} = \begin{bmatrix} 0 & 0 & \ldots & 0 \\ 0 & 1 & \ddots & \vdots \\ \vdots & \ddots & \ddots & 0 \\ 0 & \ldots & 0 & Q-1 \end{bmatrix}, \tag{3.63}$$

it can be shown that

$$\sum_{r=0}^{Q-1} r s_r \hat{s}_r = \mathbf{s}^T \mathbf{\Psi} \hat{\mathbf{s}} \tag{3.64}$$

Substituting Eq. (3.64) into (3.62) results in

$$\begin{aligned}
\triangle J_{ex}(n) &= \mu^2 \|\hat{\mathbf{s}}\|^2 \|\mathbf{s}\|^2 \lambda_{rms}^2 L J_o \\
&+ \mu^2 \|\hat{\mathbf{s}}\|^2 L \lambda_{rms}^2 \sum_{q,p=0}^{Q-1} \sum_{k=0}^{L-1} \lambda_k s_q^2 s_p^2 m_k(n-p-q) \\
&- 2\mu \sum_{p,q=0}^{Q-1} \sum_{l=0}^{L-1} \lambda_l^2 s_q^2 s_p \hat{s}_p m_l(n-p-q) \\
&+ 2\mu^2 \left(\mathbf{s}^T \mathbf{\Psi} \hat{\mathbf{s}} \right) \sum_{p,q=0}^{Q-1} \sum_{l=0}^{L-1} \lambda_l^3 s_q^2 s_p \hat{s}_p m_l(n-p-q),
\end{aligned} \tag{3.65}$$

Eq. (3.65) can be simplified to

$$\triangle J_{ex}(n) = \mu^2 \|\hat{\mathbf{s}}\|^2 \|\mathbf{s}\|^2 \lambda_{rms}^2 L J_o - \mu \sum_{q,p=0}^{Q-1} \sum_{l=0}^{L-1} \gamma_{l,p,q} m_l (n-p-q), \tag{3.66}$$

where scalar parameter $\gamma_{l,p,q}$ is defined as

$$\gamma_{l,p,q} = \lambda_l s_q^2 \left[2\lambda_l s_p \hat{s}_p - \mu \lambda_{rms}^2 \|\hat{\mathbf{s}}\|^2 \left(L s_p^2 + 2 \left(\frac{\lambda_l}{\lambda_{rms}} \right)^2 \times \frac{\mathbf{s}^T \boldsymbol{\Psi} \hat{\mathbf{s}}}{\|\hat{\mathbf{s}}\|^2} s_p \hat{s}_p \right) \right], \tag{3.67}$$

Eqs. (3.17), (3.66) and (3.67) describe a linear stochastic model for the excess-MSE function, considering an arbitrary acoustic noise, an arbitrary secondary path, and an arbitrary secondary path model. This model is the core of the analysis which is performed in the next chapters. The general validity of this model is shown in Chapter 7 by using several computer simulations.

Chapter 4

Analysis of FxLMS-Based ANC Systems Considering General Secondary Paths

Available mathematical expressions for formulating behaviours of FxLMS-based ANC systems are derived from simplified models. These models are usually developed by using a number of simplifying assumptions regarding the actual secondary path, acoustic noise, and secondary path model. For example, the well-known expression for the step-size upper-bound, suggested by Elliott in [8, 21], were derived by assuming a pure delay secondary path, a broad-band white acoustic noise, and a perfect secondary path model. Also, closed-form expressions for steady-state performance and step-size upper-bound, suggested by Bjarnason in [49], were derived under the same simplifying assumptions. Unfortunately, these assumptions (specially the first one) are not realistic and, consequently, none of the available mathematical expressions can accurately describe behaviours of FxLMS-based ANC systems in practise [51].

In order to take the first step towards matching theoretical and practical findings, this chapter uses the stochastic model, developed in the previous chapter, to derive closed-form expressions for formulating behaviours of FxLMS-based ANC systems, without using any simplifying assumption regarding the actual secondary path.

Figure 4.1 shows the main contributions of this chapter. As shown in this figure, the expressions derived in this chapter thoroughly cover the commonly-used expressions. Moreover, they can apply to any arbitrary secondary path in general form, unlike the commonly-used expressions. Also, it can be seen from this figure that the classic simplifying assumptions regarding the acoustic noise and secondary path model are still used in this chapter. Removing the constraints caused by these two assumptions are left to the next two succeeding chapters.

4.1 System Model with General Secondary Path

When the acoustic noise is a broad-band white signal, the reference signal $x(n)$ can also be considered as a broad-band white signal. In this case, all the Eigenvalues of the auto-correlation matrix $\mathbf{R}$ are equal

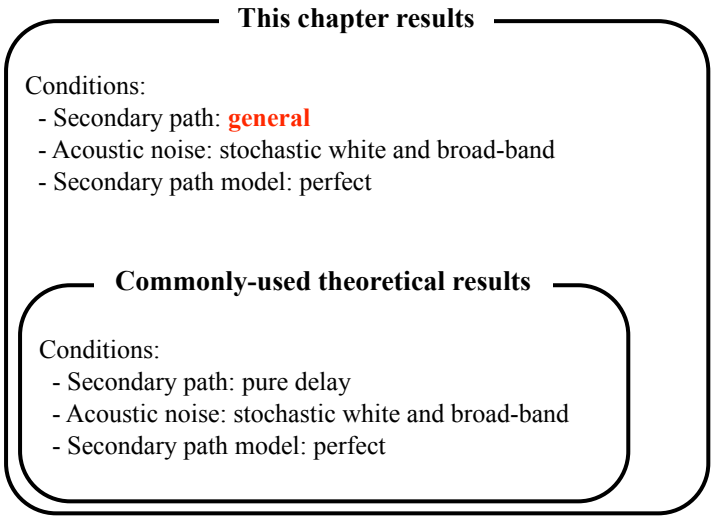

Figure 4.1: Contribution of Chapter 4: closed-form expressions for formulating behaviours of FxLMS-based ANC systems, considering a general secondary path

to the power of the reference signal, σ_x^2 [64]:

$$\lambda_0 = \lambda_1 = \ldots = \lambda_{L-1} = \sigma_x^2, \tag{4.1}$$

In this situation, the RMS value of the Eigenvalues is also equal to σ_x^2:

$$\lambda_{rms} = \sigma_x^2 \tag{4.2}$$

By substituting Eq. (4.1) into Eq. (3.15), $J_{ex}(n)$ can be expressed as

$$J_{ex}(n) = \sigma_x^2 \sum_{q=0}^{Q-1} \sum_{l=0}^{L-1} s_q^2 m_l (n-q) \tag{4.3}$$

Similarly, by substituting Eqs. (4.1) and (4.2) into Eq. (3.67), $\gamma_{l,p,q}$ is obtained as

$$\gamma_{l,p,q} = \sigma_x^4 s_q^2 \left[2 s_p \hat{s}_p - \mu \sigma_x^2 \left\| \hat{\mathbf{s}} \right\|^2 \left(L s_p^2 + 2 \frac{\mathbf{s}^T \mathbf{\Psi} \hat{\mathbf{s}}}{\left\| \hat{\mathbf{s}} \right\|^2} s_p \hat{s}_p \right) \right] \tag{4.4}$$

Now, assuming that the secondary path model is perfect ($\hat{\mathbf{s}} = \mathbf{s}$), Eq. (4.4) is simplified to

$$\gamma_{l,p,q} = \sigma_x^4 s_q^2 s_p^2 \left[2 - \mu \sigma_x^2 \left\| \mathbf{s} \right\|^2 \left(L + 2 \frac{\mathbf{s}^T \mathbf{\Psi} \mathbf{s}}{\left\| \mathbf{s} \right\|^2} \right) \right] \tag{4.5}$$

By substituting Eq. (4.5) into (3.66) and considering $\lambda_{rms} = \sigma_x^2$ and $\hat{\mathbf{s}} = \mathbf{s}$, $\triangle J_{ex}(n)$ is simplified to

$$\begin{aligned} \triangle J_{ex}(n) &= \mu^2 \left\| \mathbf{s} \right\|^4 \sigma_x^4 L J_o \\ &- \mu \sigma_x^4 \left[2 - \mu \sigma_x^2 \left\| \mathbf{s} \right\|^2 \left(L + 2 \frac{\mathbf{s}^T \mathbf{\Psi} \mathbf{s}}{\left\| \mathbf{s} \right\|^2} \right) \right] \sum_{l=0}^{L-1} \sum_{q,p=0}^{Q-1} s_q^2 s_p^2 m_l (n-p-q) \end{aligned} \tag{4.6}$$

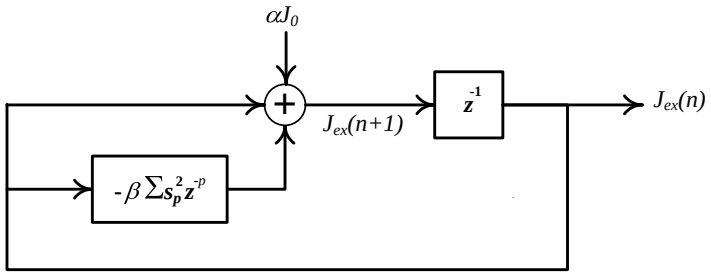

Figure 4.2: Proposed model for FxLMS-based ANC systems with a general secondary path

Combining Eqs. (4.3) and (4.6) results in

$$\begin{aligned} \triangle J_{ex}(n) &= \mu^2 \|\mathbf{s}\|^4 \sigma_x^4 L J_o \\ &- \mu\sigma_x^2 \left[2 - \mu\sigma_x^2 \|\mathbf{s}\|^2 \left(L + 2\frac{\mathbf{s}^T\boldsymbol{\Psi}\mathbf{s}}{\|\mathbf{s}\|^2}\right)\right] \sum_{p=0}^{Q-1} s_p^2 J_{ex}(n-p) \end{aligned} \tag{4.7}$$

As a novel parameter in ANC theory, the *secondary path equivalent delay*, D_{eq} is defined as

$$D_{eq} \triangleq \frac{\mathbf{s}^T\boldsymbol{\Psi}\mathbf{s}}{\|\mathbf{s}\|^2} \tag{4.8}$$

Using this definition, Eq. (4.7) can be expressed as

$$\triangle J_{ex}(n) = \mu^2 \|\mathbf{s}\|^4 \sigma_x^4 L J_o - \mu\sigma_x^2 \left[2 - \mu \|\mathbf{s}\|^2 \sigma_x^2 (L + 2D_{eq})\right] \mathcal{J}(n) \tag{4.9}$$

where scalar function $\mathcal{J}(n)$ is given by

$$\mathcal{J}(n) = \sum_{p=0}^{Q-1} s_p^2 J_{ex}(n-p) \tag{4.10}$$

Now, time-invariant parameters α and β are defined as

$$\alpha \triangleq \mu^2 \|\mathbf{s}\|^4 \sigma_x^4 L \tag{4.11}$$

and

$$\beta \triangleq \mu\sigma_x^2 \left[2 - \mu \|\mathbf{s}\|^2 \sigma_x^2 (L + 2D_{eq})\right] \tag{4.12}$$

By using the above definitions for α and β, Eq. (4.9) can be expressed as

$$\triangle J_{ex}(n) = \alpha J_o - \beta \mathcal{J}(n) \tag{4.13}$$

The dynamic model, given in Eq. (4.13), along with Eqs. (3.17), (4.8), (4.10) , (4.11) and (4.12) compose a theoretical model for FxLMS-based ANC systems. For the sake of clarity, these equations are collected in Table 4.1. Also, the functional block diagram of this model is shown in Figure 4.2. The main distinction of this model is that it considers a general secondary path. However, it is derived

Table 4.1: Theoretical model for FxLMS-based ANC systems with a general secondary path (assuming a broad-band acoustic noise and a perfect secondary path model)

Equation		Description
Eq. (3.17)	$\triangle J_{ex}(n) = J_{ex}(n+1) - J_{ex}(n)$	
Eq. (4.13)	$\triangle J_{ex}(n) = \alpha J_o - \beta \mathcal{J}(n)$	- J_o is the minimum attainable residual acoustic noise power, as defined in Eq. (2.16).
Eq. (4.10)	$\mathcal{J}(n) = \sum_{p=0}^{Q-1} s_p^2 J_{ex}(n-p)$	- $s_0, s_1, \ldots, s_{Q-1}$ are elements of $\mathbf{s}$
Eq. (4.11)	$\alpha = \mu^2 \|\mathbf{s}\|^4 \sigma_x^4 L$	- μ is the adaptation step size. - L is the ANC controller length. - σ_x^2 is the power of the reference signal.
Eq. (4.12)	$\beta = \mu\sigma_x^2 \left[2 - \mu \|\mathbf{s}\|^2 \sigma_x^2 (L + 2D_{eq})\right]$	
Eq. (4.8)	$D_{eq} \triangleq \frac{\mathbf{s}^T \mathbf{\Psi} \mathbf{s}}{\|\mathbf{s}\|^2}$	- constant matrix $\mathbf{\Psi}$ is given in Eq. (3.63). - $\mathbf{s}$ is the secondary path weight vector as defined in Eq. (2.5).

only for a broad-band acoustic noise and perfect secondary path model. Influences of the acoustic noise band-width and secondary path models on this model are investigated in Chapters 5 and 6, respectively.

4.2 Steady-State Performance

By using the dynamic model, developed in Section 4.1, this section formulates steady-state behaviours of FxLMS-based ANC systems. The obtained formulations are derived for a general secondary path, unlike the commonly-used formulations which were derived only for pure delay secondary paths.

4.2.1 Steady-State Residual Noise Power

Since the MSE function $J(n)$ is defined as the variance of the residual noise, the power of the residual noise in steady-state conditions (denoted by σ_e^2) can be expressed as

$$\sigma_e^2 = \lim_{n\to\infty} E\left\{e^2(n)\right\} = \lim_{n\to\infty} J(n) \tag{4.14}$$

Combining Eqs. (3.11) and (4.14) results in

$$\sigma_e^2 = J_o + \lim_{n\to\infty} J_{ex}(n) \tag{4.15}$$

On the other hand, for a stable adaptation process, it is expected that

$$\lim_{n\to\infty} \triangle J_{ex}(n) = 0 \tag{4.16}$$

Now, substituting Eq. (4.13) into (4.16) results in

$$\beta \lim_{n\to\infty} \mathcal{J}(n) = \alpha J_o \tag{4.17}$$

Also, from Eq. (4.10), it can be shown that

$$\begin{aligned} \lim_{n\to\infty} \mathcal{J}(n) &= \lim_{n\to\infty} \sum_{p=0}^{Q-1} s_p^2 J_{ex}(n-p) \\ &= \|\mathbf{s}\|^2 \lim_{n\to\infty} J_{ex}(n) \end{aligned} \tag{4.18}$$

Substituting Eq. (4.18) into (4.17) results in

$$\|\mathbf{s}\|^2 \beta \lim_{n\to\infty} J_{ex}(n) = \alpha J_o \tag{4.19}$$

Therefore,

$$\lim_{n\to\infty} J_{ex}(n) = \frac{\alpha}{\|\mathbf{s}\|^2 \beta} J_o \tag{4.20}$$

Now, σ_e^2 can be obtained by substituting Eq. (4.20) into (4.15) as

$$\sigma_e^2 = J_o + \frac{\alpha}{\|\mathbf{s}\|^2 \beta} J_o \tag{4.21}$$

Subsequently, substituting Eqs. (4.11) and (4.12) into (4.21) results in

$$\sigma_e^2 = \left(1 + \frac{\mu L \|\mathbf{s}\|^2 \sigma_x^2}{2 - \mu \|\mathbf{s}\|^2 \sigma_x^2 (L + 2D_{eq})}\right) J_o \tag{4.22}$$

Eq. (4.22) gives the steady-state power of the residual noise for a general secondary path.

4.2.2 Misadjustment Level

The steady-state performance of adaptive ANC systems is usually measured using a relative parameter, called the *misadjustment*. This parameter, denoted by $\mathcal{M}$, is defined as the ratio of the steady-state excess-MSE function to the optimal MSE level:

$$\mathcal{M} \triangleq \frac{1}{J_o} \lim_{n \to \infty} J_{ex}(n) \tag{4.23}$$

Or, equivalently

$$\mathcal{M} \triangleq \frac{\sigma_e^2 - J_o}{J_o} \tag{4.24}$$

By combining Eqs. (4.20) and (4.23), $\mathcal{M}$ is obtained as

$$\mathcal{M} = \frac{\alpha}{\|\mathbf{s}\|^2 \beta} \tag{4.25}$$

Alternatively, substituting Eqs. (4.11) and (4.12) into Eq. (4.25) results in

$$\mathcal{M} = \frac{\mu L \|\mathbf{s}\|^2 \sigma_x^2}{2 - \mu \|\mathbf{s}\|^2 \sigma_x^2 (L + 2D_{eq})} \tag{4.26}$$

As can be seen in Eq. (4.26), influences of the secondary path on the misadjustment level is taken into account by two scalar parameters of the secondary path: the static gain $\|\mathbf{s}\|$, and the equivalent delay D_{eq}. The influence of $\|\mathbf{s}\|$ can be compensated for by adjusting the step-size μ (usually μ is normalised by the filtered-reference signal power that is $\|\mathbf{s}\|^2 \sigma_x^2$). Therefore, the equivalent delay can be considered as the major parameter of the secondary path which affects on the steady-state performance of the system. By using Eq. (4.26), the variation of $\mathcal{M}$ with respect to D_{eq} can be plotted as shown in Figure 4.3. From this figure, the direct relationship between D_{eq} and $\mathcal{M}$ is apparent; therefore, it can be stated that D_{eq} causes the steady-state performance to be degraded.

4.3 Stability Analysis

This section studies stability of FxLMS-based ANC systems and derives a mathematical expression for the upper-bound of the step-size beyond which these systems become unstable. This upper-bound is

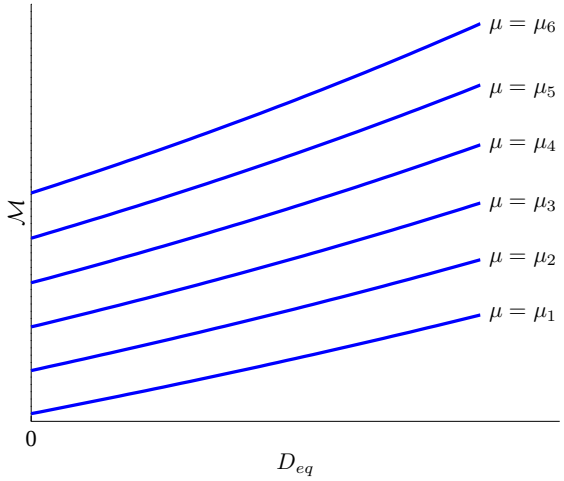

Figure 4.3: Influences of secondary path equivalent delay (D_{eq}) on misadjustment level ($\mathcal{M}$) for different values of step-size ($\mu_1 < \mu_2 < \mu_3 < \mu_4 < \mu_5 < \mu_6$)

derived for a general secondary path, unlike the commonly-used upper-bound which was derived for only pure delay secondary paths.

4.3.1 Stability in Steady-State Conditions

From Eq. (3.13), it can be seen that the excess-MSE function is always a positive definite function of the second-order moments of the adaptive weights. Therefore, the steady-state stability of the system requires that the steady-state excess-MSE function to be finite and positive:

$$0 < \lim_{n\to\infty} J_{ex}(n) < c, \quad \exists c \in \mathbb{R} \tag{4.27}$$

where c is a finite positive real number. Combining this inequality and Eq. (4.20) results in the following stability condition.

$$0 < \frac{\alpha}{\|\mathbf{s}\|^2 \beta} J_o < c \tag{4.28}$$

Since J_o, α and $\|\mathbf{s}\|^2$ are positive scalars, the only condition for the steady-state stability is

$$\beta > 0 \tag{4.29}$$

In the following, it is proved that this condition is a sufficient condition for the stability of FxLMS-based ANC systems in transient conditions.

4.3.2 Stability in Transient Conditions

As discussed in Chapter 3, the excess-MSE function is a positive definite function of the second-order moments of the adaptive weights. Therefore, according to the Lyapunov stability theorems, if this function is an decreasing function then the system is stable and the second-order moments will converge to

their equilibrium point at the origin:

$$\lim_{n\to\infty} m_l(n) = 0, \qquad l = 0, 1, \ldots, L-1 \tag{4.30}$$

Combining Eqs. (2.47) and (4.30) results in

$$\lim_{n\to\infty} \mathbf{w}(n) = \mathbf{w}_o \tag{4.31}$$

This means that if Lyapunov stability condition is satisfied then the adaptive weight vector converges to the optimal Wiener-Hopf vector $\mathbf{w}_o$.

Now, let us assume that, at time index n, the excess-MSE function does not reach its steady-state level. In this situation, since the FxLMS is a gradient-based algorithm, it is expected that the current value of the excess-MSE function and its past values are greater than its steady-state level; therefore,

$$J_{ex}(n-p) > \epsilon, \qquad p = 0, 1, 2, \ldots \tag{4.32}$$

where ϵ denotes the steady-state excess-MSE level:

$$\epsilon \triangleq \lim_{n\to\infty} J_{ex}(n) \tag{4.33}$$

Since $s_p^2 > 0$, the following inequalities set can be derived from Eq. (4.32).

$$\begin{cases} s_0^2 J_{ex}(n) > s_0^2 \epsilon \\ \vdots \\ s_p^2 J_{ex}(n-p) > s_p^2 \epsilon \\ \vdots \\ s_{Q-1}^2 J_{ex}(n-Q+1) > s_{Q-1}^2 \epsilon \end{cases}$$

Adding all of the above inequalities results in:

$$\sum_{p=0}^{Q-1} s_p^2 J_{ex}(n-p) > \left(\sum_{p=0}^{Q-1} s_p^2 \right) \epsilon \tag{4.34}$$

The left side of Eq. (4.34) equals to $\mathcal{J}(n)$ and its right side equals to $\|\mathbf{s}\|^2 \epsilon$; therefore,

$$\mathcal{J}(n) > \|\mathbf{s}\|^2 \epsilon \tag{4.35}$$

As shown in Section 4.3.1, the steady-state stability of FxLMS-based ANC systems requires β to be positive. Therefore, multiplying both sides of Eq. (4.35) by positive scalar β results in

$$-\beta \mathcal{J}(n) < -\beta \|\mathbf{s}\|^2 \epsilon \tag{4.36}$$

Now, αJ_o is added to the both sides of Eq. (4.36):

$$\alpha J_o - \beta \mathcal{J}(n) < \alpha J_o - \beta \|\mathbf{s}\|^2 \epsilon \tag{4.37}$$

Combining Eqs. (4.13) and (4.37) results in

$$\triangle J_{ex}(n) < \alpha J_o - \beta \|\mathbf{s}\|^2 \epsilon \tag{4.38}$$

By substituting Eqs. (4.20) and (4.33) into (4.38), the following inequality is obtained.

$$\triangle J_{ex}(n) < \alpha J_o - \beta \|\mathbf{s}\|^2 \frac{\alpha}{\|\mathbf{s}\|^2 \beta} J_o \tag{4.39}$$

The right side of the inequality given in Eq. (4.39) can be simplified to zero; therefore,

$$\triangle J_{ex}(n) < 0 \tag{4.40}$$

As a result, when $\beta > 0$, the Lyapunov function $J_{ex}(n)$ is a decreasing function in transient conditions (because its time difference is negative). Therefore, $\beta > 0$ causes the Lyapunov stability condition to be satisfied. In this case, the weight vector converges to the Wiener-Hopf filter and the MSE function converges to the optimal MSE level J_o.

4.3.3 Step-Size Upper-Bound

From the two stability analyses conducted in Sections 4.3.1 and 4.3.2, it can be shown that an FxLMS-based ANC system is always stable if $\beta > 0$. Accordingly, from Eq. (4.12) it can be shown that

$$\beta > 0 \quad \Rightarrow \quad \mu\sigma_x^2 \left[2 - \mu \|\mathbf{s}\|^2 \sigma_x^2 (L + 2D_{eq})\right] > 0 \tag{4.41}$$

This inequality leads to obtain the following condition for the step-size,

$$0 < \mu < \frac{2}{\|\mathbf{s}\|^2 \sigma_x^2 (L + 2D_{eq})} \tag{4.42}$$

In other words, there is an upper-bound for the step-size beyond which the system becomes unstable. This upper-bound which is referred to as the *step-size upper-bound* (or stability bound) is given by

$$\mu_{max} = \frac{2}{\|\mathbf{s}\|^2 \sigma_x^2 (L + 2D_{eq})} \tag{4.43}$$

As can be seen in Eq. (4.43), influences of the secondary path on the stability bound is taken into account by two scalar parameters of the secondary path: the static gain $\|\mathbf{s}\|$, and the equivalent delay D_{eq}. Usually, μ is normalised by the filtered-reference signal power that is $\|\mathbf{s}\|^2 \sigma_x^2$; therefore, D_{eq} can be considered as the major parameter of the secondary path which affects on μ_{max}. The variation of μ_{max} with respect to D_{eq} can be plotted by using Eq. (4.43), as shown in Figure 4.4. As can be seen in

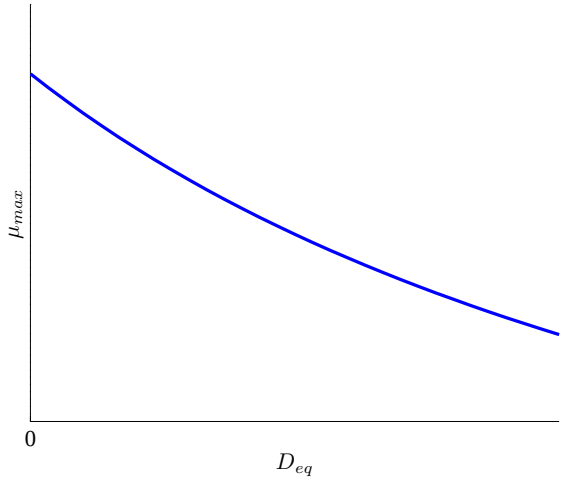

Figure 4.4: Influence of secondary path equivalent delay (D_{eq}) on upper-bound of stability (μ_{max})

this figure, by increasing D_{eq}, μ_{max} is also decreased; therefore, D_{eq} causes the stability behaviour of the system to be degraded.

Also, it can be seen from Eq. (4.43) that the proposed expression for μ_{max} is in the form of the commonly-used expression, derived by Elliott in [8]. In fact, Elliott derived the same expression, but instead of the secondary path equivalent delay, the physical time delay in the secondary path appeared in his expression. This is because Elliott simplified his analysis by assuming a pure delay secondary path but this thesis considers an arbitrary secondary path in a general form. The novel parameter of the secondary path equivalent delay, defined in this thesis, makes this generalisation possible (Elliott's expression for the step-size upper-bound is derived later in Section 4.5.2.).

4.4 Convergence Speed

This section introduces a measure for the convergence speed of FxLMS-based ANC systems in transient conditions and discusses influences of a general secondary path on this measure. Also, this section derives a mathematical expression for the step-size leading to the fastest convergence speed.

4.4.1 Convergence Speed Measure

In transient conditions, the MSE function is greater than the optimal MSE level: $J(n) \gg J_o$. In this situation, the first term in Eq. (4.13) is neglectable. Thus, this equation can be approximated to

$$\triangle J_{ex}(n) \approx -\beta \mathcal{J}(n) \tag{4.44}$$

According to the Lyapunov stability theory, the convergence speed of a dynamic system is directly related to the gradient of its Lyapunov function; therefore,

$$\text{transient convergence speed} \propto \beta \mathcal{J}(n) \tag{4.45}$$

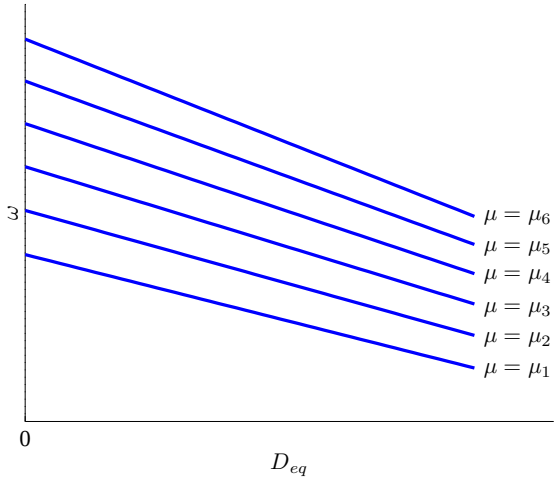

Figure 4.5: Influences of secondary path equivalent delay (D_{eq}) on convergence speed (ω) for different values of step-size ($\mu_1 < \mu_2 < \mu_3 < \mu_4 < \mu_5 < \mu_6 < 0.5\mu_{max}$)

Accordingly, a convergence speed measure for FxLMS-based ANC systems (denoted by ω) is defined as

$$\omega = \beta = \mu\sigma_x^2 \left[2 - \mu \left\|\mathbf{s}\right\|^2 \sigma_x^2 \left(L + 2D_{eq}\right)\right] \tag{4.46}$$

It is shown later (in Chapter 7) that how the proposed theoretical measure can efficiently describe the convergence speed of FxLMS-based ANC systems. By using Eq. (4.46), the variation of the convergence speed measure ω with respect to D_{eq} can be plotted, as shown in Figure 4.5. From this figure, it can be seen that D_{eq} causes the convergence speed to be decreased. It is well known that for pure delay secondary paths, increasing the secondary path delay causes the convergence speed to be decreased. However, herein, it is shown that, for general secondary paths, there is a similar relationship between the convergence speed and secondary path equivalent delay D_{eq}, which is a novel parameter introduced in this thesis. It is while D_{eq} can be computed for any arbitrary secondary path, rather than the secondary path delay which is a physical parameter relevant to only pure delay secondary paths.

4.4.2 Fastest Convergence Speed

Combining Eqs. (4.43) and (4.46), ω can be expressed as

$$\omega = 2\mu\sigma_x^2 \left(1 - \frac{\mu}{\mu_{max}}\right) \tag{4.47}$$

By using Eq. (4.47), the variation of ω with respect to μ can be plotted, as shown in Figure 4.6. As can be seen in this figure, the maximum attainable convergence speed can be obtained when the step-size is set to the half of its upper-bound. Therefore,

$$\mu^* = \frac{\mu_{max}}{2} \tag{4.48}$$

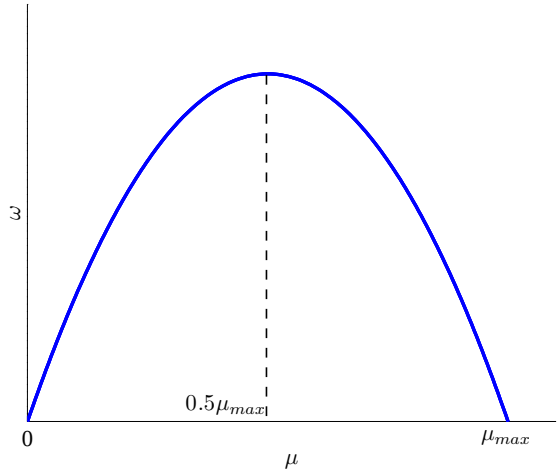

Figure 4.6: Variation of convergence speed measure (ω) with respect to adaptation step-size (μ)

where μ^* denotes the step-size leading to the fastest convergence rate[1]. By setting $\mu = \mu^*$ in Eq. (4.47), the maximum convergence speed measure can be computed as

$$\omega_{max} = \frac{1}{2}\mu_{max}\sigma_x^2 \tag{4.49}$$

As can be seen, the maximum attainable convergence speed is directly related to μ_{max}. On the other hand, Eq. (4.43) shows that D_{eq} causes μ_{max} to be decreased. Consequently, D_{eq} is a limiting factor for the the maximum attainable convergence speed.

4.5 Simplified Cases

One way to verify the general theoretical formulations, obtained in this chapter, is to re-derive commonly-used formulations from them as special and simplified cases. This section derives the commonly-used formulations for the misadjustment level and stability bound of FxLMS-based ANC systems, as special cases of the proposed general formulations. The validity of the proposed formulations in a general case will be discussed later in Chapters 7 and 10 using simulation and experimental results, respectively.

4.5.1 Identity Control Path (LMS Algorithm)

In the LMS algorithm, there is no secondary path following the adaptive controller. Therefore, it can be assumed that the secondary path is an identity system with the impulse response given by

$$s\left(n\right) = 1 \tag{4.50}$$

For such secondary path, $Q = 1$ and $s_0 = 1$. Substituting these parameters into Eq. (3.60) and (3.63) results in

$$\left\|\mathbf{s}\right\|^2 = 1 \tag{4.51}$$

[1]This result can be also proved analytically; $\mu^* = 0.5\mu_{max}$ maximises the expression given for ω in Eq. (4.47).

and

$$\mathbf{\Psi} = 0 \tag{4.52}$$

Now, setting $\mathbf{\Psi} = 0$ in Eq. (4.8) results in

$$D_{eq} = 0 \tag{4.53}$$

Substituting the above expressions for $\|\mathbf{s}\|^2$ and D_{eq} into Eq. (4.26) results in

$$\mathcal{M} = \frac{\mu L \sigma_x^2}{2 - \mu \sigma_x^2} \tag{4.54}$$

This expression for $\mathcal{M}$ is identical to that given in [61] or [64]. Similarly, substituting $D_{eq} = 0$ and $\|\mathbf{s}\|^2 = 1$ into Eq. (4.43) results in

$$\mu_{max} = \frac{2}{\sigma_x^2 L} \tag{4.55}$$

which is the well-known expression for the step-size upper-bound in the LMS algorithm [41, 61].

4.5.2 Pure Delay Secondary Path

Let us assume that the secondary path is a pure delay system with the impulse response given by

$$s(n) = A\delta(n - D) \tag{4.56}$$

where D is the *physical time delay* in the secondary path and scalar parameter A is the static gain of the secondary path. For such system, it can be shown that $Q = D + 1$, $s_0 = s_1 = \ldots s_{Q-2} = 0$ and $s_{Q-1} = A$. Substituting these parameters into Eqs. (3.60), (3.63) and (4.8) results in

$$\|\mathbf{s}\|^2 = A^2 \tag{4.57}$$

and

$$D_{eq} = D \tag{4.58}$$

This equality means that, for a pure delay secondary path, the equivalent delay is exactly equal to the physical time delay in the secondary path. Now, substituting the above expressions for $\|\mathbf{s}\|^2$ and D_{eq} into Eq. (4.26) results in

$$\mathcal{M} = \frac{\mu L \sigma_f^2}{2 - \mu \sigma_f^2 (L + 2D)} \tag{4.59}$$

where $\sigma_f^2 = A^2 \sigma_x^2$ denotes the power of the filtered reference signal. This expression for $\mathcal{M}$ is identical to that given in [8, 21]. Similarly, substituting $D_{eq} = D$ and $\|\mathbf{s}\|^2 = A^2$ into Eq. (4.43) results in

$$\mu_{max} = \frac{2}{\sigma_f^2 (L + 2D)} \tag{4.60}$$

which is the commonly used expression (Elliott's expression) for the step-size upper-bound in the FxLMS algorithm with pure delay secondary paths [8, 21].

4.6 Summary

From the theoretical results obtained in this chapter, the following statements can be expressed.

- For a general secondary path with the impulse response, given by vector $\mathbf{s}$, the equivalent delay is defined as

$$D_{eq} \triangleq \frac{\mathbf{s}^T \mathbf{\Psi} \mathbf{s}}{\|\mathbf{s}\|^2}$$

  This parameter can be computed for any arbitrary secondary path, unlike the secondary path delay which is a physical parameter relevant to only pure delay secondary paths.

- Considering a general secondary path with the equivalent delay of D_{eq}, the step-size upper-bound μ_{max}, steady-state noise power σ_e^2, misadjustment level $\mathcal{M}$, and transient convergence speed measure ω can be formulated as

$$\begin{cases} \mu_{max} = \dfrac{2}{\|\mathbf{s}\|^2 \sigma_x^2 (L + 2D_{eq})} \\ \sigma_e^2 = J_o + \dfrac{\mu L \|\mathbf{s}\|^2 \sigma_x^2 J_o}{2 - \mu \|\mathbf{s}\|^2 \sigma_x^2 (L + 2D_{eq})} \\ \mathcal{M} = \dfrac{\mu L \|\mathbf{s}\|^2 \sigma_x^2}{2 - \mu \|\mathbf{s}\|^2 \sigma_x^2 (L + 2D_{eq})} \\ \omega = 2\mu\sigma_x^2 \left(1 - \dfrac{\mu}{\mu_{max}}\right) \end{cases}$$

- The step-size leading to the fastest convergence speed is

$$\mu^* = \frac{\mu_{max}}{2}$$

- The steady-state performance, stability bound, and convergence speed of FxLMS-based ANC systems are inversely related to the equivalent secondary path delay D_{eq} . This is similar to the physical time delay in the secondary path (D) which has an indirect relationship with the performance of the FxLMS algorithm with pure delay secondary paths. However, unlike the physical delay in the pure delay secondary paths (D), the equivalent delay D_{eq} can be computed for any arbitrary secondary path.

Chapter 5

Influences of Acoustic Noise band-width on FxLMS-Based ANC Systems

Chapter 4 extends the available theoretical knowledge on FxLMS-based ANC systems; however, in order to match theoretical and practical results, another step towards the generalisation of the obtained results should be taken. This is because it is usually assumed in theory that the acoustic noise is a broad-band stochastic white signal but, this signal can only be white over a limited range of frequencies in practise. Even if the acoustic noise is white over a wide frequency range, the reference signal is required to be processed by a low-pass filter, as shown in Figure 5.1. Obviously, the sampling frequency used in the filter, should be higher than the maximum frequency of the reference signal. Therefore, a realistic reference signal can not have a perfect flat spectrum over its entire frequency range so that it can be considered as a broad-band white signal.

This chapter studies influences of the acoustic noise band-width on behaviours of FxLMS-based ANC systems. Referring to Figure 5.2, it can be seen that this chapter generalises the closed-form expressions, derived in Chapter 4, to a more general case with any arbitrary acoustic noise band-width . However, it is still assumed that the secondary path model is perfectly accurate. Removing the constraint caused by this assumption is left to the next chapter.

5.1 Band-Limited White Signal

This section describes a general band-limited white signal and shows the relationship between its power spectrum and Eigenvalues. Also, mathematical expressions for the signal power and the RMS value of the Eigenvalues are derived. These expressions are widely used in this chapter.

5.1.1 Power Spectrum

The power spectrum of a band-limited stochastic white signal is flat (and non-zero) over a particular frequency range, called the *band-width*, and zero over the rest of frequencies. For a general case, this power spectrum is shown in Figure 5.3. In this figure, the frequency axis is normalised with respect to

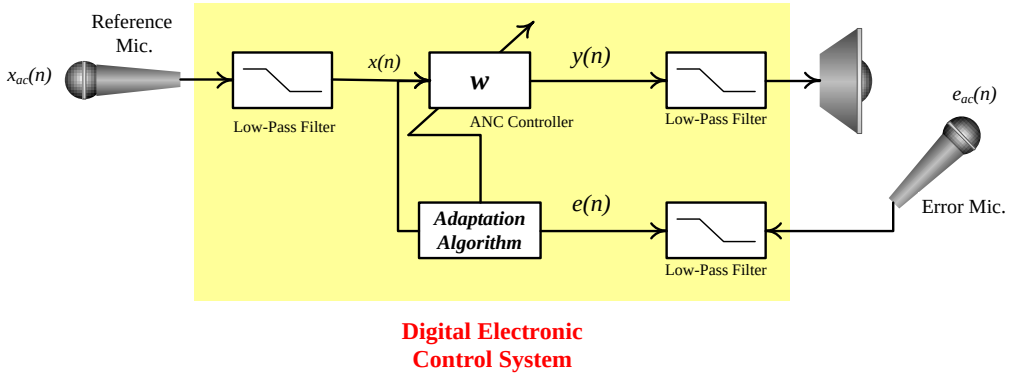

Figure 5.1: Low-pass filtering of reference signal before being used by ANC algorithm

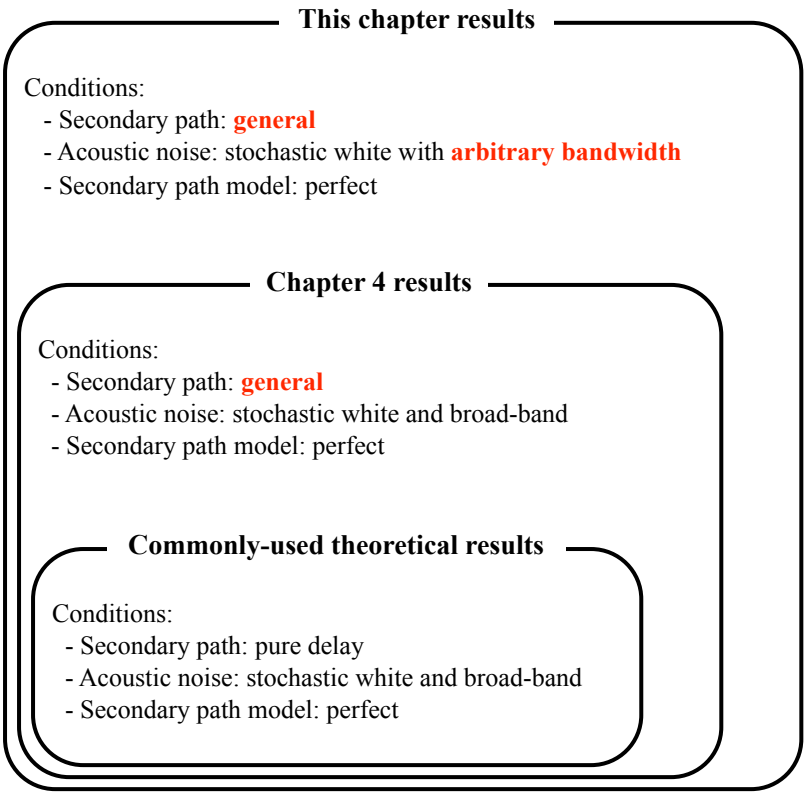

Figure 5.2: Contribution of Chapter 5: generalisation of the theoretical findings considering a band-limited acoustic noise with an arbitrary band-with

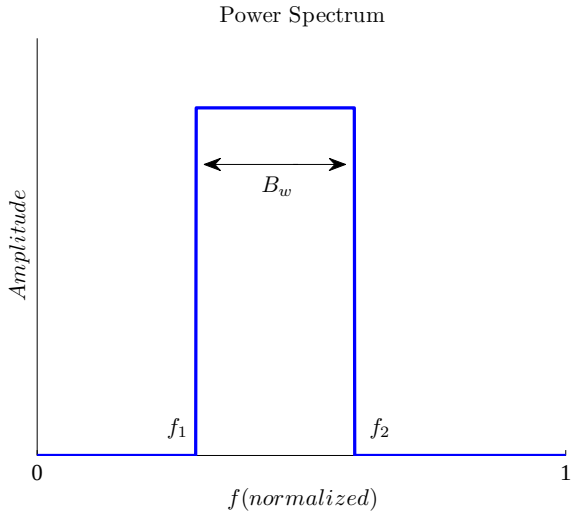

Figure 5.3: Power spectrum of band-limited white noise

$0.5f_s$, where f_s is the sampling frequency. Also, f_1 is the minimum frequency component of the signal, f_2 is the maximum frequency component of the signal, and B_w is the signal band-width, given by

$$B_w \triangleq f_2 - f_1 \tag{5.1}$$

5.1.2 Application of Szego Theorem

According to the Szego theorem [65], for a stationary signal, the Eigenvalues of the ACM matrix are asymptotically equal to the power spectrum at (normalised) frequencies spread $\frac{1}{L}$ apart, where L is the size of the ACM matrix. Based on this theorem, the Eigenvalues of the ACM matrix of a band-limited white signal can be expressed as

$$\lambda_l \in \{\varepsilon, \kappa\} \qquad l = 0, 1, \ldots, L-1 \tag{5.2}$$

where λ_l denotes the l-th eigenvalue of the ACM matrix, κ is a non-zero positive number, and ϵ is a nearly zero positive number ($\epsilon \approx 0$). The Eigenvalues with the value of κ correspond to the frequency range over which the noise power is uniformly distributed and the Eigenvalues with the value of ε correspond to the frequency range over which the noise power is approximately zero. Also, it can be shown from the Szego theorem [65] that, for a high order ACM matrix (large L), the noise band-width B_w is equal to

$$B_w \approx \frac{L_w}{L} \tag{5.3}$$

where L_w is the number of the Eigenvalues with values of κ and L is the total number of Eigenvalues. Also, the power of a band-limited signal (denoted by σ_x^2) can be obtained as [65, 66]

$$\begin{aligned}\sigma_x^2 &= \frac{1}{L}\text{trace}\left(\mathbf{\Lambda}\right) \\ &= \frac{1}{L}\sum_{l=0}^{L-1}\lambda_l = \frac{L_w}{L}\kappa + \frac{L-L_w}{L}\varepsilon\end{aligned} \tag{5.4}$$

Since ϵ is approximately zero, σ_x^2 can be estimated by

$$\sigma_x^2 = \frac{L_w}{L}\kappa \tag{5.5}$$

Now, combining Eqs. (5.3) and (5.5) results in

$$\kappa = \frac{\sigma_x^2}{B_w} \tag{5.6}$$

Similarly, the RMS value of the Eigenvalues can be obtained as

$$\lambda_{rms}^2 = \frac{1}{L}\sum_{l=0}^{L-1}\kappa^2 = \frac{L_w}{L}\kappa^2 \tag{5.7}$$

Combining Eqs. (5.3), (5.6) and (5.7) results in

$$\lambda_{rms}^2 = \frac{\sigma_x^4}{B_w} \tag{5.8}$$

This equation shows that the RMS value of the Eigenvalues is inversely proportional to the band-width.

5.2 System Model with Band-Limited Acoustic Noise

In Chapter 4, a dynamic model for FxLMS-based ANC systems with general secondary paths is derived. However, this model assumes a broad-band white acoustic noise and a perfect secondary path model. This chapter removes the constraint, caused by assuming a broad-band white acoustic noise. For this purpose, a general band-limited reference signal $x\left(n\right)$ with band-width of B_w is considered. In this situation, the Eigenvalues $\lambda_0, \lambda_1, \ldots, \lambda_{L-1}$ and and their RMS value λ_{rms} are given in Eqs. (5.2) and (5.8), respectively. Therefore, substituting Eqs. (5.2) and (5.8) into (3.67), the following expression for $\gamma_{l,p,q}$ can be obtained.

$$\gamma_{l,p,q} = \begin{cases} \kappa s_q^2\left[2\kappa s_p\hat{s}_p - \mu\frac{\sigma_x^4}{B_w}\left\|\hat{\mathbf{s}}\right\|^2\left(Ls_p^2 + \frac{2}{B_w}\times\frac{\mathbf{s}^T\mathbf{\Psi}\hat{\mathbf{s}}}{\left\|\hat{\mathbf{s}}\right\|^2}s_p\hat{s}_p\right)\right] & when\ \lambda_l = \kappa \\ \varepsilon s_q^2\left[2\varepsilon s_p\hat{s}_p - \mu\frac{\sigma_x^4}{B_w}\left\|\hat{\mathbf{s}}\right\|^2\left(Ls_p^2 + \frac{2}{B_w}\times\frac{\mathbf{s}^T\mathbf{\Psi}\hat{\mathbf{s}}}{\left\|\hat{\mathbf{s}}\right\|^2}s_p\hat{s}_p\right)\right] & when\ \lambda_l = \varepsilon \end{cases} \tag{5.9}$$

By using Eq. (5.6) and considering that ε is nearly zero, $\gamma_{l,p,q}$ can be approximated to

$$\gamma_{l,p,q} = \begin{cases} \frac{\sigma_x^4}{B_w^2} s_q^2 \left[2 s_p \hat{s}_p - \mu \sigma_x^2 \left\| \hat{\mathbf{s}} \right\|^2 \left(L s_p^2 + \frac{2}{B_w} \times \frac{\mathbf{s}^T \boldsymbol{\Psi} \hat{\mathbf{s}}}{\left\| \hat{\mathbf{s}} \right\|^2} s_p \hat{s}_p \right) \right] & when\ \lambda_l = \kappa \\ \\ 0 & when\ \lambda_l = \varepsilon \end{cases} \tag{5.10}$$

On the other hand, from Eqs. (5.2) and (5.6) it can be shown that

$$\frac{B_w \lambda_l}{\sigma_x^2} \approx \begin{cases} 1 & when\ \lambda_l = \kappa \\ \\ 0 & when\ \lambda_l = \epsilon \end{cases} \tag{5.11}$$

Now, combining Eqs. (5.10) and (5.11), a single closed-form expression for $\gamma_{l,p,q}$ can be obtained as

$$\gamma_{l,p,q} = \frac{\sigma_x^4}{B_w^2} s_q^2 \left[2 s_p \hat{s}_p - \mu \sigma_x^2 \left\| \hat{\mathbf{s}} \right\|^2 \left(L s_p^2 + \frac{2}{B_w} \times \frac{\mathbf{s}^T \boldsymbol{\Psi} \hat{\mathbf{s}}}{\left\| \hat{\mathbf{s}} \right\|^2} s_p \hat{s}_p \right) \right] \left(\frac{B_w \lambda_l}{\sigma_x^2} \right) \tag{5.12}$$

This equation can be simplified to

$$\gamma_{l,p,q} = \frac{\sigma_x^2}{B_w} s_q^2 \left[2 s_p \hat{s}_p - \mu \sigma_x^2 \left\| \hat{\mathbf{s}} \right\|^2 \left(L s_p^2 + \frac{2}{B_w} \times \frac{\mathbf{s}^T \boldsymbol{\Psi} \hat{\mathbf{s}}}{\left\| \hat{\mathbf{s}} \right\|^2} s_p \hat{s}_p \right) \right] \lambda_l \tag{5.13}$$

Assuming that the secondary path model is perfect ($\hat{\mathbf{s}} = \mathbf{s}$), $\gamma_{l,p,q}$ is simplified to

$$\gamma_{l,p,q} = \frac{\sigma_x^2}{B_w} s_q^2 s_p^2 \left[2 - \mu \sigma_x^2 \left\| \mathbf{s} \right\|^2 \left(L + \frac{2}{B_w} \times \frac{\mathbf{s}^T \boldsymbol{\Psi} \mathbf{s}^2}{\left\| \mathbf{s} \right\|^2} \right) \right] \lambda_l \tag{5.14}$$

As can be seen, the secondary path equivalent delay (D_{eq}), as defined in Eq. (4.8), appears in Eq. (5.14); therefore,

$$\gamma_{l,p,q} = \frac{\sigma_x^2}{B_w} s_q^2 s_p^2 \left[2 - \mu \sigma_x^2 \left\| \mathbf{s} \right\|^2 \left(L + \frac{2}{B_w} D_{eq} \right) \right] \lambda_l \tag{5.15}$$

Now, by substituting the above simplified expression for $\gamma_{l,p,q}$ into Eq. (3.66), $\triangle J_{ex}(n)$ is obtained as

$$\begin{aligned} \triangle J_{ex}(n) &= \mu^2 \left\| \mathbf{s} \right\|^4 \frac{\sigma_x^4}{B_w} L J_o \\ &- \mu \frac{\sigma_x^4}{B_w^2} \left[2 - \mu \sigma_x^2 \left\| \mathbf{s} \right\|^2 \left(L + \frac{2}{B_w} D_{eq} \right) \right] \sum_{q,p=0}^{Q-1} \sum_{l=0}^{L-1} \lambda_l s_q^2 s_p^2 m_l (n-p-q) \end{aligned} \tag{5.16}$$

Combining Eqs. (3.15) and (5.16) results in

$$\begin{aligned} \triangle J_{ex}(n) &= \mu^2 \left\| \mathbf{s} \right\|^4 \frac{\sigma_x^4}{B_w} L J_o \\ &- \mu \frac{\sigma_x^4}{B_w^2} \left[2 - \mu \sigma_x^2 \left\| \mathbf{s} \right\|^2 \left(L + \frac{2}{B_w} D_{eq} \right) \right] \underbrace{\sum_{q=0}^{Q-1} s_p^2 J_{ex}(n-p)}_{\mathcal{J}(n)} \end{aligned} \tag{5.17}$$

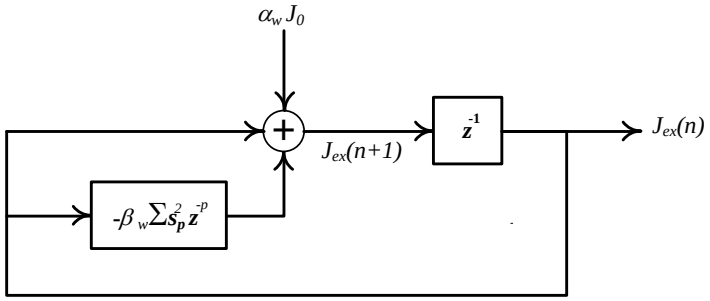

Figure 5.4: Proposed model for FxLMS-based ANC systems with a general secondary path and a band-limited acoustic noise

As can be seen, the scalar function $\mathcal{J}(n)$, as defined in Eq. (4.10), appears in Eq. (5.17); therefore,

$$\triangle J_{ex}(n) = \mu^2 \|\mathbf{s}\|^4 \frac{\sigma_x^4}{B_w} L J_o - \mu \frac{\sigma_x^2}{B_w} \left[2 - \mu \|\mathbf{s}\|^2 \sigma_x^2 \left(L + \frac{2}{B_w} D_{eq}\right)\right] \mathcal{J}(n) \tag{5.18}$$

Now, time-invariant parameters α_w and β_w are defined as

$$\alpha_w = \mu^2 \|\mathbf{s}\|^4 \frac{\sigma_x^4}{B_w} L \tag{5.19}$$

and

$$\beta_w = \mu \frac{\sigma_x^2}{B_w} \left[2 - \mu \|\mathbf{s}\|^2 \sigma_x^2 \left(L + \frac{2}{B_w} D_{eq}\right)\right] \tag{5.20}$$

Using these definitions, Eq. (5.18) can be re-expressed as

$$\triangle J_{ex}(n) = \alpha_w J_o - \beta_w \mathcal{J}(n) \tag{5.21}$$

The dynamic model, given in Eq. (5.21), along with the definitions, given in Eqs. (3.17), (4.8), (4.10) , (5.19) and (5.20) compose a theoretical model for FxLMS-based ANC systems with general secondary paths and band-limited acoustic noise (still assuming a perfect secondary path model). For the sake of clarity, these equations are collected in Table 5.1. The functional block diagram of this model is also shown in Figure 5.4.

From Eqs. (5.19) and (5.20), it can be seen that for a broad-band acoustic noise ($B_w = 1$), these expressions results in $\alpha_w = \alpha$ and $\beta_w = \beta$ and, thereby, the proposed model is simplified to the one derived in Chapter 4. In other words, the dynamic model developed in this chapter is a generalisation of the model given in Chapter 4.

Comparing the model derived in this chapter and the one derived in Chapter 4 shows that the only difference between these two models is due to the changing in scalar coefficients α and β to α_w and β_w. However, both of them have a similar structure. Therefore, the theoretical results, obtained in Chapter 4, are valid for the model, developed in this chapter, after replacing α and β with α_w and β_w.

Table 5.1: Theoretical model for FxLMS-based ANC systems with a general secondary path and band-limited acoustic noise (assuming a perfect secondary path model)

Equation		Description
Eq. (3.17)	$\triangle J_{ex}(n) = J_{ex}(n+1) - J_{ex}(n)$	
Eq. (5.21)	$\triangle J_{ex}(n) = \alpha_w J_o - \beta_w \mathcal{J}(n)$	- J_o is the minimum attainable residual acoustic noise power, as defined in Eq. (2.16).
Eq. (4.10)	$\mathcal{J}(n) = \sum_{p=0}^{Q-1} s_p^2 J_{ex}(n-p)$	- $s_0, s_1, \ldots, s_{Q-1}$ are elements of $\mathbf{s}$
Eq. (5.19)	$\alpha_w = \mu^2 \|\mathbf{s}\|^4 \frac{\sigma_x^4}{B_w} L$	- μ is the adaptation step size. - L is the ANC controller length. - σ_x^2 is the power of the reference signal. - B_w is the reference signal band-width.
Eq. (5.20)	$\beta_w = \mu \frac{\sigma_x^2}{B_w} \left[2 - \mu \|\mathbf{s}\|^2 \sigma_x^2 \left(L + \frac{2}{B_w} D_{eq} \right) \right]$	
Eq. (4.8)	$D_{eq} \triangleq \frac{\mathbf{s}^T \mathbf{\Psi} \mathbf{s}}{\|\mathbf{s}\|^2}$	- constant matrix $\mathbf{\Psi}$ is given in Eq. (3.63). - $\mathbf{s}$ is the secondary path weight vector as defined in Eq. (2.5).

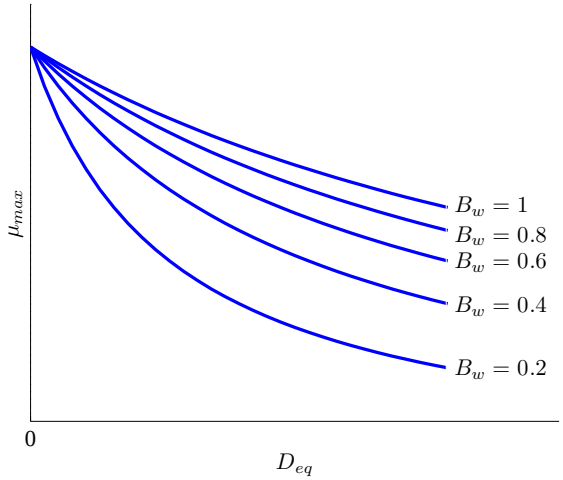

Figure 5.5: Influences of secondary path equivalent delay (D_{eq}) on upper-bound of stability (μ_{max}) for different noise band-widths

5.3 System Behaviours with Band-Limited Acoustic Noise

By using the dynamic model, shown in Figure 5.4, this section studies behaviours of FxLMS-based ANC systems and derives closed-form expressions for the steady-state performance, stability bound, and transient convergence speed of these systems. These expressions can apply to a general secondary path, unlike the commonly-used expressions which can apply to only a pure delay secondary path. Also these expressions are derived considering a white noise with an arbitrary band-width, unlink the expressions derived in Chapter 4 which are derived assuming a broad-band white noise.

5.3.1 Step-Size Upper-Bound

Based on the same logic[1] used in Section 4.3 and from Eq. (5.21), it can be shown that the stability of FxLMS-based ANC systems with a band-limited reference signal requires that

$$\beta_w > 0 \tag{5.22}$$

Substituting Eq. (5.20) into this inequality, results in the following step-size upper-bound beyond which the system becomes unstable.

$$\mu_{max} = \frac{2}{\|\mathbf{s}\|^2 \sigma_x^2 \left(L + \frac{2}{B_w} D_{eq} \right)} \tag{5.23}$$

Figure 5.5 shows variations of μ_{max} with respect to D_{eq} for different noise band-widths. This figure is obtained by plotting Eq. (5.23). The curve, shown by $B_w = 1$, corresponds to the case with a broad-band white noise, as described in the previous chapter. From this figure, it can be seen that by decreasing B_w, the step-size upper-bound is also decreased. Also, by decreasing B_w, the influence of the secondary path equivalent delay on the step-size upper-bound is more pronounced.

[1] This is because both the dynamic models, derived in the previous chapter and this chapter, have similar structure; the only differences are due to the changing the scalar coefficients α and β to α_w and β_w.

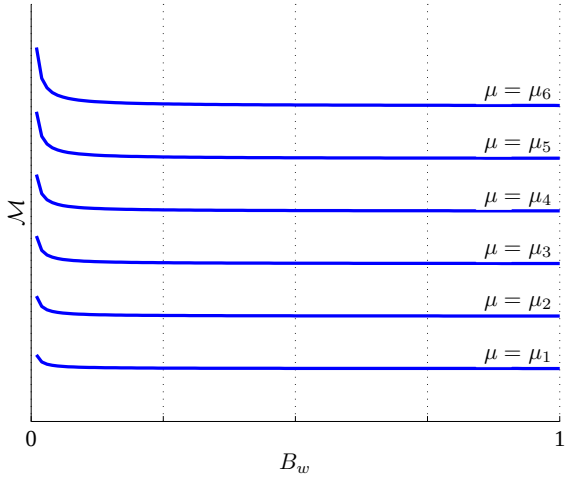

Figure 5.6: Influences of noise band-width (B_w) on misadjustment level ($\mathcal{M}$) for different values of step-size ($\mu_1 < \mu_2 < \mu_3 < \mu_4 < \mu_5 < \mu_6$)

In [49], Bjarnason studied the influence of B_w on μ_{max}. However, he did not intend to formulate this influence based on a theoretical model. He tried to fit a closed-form expression to data obtained from computer simulations. As one of the contribution of this thesis, Eq. (5.23) gives a closed-form expression for μ_{max} in terms of acoustic noise band-width B_w and considering a general secondary path.

5.3.2 Steady-State Performance

Based on the same logic used in the derivation of Eq. (4.21), the steady-state residual noise power can be obtained by replacing α and β with α_w and β_w in Eq. (4.21) as

$$\sigma_e^2 = J_o + \frac{\alpha_w}{\|\mathbf{s}\|^2 \beta_w} J_o \tag{5.24}$$

Now, substituting Eqs. (5.19) and (5.20) into (5.24) results in

$$\sigma_e^2 = J_o + \frac{\mu L \|\mathbf{s}\|^2 \sigma_x^2 J_o}{2 - \mu \|\mathbf{s}\|^2 \sigma_x^2 \left(L + \frac{2}{B_w} D_{eq} \right)} \tag{5.25}$$

Eq. (5.25) can be re-expressed as

$$\sigma_e^2 = J_o + \frac{\mu L \|\mathbf{s}\|^2 \sigma_x^2 J_o}{2 \left(1 - \frac{\mu}{\mu_{max}} \right)} \tag{5.26}$$

where μ_{max} is given in Eq. (5.23). For determining influences of the noise band-width B_w on the steady-state residual noise power σ_e^2, its influences on the minimum MSE level J_o should be also considered. This is because J_o is a function of noise statistics and, thereby, it is dependant of B_w. However, J_o is an optimal value and independent of the FxLMS adaptation process (as discussed in Chapter 2).

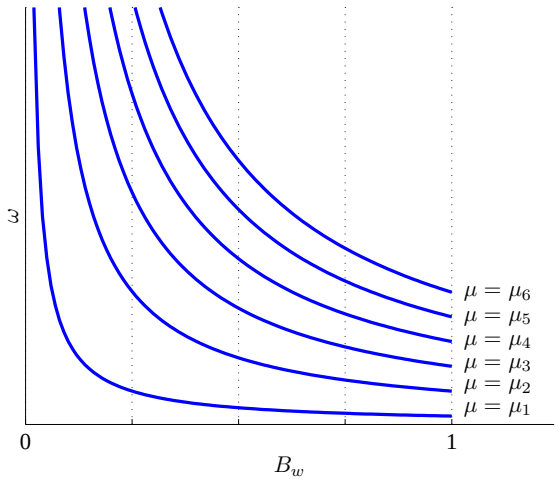

Figure 5.7: Influences of noise band-width (B_w) on convergence speed measure (ω) for different values of step-size ($\mu_1 < \mu_2 < \mu_3 < \mu_4 < \mu_5 < \mu_6 < 0.5\mu_{max}$)

For determining the influence of B_w on the steady-state performance of the FxLMS algorithm, the variation of the misadjustment level ($\mathcal{M}$) with respect to B_w can be analysed. This is because $\mathcal{M}$ is independent of J_o. This parameter can be obtained by combining Eqs. (4.24) and (5.26) as

$$\mathcal{M} = \frac{\mu \left\|\mathbf{s}\right\|^2 \sigma_x^2 L}{2\left(1 - \dfrac{\mu}{\mu_{max}}\right)} \tag{5.27}$$

As can be seen in Eq. (5.27), $\mathcal{M}$ is independent of J_o. However, $\mathcal{M}$ is a function of B_w (because μ_{max} is a function of B_w). By using Eqs. (5.27) and (5.23), variations of $\mathcal{M}$ with respect to B_w and for different values of μ can be plotted, as shown in Figure 5.6. From this figure, it can be seen that increasing B_w causes $\mathcal{M}$ to be decreased. For very narrow noise band-widths ($B_w < 0.1$), $\mathcal{M}$ is highly decreased. However, for wider noise band-widths, the influence of B_w on $\mathcal{M}$ is less pronounced.

5.3.3 Convergence Speed

Based on the the same logic, used in the derivation of Eq. (4.46), the convergence speed measure of FxLMS-based ANC systems with band-limited white reference signals can be represented by

$$\omega = \beta_w \tag{5.28}$$

Substituting Eq. (5.20) into this equation, results in

$$\omega = \mu \frac{\sigma_x^2}{B_w}\left[2 - \mu \left\|\mathbf{s}\right\|^2 \sigma_x^2 \left(L + \frac{2}{B_w} D_{eq}\right)\right] \tag{5.29}$$

which can be expressed as

$$\omega = 2\mu \frac{\sigma_x^2}{B_w}\left(1 - \frac{\mu}{\mu_{max}}\right) \tag{5.30}$$

By using Eq. (5.30), variations of the convergence speed measure with respect to the noise band-width can be plotted, as shown in Figure 5.7. From this figure, it can be seen that by increasing B_w, the convergence speed is decreased.

The step-size leading to the fastest convergence speed (μ^*) can be obtained by maximising ω with respect to μ. Therefore,

$$\left.\frac{d\omega}{d\mu}\right|_{\mu^*} = 0 \tag{5.31}$$

Combining Eqs. (5.30) and (5.31) results in

$$\mu^* = 0.5\mu_{max} \tag{5.32}$$

Therefore, the maximum attainable convergence speed can be obtained by setting the step-size to $0.5\mu_{max}$.

5.4 Tonal Acoustic Noise

The performance analysis of FxLMS-based ANC systems with tonal acoustic noise is another area of interest. This subject has been relatively matured, specially, in research reports published by Bjarnason in 1995 [49] and Vicente in 2006 [50]. This section shows that the theoretical results, reported in [50], can be obtained from a special and simplified case of the analysis conducted in this chapter. The similarity between these results shows the validity of the general analysis conducted in this chapter. Checking the validity of the results in a more general case is left to Chapters 7 and 10 using computer simulation and experimental results, respectively.

For a tonal acoustic noise, there is only a dominant Eigenvalue in the ACM matrix $(L_w = 1)$ which corresponds to the signal power at the tonal frequency. In this case, from Eq. (5.3), it can be shown that

$$B_w = \frac{1}{L} \tag{5.33}$$

Also, in this situation, the secondary path can be represented by a static gain A and a time delay D as

$$s\left(n\right) = A\delta\left(n - D\right) \tag{5.34}$$

For such secondary path, $\|\mathbf{s}\|^2 = A^2$ and $D_{eq} = D$. Now, setting B_w, $\|\mathbf{s}\|^2$ and D_{eq} in Eq. (5.27) gives the following expression for the misadjustment level:

$$\mathcal{M} = \frac{\mu\sigma_{x_f}^2 L}{2 - \mu\sigma_{x_f}^2 L\left(1 + 2D\right)} \tag{5.35}$$

where $\sigma_{x_f}^2 = A^2\sigma_x^2$ denotes the power of the filtered reference signal. Also, setting B_w, $\|\mathbf{s}\|^2$ and D_{eq} into Eq. (5.23) results in the following stability bound.

$$\mu_{max} = \frac{2}{\sigma_{x_f}^2 L\left(1 + 2D\right)} \tag{5.36}$$

As can be seen, for a tonal noise, μ_{max} is inversely proportional to the multiplication of the filter length L and secondary path time delay D, rather than their summation. The expressions given in Eqs. (5.35) and (5.36) are identical to those obtained in [50].

5.5 Summary

From the theoretical results obtained in this chapter, the following statements can be expressed.

- Considering a general secondary path with the equivalent delay of D_{eq} and a general band-limited acoustic noise, the step-size upper-bound μ_{max}, steady-state noise power σ_e^2, misadjustment level $\mathcal{M}$, and transient convergence speed measure ω can be formulated as

$$\begin{cases} \mu_{max} = \dfrac{2}{\|\mathbf{s}\|^2 \sigma_x^2 \left(L + \dfrac{2}{B_w} D_{eq} \right)} \\ \sigma_e^2 = J_o + \dfrac{\mu L \|\mathbf{s}\|^2 \sigma_x^2 J_o}{2 \left(1 - \dfrac{\mu}{\mu_{max}} \right)} \\ \mathcal{M} = \dfrac{\mu L \|\mathbf{s}\|^2 \sigma_x^2}{2 \left(1 - \dfrac{\mu}{\mu_{max}} \right)} \\ \omega = 2\mu \dfrac{\sigma_x^2}{B_w} \left(1 - \dfrac{\mu}{\mu_{max}} \right) \end{cases}$$

- Similar to the case with broad-band acoustic noise, the step-size leading to the fastest convergence speed is

$$\mu^* = \frac{\mu_{max}}{2}$$

- The step-size upper-bound is an increasing function of B_w; therefore, in the case with a broad-band white noise, the step-size can be chosen from a wider range, compared to the case with band-limited white acoustic noise.

- The misadjustment is a decreasing function of B_w; therefore, by increasing the acoustic noise band-width the misadjustment level is reduced.

- The convergence speed measure is a decreasing function of B_w; therefore, by increasing the acoustic noise band-width the convergence speed is reduced.

Chapter 6

Influences of Secondary Path Models on FxLMS-Based ANC Systems

As discussed in Chapter 2, for implementing FxLMS-based ANC systems, an estimate model of the secondary path is required. This model, usually referred to as the secondary path model, is estimated by either off-line or on-line system identification techniques (which are beyond the scope of this thesis). Ideally, the secondary path model is identical to the actual secondary path. In this case, the secondary path model is considered as a perfect model. However, a realistic secondary path model is not necessarily perfect.

Commonly-used theoretical expressions for formulating behaviours of FxLMS-based ANC systems are usually derived by assuming a perfect secondary path model, to avoid mathematical difficulties. Even the relatively more generalised expressions, obtained in Chapters 4 and 5 of this thesis, are derived under this simplifying assumption. Referring to Figure 6.1, it can be seen that this chapter removes the constraint caused by assuming a perfect secondary path model from the theoretical results obtained in Chapters 4 and 5. Consequently, the expressions, obtained in this chapter, are the most general theoretical expressions which have been so far derived for formulating behaviours of FxLMS-based ANC systems.

6.1 System Model with Imperfect Secondary Path Model

In Chapter 5, $\gamma_{l,p,q}$ is computed for a general secondary path and band-limited acoustic noise. This parameter is then simplified by assuming a perfect secondary path model: $\hat{\mathbf{s}} = \mathbf{s}$. Herein, this simplifying assumption is not used. Therefore, substituting the expression given in Eq. (5.13) for $\gamma_{l,p,q}$ into Eq. (3.66) results in a more general expression for $\triangle J_{ex}(n)$ as

$$\begin{aligned} \triangle J_{ex}(n) &= \mu^2 \|\hat{\mathbf{s}}\|^2 \|\mathbf{s}\|^2 \frac{\sigma_x^4}{B_w} L J_o \\ &- \mu \frac{\sigma_x^2}{B_w} \sum_{q,p=0}^{Q-1} \sum_{l=0}^{L-1} s_q^2 \left[2 s_p \hat{s}_p - \mu \sigma_x^2 \|\hat{\mathbf{s}}\|^2 \left(L s_p^2 + \frac{2}{B_w} s_p \hat{s}_p \frac{\mathbf{s}^T \boldsymbol{\Psi} \hat{\mathbf{s}}}{\|\hat{\mathbf{s}}\|^2} \right) \right] \lambda_l m_l (n-p-q) \end{aligned} \tag{6.1}$$

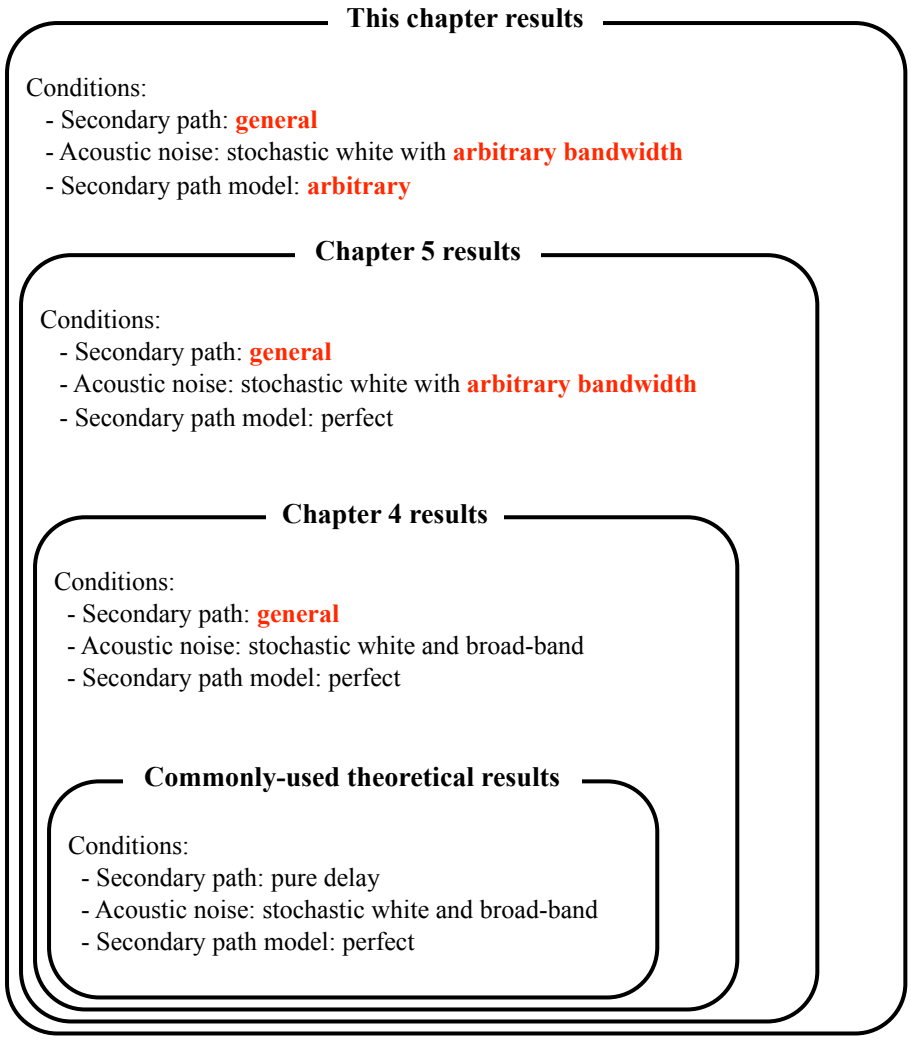

Figure 6.1: Contribution of Chapter 6: generalisation of the theoretical findings considering an arbitrary (imperfect) secondary path model

Combining Eqs. (3.15) and (6.1) results in

$$\begin{aligned} \triangle J_{ex}(n) &= \mu^2 \|\hat{\mathbf{s}}\|^2 \|\mathbf{s}\|^2 \frac{\sigma_x^4}{B_w} L J_o \\ &- \mu \frac{\sigma_x^2}{B_w} \sum_{p=0}^{Q-1} \left[2 s_p \hat{s}_p - \mu \sigma_x^2 \|\hat{\mathbf{s}}\|^2 \left(L s_p^2 + \frac{2}{B_w} s_p \hat{s}_p \frac{\mathbf{s}^T \mathbf{\Psi} \hat{\mathbf{s}}}{\|\hat{\mathbf{s}}\|^2} \right) \right] J_{ex}(n-p) \end{aligned} \tag{6.2}$$

Now, scalar functions $\mathcal{J}(n)$ and $\hat{\mathcal{J}}(n)$ are defined as

$$\mathcal{J}(n) = \sum_{p=0}^{Q-1} s_p^2 J_{ex}(n-p) \tag{6.3}$$

and

$$\hat{\mathcal{J}}(n) = \sum_{p=0}^{Q-1} s_p \hat{s}_p J_{ex}(n-p) \tag{6.4}$$

Substituting these definitions into Eq. (6.2) results in

$$\begin{aligned} \triangle J_{ex}(n) &= \mu^2 \|\hat{\mathbf{s}}\|^2 \|\mathbf{s}\|^2 \frac{\sigma_x^4}{B_w} L J_o - 2\mu \frac{\sigma_x^2}{B_w} \left[1 - \mu \frac{\sigma_x^2}{B_w} \left(\mathbf{s}^T \mathbf{\Psi} \hat{\mathbf{s}} \right) \right] \hat{\mathcal{J}}(n) \\ &+ \mu^2 \|\hat{\mathbf{s}}\|^2 L \frac{\sigma_x^4}{B_w} \mathcal{J}(n) \end{aligned} \tag{6.5}$$

For a perfect secondary path model, it can be shown that $\hat{\mathcal{J}}(n) = \mathcal{J}(n)$; however, for an imperfect model, this equality is not valid. In the following, it can be shown that, for a slow adaptation process, there is a relationship between these two scalar functions. Assuming that the adaptation process is slow, the variation of the excess-MSE function is also slow so:

$$J_{ex}(n-p) \approx J_{ex}(n), \qquad p = 0, 1, \ldots, Q-1 \tag{6.6}$$

In this case, from Eq. (6.3), it can be shown that

$$\mathcal{J}(n) \approx \left(\sum_{p=0}^{Q-1} s_p^2 \right) J_{ex}(n) \tag{6.7}$$

Using the same logic, it can be shown from Eq. (6.4) that

$$\hat{\mathcal{J}}(n) \approx \left(\sum_{p=0}^{Q-1} s_p \hat{s}_p \right) J_{ex}(n) \tag{6.8}$$

Now, combining Eqs. (6.7) and (6.8) results in

$$\hat{\mathcal{J}}(n) = \frac{\sum_{p=0}^{Q-1} s_p \hat{s}_p}{\sum_{p=0}^{Q-1} s_p^2} \mathcal{J}(n) \tag{6.9}$$

which can be expressed in the following form.

$$\hat{\mathcal{J}}(n) = \frac{\mathbf{s}^T \hat{\mathbf{s}}}{\|\mathbf{s}\|^2} \mathcal{J}(n) \tag{6.10}$$

Eq. (6.10) shows the existence of a linear proportional relationship between scalar functions $\mathcal{J}(n)$ and $\hat{\mathcal{J}}(n)$. Now, by substituting Eq. (6.10) into (6.5), $\triangle J_{ex}(n)$ is simplified to

$$\begin{aligned} \triangle J_{ex}(n) &= \mu^2 \|\hat{\mathbf{s}}\|^2 \|\mathbf{s}\|^2 \frac{\sigma_x^4}{B_w} L J_o \\ &- \left\{ 2\mu \frac{\sigma_x^2}{B_w} \left[1 - \mu \frac{\sigma_x^2}{B_w} \left(\mathbf{s}^T \mathbf{\Psi} \hat{\mathbf{s}} \right) \right] \left(\frac{\mathbf{s}^T \hat{\mathbf{s}}}{\|\mathbf{s}\|^2} \right) - \mu^2 \|\hat{\mathbf{s}}\|^2 L \frac{\sigma_x^4}{B_w} \right\} \mathcal{J}(n) \end{aligned} \tag{6.11}$$

Therefore,

$$\begin{aligned} \triangle J_{ex}(n) &= \mu^2 \|\hat{\mathbf{s}}\|^2 \|\mathbf{s}\|^2 \frac{\sigma_x^4}{B_w} L J_o \\ &+ \left[\mu^2 \|\hat{\mathbf{s}}\|^2 L \frac{\sigma_x^4}{B_w} - 2\mu \frac{\sigma_x^2}{B_w} \left(\frac{\mathbf{s}^T \hat{\mathbf{s}}}{\|\mathbf{s}\|^2} \right) + 2\mu^2 \left(\mathbf{s}^T \mathbf{\Psi} \hat{\mathbf{s}} \right) \frac{\sigma_x^4}{B_w^2} \left(\frac{\mathbf{s}^T \hat{\mathbf{s}}}{\|\mathbf{s}\|^2} \right) \right] \mathcal{J}(n) \end{aligned} \tag{6.12}$$

Herein, perfectness ratios ρ_1, ρ_2 and ρ_3 are defined as

$$\rho_1 = \frac{\|\hat{\mathbf{s}}\|^2}{\|\mathbf{s}\|^2} \tag{6.13}$$

and

$$\rho_2 = \frac{\mathbf{s}^T \hat{\mathbf{s}}}{\|\hat{\mathbf{s}}\|^2} \tag{6.14}$$

and

$$\rho_3 = \frac{\mathbf{s}^T \mathbf{\Psi} \hat{\mathbf{s}}}{\mathbf{s}^T \mathbf{\Psi} \mathbf{s}} \tag{6.15}$$

Obviously, for a perfect model ($\hat{\mathbf{s}} = \mathbf{s}$) all the perfectness ratios are equal to 1. Now, by using the above definitions for ρ_1, ρ_2 and ρ_3, Eq. (6.12) can be expressed as

$$\begin{aligned} \triangle J_{ex}(n) &= \rho_1 \mu^2 \|\mathbf{s}\|^4 \frac{\sigma_x^4}{B_w} L J_o \\ &+ \left[\rho_1 \mu^2 \|\mathbf{s}\|^2 L \frac{\sigma_x^4}{B_w} - 2\mu \frac{\sigma_x^2}{B_w} \rho_1 \rho_2 + 2\mu^2 \rho_1 \rho_2 \rho_3 \left(\mathbf{s}^T \mathbf{\Psi} \mathbf{s} \right) \frac{\sigma_x^4}{B_w^2} \right] \mathcal{J}(n), \end{aligned} \tag{6.16}$$

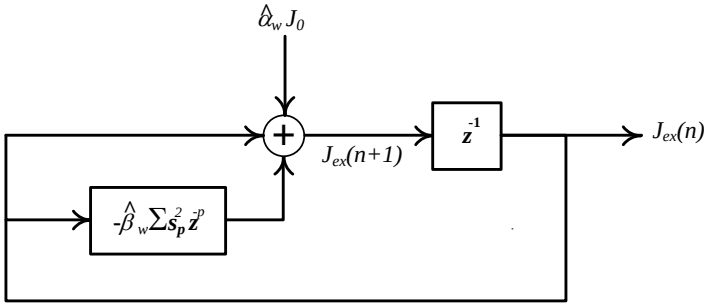

Figure 6.2: Proposed model for FxLMS-based ANC systems with a general secondary path, a band-limited acoustic noise, and an arbitrary (imperfect) secondary path model

which can be simplified to

$$\begin{aligned} \triangle J_{ex}(n) &= \rho_1 \mu^2 \|\mathbf{s}\|^4 \frac{\sigma_x^4}{B_w} L J_o \\ &- \rho_1 \mu \frac{\sigma_x^2}{B_w} \left[2\rho_2 - \mu \sigma_x^2 \|\mathbf{s}\|^2 \left(L + \frac{2\rho_2 \rho_3}{B_w} \left(\frac{\mathbf{s}^T \mathbf{\Psi} \mathbf{s}}{\|\mathbf{s}\|^2} \right) \right) \right] \mathcal{J}(n), \end{aligned} \tag{6.17}$$

As can be seen, the secondary path equivalent delay D_{eq}, as defined in Chapter 4, appears in Eq. (6.17); therefore

$$\begin{aligned} \triangle J_{ex}(n) &= \rho_1 \mu^2 \|\mathbf{s}\|^4 \frac{\sigma_x^4}{B_w} L J_o \\ &- \rho_1 \mu \frac{\sigma_x^2}{B_w} \left[2\rho_2 - \mu \sigma_x^2 \|\mathbf{s}\|^2 \left(L + \frac{2\rho_2 \rho_3}{B_w} D_{eq} \right) \right] \mathcal{J}(n), \end{aligned} \tag{6.18}$$

Now, time-invariant parameters $\hat{\alpha_w}$ and $\hat{\beta_w}$ are defined as

$$\hat{\alpha}_w = \rho_1 \mu^2 \|\mathbf{s}\|^4 \frac{\sigma_x^4}{B_w} L J_o \tag{6.19}$$

and

$$\hat{\beta}_w = \rho_1 \mu \frac{\sigma_x^2}{B_w} \left[2\rho_2 - \mu \sigma_x^2 \|\mathbf{s}\|^2 \left(L + \frac{2\rho_2 \rho_3}{B_w} D_{eq} \right) \right] \tag{6.20}$$

Using these definitions, Eq. (5.18) can be re-expressed as

$$\triangle J_{ex}(n) = \hat{\alpha}_w J_o - \hat{\beta}_w \mathcal{J}(n) \tag{6.21}$$

The dynamic model, given in Eq. (6.21), along with Eqs. (3.17), (6.3), (6.19) and (6.20) compose a theoretical model for FxLMS-based ANC systems, considering a general secondary path, a band-limited acoustic noise, and an arbitrary secondary path model. For the sake of clarity, these equations are collected in Table 6.1. The functional block diagram of this model is also shown in Figure 6.2.

From Eqs.(6.19) and (6.20), it can be seen that by setting $B_w = 1$ (broad-band noise) and $\hat{\mathbf{s}} = \mathbf{s}$ (perfect model) the expressions, given for $\hat{\alpha}_w$ and $\hat{\beta}_w$, results in $\hat{\alpha}_w = \alpha$ and $\hat{\beta}_w = \beta$. In this case, the proposed model is simplified to the one derived in Chapter 4. In other words, the dynamic model obtained in this chapter is a generalisation of the models previously obtained in Chapters 4 and 5 of this thesis. However,

Table 6.1: Theoretical model for FxLMS-based ANC systems with a general secondary path, band-limited acoustic noise, and an arbitrary secondary path model

Equation		Description
Eq. (3.17)	$\triangle J_{ex}(n) = J_{ex}(n+1) - J_{ex}(n)$	
Eq. (6.21)	$\triangle J_{ex}(n) = \hat{\alpha}_w J_o - \hat{\beta}_w \mathcal{J}(n)$	- J_o is the minimum attainable residual acoustic noise power, as defined in Eq. (2.16).
Eq. (6.3)	$\mathcal{J}(n) = \sum_{p=0}^{Q-1} s_p^2 J_{ex}(n-p)$	- $s_0, s_1, \ldots, s_{Q-1}$ are elements of $\mathbf{s}$
Eq. (6.19)	$\hat{\alpha}_w = \rho_1 \mu^2 \|\mathbf{s}\|^4 \frac{\sigma_x^4}{B_w} L J_o$	- μ is the adaptation step size. - L is the ANC controller length. - σ_x^2 is the power of the reference signal. - B_w is the reference signal bandwidth.
Eq. (6.20)	$\hat{\beta}_w = \rho_1 \mu \frac{\sigma_x^2}{B_w} \left[2\rho_2 - \mu \sigma_x^2 \|\mathbf{s}\|^2 \left(L + \frac{2\rho_2 \rho_3}{B_w} D_{eq} \right) \right]$	
Eq. (4.8)	$D_{eq} = \frac{\mathbf{s}^T \mathbf{\Psi} \mathbf{s}}{\|\mathbf{s}\|^2}$	- constant matrix $\mathbf{\Psi}$ is given in Eq. (3.63). - $\mathbf{s}$ is the secondary path weight vector as defined in Eq. (2.5).
Eqs. (6.13) -(6.15)	$\rho_1 = \frac{\|\hat{\mathbf{s}}\|^2}{\|\mathbf{s}\|^2}$ $\rho_2 = \frac{\mathbf{s}^T \hat{\mathbf{s}}}{\|\hat{\mathbf{s}}\|^2}$ $\rho_3 = \frac{\mathbf{s}^T \mathbf{\Psi} \hat{\mathbf{s}}}{\mathbf{s}^T \mathbf{\Psi} \mathbf{s}}$	- $\hat{\mathbf{s}}$ is the secondary path model weight vector as defined in Eq. (2.7).

the structure of both of them is similar. Therefore, the theoretical findings, obtained in Chapter 4, are also valid for the model given in Eq. (6.21), after replacing α and β with $\hat{\alpha}_w$ and $\hat{\beta}_w$.

6.2 System Behaviours with Imperfect Secondary Path Models

By using the dynamic model, developed in Section 6.1, this section studies behaviours of FxLMS-based ANC systems and derives closed-form expressions for the steady-state performance, step-size upper-bound, and convergence speed of these system. In the derivation of these expressions, a general secondary path, an arbitrary secondary path model and, an stochastic acoustic white noise with an arbitrary band-width are considered. The obtained expressions are the most general theoretical expressions which have been so far derived for formulating behaviours of FxLMS-based ANC systems.

6.2.1 Step-Size Upper-Bound

In Chapter 4, it was proved that the stability of the dynamic model, given in Eq. (4.13), requires the scalar parameter β to be positive: $\beta > 0$. The only difference between the model, given in Eq. (4.13) and the one given in Eq. (6.21) of this chapter, is due to the changing of scalar (constant) parameters α and β to $\hat{\alpha}_w$ and $\hat{\beta}_w$. Accordingly, the stability of the model, given in Eq. (6.21) requires the scalar parameter $\hat{\beta}_w$ to be positive (because the model given in Eq. (4.13) is stable when $\beta > 0$):

$$\hat{\beta}_w > 0 \tag{6.22}$$

Combining Eqs. (6.20) and (6.22), it can be shown that $\hat{\beta}_w > 0$ requires that

$$\rho_1 \mu \frac{\sigma_x^2}{B_w} \left[2\rho_2 - \mu \sigma_x^2 \left\| \mathbf{s} \right\|^2 \left(L + \frac{2\rho_2 \rho_3}{B_w} D_{eq} \right) \right] > 0 \tag{6.23}$$

From Eq. (6.13), it can be seen that ρ_1 is a positive scalar. Also, parameters σ_x^2 and B_w are positive; therefore, the above inequality is identical to

$$\mu \left[2\rho_2 - \mu \sigma_x^2 \left\| \mathbf{s} \right\|^2 \left(L + \frac{2\rho_2 \rho_3}{B_w} D_{eq} \right) \right] > 0 \tag{6.24}$$

From this result, it can be deduced that the stability of the system requires

$$0 < \mu < \hat{\mu}_{max} \tag{6.25}$$

where the step-size upper-bound, $\hat{\mu}_{max}$ is given by

$$\hat{\mu}_{max} = \frac{2\rho_2}{\sigma_x^2 \left\| \mathbf{s} \right\|^2 \left(L + \frac{2\rho_2 \rho_3}{B_w} D_{eq} \right)} \tag{6.26}$$

In this equation, $\hat{\mu}_{max}$ represents the step-size upper-bound in the case of using the imperfect secondary path model $\hat{\mathbf{s}}$, instead of the perfect model $\mathbf{s}$. The closed-form expression for $\hat{\mu}_{max}$, given in Eq. (6.26),

can apply to a general case, where the actual secondary path and secondary path model are two arbitrary general systems and the acoustic noise is a stochastic white signal with an arbitrary band-width.

6.2.2 Instability Caused by Secondary Path Models

According to Eq. (6.26), it is possible that the secondary path model causes $\hat{\mu}_{max}$ to become always negative. In this case, there is no positive step-size for which the FxLMS algorithm can become stable. Based on this logic, secondary path models causing the FxLMS algorithm to become unstable can be determined.

Usually L is set to a large number, therefore it can be assumed that even if ρ_2 and ρ_3 have opposite signs, the denominator of the fraction given in Eq. (6.26) remains positive. Accordingly, the sign of $\hat{\mu}_{max}$ can be determined only by considering the numerator of the fraction given in Eq. (6.26).

Initially, let us consider the case in which the second perfectness ratio is positive ($\rho_2 > 0$). In this case, from Eq. (6.14) it can be shown that $\hat{\mu}_{max}$ is also positive. In the next case, let us consider the case in which the second perfectness ratio is negative ($\rho_2 < 0$). In this case $\hat{\mu}_{max}$ becomes negative and, thereby, there is no positive step-size for which the FxLMS algorithm can become stable.

According to the above discussion, only for secondary path models with $\rho_2 < 0$, the FxLMS algorithm cannot become stable. Eq. (6.14) gives ρ_2 in terms of actual secondary path and its model vectors. On the other hand, the inner product of two vectors can be expressed as

$$\mathbf{s}^T\hat{\mathbf{s}} = \|\mathbf{s}\|\,\|\hat{\mathbf{s}}\|\cos\phi \tag{6.27}$$

where ϕ is the angle between vectors $\mathbf{s}$ and $\hat{\mathbf{s}}$ in Q-dimensional space. Now, combining Eqs. (6.14) and (6.27) results in

$$\rho_2 = \frac{\|\mathbf{s}\|}{\|\hat{\mathbf{s}}\|}\cos\phi \tag{6.28}$$

Since both $\|\mathbf{s}\|$ and $\|\hat{\mathbf{s}}\|$ are positive, the instability condition of the FxLMS algorithm (which is $\rho_2 < 0$) requires that

$$\cos\phi < 0 \tag{6.29}$$

As an elegant result, when the angle between the actual secondary path vector and its model vector is greater than 90^o, then the FxLMS algorithm cannot become stable. This result is in an excellent agreement with the 90^o condition, derived by Boucher for pure delay secondary paths and tonal acoustic noise [56] or by Morgan for an identity secondary path model [10]. For these simplified cases, in which only one element in vectors $\mathbf{s}$ and $\hat{\mathbf{s}}$ are non-zero, Boucher showed that if the secondary path model is 90^o out of phase, then the FxLMS algorithm cannot become stable. However, in the derivation of Eq. (6.29), a general secondary path, its arbitrary model, and an arbitrary acoustic noise band-width are considered. This generalisation is one of the contributions of this thesis.

6.2.3 Steady-State Performance

According to the similarity between the models, given in Eqs. (4.13) and (6.21), the steady-state residual noise power of the system given in Eq. (6.21) can be expressed by replacing α and β with $\hat{\alpha}_w$ and $\hat{\beta}_w$ in Eq. (4.22) as

$$\hat{\sigma}_e^2 = J_o + \frac{\hat{\alpha_w}}{\|\mathbf{s}\|^2 \hat{\beta_w}} J_o \tag{6.30}$$

where $\hat{\sigma}_e^2$ denotes the residual acoustic noise power in steady-state conditions for the imperfect secondary path model $\hat{\mathbf{s}}$. Note that the secondary path model does not have any influence on the minimal MSE level J_o. Now, substituting Eqs. (6.19) and (6.20) into (6.30) results in

$$\hat{\sigma}_e^2 = J_o + \frac{\mu\sigma_x^2 \|\mathbf{s}\|^2 L}{2\rho_2 - \mu\sigma_x^2 \|\mathbf{s}\|^2 \left(L + \frac{2\rho_2\rho_3}{B_w} D_{eq}\right)} J_o \tag{6.31}$$

which can be re-expressed in the following form.

$$\hat{\sigma}_e^2 = J_o + \frac{\mu\sigma_x^2 \|\mathbf{s}\|^2 L}{2\rho_2 \left(1 - \frac{\mu}{\hat{\mu}_{max}}\right)} J_o \tag{6.32}$$

This equation shows that influences of the secondary path model on the steady-state residual noise can be formulated by two parameters ρ_2 and ρ_3 (note that $\hat{\mu}_{max}$ is a function of ρ_2 and ρ_3) [1].

Now, the misadjustment level can be obtained by combining Eqs. (4.24) and (6.31) as

$$\hat{\mathcal{M}} = \frac{\mu\sigma_x^2 \|\mathbf{s}\|^2 L}{2\rho_2 \left(1 - \frac{\mu}{\hat{\mu}_{max}}\right)} \tag{6.33}$$

Eq. (6.33) gives a closed-form expression for the misadjustment level in FxLMS-based ANC systems when the actual secondary path and its model are two arbitrary systems and the acoustic noise is a white stochastic signal with an arbitrary band-width. This expression is more general than those derived in Chapters 4 and 5.

It can be shown from Eq. (6.33) that an imperfect secondary path model does not necessarily degrade the steady-state performance of FxLMS-based ANC systems. For the case in which the secondary path model causes the steady-state performance to be improved, the misadjustment level $\hat{\mathcal{M}}$ is smaller than $\mathcal{M}$:

$$\hat{\mathcal{M}} < \mathcal{M} \tag{6.34}$$

Now, substituting Eqs. (5.27) and (6.33) into this inequality results in

$$\frac{1}{\rho_2} < \frac{1 - \frac{\mu}{\hat{\mu}_{max}}}{1 - \frac{\mu}{\mu_{max}}} \tag{6.35}$$

[1] Since the secondary path model is a part of the adaptation process (not a part of physical plant) it has no influence on the optimal MSE level J_o.

For small step-sizes, where $\mu \ll \mu_{max}$ and $\mu \ll \hat{\mu}_{max}$, this condition becomes

$$\rho_2 > 1 \tag{6.36}$$

As an interesting result, when the second perfectness ratio is greater than 1, then the imperfect secondary path model improves the steady-state performance of FxLMS-based ANC systems.

6.2.4 Convergence Speed

According to the similarity between the models, given in Eqs. (4.13) and (6.21), the convergence speed measure of the model given in Eq. (6.21) can be expressed by replacing β with $\hat{\beta}_w$ in Eq. (4.46) as

$$\hat{\omega} = \hat{\beta}_w \tag{6.37}$$

where $\hat{\omega}$ denotes the convergence speed measure in the case of using the imperfect secondary path model $\hat{\mathbf{s}}$. Substituting Eq. (6.20) into (6.37), results in

$$\hat{\omega} = \rho_1 \mu \frac{\sigma_x^2}{B_w} \left[2\rho_2 - \mu \sigma_x^2 \left\| \mathbf{s} \right\|^2 \left(L + \frac{2\rho_2 \rho_3}{B_w} D_{eq} \right) \right] \tag{6.38}$$

which can be described as

$$\hat{\omega} = 2\mu \frac{\sigma_x^2}{B_w} \rho_1 \rho_2 \left(1 - \frac{\mu}{\hat{\mu}_{max}} \right) \tag{6.39}$$

As another interesting result, it can be shown from Eq. (6.39) that an imperfect secondary path model does not necessarily degrade the transient convergence speed. For the case in which the secondary path model causes the transient convergence speed to be improved, $\hat{\omega}$ is greater than ω:

$$\hat{\omega} > \omega \tag{6.40}$$

Now, substituting Eqs. (5.30) and (6.39) into this inequality results in

$$\rho_1 \rho_2 \left(1 - \frac{\mu}{\hat{\mu}_{max}} \right) > 1 - \frac{\mu}{\mu_{max}} \tag{6.41}$$

Therefore,

$$\rho_1 \rho_2 > \frac{1 - \dfrac{\mu}{\mu_{max}}}{1 - \dfrac{\mu}{\hat{\mu}_{max}}} \tag{6.42}$$

For small step-sizes, where $\mu \ll \mu_{max}$ and $\mu \ll \hat{\mu}_{max}$, this condition becomes

$$\rho_1 \rho_2 > 1 \tag{6.43}$$

Therefore, when $\rho_1 \rho_2 > 1$ holds, then the imperfect secondary path model improves the convergence speed of the FxLMS algorithm.

Let us derive the step-size leading to the fastest convergence speed (μ^*) for imperfect secondary path models. This step-size can be obtained by maximising $\hat{\omega}$ with respect to μ. Therefore,

$$\left.\frac{d\hat{\omega}}{d\mu}\right|_{\mu^*} = 0 \tag{6.44}$$

Combining Eqs. (6.39) and (6.44) results in

$$\mu^* = 0.5\hat{\mu}_{max} \tag{6.45}$$

It means that the FxLMS algorithm has its fastest possible convergence speed if the step-size is set to the half of its upper-bound. Combination of this result and those obtained in Sections 4.4.2 and 5.3.3 shows that the ratio of μ^* and step-size upper-bound is constant and equal to 0.5, independent of the acoustic noise band-width and secondary path model.

6.3 Discussion

As an interesting result from the previous section, an imperfect secondary path model does not necessarily degrade the steady-state performance or convergence speed of FxLMS-based ANC systems. This section studies the possibility of the existence of a secondary path model which can improve both the steady-state performance and convergence speed of FxLMS-based ANC systems.

In linear algebra [67], it is well known that for any two arbitrary vectors $\mathbf{x}$ and $\mathbf{y}$ (with similar dimensions) the Cauchy Schawrs inequality always hold. This inequality can be stated as

$$\mathbf{x}^T\mathbf{y} \leq \|\mathbf{x}\|\,\|\mathbf{y}\| \tag{6.46}$$

Setting $\mathbf{x} = \mathbf{s}$ and $\mathbf{y} = \hat{\mathbf{s}}$ in Eq. (6.46) results in

$$\mathbf{s}^T\hat{\mathbf{s}} \leq \|\mathbf{s}\|\,\|\hat{\mathbf{s}}\| \tag{6.47}$$

By dividing both sides of this inequality by $\|\hat{\mathbf{s}}\|^2$ and considering Eq. (6.14), the following inequality for the second perfectness ratio can be derived.

$$\frac{\mathbf{s}^T\hat{\mathbf{s}}}{\|\hat{\mathbf{s}}\|^2} \leq \frac{\|\mathbf{s}\|}{\|\hat{\mathbf{s}}\|} \quad \Rightarrow \quad \rho_2 \leq \frac{\|\mathbf{s}\|}{\|\hat{\mathbf{s}}\|} \tag{6.48}$$

As mentioned in Section 6.2.3, when the secondary path model causes the steady-state performance to be improved, it is necessary that $\rho_2 > 1$. Therefore, by combining the inequality of $\rho_2 > 1$ and the one given in Eq. (6.48), it can be shown that the improvement in the steady-state performance occurs if the following necessary condition holds.

$$\frac{\|\mathbf{s}\|}{\|\hat{\mathbf{s}}\|} > 1 \tag{6.49}$$

Similarly, dividing both sides of the Cauchy Schawrs inequality, given in Eq. (6.47), by $\|\mathbf{s}\|^2$ results in

$$\frac{\mathbf{s}^T\hat{\mathbf{s}}}{\|\mathbf{s}\|^2} \leq \frac{\|\hat{\mathbf{s}}\|}{\|\mathbf{s}\|} \quad \Rightarrow \quad \rho_1\rho_2 \leq \frac{\|\hat{\mathbf{s}}\|}{\|\mathbf{s}\|} \tag{6.50}$$

According to Section 6.2.4, when the secondary path causes the convergence speed to be improved it is necessary that $\rho_1\rho_2 > 1$. Therefore, by combining the inequality of $\rho_1\rho_2 > 1$ and the one given in Eq. (6.50), it can be shown that the improvement in the convergence speed occurs if the following necessary condition holds.

$$\frac{\|\hat{\mathbf{s}}\|}{\|\mathbf{s}\|} > 1 \tag{6.51}$$

Considering the inequalities, given in Eqs. (6.49) and (6.50), it can be shown that there is no secondary path model $\hat{\mathbf{s}}$ for which both the necessary conditions for the improvement of the steady-state performance and convergence speed hold. Therefore, there is no secondary path model which improves both the steady-state performance and convergence speed of FxLMS-based ANC systems.

6.4 Summary

From the theoretical results obtained in this chapter, the following statements can be expressed.

- The deviation of a secondary path model from the actual secondary path can be represented by using three perfectness ratios ρ_1, ρ_2 and ρ_3, defined in Eqs. (6.13)-(6.15).
- Considering a general secondary path, an arbitrary acoustic noise band-width, and an arbitrary (imperfect) secondary path model, the step-size upper-bound μ_{max}, steady-state noise power σ_e^2, misadjustment level $\mathcal{M}$, and convergence speed measure ω can be formulated as

$$\begin{cases} \hat{\mu}_{max} = \dfrac{2\rho_2}{\sigma_x^2\|\mathbf{s}\|^2\left(L + \dfrac{2\rho_2\rho_3}{B_w}D_{eq}\right)} \\ \hat{\sigma}_e^2 = J_o + \dfrac{\mu\sigma_x^2\|\mathbf{s}\|^2 L}{2\rho_2\left(1 - \dfrac{\mu}{\hat{\mu}_{max}}\right)}J_o \\ \hat{\mathcal{M}} = \dfrac{\mu\sigma_x^2\|\mathbf{s}\|^2 L}{2\rho_2\left(1 - \dfrac{\mu}{\hat{\mu}_{max}}\right)} \\ \hat{\omega} = 2\mu\frac{\sigma_x^2}{B_w}\rho_1\rho_2\left(1 - \frac{\mu}{\hat{\mu}_{max}}\right) \end{cases}$$

These equation are in the most general form, compared to those derived in available literature and also in previous chapters of this thesis.

- When the phase difference between the actual secondary path $\mathbf{s}$ and its model $\hat{\mathbf{s}}$ becomes greater than 90^o ($\mathbf{s}^T\hat{\mathbf{s}} < 0$), the FxLMS algorithm becomes unstable. This result is the generalisation of the 90^o condition which was previously derived for simplified cases by other researchers.
- The imperfectness in a given secondary path model does not necessarily degrade steady-state performance or convergence speed of FxLMS-based ANC systems; however, improving both of them is impossible.

Chapter 7

Behaviours of FxLMS-Based ANC Systems in Computer Simulation

Based on the theoretical model developed in Chapter 3 a number of closed-form expressions for formulating behaviours of FxLMS-based ANC systems are derived in Chapters 4-6. In order to check the general validity of these expressions, this chapter studies behaviours of FxLMS-based ANC systems in computer simulation.

Section 7.1 starts with describing the simulated system, its components, and the numerical techniques used in the analysis of simulation results. Then this section shows that simulated system behaviours can be described precisely by using the theoretical model, developed in Chapter 3. Focusing on the stability behaviour, Section 7.2 shows the validity of the proposed expression for the step-size upper-bound. Also, this section shows that influences of the acoustic noise band-width and secondary path models on the step-size upper-bound of the simulated system can be formulated as proposed in Chapters 4-6. Section 7.3 shows the validity of the proposed expressions for the misadjustment level and steady-state residual noise power. Also, this section shows that influences of the acoustic noise band-width and secondary path models on the steady-state performance of the simulated system can be formulated as proposed in Chapters 4-6. Finally, Section 7.4 shows the validity of the proposed theoretical expressions for the transient convergence speed.

7.1 Verification of the Proposed Model

Figure 7.1 shows the primary and secondary paths impulse responses of the simulated ANC system. Also, Figure 7.2 shows impulse responses of the two imperfect secondary path models (M_1 and M_2), used in the implementation of the FxLMS algorithm. In this figure, the impulse response of the actual secondary path (perfect model) is also shown by a dashed line.

Figure 7.3a shows the power spectrum of the broad-band white signal, generated by the computer to be used as the reference signal $x(n)$ in simulation experiments. As can be seen, the power spectrum of this signal is approximately flat over its entire frequency range. Hence, this signal can be considered as

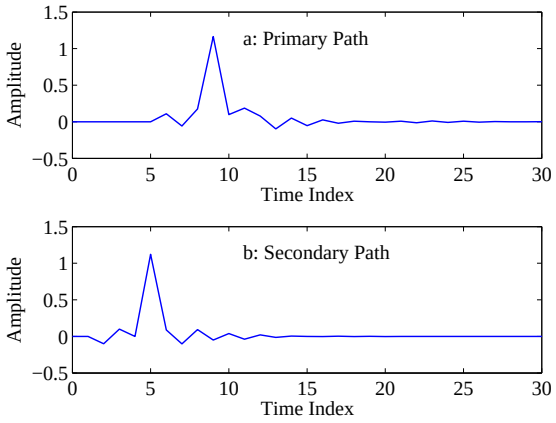

Figure 7.1: Impulse responses of primary and secondary paths in computer simulation

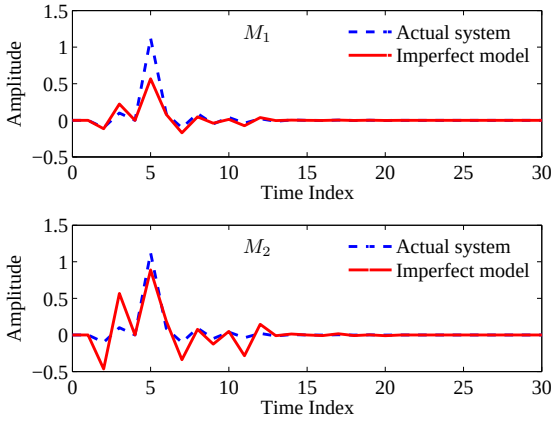

Figure 7.2: Impulse responses of secondary path models M_1 and M_2

a broad-band white signal. The total power of the signal is limited to $\sigma_x^2 = 1$. By passing this broad-band signal through standard low-pass filters, different band-limited white signals can be produced. For example, by using a low-pass filter of normalised band-width 0.5, a band-limited reference signal with band-width $B_w = 0.5$ can be produced. The power spectrum of such signal is shown in Figure 7.3b. The magnitude of the obtained signal is scaled in such a way that its power remains constant at $\sigma_x^2 = 1$.

Using the same procedure, different band-limited reference signals with different band-widths can be generated.

Note that, in Figures 7.3, blue solid lines show the power spectrum, obtained using numerical methods (FFT length: 512, averaging over 1000 FFT transforms) and red dashed lines show the theoretical power spectrum, as it is assumed in our theoretical investigations. In addition to this theoretical assumption, the independence assumptions are used in the derivation of the analytical model developed in Chapter 3. Based on this model, most of the theoretical contributions of Chapters 4-6 are obtained. Therefore, before checking the validity of the derived theoretical results, it is necessary to check the general validity of this fundamental model.

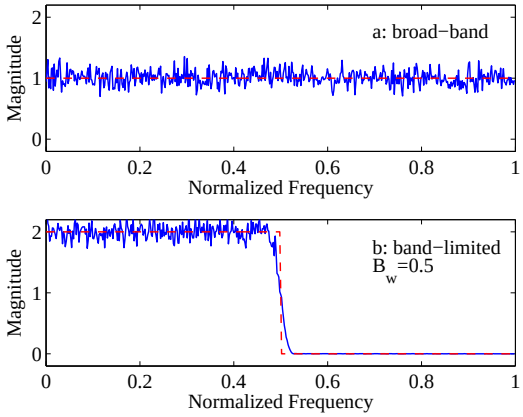

Figure 7.3: Power spectrum of two reference signals generated by computer ($\sigma_x^2 = 1$)

7.1.1 Dynamic Simulation

Here, it is shown that the model, developed in Chapter 3, can precisely describe behaviours of the simulated FxLMS-based ANC system, despite using theoretical independence assumptions in the derivation of this model. Each simulation experiment includes 100 simulation runs with independent noise sequences (reference signal). The variation of the square of the residual acoustic noise, obtained from each run, is stored in the computer memory. The MSE function is then estimated by averaging over the stored data as

$$J(n) \approx \frac{1}{100} \sum_{i=1}^{100} e_i^2(n) \tag{7.1}$$

where $e_i(n)$ is the residual acoustic noise, obtained from i-th simulation run. Now, it is required to find an estimate for the excess-MSE function form the obtained simulation results. According to Eq. (3.11), it can be shown that the difference of the excess-MSE function, $\triangle J_{ex}(n)$, is equal to the difference of $\triangle J(n)$; therefore, $\triangle J_{ex}(n)$ can be evaluated as

$$\triangle J_{ex}(n) = J(n+1) - J(n) \tag{7.2}$$

Based on Eqs. (7.1) and (7.2), the variation of $\triangle J_{ex}(n)$ can be computed using the data obtained from the computer simulation. On the other hand, the theoretical variation of $\triangle J_{ex}(n)$ can be computed by using the analytical model, given in Eqs. (3.66) and (3.67). Accordingly, comparing the result obtained from this model and the one obtained from the computer simulation leads to the verification of the validity of the proposed theoretical model. For this purpose, several simulation experiments in different cases are conducted.

Case 1: In the first case, simulation experiments are conducted in classical working conditions, which were usually considered in the theoretical analysis of FxLMS-based ANC systems. In these conditions, the reference signal is assumed to be a broad-band white stochastic signal with a flat power spectrum, as shown in Figure 7.3a. Also, the secondary path model is assumed to be a perfectly accurate model (identical to the actual secondary path).

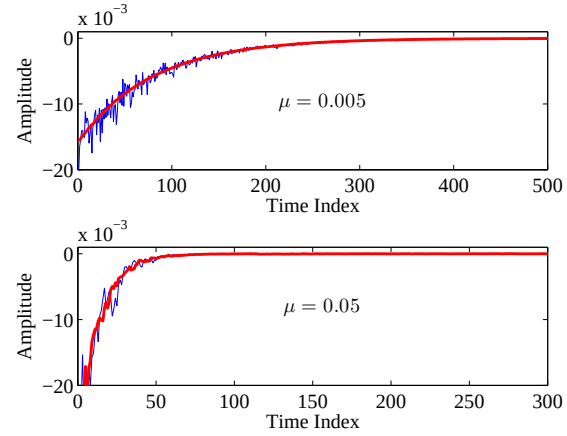

(a) Case 1

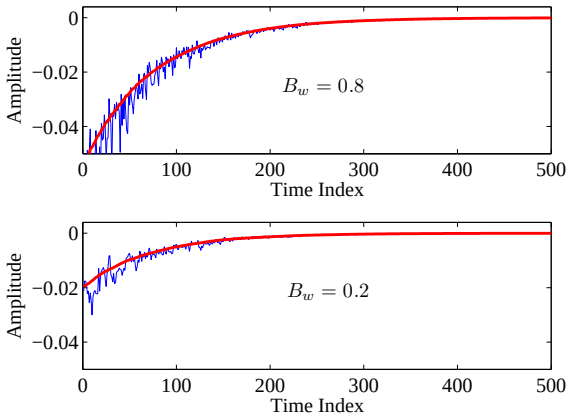

(b) Case 2

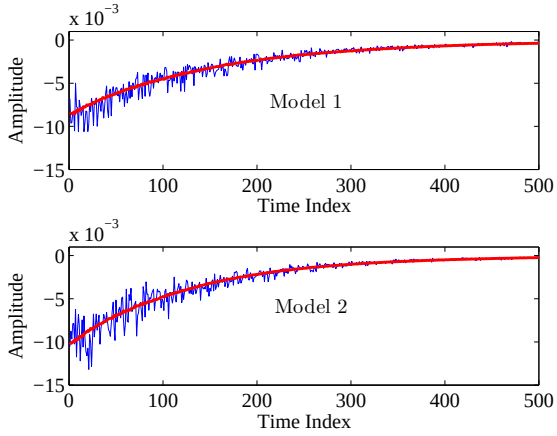

(c) Case 3

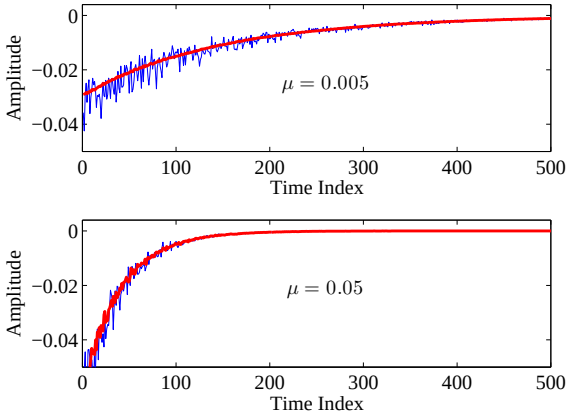

(d) Case 4

Figure 7.4: Variations of $\triangle J_{ex}(n)$ for different step-sizes and in different working conditions, red lines: theoretical results, blue lines: computer simulation

In this situation, two simulation experiments with two different step-sizes are conducted. In the first experiment, a relatively small step-size of $\mu = 0.005$ and in the second one a relatively large step-size of $\mu = 0.05$ is used. The variation of $\triangle J_{ex}(n)$ for each experiment can be then plotted, as shown in Figure 7.4a (blue lies). Also, the theoretical variation of $\triangle J_{ex}(n)$, obtained from Eqs. (3.66) and (3.67) is shown in Figure 7.4a by using red lines. As can be seen, the proposed theoretical model can precisely describe behaviours of the simulated system in both the transient and steady-state modes.

Case 2: In the second case, band-limited acoustic noise signals are considered; however, the secondary path model is still set to a perfect model. In this situation, two experiments with two different band-limited signals are conducted ($B_w = 0.2$ and $B_w = 0.8$). In both of the experiments, the step-size is set to $\mu = 0.005$. For each experiment, experimental and theoretical variations of $\triangle J_{ex}(n)$ are plotted in Figure 7.4b. The agreement between the theoretical and simulation results is evident. This agreement can be also shown for other values of the step-size.

Case 3: In this case, a broad-band white noise, as described in Case 1, is considered; however, imperfect secondary path models M_1 and M_2, shown in Figure 7.2, are used in the FxLMS algorithm. For each secondary path model, a separate experiment is conducted. In both of the experiments, the step-size is set to $\mu = 0.005$. Theoretical and experimental variations of $\triangle J_{ex}(n)$ are plotted in Figure 7.4c. As this figure shows, the proposed theoretical model can precisely describe the simulated system behaviours in both the transient and steady-state modes.

Case 4: Now, the most general case with a band-limited noise and an imperfect secondary path model is considered. In this case, the acoustic noise is a band-limited white signal of band-width $B_w = 0.8$, and the secondary path model is set to M_1. Two simulation experiments for relatively small step-size of $\mu = 0.005$ and relatively large step-size of $\mu = 0.05$ are conducted. The variation of $\triangle J_{ex}(n)$ for each experiment is plotted in Figure 7.4d. Similar to the previous cases, the agreement between the theoretical and simulation results is evident.

The above simulation experiments can be repeated for different cases with different step-sizes, acoustic noise signals, and secondary path models. However, in all of the cases, the theoretical model, given by Eqs. (3.66) and (3.67) in Chapter 3, can effectively describe system behaviours in the simulation. In fact, the agreement between the theoretical and simulation results takes away the ambiguity of the independence assumptions used in the derivation of the theoretical model developed in Chapter 3. The verification of this model is important at this stage because this model is used in Chapters 4-6 to derive theoretical expressions for formulating behaviours of FxLMS-based ANC systems. The validity and accuracy of each expression is discussed in the following sections separately.

7.2 Stability Behaviours

In this section, the validity of the theoretical expression for the step-size upper-bound μ_{max}, given in Eq. (4.43), is confirmed using different computer simulations. Also, it is confirmed that influences of the acoustic noise band-width and secondary path models on μ_{max} can be formulated by using Eqs. (5.23) and (6.26), respectively.

7.2.1 Step-Size Upper-Bound

The existence of an step-size upper-bound (μ_{max}) can be proved by using computer simulation. For this purpose, different simulation experiments with different step-sizes (μ) are conducted. For example, Figure 7.5 shows variations of the MSE function in the simulated system for three different step-sizes. In all the three cases, a broad-band white noise and a perfect secondary path model are used. Referring to this figure, it can be seen that when μ is set to 0.02 or 0.08, the system becomes stable but when it is set to 0.12, the system becomes unstable. Hence, μ_{max} should be between 0.08 and 0.12.

In order to find a more accurate value for μ_{max}, more simulation experiments are conducted. The step-size μ should be changed incrementally (e.g. with the small incremental step of 0.001) until the simulated system becomes unstable. For each value of μ, 100 independent simulation runs are repeated and the number of stable experiments is considered as the percentage of the stable experiments. The results can

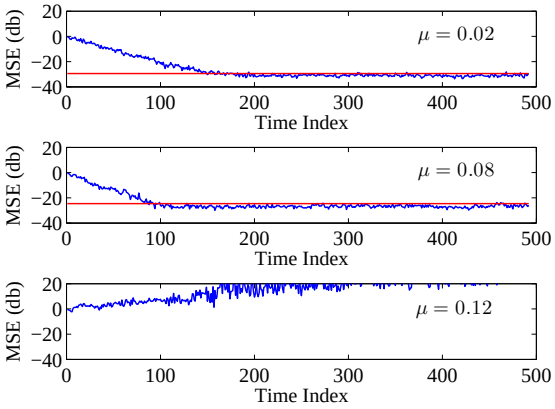

Figure 7.5: Variations of MSE function for three different step-sizes in computer simulation (broad-band reference signal, perfect secondary path model)

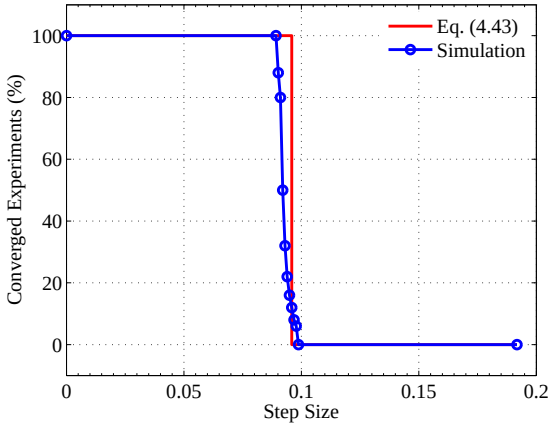

Figure 7.6: Verification of the proposed theoretical expression for μ_{max} using computer simulation

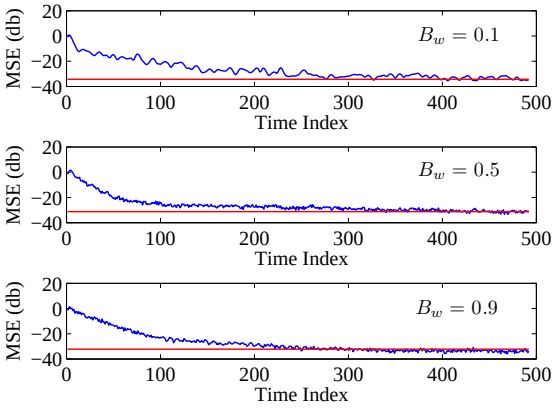

Figure 7.7: Variations of MSE function for different noise band-widths in computer simulation ($\mu = 0.02$, perfect secondary path model)

be plotted as shown in Figure 7.6. According to this figure, when μ is below 0.089, all the simulation experiments are stable ($\mu_D = 0.089$) and when μ is beyond 0.099, there is no stable experiment ($\mu_U = 0.102$). Accordingly, it can be deduced that μ_{max} locates between μ_D and μ_U. To obtain a particular value, it is assumed that

$$\mu_{max} \approx \frac{\mu_D + \mu_U}{2} \tag{7.3}$$

Now, substituting the obtained values of μ_D and μ_U into Eq. (7.3) results in

$$\mu_{max} \approx 0.0955, \qquad in\ simulation \tag{7.4}$$

On the other hand, a theoretical value for μ_{max} can be obtained by using Eq. (4.43). Note that Eq. (4.43) can apply to this simulation experiment because a broad-band reference signal and a perfect secondary path model are used. Before achieving this, secondary path parameters should be computed. For the secondary path impulse response, shown in Figure 7.1, $\|\mathbf{s}\|$, and D_{eq}, can be computed by using Eqs. (3.60) and (4.8) as

$$\|\mathbf{s}\| = 1.1440 \tag{7.5}$$

and

$$D_{eq} = 3.0263 \tag{7.6}$$

Substituting these values and also substituting $\sigma_x^2 = 1$ into Eq. (4.43), the theoretical upper-bound for the step-size is computed as[1]

$$\mu_{max} = 0.0971, \qquad in\ theory \tag{7.7}$$

Comparing the two values of μ_{max}, obtained in Eqs. (7.4) and (7.7), confirms the validity and accuracy of Eq. (4.43) .

In ideal conditions and for a perfectly accurate μ_{max}, it is expected that for step-sizes below μ_{max}, all ($\%100$) of simulation runs become stable and for step-sizes beyond μ_{max}, none ($\%0.00$) of simulation runs become stable. Therefore, if the theoretical value of $\mu_{max} = 0.0971$, is accurate enough, then for $\mu < 0.0971$), $\%100$ of simulation runs should become stable and for $\mu > 0.0971$, none of them ($\%0.00$) should become stable. Figure 7.6 shows the difference between this ideal expectation in theory and the results obtained from computer simulation. The agreement between the results is evident in this figure.

7.2.2 Influences of Acoustic Noise Band-Width on Step-Size Upper-Bound

In order to determine influences of the acoustic noise band-width on μ_{max} in the computer simulation, the process, described in Subsection 7.2.1, is repeated for 10 values of the acoustic noise band-width ($B_w = 0.1, 0.2, \ldots, 1$). For example, variations of the MSE function for three different values of B_w are shown in Figure 7.7. For each experiment, an actual value for μ_{max} can be obtained, based on the method described in Subsection 7.2.1. The results can be then plotted as a function of B_w, as shown in Figure 7.8. Also, the theoretical results, obtained by plotting Eq. (5.23) with respect to B_w, is shown in this figure. The agreement between the theoretical and experimental curves is evident.

[1] The adaptive filter length is set to $L = 12$

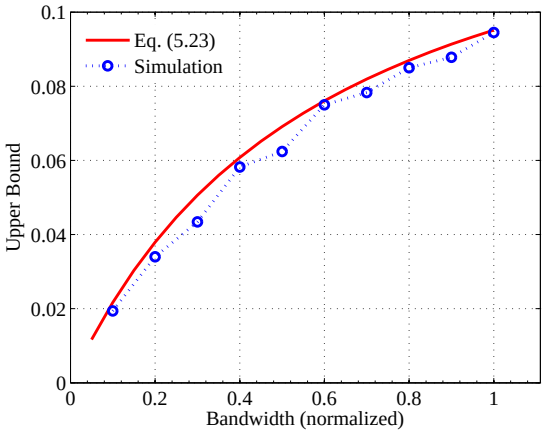

Figure 7.8: Verification of the proposed theoretical expression for formulating influences of acoustic noise bandwidth on μ_{max}

7.2.3 Influences of Control Path Models on Step-Size Upper-Bound

Now, it is desired to confirm the validity of Eq. (6.26), which formulates influences of secondary path models on μ_{max}. For this purpose, the simulation experiment, described in Subsection 7.2.1, is repeated for the two different imperfect models, shown in Figure 7.2 and also for another imperfect model, introduced later.

Experiment 1: In the first experiment, the imperfect secondary path model M_1 (shown in Figure 7.2a) is used. Figure 7.9 shows variations of the MSE function in the simulated system when μ is set to 0.02, 0.08 and 0.12. As shown earlier in Figure 7.5, in the case of using a perfect secondary path model, the simulated system becomes unstable when μ is set to 0.12. However, referring to Figure 7.9, it can be seen that, in the case of using the imperfect model M_1, the system can retain its stability even if μ is set to 0.12. This is because the imperfect model M_1 causes μ_{max} to increase.

Now, in order to estimate μ_{max} from simulation results, μ is incrementally changed with incremental step of 0.001. For each value of μ, 100 independent simulation runs are conducted and the number of stable runs are recorded. The results are then plotted as a function of μ in Figure 7.10a. Also, the theoretical value of μ_{max}, obtained by using Eq. (4.43), is shown in this figure ($\mu_{max} = 0.0971$). As mentioned in Chapter 4, Eq. (4.43) does not consider effects of imperfect secondary path models, resulting in the disagreement between the simulation results and the theoretical results, obtained from Eq. (4.43). In Figure 7.10 , the theoretical μ_{max}, computed by using Eq. (6.26) is also shown ($\mu_{max} = 0.1631$). As can be seen, the simulation result is in a good agreement with this theoretical result. This is because in the derivation of Eq. (6.26), the deviation of the secondary path model from the actual system is considered.

Experiment 2: In the second experiment, the imperfect secondary path model M_2 is used. In this situation , the simulated system becomes unstable even when μ is set to 0.08, as shown in Figure 7.11. This is because the imperfect model M_2 causes μ_{max} to decrease below 0.08. In order to estimate μ_{max} from simulation results, the procedure conducted in Experiment 1, is repeated. The obtained results are then plotted in Figure 7.12. As can be seen, simulation and experimental results are in an excellent agreement.

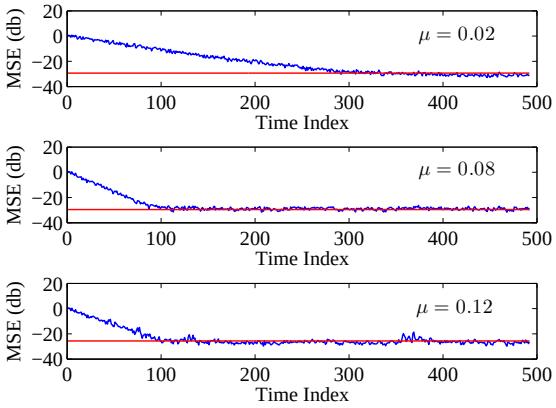

Figure 7.9: Variations of MSE function for different step-sizes in computer simulation (broad-band white acoustic noise, secondary path model M_1)

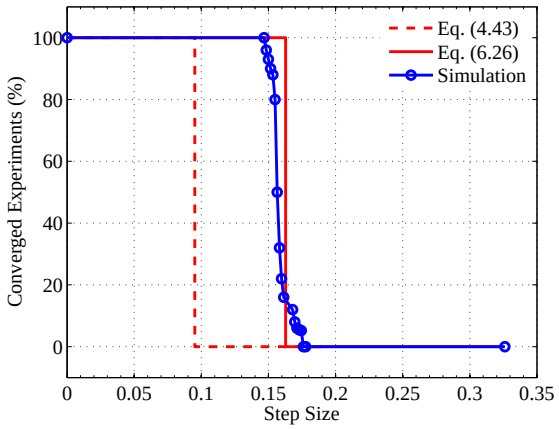

Figure 7.10: Verification of the proposed theoretical expression for formulating influences of imperfect secondary path models on μ_{max} (imperfect model used: M_1)

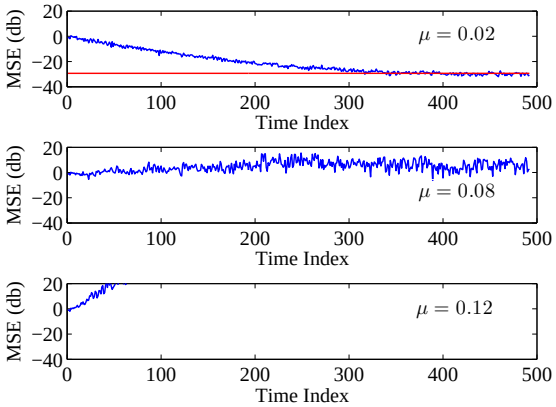

Figure 7.11: Variations of MSE function for different step-sizes in computer simulation (broad-band white acoustic noise, secondary path model M_2)

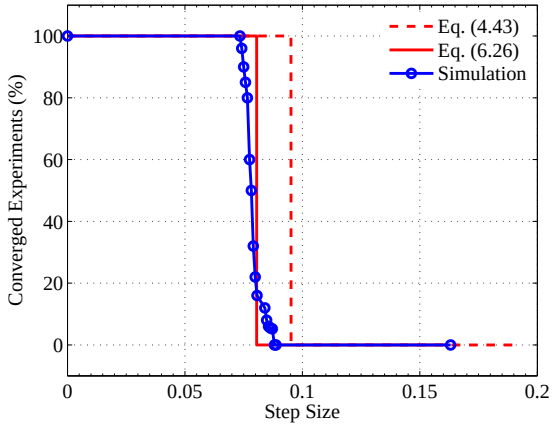

Figure 7.12: Verification of the proposed theoretical expression for formulating influences of imperfect secondary path models on μ_{max} (imperfect model used: M_2)

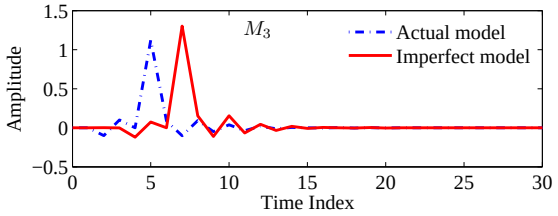

Figure 7.13: Impulse responses of secondary path model M_3

Experiment 3: In the last experiment, the imperfect model, shown in Figure 7.13 (M_3) is used. In this case, no step-size can be found so that the simulated system becomes stable. For example, Figure 7.14 shows variations of the MSE function for the three values of the step-size, as used in the previous experiments. As can be seen, in all cases, the system becomes unstable. This behaviour can be also described by using the theoretical results obtained in Chapter 6. According to Eq. (6.26), for the imperfect model M_3 the step-size upper-bound is $\mu_{max} = -0.0018$. Therefore, there is no positive value for the step-size which causes the system to become stable.

Based to the results obtained from experiments 1-3, it can be seen that Eq. (6.26) can efficiently formulate influences of imperfect secondary path models on the step-size upper-bound.

7.3 Steady-State Behaviours

This section verifies the theoretical expression, given for the steady-state residual noise power in Eq. (4.22). Also, it is shown that influences of the acoustic noise band-width and secondary path model on the steady-state performance can be precisely formulated by using Eqs. (5.26) and (6.32).

7.3.1 Steady-State Residual Acoustic Noise Power

As one of the theoretical contributions of this thesis, Eq. (4.22) gives a closed-form expression for the steady-state residual noise power when a general secondary path is considered. Simulation results confirm the validity and accuracy of this expression. For example, in Figure 7.5, horizontal lines show

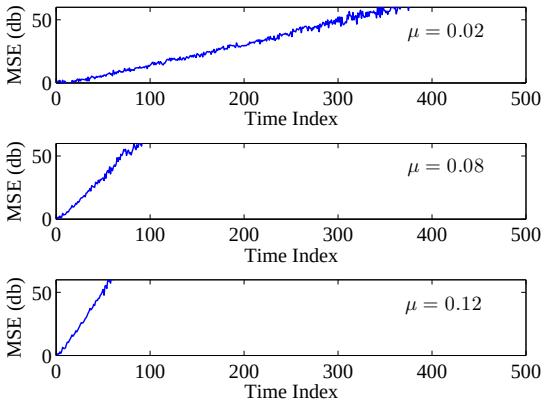

Figure 7.14: Variations of MSE function for different step-sizes in computer simulation (broad-band white acoustic noise, secondary path model M_3)

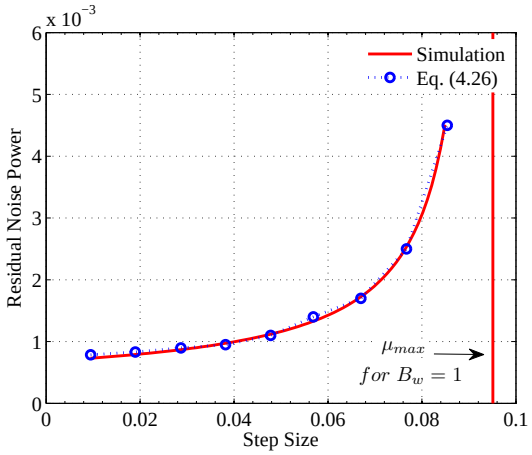

Figure 7.15: Verification of the proposed theoretical expression for steady-state noise power

the theoretical steady-state level of each MSE function. These lines are obtained by using Eq. (4.22). As can be seen, for all of the three cases shown in this figure, the theoretical results are in a good agreement with simulation results.

Note that, for computing the theoretical steady-state MSE level using Eq. (4.22), it is required to compute constant J_o. This parameter can be computed by substituting the reference signal statistics into Eqs. (2.17), (2.18) and (2.23). For the broad-band reference signal and physical plant, used in the computer simulations, this value is obtained as

$$J_o = 9.6864 \times 10^{-4} \tag{7.8}$$

In order to show the general validity of Eq. (4.22), more simulation experiments with different step-sizes are conducted. The results can be then plotted as a function of the step-size, as shown in Figure 7.15. In this figure, the theoretical curve is obtained by plotting Eq. (4.22) with respect to μ. As can be seen, theoretical and simulation results are in an excellent agreement.

7.3.2 Influences of Acoustic Noise Band-Width on Steady-State Performance

In order to investigate influences of the acoustic noise band-width (B_w) on the steady-state performance of the simulated system, the simulation experiment, discussed in Subsection 7.3.1, should be repeated for different values of B_w. In this case, Eq. (4.22) does not give an accurate theoretical estimate for the steady-state residual noise power. This is because in the derivation of this equation, a broad-band acoustic noise is considered. Instead of this equation, Eq. (5.26) can be used. For example, Figure 7.16 shows variations of the steady-state residual acoustic noise power with respect to the step-size for $B_w = 0.8$. The three curves, shown in this figure, are obtained from the computer simulation, Eq. (4.22) and Eq. (5.26), respectively. As can be seen, Eq. (5.26) can precisely consider the influence of the acoustic noise band-width on the steady-state residual noise power. The results obtained from other simulation experiments with different values for B_w leads to the same conclusion.

7.3.3 Influences of Control Path Models on Steady-State Performance

Now the validity of Eq. (6.32), which formulates influences of imperfect secondary path models on the steady-state residual noise power, is shown. For this purpose, the simulation experiment, described in Subsection 7.3.1, is repeated for two different imperfect models, shown in Figure 7.2. In the first experiment, the imperfect model M_1 and the broad-band acoustic noise ($B_w = 1$) with the flat spectrum, shown in Figure 7.3, are used. This experiment is repeated for different values of the step-size and the obtained results are then plotted as a function of the step-size in Figure 7.17a. The theoretical result, shown in this figure, is obtained by plotting Eq. (6.32) with respect to the step-size. As can be seen, the two curves are in an excellent agreement.

In the second experiment, the imperfect model M_2 and a band-limited acoustic noise with $B_w = 0.8$ are used. Similar to the previous case, this experiment is repeated for different step-sizes and the obtained results are then plotted in Figure 7.17b. The agreement between theoretical and simulation results is evident. Therefore, the expression given in Eq. (6.32) can precisely formulate influences of secondary path models on the steady-state residual noise power.

7.4 Convergence Speed

This section shows that the expression, developed for the convergence speed measure in Chapter 4, can efficiently determine the convergence speed of the simulated FxLMS-based ANC system. It is also shown that influences of the acoustic noise band-width and secondary path model on this parameter can be formulated, as described in Chapters 5 and 6.

7.4.1 Convergence Speed in Simulation

In order to show the validity of the proposed theoretical expressions for the convergence speed measure, the simulation results are plotted in standard linear scale. The theoretical value of the convergence speed

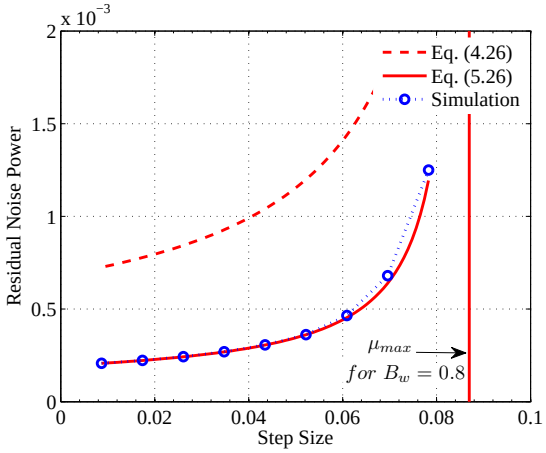

Figure 7.16: Verification of the proposed theoretical expression for formulating influences of acoustic noise bandwidth on steady-state performance

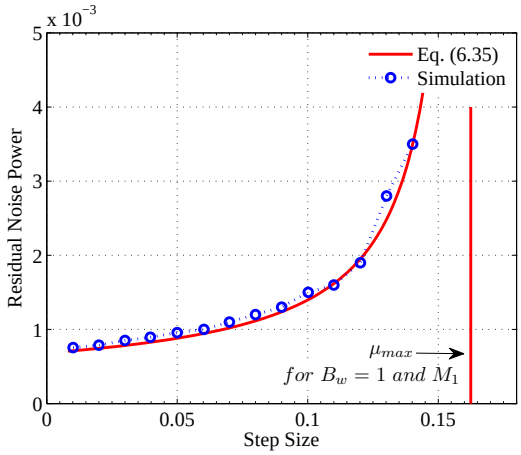

(a) model: M_1, noise: broad-band

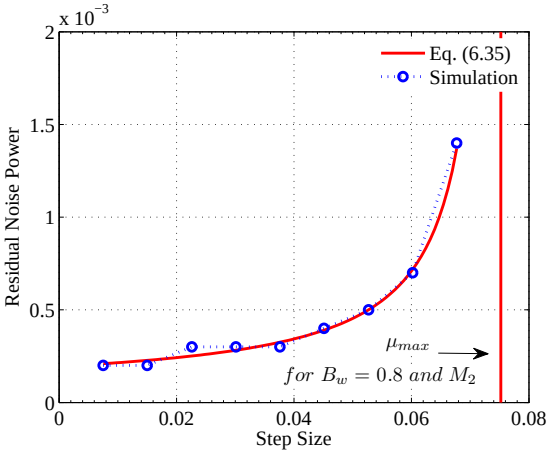

(b) model: M_2, noise: band-limited with $B_w = 0.8$

Figure 7.17: Verification of the proposed theoretical expression for formulating influences of secondary path models on steady-state performance

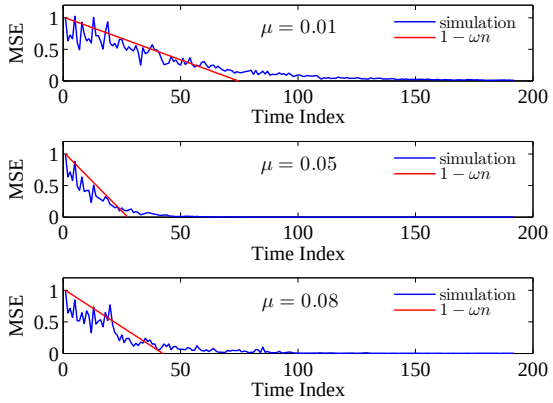

Figure 7.18: Convergence speed of MSE function for different values of step-size

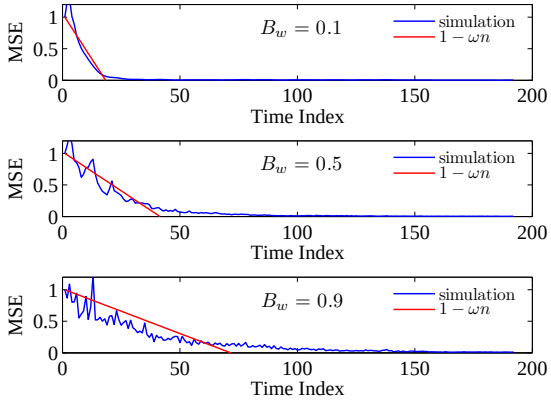

Figure 7.19: Convergence speed of MSE function for different values of acoustic noise band-widths

measure ω can be computed by using Eqs. (4.46), (5.30) or (6.39). In this case, the slope of the following line can represent the theoretical convergence speed of the simulated system.

$$J(n) = \sigma_d^2 - \omega n \tag{7.9}$$

where $\sigma_d^2 = 1$ is power of the primary noise and n is the discrete time index .

Figure 7.18 shows variations of the MSE function for different values of the step-size in the standard linear scale. At this stage, a broad-band acoustic noise and a perfect secondary path model (as assumed in Chapter 4) are used in the computer simulation. For the three cases, shown in Figure 7.18, values of the convergence speed measure ω can be computed by using Eq. (4.46) as 0.0171, 0.0476 and 0.0305. Based on these values for ω, the theoretical line, given in Eq. (7.9) can be then plotted. As can be seen, for all cases, the slope of this line (that is ω) can efficiently represents the convergence rate of the MSE function in transient conditions .

7.4.2 Influences of Acoustic Noise Band-Width on Convergence Speed

Now, different band-limited acoustic noise signals are used in the computer simulation. For example, three acoustic noise signals with band-widths of 0.1, 0.5 and 0.9 are generated by the computer, and then

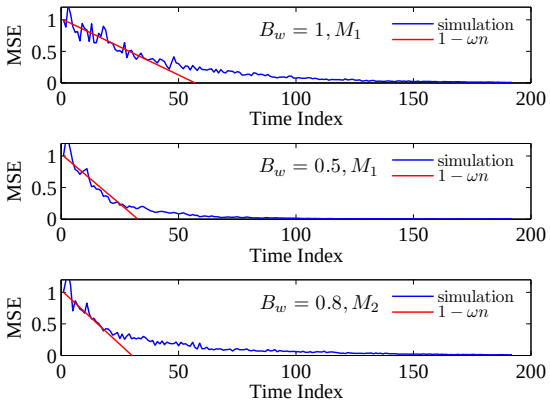

Figure 7.20: Convergence speed of MSE function for different values of acoustic noise band-widths and different secondary path models

used in three different computer simulation experiments. The results are shown in Figure 7.19. In this figure, the theoretical line of $J(n) = \sigma_d^2 - \omega n$ is also shown. Note that, in this case, the value of ω must be computed from Eq. (5.30) because this equation can consider the acoustic noise band-width. As can be seen, there is a good agreement between the slope of this line and the transient convergence rate of the MSE function in all the three cases. This agreement can be also shown for other band-limited acoustic noise signals.

7.4.3 Influences of Control Path Models on Convergence Speed

Different imperfect secondary path models are used in the computer simulation. In this case, the convergence speed measure can be computed from Eq. (6.39) as this equation considers imperfect secondary path models. In the first experiment, a broad-band acoustic noise and the secondary path model M_1 are used. In the second experiment, the band-width of the noise is changed to 0.5. Finally, in the third experiment, the acoustic noise band-width is changed to 0.8 and the secondary path model is also changed to M_2. The results are shown in Figure 7.20. As can be seen in this figure, there is a good agreement between the slope of the theoretical line $J(n) = \sigma_d^2 - \omega n$ and the convergence rate of the simulated system in all of the cases.

Chapter 8

Root Locus of FxLMS Adaptation Process

Based on the novel model, developed in Chapter 3, Chapters 4-6 perform a comprehensive analysis with the purpose of formulating behaviours of the FxLMS adaptation process in ANC systems. However, when developing a control mechanism for the FxLMS adaptation process is desired, this model is not useful. This is because this model is formulated in terms of the second-order moments of the adaptive weights while the system state variables are the first-order moments of the adaptive weights.

This chapter applies the *Root Locus Theory* to derive a novel model for the FxLMS adaptation process in ANC systems. This model is formulated in terms of the first-order moments of the adaptive weights; therefore, it can be used for designing a control mechanism for the FxLMS adaptation process. The development of this control mechanism is left to Chapter 9.

8.1 FxLMS Characteristic Equations

In this section, a characteristic equation for the first-order moments in the FxLMS adaptation process is derived. Also, a characteristic equation for the excess-MSE function is derived. It is shown that these two equations are only different in a static gain and, thereby, their roots in the z-plane follow similar loci.

8.1.1 Characteristic Equation for First-Order Moments

In Chapter 2, it is shown that the FxLMS adaptation process can be modelled by using Eq. (2.80) as

$$\bar{\mathbf{c}}\left(n+1\right)-\bar{\mathbf{c}}\left(n\right)+\mu\sigma_x^2\sum_{q=0}^{Q-1}s_q^2\bar{\mathbf{c}}\left(n-q\right)=0 \tag{8.1}$$

where σ_x^2 is the power of the reference signal, μ is the adaptation step-size and vector $\bar{\mathbf{c}}\left(n\right)$ contains the first-order moments of the adaptive weights. The characteristic equation, corresponding to Eq. (8.1), can thus be obtained by mapping this equation into the z-domain as

$$\left(z-1\right)+\mu\sigma_x^2\sum_{q=0}^{Q-1}s_q^2z^{-q}=0 \tag{8.2}$$

By multiplying Eq. (8.2) by z^{Q-1}, the characteristic equation becomes

$$z^{Q} - z^{Q-1} + \mu\sigma_x^2 G(z) = 0 \tag{8.3}$$

where transfer function $G(z)$ is defined as

$$G(z) = \sum_{q=0}^{Q-1} s_q^2 z^{Q-q-1}. \tag{8.4}$$

Eq. (8.3) represents a parametric characteristic equation for the FxLMS adaptation process (where μ is the scalar parameter).

8.1.2 Characteristic Equation for Excess-MSE Function

A dynamic model for the excess-MSE function is proposed in Chapter 4 earlier. Referring to this model, it can be seen that the excess-MSE is a linear combination of the second-order moments of the adaptive weights. This is while the dynamic model, given in Eq. (8.1), is in terms of the first-order moments of the adaptive weights. Since there is no analytical relationship between the first and second-order moments, it is not possible to derive the dynamic model, given in Eq. (8.1), from the one derived in Chapter 4 or vice-verse. However, there is an interesting correspondence between these two models. This issue is discussed in the following.

From the block diagram, shown in Figure 4.2, the characteristic equation, corresponding to the excess MSE function, can be obtained as

$$1 - z^{-1} + \gamma\sigma_x^2 \sum_{q=0}^{Q-1} s_q^2 z^{-q-1} \tag{8.5}$$

where scalar parameter γ can be obtained from Eq. (4.12) as

$$\gamma = \frac{\beta}{\sigma_x^2} = \mu\left(2 - \mu\left\|\mathbf{s}\right\|^2 \sigma_x^2 \left(L + 2D_{eq}\right)\right) \tag{8.6}$$

By multiplying Eq. (8.5) by z^{Q}, the characteristic equation becomes

$$z^{Q} - z^{Q-1} + \gamma\sigma_x^2 G(z) = 0 \tag{8.7}$$

where transfer function $G(z)$ is defined in Eq. (8.4) earlier. Comparing the characteristic equations, given in Eqs. (8.3) and (8.7), shows that they are only different in their scalar parameter (static gains μ and γ); therefore, their roots in the z-plane follow similar loci.

8.1.3 Root Locus Criteria

Dynamics of any system can be analysed by finding the roots of its characteristic equation. This equation can be represented by a standard polynomial for a linear system. Unfortunately, determining all the roots

of a general parametric polynomial, e.g. those given in Eqs. (8.3) or (8.7), is an unsolved problem in mathematics. However, the trajectory of the roots with respect to a scalar parameter can be plotted by the *Root Locus Method* [68, 69]. In fact, this method examines how the roots of a polynomial change as a scalar parameter varies. To plot a root locus for a system or process, its characteristic equation should be written in the root locus form that is

$$1 + kH(z) = 0 \tag{8.8}$$

where $H(z)$ is called the open loop transfer function and k is the scalar parameter of the characteristic equation, called the root locus parameter. According to the root locus theory, the root locus is the set of values of z for which the amplitude criterion,

$$|kH(z)| = 1 \tag{8.9}$$

and the phase criterion,

$$\measuredangle H(z) = \pi \tag{8.10}$$

are satisfied as k varies. The root locus consists of a number of branches. For $k = 0$ the roots of the characteristic equation locate on the start points of the root locus branches. These roots move on the root locus branches as k increases from zero to infinity.

Now, the FxLMS characteristic equation, given in Eq. (8.3), should be expressed in the root locus form. For this purpose, after dividing both side of Eq. (8.3) by $z^Q - z^{Q-1}$, the following equation is obtained.

$$1 + \mu\sigma_x^2 \frac{G(z)}{z^Q - z^{Q-1}} = 0 \tag{8.11}$$

Eq. (8.11) gives the FxLMS characteristic equation in the root locus form. From this equation, the FxLMS open loop transfer function can be expressed as

$$H(z) = \frac{G(z)}{z^Q - z^{Q-1}} \tag{8.12}$$

and the FxLMS root locus parameter can be expressed as

$$k = \mu\sigma_x^2 \tag{8.13}$$

Also, from Eq. (8.7), it can be shown that the open loop transfer function for the characteristic equation corresponding to the excess-MSE function dynamics is similar to the one given in Eq. (8.12). The difference between the two systems is only due to the scalar parameter.

8.2 FxLMS Root Locus

As another contribution of this thesis, this section develops fundamental rules, governing the FxLMS root locus. Also, this section derives closed form expression for main parameters of this root locus, including start points, asymptotes, departure angles and breakaway points.

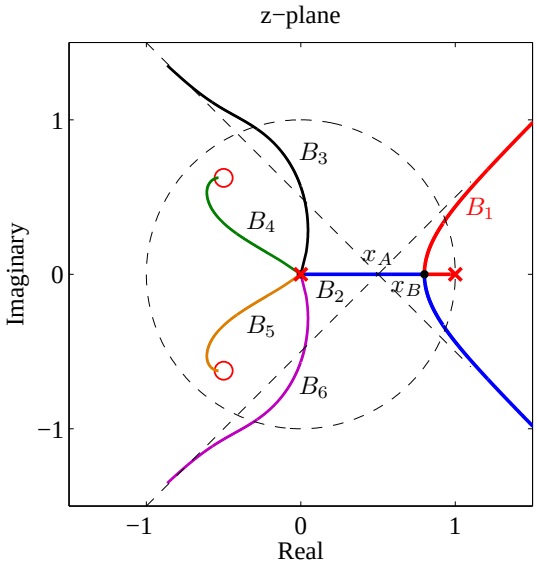

Figure 8.1: An example for FxLMS root locus when $s_0 = s_1 = s_2 = 0$, $s_3 = s_4 = 1$ and $s_5 = 0.8$

8.2.1 Number of Branches

According to the root locus theory, the number of branches of a root locus is equal to the number of poles of its open loop transfer function $H(z)$. For the FxLMS adaptation process, this function is given in Eq. (8.12). Based on this equation, it can be shown that $H(z)$ has Q poles:

$$N_P = Q \tag{8.14}$$

where N_P denotes number of the poles of $H(z)$. Hence, it can be deduced that the FxLMS root locus has Q branches. Hereafter, these branches are denoted by $B_1, B_2, ...$and B_Q.

As a particular example, for the secondary path impulse response, given by parameters $s_0 = s_1 = s_2 = 0$, $s_3 = s_4 = 1$ and $s_5 = 0.8$, transfer functions $G(z)$ and $H(z)$ can be computed as

$$G(z) = z^2 + z + 0.8 \tag{8.15}$$

and

$$H(z) = \frac{z^2 + z + 0.8}{z^6 - z^5} \tag{8.16}$$

In this case $N_P = Q = 6$ and, therefore, the FxLMS root locus contains 6 distinct branches. Trajectories of these branches in the z-plane can be numerically computed in MATLAB. The set of these branches compose the FxLMS root locus for the given secondary path. The obtained root locus, which is plotted in Figure 8.1, can be considered as the numerical result.

In the following, properties of the FxLMS root locus with a general secondary path are analytically studied and closed-form expressions for formulating main parameters of this root locus are derived. The sample root locus plot, given in Figure 8.1, is used to show the validity of the obtained results. Later, more examples are discussed.

8.2.2 Start Points

In the FxLMS root locus, the start point of B_1 locates at $z = 1$ and those of $B_2, B_3, ...$ and B_Q locate commonly at $z = 0$.

Proof: according to the root locus theory, start points of $B_1, B_2, ...$and B_Q locate at the poles of $H(z)$. Let us assume that p_q is the start point of B_q. In this case, p_q can be expressed as

$$p_q = \arg_z \left\{ \frac{1}{H(z)} = 0 \right\} \tag{8.17}$$

Combining Eqs. (8.12) and (8.17) results in

$$p_q = \arg_z \left\{ z^Q - z^{Q-1} = 0 \right\} \Rightarrow \begin{cases} p_1 = 1 \\ p_2, p_3, \ldots, p_Q = 0 \end{cases} \tag{8.18}$$

Therefore, for each branch of the root locus, there is a finite start point in the z-plane. Also, the start point of B_1 always locates at $z = 1$ and those of $B_2, B_3, ...$ and B_Q always locate at $z = 0$. In other words, the location of the start points of the FxLMS root locus is constant and independent of the secondary path. The validity of this theoretical finding can be seen in the root locus sample, shown in Figure 8.1 (in this figure, start points are marked by 'x').

8.2.3 End Points

A certain number of branches of the FxLMS root locus end at finite points in the z-plane and the rest of them approach infinity.

Proof: end points of $B_1, B_2, ...$and B_Q locate at the zeros of $H(z)$. Let us assume that z_q is the end point of B_q. In this case, z_q can be expressed as

$$z_q = \arg_z \{H(z) = 0\} \tag{8.19}$$

Combining Eqs. (8.12) and (8.19) results in

$$z_q = \arg_z \{G(z) = 0\} \tag{8.20}$$

Therefore, unlike start points, end points are not constants and their location is a function of secondary path parameters. In this case, these points can not be given by a closed-form expression. However, it is obvious from Eq. (8.12) that the number of zeros of $H(z)$ can be less than the number of branches (that is Q). This is because, an actual secondary path is usually associated with a time delay and, thereby, the first few coefficients of its impulse response are likely to be zero.

Assuming that the first Q_0 coefficients of a general secondary path impulse response are zero (or assuming that the secondary path impulse response is associated with a time delay of Q_0 samples), it can be stated that

$$s_0 = s_1 = \ldots = s_{Q_o - 1} = 0, \tag{8.21}$$

$H(z)$ can be then expressed as

$$H(z) = \frac{\sum_{q=0}^{Q-1} s_q^2 z^{Q-q-1}}{z^Q - z^{Q-1}} \tag{8.22}$$

$$= \frac{s_{Q_0}^2 z^{Q-Q_0-1} + s_{Q_0+1}^2 z^{Q-Q_0} + \ldots + s_{Q-1}^2}{z^Q - z^{Q-1}} \tag{8.23}$$

As can be seen, the numerator of $H(z)$ is a polynomial of order $Q - Q_0 - 1$; therefore, $H(z)$ can have only $Q - Q_0 - 1$ finite zeros:

$$N_Z = Q - Q_0 - 1 \tag{8.24}$$

where N_Z denotes the number of $H(z)$ zeros. Based on the above discussion, the FxLMS root locus has $Q - Q_0 - 1$ end points but it has Q distinct branches in the z-plane. In this case, the branches for excess poles must approach one asymptote each. Accordingly, the number of branches approaching to infinity (or the number of asymptotes) is $Q_0 + 1$.

For the example, shown in Figure 8.1, the three first coefficients of the secondary path impulse response are zero ($Q_0 = 3$). Consequently, $G(z)$ and $H(z)$ have only 2 finite zeros at which two branches of the root locus can end. These points are marked by "o" in Figure 8.1. As can be seen, B_4 and B_5 ends at these points. The other 4 branches approach infinity along with 4 distinct asymptotes of the root locus. This is in an excellent agreement with the above theoretical findings.

8.2.4 Asymptotes

Asymptotes of the FxLMS root locus originate from a centroid point on the real axis, given by

$$x_A = \frac{1 + \left(\frac{s_{Q_0+1}}{s_{Q_0}}\right)^2}{Q_0 + 1} \tag{8.25}$$

Also, these asymptotes form the following angles with the real axis.

$$\varphi_k = \frac{(2k+1)}{Q_0+1}\pi \qquad k = 0, 1, ..., Q_0 \tag{8.26}$$

where Q_0 is the time delay, associated with the secondary path impulse response.

Proof: according to the root locus theory, asymptotes of the root locus originate on the real axis from the centroid point x_A, given by

$$x_A = \frac{\sum p_q - \sum z_q}{N_P - N_Z} \tag{8.27}$$

and form angles with respect to the real axis of

$$\varphi_k = \frac{(2k+1)}{N_P - N_Z}\pi \qquad k = 0, 1, ..., N_P - N_Z \tag{8.28}$$

N_P and N_Z are computed earlier in Eqs. (8.14) and (8.24). Also, from Eq. (8.18), it can be shown that

$$\sum p_q = 1 \tag{8.29}$$

Accordingly, the only unknown term of Eq. (8.27) is $\sum z_q$. This term is evaluated in the following. In linear Algebra, it is known that the summation of the roots of a general polynomial of form

$$f(z) = a_N z^N + a_{N-1} z^{N-1} + \ldots + a_0 = 0 \tag{8.30}$$

can be expressed as

$$\sum [zeros\ of\ f(z)] = -\frac{a_{N-1}}{a_N} \tag{8.31}$$

Therefore, for the FxLMS open loop transfer function, given in Eq. (8.23), it can be shown that

$$\sum z_q = \sum [zeros\ of\ G(z)] = -\left(\frac{s_{Q_0+1}}{s_{Q_0}}\right)^2 \tag{8.32}$$

Now, substituting Eqs. (8.14), (8.24), (8.29) and (8.32) into (8.27), the location of the centroid point is computed as

$$x_A = \frac{1 + \left(\frac{s_{Q_0+1}}{s_{Q_0}}\right)^2}{Q_0 + 1} \tag{8.33}$$

Also, asymptotes angles can be obtained by substituting Eqs. (8.14) and (8.24) into (8.28) as

$$\varphi_k = \frac{(2k+1)}{Q_0+1}\pi \qquad\qquad k = 0, 1, ..., Q_0 \tag{8.34}$$

For the sample root locus, shown in Figure 8.1, x_A can be obtained by setting $Q_0 = 3$, $s_{Q_0} = s_3 = 1$ and $s_{Q_0+1} = s_4 = 1$ in Eq. (8.25) as $x_A = \frac{1}{2}$. Also, the angles of the 4 asymptotes can be obtained by setting $Q_0 = 3$ in Eq. (8.34) as $\varphi_1 = \frac{\pi}{4}$, $\varphi_2 = \frac{3\pi}{4}$, $\varphi_3 = \frac{5\pi}{4}$ and $\varphi_4 = \frac{7\pi}{4}$. The centroid point and specified 4 asymptotes are shown in Figure 8.1. As can be seen, analytical and numerical results are in an excellent agreement.

8.2.5 Departure Angles

The departure angles of the FxLMS root locus branches from their start points can be formulated as

$$\theta_q = \begin{cases} \pi, & q = 1 \\ \frac{2(q-2)}{Q-1}\pi, & q = 2, 3, ..., Q \end{cases} \tag{8.35}$$

Proof: the departure angles of the root locus branches from their start points can be obtained by using the root locus angle criterion, given in Eq. (8.10). Let us assume that θ_q is the departure angle of B_q from its start point at $z = p_q$. According to the root locus theory, provided that p_q is a single pole of

$H(z)$, θ_q is given by

$$\theta_q = \pi - \sum_{k=1}^{N_Z} \measuredangle (z_k, p_q) - \sum_{\substack{k=1 \\ k \neq q}}^{N_P} \measuredangle (p_k, p_q) \tag{8.36}$$

where $\measuredangle (x, y)$ denotes the angle between complex numbers x and y. If p_q is a multiple pole of order M, departure angles of the M branches departing from this point ($B_q, B_{q+1}, \ldots$ and B_{q+M-1}), are given by

$$\theta_{q+m} = \frac{2m+1}{M}\pi - \frac{1}{M}\sum_{k=1}^{N_Z} \measuredangle (z_k, p_q) - \frac{1}{M}\sum_{\substack{k=1 \\ p_k \neq p_q}}^{N_P} \measuredangle (p_k, p_q), \qquad m = 0, 2, \ldots, M-1 \tag{8.37}$$

Since the numerator of $H(z)$ has only real coefficients, its roots ($z_1, z_2, \ldots, z_{N_Z}$) are necessarily real or complex conjugates; therefore, for a p_q on the real axis, e.g. $p_1 = 1$, it can be shown that

$$\sum_{k=1}^{N_Z} \measuredangle (z_k, p_1) = \sum_{k=1}^{N_Z} \measuredangle (z_k, 1) = 0 \tag{8.38}$$

Also, it can be shown from Eq. (8.18) that

$$\sum_{\substack{k=1 \\ p_k \neq p_q}}^{N_P} \measuredangle (p_k, p_1) = \sum_{\substack{k=1 \\ p_k \neq p_q}}^{N_P} \measuredangle (0, 1) = (N_P - 1) \measuredangle (0, 1) = 0 \tag{8.39}$$

Now, substituting Eqs. (8.38) and (8.39) into (8.36) results in

$$\theta_1 = \pi \tag{8.40}$$

Therefore, the departure angle of B_1 from its origin at $z = p_1$ is π. In other words, this branch departs from $z = 1$ along the real axis and towards the origin. The remainder of branches depart from the multiple pole locating at the origin with the order of $M = Q - 1$. Similar to the previous case, it can be shown that

$$\sum_{k=1}^{N_Z} \measuredangle (z_k, p_q) = \sum_{k=1}^{N_Z} \measuredangle (z_k, 0) = 0 \tag{8.41}$$

and

$$\sum_{\substack{k=1 \\ p_k \neq p_q}}^{N_P} \measuredangle (p_k, p_q) = \sum_{\substack{k=1 \\ p_k \neq 0}}^{N_P} \measuredangle (p_k, 0) = \measuredangle (1, 0) = \pi \tag{8.42}$$

Substituting these results into Eq. (8.37) results in

$$\theta_{2+m} = \frac{2m}{Q-1}\pi, \qquad m = 0, 1, \ldots, Q-2 \tag{8.43}$$

This equation gives the departure angle of $B_2, B_3, \ldots$ and B_{Q-1}. In order to obtain a single and unified equation for all of the departure angles, Eq. (8.43) can be re-expressed as

$$\theta_q = \frac{2\,(q-2)}{Q-1}\pi \qquad\qquad q = 2, 3, ..., Q \tag{8.44}$$

Now, combining Eqs. (8.40) and (8.44) results in

$$\theta_q = \begin{cases} \pi, & q = 1 \\ \frac{2(q-2)}{Q-1}\pi, & q = 2, 3, ..., Q \end{cases} \tag{8.45}$$

For the root locus, shown in Figure 8.1, the departure angles can be computed by setting $Q = 6$ in Eq. (8.35) as $\theta_1 = \pi$, $\theta_2 = 0$, $\theta_3 = \frac{2\pi}{5}$, $\theta_4 = \frac{4\pi}{5}$, $\theta_5 = \frac{6\pi}{5}$ and $\theta_6 = \frac{8\pi}{5}$. As can be seen, analytical and numerical results are in a perfect agreement.

8.2.6 Real Sections

The only interval on the positive real axis, which belongs to the FxLMS root locus, is $(0, 1)$.

Proof: an interval on the real axis belongs to the root locus if the open loop transfer function $H\,(z)$ has an odd number of zeros and poles to its right. According to Eq. (8.12), the zeros of $H\,(z)$ are identical to the roots of $G\,(z)$.

$$H\,(z) = 0 \Leftrightarrow G\,(z) = 0 \tag{8.46}$$

Since all the coefficients of $G(z)$ are positive real scalars, the real roots of $G(z)$ can be only negative. Therefore, $G\,(z)$ has no real roots to the right of the imaginary axis. However, $G(z)$ may have complex conjugate pairs of roots with positive real parts. As a conclusion, the roots of $G(z)$, which have positive real parts, are complex conjugate pairs. Therefore, $G\,(z)$ and, consequently, $H\,(z)$ has an even number of roots to the right side of any point in the positive real axis. Besides, $H\,(z)$ has only a single pole at $z = 1$. Considering this pole, the following statements can be deduced.

- $H\,(z)$ has always an even number of roots and zeros to the right side of any point in $(1, +\infty)$; therefore this interval does not belong to the FxLMS root locus.
- $H\,(z)$ has an odd number of zeros and poles to the right side of any point in $(0, 1)$; therefore this interval always belongs to the FxLMS root locus.

However, some intervals of the negative real axis may belongs to the FxLMS root locus, depending on the order of the repeated zero at the origin and the location of the other zeros of $G\,(z)$. However, these possible intervals have less degrees of importance, compared to the interval of $(0, 1)$. Later it is shown that the interval of $(0, 1)$ is the most important part of the FxLMS root locus.

8.2.7 Breakaway Points

The FxLMS root locus always has a breakaway point on the interval of $(0, 1)$ given by

$$x_B = \frac{D_{eq}}{D_{eq} + 1} \tag{8.47}$$

where D_{eq} is the secondary path equivalent delay (as defined in Chapter 4).

Proof: breakaway points occur when branches of the root locus coincide. If $z = z_B$ is a breakaway point of the root locus then it satisfies the breakaway point equation given by

$$z_B = \arg_z \left\{ \frac{\partial}{\partial z} \frac{1}{H(z)} = 0 \right\} \tag{8.48}$$

Substituting Eq. (8.12) into (8.48) results in the following breakaway points equation.

$$(Qz_B - Q + 1) G(z_B) - \left(z_B^2 - z_B\right) \acute{G}(z_B) = 0 \tag{8.49}$$

where

$$\acute{G}(z) = \frac{\partial G(z)}{\partial z} \tag{8.50}$$

In the previous subsection, it is shown that the real axis between 0 and 1 always belongs to the FxLMS root locus; also, in Subsection 8.2.2, it is shown that both of $z = 0$ and $z = 1$ are start points of the FxLMS root locus. Therefore, there is always a real breakaway point x_B on the real interval $(0, 1)$. In the following the location of x_B is computed. For this purpose, the breakaway point equation, given in Eq. (8.49), is re-expressed as

$$\frac{\acute{G}(x_B)}{G(x_B)} \left(x_B^2 - x_B\right) - Qx_B + Q - 1 = 0 \tag{8.51}$$

Assuming that x_B is close to 1, the following approximation can be made.

$$\frac{\acute{G}(x_B)}{G(x_B)} \approx \frac{\acute{G}(1)}{G(1)} \tag{8.52}$$

Now, it is required to estimate $\frac{\acute{G}(1)}{G(1)}$. Setting $z = 1$ in Eq. (8.4) results in

$$G(1) = \sum_{q=0}^{Q-1} s_q^2 = \|\mathbf{s}\|^2 \tag{8.53}$$

Moreover, the following equation can be obtained from Eq. (8.4).

$$z^{-(Q-1)} G(z) = \sum_{q=0}^{Q-1} s_q^2 z^{-q} \tag{8.54}$$

Differentiating both sides of Eq. (8.54) gives

$$-(Q-1)z^{-Q}G(z)+z^{-Q+1}\acute{G}(z)=-\sum_{q=0}^{Q-1}qs_q^2z^{-q-1} \tag{8.55}$$

Now, setting $z=1$ in Eq. (8.55) results in

$$-(Q-1)G(1)+\acute{G}(1)=-\sum_{q=0}^{Q-1}qs_q^2 \tag{8.56}$$

Combining Eqs. (8.53) and (8.56) results in

$$\acute{G}(1)=(Q-1)\sum_{q=0}^{Q-1}s_q^2-\sum_{q=0}^{Q-1}qs_q^2 \tag{8.57}$$

Dividing both sides of Eq. (8.57) by $G(1)$ and, then, using Eq. (8.53) leads to write

$$\frac{\acute{G}(1)}{G(1)}=Q-1-\frac{\sum_{q=Q_0}^{Q-1}qs_q^2}{\sum_{q=Q_0}^{Q-1}s_q^2} \tag{8.58}$$

As can be seen, the secondary path equivalent delay (as defined in Chapter 4) appears in the left side of Eq. (8.58). Therefore;

$$\frac{\acute{G}(1)}{G(1)}=Q-1-D_{eq} \tag{8.59}$$

Now, substituting Eq. (8.59) into (8.51) results in the following equation for x_B.

$$(Q-1-D_{eq})\left(x_B^2-x_B\right)-Qx_B+Q-1=0 \tag{8.60}$$

This second-order equation can be re-written as:

$$(Q-1-D_{eq})(x_B-1)^2-(1+D_{eq})x_B+D_{eq}=0 \tag{8.61}$$

The first term can be neglected because the answer is close to $1:(x_B-1)^2\approx 0$. Thus,

$$-(1+D_{eq})x_B+D_{eq}=0 \tag{8.62}$$

Solving this equation results in

$$x_B=\frac{D_{eq}}{D_{eq}+1} \tag{8.63}$$

This equation shows that the secondary path equivalent delay (D_{eq}) is an important factor in the location of the FxLMS root locus breakaway point. In the next section it is shown that the location of this point has an important role in dynamic behaviours of the FxLMS adaptation process. Before achieving this,

let us check the validity of Eq. (8.63) in the sample root locus plot, shown in Figure 8.1. For this root locus, D_{eq} can be computed as

$$D_{eq} = \frac{3 \times 1^2 + 4 \times 1^2 + 5 \times 0.8^2}{1^2 + \times 1^2 + \times 0.8^2} = 3.8636 \tag{8.64}$$

Setting $D_{eq} = 3.8636$ in Eq. (8.47) results in

$$x_B = \frac{3.8636}{3.8636 + 1} = 0.794 \tag{8.65}$$

The location of this point is also shown in the root locus plot, shown in Figure 8.1. According to this figure, it can be seen that Eq. (8.47) can efficiently evaluate the location of the breakaway point in the FxLMS root locus.

8.3 Discussion and Examples

From the FxLMS root locus rules, derived in the previous section, it can be deduced that branches of the FxLMS root locus have some typical trajectories independent of secondary path parameters. In this section, these trajectories are discussed. Also, several examples are used to support the theoretical findings.

8.3.1 Typical Trajectory of B_1

It can be seen that B_1 always starts at $z = 1$ and moves towards the origin on the real axis. This branch leaves the real axis once it reaches the breakaway point x_B. After that, this branch may end at a complex zero of $H(z)$ or approach an asymptote of the root locus. The trajectory of B_1 just after departing from its start point (or before reaching the breakaway point) is independent of the secondary path parameters; however, the location of x_B and the possible end-point/asymptote are functions of secondary path parameters. In Figure 8.2, three different examples of the FxLMS root locus with different secondary paths are shown. In the first example, B_1 approaches an asymptote after leaving the breakaway point (Figure 8.2a). In the second example, B_1 ends at a finite zeros inside the unit circle (Figure 8.2b) and in the third example, this branch ends at a finite zeros outside the unit circle (Figure 8.2c). As can be seen, although the end point of B_1 is different in each example, its trajectory before reaching the breakaway point is constant (typical). This typical trajectory is shown in figure 8.3.

8.3.2 Typical Trajectory of B_2

As another typical behaviour of the FxLMS root locus, B_2 starts at $z = 0$ and moves towards the unit circle on the positive real axis. This branch leaves the real axis once it reaches the breakaway point x_B in such a way that points of this branch remain complex conjugates of those of B_1. This branch may end at a zero of $H(z)$, which is the complex conjugate of the end point of B_1, or approach an asymptote of the locus. Before reaching the breakaway point, the trajectory of B_2 is independent of the secondary

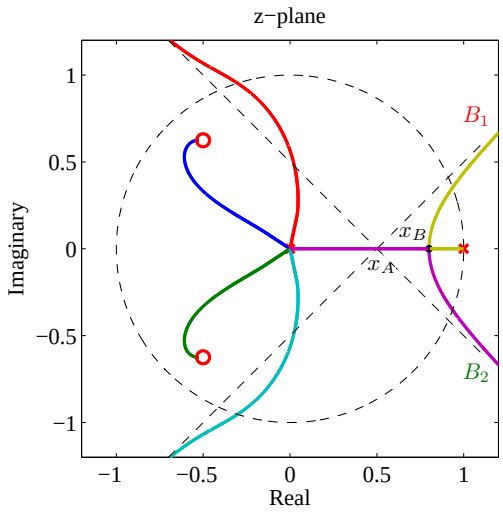

(a) $S(z) = z^{-3} + z^{-4} + 0.8z^{-5}$

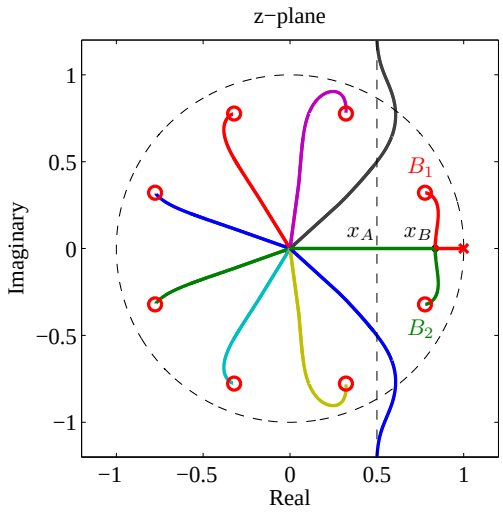

(b) $S(z) = z^{-3} + 0.5z^{-11}$

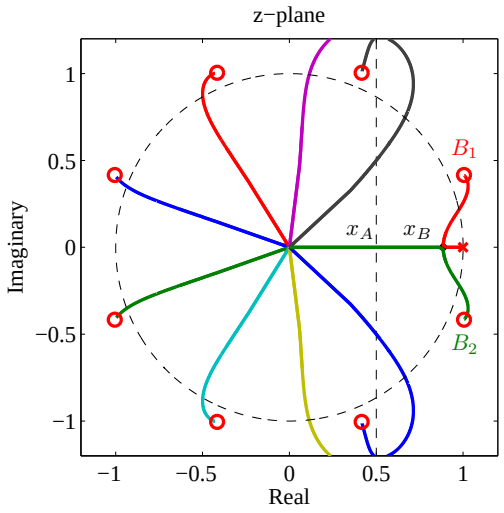

(c) $S(z) = z^{-3} + 1.4z^{-11}$

Figure 8.2: FxLMS root locus plots for three different secondary paths

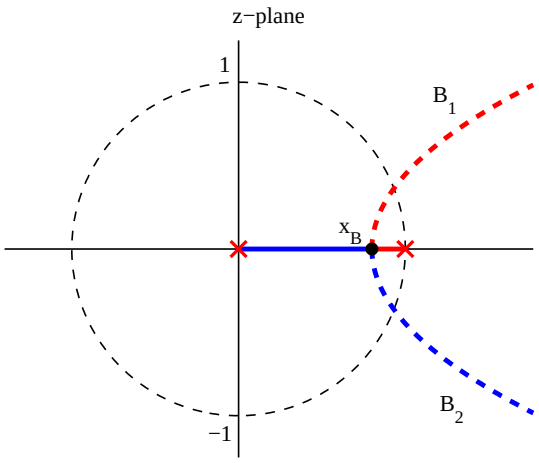

Figure 8.3: Typical trajectories of B_1 and B_2 before reaching the breakaway point x_B

path parameters; however, after reaching this point, this trajectory is affected by the secondary path parameters (similar to B_1). Three different examples of trajectories of B_2 are shown in plots of figure 8.2. As can be seen, the end point of B_2 in each example is different but its trajectory before reaching the breakaway point is constant (typical). This typical trajectory is also shown in figure 8.3.

8.3.3 Typical Trajectories of Other Branches

Branches $B_3, B_4, \ldots,$ and B_Q start at $z = 0$ (with different departure angles) and move towards the unit circle. They end at the zeros of $H(z)$ or approach the asymptotes. According to Eq. (8.35), departure angles of these branches form the origin is independent of the parameters of the secondary path; however, they are depended on the order of the secondary path (Q).

8.3.4 Dominant Pole of FxLMS Adaptation Process

According to the typical trajectories of the FxLMS root locus branches, discussed above, it can be deduced that the root moving on B_1 is closer to the unit circle than the other roots. Therefore, the dominant pole of the FxLMS root locus (which is the dominant pole of the FxLMS adaptation process) always locates on B_1. This theoretical finding can be seen in all of the previous examples (shown in Figure 8.2). Based on this finding, the next chapter develops a mechanism to improve the dynamic behaviour of the FxLMS adaptation process.

Chapter 9

Dominant Pole Localisation of FxLMS Adaptation Process

In the previous chapter, it was shown that the FxLMS adaptation process has a dominant pole, governing the adaptation process dynamics. However, there is no control mechanism in the FxLMS algorithm which enable us to localise this pole.

This chapter develops a mechanism for localising the dominant pole of the FxLMS adaptation process, resulting in the development of a new adaptation algorithm. After introducing this algorithm in Section 9.1, it is shown that its update equation is similar to that of the FxLMS algorithm. However, in the proposed algorithm, the weight vector should be first filtered by a simple recursive filter before being updated. For this reason, this algorithm is called *Filtered Weight FxLMS* (FwFxLMS) in this thesis. Section 9.2 shows that filtering weights in the FwFxLMS algorithm results in the creation of a simple zero in the open loop transfer function of the adaptation process. Section 9.3 shows how the location of this open loop zero pushes the dominant pole of the adaptation process towards the origin and, thereby, the adaptation process becomes faster.

9.1 Filtered Weights FxLMS Algorithm

This section introduces the FwFxLMS algorithm, in which the weight vector is filtered by using a simple recursive filter before being updated. Also, this section shows that the proposed algorithm behaves similar to the FxLMS in steady-state conditions; therefore, steady-state performance of this algorithm is the same as that of the FxLMS algorithm.

9.1.1 Update Equation

The FwFxLMS update equation is given by

$$\mathbf{w}\left(n+1\right)=\widetilde{\mathbf{w}}\left(n\right)+\mu e\left(n\right)\sum_{p=0}^{Q-1}s_{p}\mathbf{x}\left(n-p\right) \tag{9.1}$$

where $\widetilde{\mathbf{w}}(n)$, called the *filtered weight vector*, is obtained by passing the weight vector $\mathbf{w}(n)$ through a recursive filter with the transfer function given by

$$A(z) = \frac{1-\xi}{1-\xi z^{-1}} \tag{9.2}$$

Obviously, internal stability of $A(z)$ requires $-1 < \xi < 1$. Here, it is assumed that ξ is a positive scalar between 0 and 1:

$$0 < \xi < 1 \tag{9.3}$$

Later, the logic behind the current form of $A(z)$ and choice of ξ will be apparent. Assuming that $a(n)$ is the inverse z-transform of $A(z)$, the filtered weight vector $\widetilde{\mathbf{w}}(n)$ can be expressed as

$$\begin{aligned} \widetilde{\mathbf{w}}(n) &= a(n) * \mathbf{w}(n) \\ &= (1-\xi)\,\mathbf{w}(n) + \xi\widetilde{\mathbf{w}}(n-1) \\ &= \mathbf{w}(n) - \xi\left[\mathbf{w}(n) - \widetilde{\mathbf{w}}(n-1)\right] \end{aligned} \tag{9.4}$$

By using Eqs. (9.1) and (9.4), the FwFxLMS algorithm can be implemented.

9.1.2 Alternative Expression for Update Equation

Now, it is required to express the FwFxLMS update equation in terms of the rotated weight misalignment vector. For this purpose, both sides of Eq. (9.1) should be modified as follows.

$$\mathbf{F}^T\left[\mathbf{w}(n+1) - \mathbf{w}_{opt}\right] = \mathbf{F}^T\left[\widetilde{\mathbf{w}}(n) - \mathbf{w}_{opt}\right] + \mu e(n)\sum_{p=0}^{Q-1} s_p \mathbf{F}^T\mathbf{x}(n-p) \tag{9.5}$$

By using the definitions given in Eq. (2.43) for the rotated reference vector: $\mathbf{z}(n) = \mathbf{F}^T\mathbf{x}(n)$ and Eq. (2.47) for the misalignment weight vector: $\mathbf{c}(n) = \mathbf{F}^T\left[\mathbf{w}(n) - \mathbf{w}_{opt}\right]$, Eq. (9.5) can be expressed as

$$\mathbf{c}(n+1) = \mathbf{F}^T\left[\widetilde{\mathbf{w}}(n) - \mathbf{w}_{opt}\right] + \mu e(n)\sum_{p=0}^{Q-1} s_p \mathbf{z}(n-p) \tag{9.6}$$

Now, vector process $\mathbf{u}(n)$ is defined as

$$\mathbf{u}(n) = \mathbf{F}^T\left[\widetilde{\mathbf{w}}(n) - \mathbf{w}_{opt}\right] \tag{9.7}$$

Combining Eqs. (9.4) and (9.7) results in

$$\mathbf{u}(n) = \mathbf{F}^T\left[\mathbf{w}(n) - \xi\left[\mathbf{w}(n) - \widetilde{\mathbf{w}}(n-1)\right] - \mathbf{w}_{opt}\right] \tag{9.8}$$

which can be modified to

$$\mathbf{u}(n) = \mathbf{F}^T\left[\mathbf{w}(n) - \mathbf{w}_{opt}\right] - \xi\left\{\mathbf{F}^T\left[\mathbf{w}(n) - \mathbf{w}_{opt}\right] - \mathbf{F}^T\left[\widetilde{\mathbf{w}}(n-1) - \mathbf{w}_{opt}\right]\right\} \tag{9.9}$$

The misalignment vector $\mathbf{c}(n)$ and the vector process $\mathbf{u}(n)$ appear in Eq.(9.9); thus

$$\mathbf{u}(n) = \mathbf{c}(n) - \xi[\mathbf{c}(n) - \mathbf{u}(n-1)] \tag{9.10}$$

Now, from Eqs. (9.4) and (9.10), it can be deduced that

$$\mathbf{u}(n) = a(n) * \mathbf{c}(n) \tag{9.11}$$

Combining Eqs. (9.7) and (9.11) results in

$$\mathbf{F}^T[\widetilde{\mathbf{w}}(n) - \mathbf{w}_{opt}] = a(n) * \mathbf{c}(n) \tag{9.12}$$

Finally, substituting Eq. (9.12) into (9.6) gives

$$\mathbf{c}(n+1) = a(n) * \mathbf{c}(n) + \mu e(n) \sum_{p=0}^{Q-1} s_p \mathbf{z}(n-p) \tag{9.13}$$

Eq. (9.13) represents an alternative expression for the FwFxLMS update equation. This equation will be used in the analysis performed in this chapter.

9.1.3 Update Equation in Steady-State Conditions

In systems theory, the steady-state gain of a transfer function, e.g. $A(z)$, can be expressed as

$$A_{ss} = \lim_{z \to 1} A(z) \tag{9.14}$$

Substituting Eq. (9.2) into (9.14) results in

$$A_{ss} = \lim_{z \to 1} \frac{1-\xi}{1-\xi z^{-1}} \tag{9.15}$$

Therefore,

$$A_{ss} = 1 \tag{9.16}$$

This means that $A(z)$ behaves similar to an identity filter in steady-state conditions. Therefore, the update equation of the FwFxLMS algorithm becomes similar to that of the FxLMS algorithm in steady-state conditions. Consequently, steady-state performances of both algorithms are identical. This finding will be verified later by using computer simulations.

9.2 FwFxLMS Characteristic Equation

Taking the statistical expectation from both sides of Eq. (9.13) results in

$$\bar{\mathbf{c}}(n+1) = a(n) * \bar{\mathbf{c}}(n) + \mu \sum_{p=0}^{Q-1} s_p E\{\mathbf{z}(n-p)\, e(n)\} \tag{9.17}$$

Now, replacing $e(n)$ with the alternative expression given in Eq. (2.72) results in

$$\begin{aligned}\bar{\mathbf{c}}(n+1) &= a(n) * \bar{\mathbf{c}}(n) + \mu \sum_{p=0}^{Q-1} s_p E\{\mathbf{z}(n-p)\, e_o(n)\} \\ &\quad -\mu \sum_{p,q=0}^{Q-1} s_p s_q E\left\{\mathbf{z}(n-p)\, \mathbf{z}^T(n-q)\, \mathbf{c}(n-q)\right\} \end{aligned} \tag{9.18}$$

Since the optimum residual noise $e_o(n)$ and the acoustic noise are statistically independent, the second term in Eq. (9.18) is zero. Also, considering the statistical independence of the adaptive weights and acoustic noise samples, the third term in this equation can be simplified. Therefore, Eq. (9.18) can be expressed as

$$\bar{\mathbf{c}}(n+1) = a(n) * \bar{\mathbf{c}}(n) - \mu \sum_{p,q=0}^{Q-1} s_p s_q E\left\{\mathbf{z}(n-p)\, \mathbf{z}^T(n-q)\right\} E\{\mathbf{c}(n-q)\} \tag{9.19}$$

Now, substituting Eqs. (2.52) and (2.76) into Eq. (9.19) results in

$$\bar{\mathbf{c}}(n+1) = a(n) * \bar{\mathbf{c}}(n) - \mu \mathbf{\Lambda} \sum_{p=0}^{Q-1} s_p^2 \bar{\mathbf{c}}(n-p) \tag{9.20}$$

For a broad-band white noise ($\mathbf{\Lambda} = \sigma_x^2 \mathbf{I}$), Eq. (9.20) can be simplified to

$$\bar{\mathbf{c}}(n+1) = a(n) * \bar{\mathbf{c}}(n) - \mu \sigma_x^2 \sum_{p=0}^{Q-1} s_p^2 \bar{\mathbf{c}}(n-p) \tag{9.21}$$

By taking the z-transform from both sides of Eq. (9.20), the FwFxLMS characteristic equation is obtained as

$$z - A(z) + \mu \sigma_x^2 \sum_{p=0}^{Q-1} s_p^2 z^{-p} = 0 \tag{9.22}$$

Now, substituting Eq. (9.2) into (9.22) results in

$$\frac{z-1}{1-\xi z^{-1}} + \mu \sigma_x^2 \sum_{p=0}^{Q-1} s_p^2 z^{-p} = 0 \tag{9.23}$$

which can be written in the standard form of

$$1 + \mu \widetilde{H}(z) = 0 \tag{9.24}$$

where

$$\widetilde{H}(z) = \frac{(z-\xi)\, G(z)}{z^{Q+1} - z^Q} \tag{9.25}$$

Comparing Eqs. (8.12) and (9.25) shows that

$$\widetilde{H}(z) = \frac{z-\xi}{z} H(z) \tag{9.26}$$

Therefore, the FwFxLMS open loop transfer function $\widetilde{H}(z)$ has one more zero (at $z=\xi$) and one more pole (at the origin) in addition to the zeros and poles of the FxLMS open loop transfer function $H(z)$. Accordingly, the following statements can be expressed:

$$\widetilde{N_P} = N_P + 1 \tag{9.27}$$

and

$$\widetilde{N_Z} = N_Z + 1 \tag{9.28}$$

where $\widetilde{N_P}$ and $\widetilde{N_Z}$ denote the number of poles and zeros of $\widetilde{H}(z)$, respectively. In fact, filtering the weight vector using the proposed form of $A(z)$ introduces a finite real zero to the open loop transfer function of the characteristic equation. In the following, it is shown that dynamics of the FwFxLMS adaptation process can be controlled by localising this zero. This is the main privilege of the FwFxLMS algorithm, compared to the FxLMS algorithm.

9.3 FwFxLMS Root Locus

This section develops the fundamental rules, governing the FwFxLMS root locus, and compares them with those of the FxLMS.

9.3.1 Number of Branches

As mentioned in Section 8.2.1, the number of branches of a root locus is equal to the number of poles of its open loop transfer function. Since $\widetilde{H}(z)$ has one pole more than $H(z)$, the FwFxLMS root locus has one branch more than the FxLMS root locus. Accordingly, this root locus has $Q+1$ branches. Here, these branches are denoted by $\widetilde{B}_1, \widetilde{B}_2, ...$and $\widetilde{B}_{Q+1}$.

9.3.2 Start Points

In the FwFxLMS root locus, the start points of $\widetilde{B}_1$ is located at $z=1$ and those of $\widetilde{B}_2, ...$and $\widetilde{B}_{Q+1}$ are located at $z=0$, commonly.

Proof: the start points of $\widetilde{B}_1, \widetilde{B}_2, ...$ and $\widetilde{B}_{Q+1}$ are located at the poles of $\widetilde{H}(z)$. Let us assume that $\tilde{p}_q$ is the start point of the q-th branch, $\widetilde{B}_q$. In this case, $\tilde{p}_q$ can be expressed as

$$\tilde{p}_q = \arg_z \left\{ \frac{1}{\widetilde{H}(z)} = 0 \right\} \tag{9.29}$$

Combining Eqs. (9.25) and (9.29) results in

$$\tilde{p}_q = \arg_z \left\{ z^{Q+1} - z^Q = 0 \right\} \Rightarrow \begin{cases} \tilde{p}_1 = 1 \\ \tilde{p}_2, \tilde{p}_3, \ldots, \tilde{p}_Q, \tilde{p}_{Q+1} = 0 \end{cases} \tag{9.30}$$

Therefore, each branch of the root locus has a finite start point in the z-plane; that of $\widetilde{B}_1$ is located at $z = 1$ and those of $\widetilde{B}_2$, ...and $\widetilde{B}_{Q+1}$ are all located at $z = 0$.

9.3.3 End Points

The FwFxLMS root locus has a finite end point in the real axis inside the unit circle, unlike the FxLMS root locus.

Proof: end points of $\widetilde{B}_1, \widetilde{B}_2, ...$ and $\widetilde{B}_{Q+1}$ locate at the zeros of $\widetilde{H}(z)$. Let us assume that $\widetilde{z}_q$ is the end point of the q-th branch, $\widetilde{B}_q$. In this case, $\widetilde{z}_q$ can be expressed as

$$\widetilde{z}_q = \arg_z \left\{ \widetilde{H}(z) = 0 \right\} \tag{9.31}$$

Combining Eqs. (9.25) and (9.31) results in

$$\widetilde{z}_q = \arg_z \left\{ (z - \xi) G(z) = 0 \right\} \tag{9.32}$$

Since $s_0^2, s_1^2, \ldots, s_{Q-1}^2$ are positive scalars, $G(z)$ can not have any zeros on the positive real axis. However, $(z - \xi)$ has a positive real zero inside the unit circle (since $0 < \xi < 1$). As a result, the FwFxLMS root locus has a single positive real zero inside the unit circle at $z = \xi$. Therefore, one of the branches of this root locus ends at a point on the positive real axis inside the unit circle, unlike the FxLMS root locus. This is one of the main distinctions between the FxLMS and FwFxLMS root loci. In the next sections, it is shown that the branch, on which the dominant root moves, ends at this point.

9.3.4 Asymptotes

Asymptotes of the FwFxLMS root locus originate on the real axis at a centroid point (denoted by $\widetilde{x}_A$), given by

$$\widetilde{x}_A = x_A - \frac{\xi}{Q_0 + 1} \tag{9.33}$$

Also, these asymptotes form the following angles with the real axis.

$$\widetilde{\varphi}_k = \frac{(2k+1)}{\widetilde{N}_P - \widetilde{N}_Z}\pi \qquad k = 0, 1, ..., Q_0 \tag{9.34}$$

where Q_0 is the time delay, associated with the secondary path impulse response.

Proof: according to the root locus theory, $\widetilde{x}_A$ can be obtained by using the following formulation.

$$\widetilde{x}_A = \frac{\sum \widetilde{p}_q - \sum \widetilde{z}_q}{\widetilde{N}_P - \widetilde{N}_Z} \tag{9.35}$$

From Eqs. (9.27) and (9.28), it can be shown that

$$\widetilde{N}_P - \widetilde{N}_Z = N_P - N_Z = Q_0 + 1 \tag{9.36}$$

Also, from Eq. (9.30), it can be shown that

$$\sum_{q=0}^{Q-1}\widetilde{p}_q = 1 \tag{9.37}$$

and from Eq. (9.26), it can be shown that

$$\sum\widetilde{z}_q = \xi + \sum z_q \tag{9.38}$$

where z_q is the q-th zero of $G(z)$. The sum of $G(z)$'s zeros are computed in Eq. (8.32). Using this equation in Eq. (9.39) results in

$$\sum\widetilde{z}_q = \xi - \left(\frac{s_{Q_0+1}}{s_{Q_0}}\right)^2 \tag{9.39}$$

Now, substituting Eqs. (8.14), (8.24), (9.37) and (9.39) into (9.35), the location of the centroid point $\tilde{x}_A$ is computed as

$$\widetilde{x}_A = x_A - \frac{\xi}{Q_0+1} \tag{9.40}$$

Also, according to the root locus theory, the angles of the asymptotes with respect to the real axis are formulated by

$$\widetilde{\varphi}_k = \frac{(2k+1)}{\widetilde{N}_P - \widetilde{N}_Z}\pi \qquad k = 0, 1, ..., \widetilde{N}_P - \widetilde{N}_Z \tag{9.41}$$

Substituting Eqs. (9.27) and (9.28) into (9.41) results in

$$\widetilde{\varphi}_k = \varphi_k \qquad k = 0, 1, ..., Q_0 \tag{9.42}$$

As can be seen in Eq. (9.42), the angles of the asymptotes in both of the FxLMS and FwFxLMS root loci are equal.

9.3.5 Departure Angles

The departure angles of $\widetilde{B}_1, \widetilde{B}_2, ...$and $\widetilde{B}_{Q+1}$ from their start points can be formulated as

$$\widetilde{\theta}_q = \begin{cases} \pi, & q = 1 \\ \frac{2(q-2)}{Q}\pi, & q = 2, 3, ..., Q+1 \end{cases} \tag{9.43}$$

Proof: let us assume that $\widetilde{\theta}_q$ is the departure angle of $\widetilde{B}_q$ from its start point at $z = \widetilde{p}_q$. Assuming that $\widetilde{p}_q$ is a single pole of $\widetilde{H}(z)$ and based on the same logic used in Eq. (8.36), $\widetilde{\theta}_q$ can be expressed as

$$\widetilde{\theta}_q = \pi - \sum_{k=1}^{\widetilde{N}_Z}\measuredangle(\widetilde{z}_k, \widetilde{p}_q) - \sum_{\substack{k=1 \\ k\neq q}}^{\widetilde{N}_P}\measuredangle(\widetilde{p}_k, \widetilde{p}_q) \tag{9.44}$$

Also, if $\widetilde{p}_q$ is a multiple pole of order M, departure angles of the M branches departing from this point ($\widetilde{B}_q, \widetilde{B}_{q+1}, \ldots$ and $\widetilde{B}_{q+M-1}$), can be computed as

$$\widetilde{\theta}_{q+m} = \frac{(2m+1)}{M}\pi - \frac{1}{M}\sum_{k=1}^{\widetilde{N}_Z} \measuredangle\left(\widetilde{z}_k, \widetilde{p}_q\right) - \frac{1}{M}\sum_{\substack{k=1 \\ \widetilde{p}_k \neq \widetilde{p}_q}}^{\widetilde{N}_P} \measuredangle\left(\widetilde{p}_k, \widetilde{p}_q\right), \qquad m = 0, 1, \ldots, M-1 \tag{9.45}$$

Since $(z-\xi)\,G(z)$ has only real coefficients, its roots (that are zeros of $\widetilde{H}(z)$) are necessarily negative real or complex conjugates. Therefore, for $\widetilde{p}_1 = 1$, it can be shown that

$$\sum_{k=1}^{\widetilde{N}_Z} \measuredangle\left(\widetilde{z}_k, \widetilde{p}_1\right) = \sum_{k=1}^{\widetilde{N}_Z} \measuredangle\left(\widetilde{z}_k, 1\right) = 0 \tag{9.46}$$

Also, since $\widetilde{p}_1 = 1$ is a simple pole, from Eq. (9.30), it can be shown that

$$\sum_{\substack{k=1 \\ \widetilde{p}_k \neq \widetilde{p}_q}}^{\widetilde{N}_P} \measuredangle\left(\widetilde{p}_k, \widetilde{p}_1\right) = \sum_{\substack{k=1 \\ \widetilde{p}_k \neq \widetilde{p}_q}}^{\widetilde{N}_P} \measuredangle\left(0, 1\right) = \left(\widetilde{N}_P - 1\right) \measuredangle\left(0, 1\right) = 0 \tag{9.47}$$

Now, substituting Eqs. (9.46) and (9.47) into (9.44) results in

$$\widetilde{\theta}_1 = \pi \tag{9.48}$$

Therefore, the departure angle of $\widetilde{B}_1$ from its start point at $z = \widetilde{p}_1$ is π. In other words, this branch departs from $z = 1$ along with the real axis and towards the origin. The remaining Q branches depart from the multiple pole locating at the origin with the order of $M = Q$. Similar to the previous case, it can be shown that (for $\widetilde{p}_2, \widetilde{p}_3, \ldots, \widetilde{p}_{Q+1} = 0$)

$$\sum_{k=1}^{\widetilde{N}_Z} \measuredangle\left(\widetilde{z}_k, \widetilde{p}_q\right) = \sum_{k=1}^{\widetilde{N}_Z} \measuredangle\left(\widetilde{z}_k, 0\right) = 0 \tag{9.49}$$

and

$$\sum_{\substack{k=1 \\ \widetilde{p}_k \neq \widetilde{p}_q}}^{\widetilde{N}_P} \measuredangle\left(\widetilde{p}_k, \widetilde{p}_q\right) = \sum_{\substack{k=1 \\ \widetilde{p}_k \neq 0}}^{\widetilde{N}_P} \measuredangle\left(\widetilde{p}_k, 1\right) = \measuredangle\left(0, 1\right) = \pi \tag{9.50}$$

Substituting these equalities into Eq. (9.45) results in

$$\widetilde{\theta}_{2+m} = \frac{2m}{Q}\pi, \qquad m = 0, 1, \ldots, Q-1 \tag{9.51}$$

In order to obtain a single equation for all of the departure angles, Eq. (9.51) can be re-expressed as

$$\widetilde{\theta}_q = \frac{2\,(q-2)}{Q}\pi \qquad\qquad q = 2, 3, ..., Q+1 \tag{9.52}$$

Now, combining Eqs. (9.48) and (9.52) results in

$$\widetilde{\theta}_q = \begin{cases} \pi, & q = 1 \\ \frac{2(q-2)}{Q}\pi, & q = 2, 3, ..., Q+1 \end{cases} \tag{9.53}$$

9.3.6 Real Sections

It can be shown that $(\xi, 1)$ is the only interval on the positive real axis, which belongs to the FwFxLMS root locus.

Proof: an interval on the real axis belongs to the FwFxLMS root locus if $\widetilde{H}(z)$ has an odd number of zeros and poles to its right. According to Eq. (9.25), the zeros of $\widetilde{H}(z)$ are identical to the roots of $(z-\xi)G(z)$.

$$\widetilde{H}(z) = 0 \Leftrightarrow (z-\xi)G(z) = 0 \tag{9.54}$$

Accordingly, the zeros of $\widetilde{H}(z)$ include the zeros of $G(z)$ and a single zero at $z = \xi$ (where $0 < \xi < 1$). As explained in Chapter 8, $G(z)$ has an even number of roots to the right side of any point in the positive real axis. Therefore, $\widetilde{H}(z)$ has an even number of zeros to the right side of any point in $(\xi, +\infty)$ and an odd number of zeros to the right side of any point in $(0, \xi)$. Now, considering the single pole of $\widetilde{H}(z)$ at $z = 1$, the following statements can be deduced.

- $\widetilde{H}(z)$ has an even number of zeros and poles to the right side of any point in $(1, +\infty)$; therefore this interval does not belong to the FwFxLMS root locus.
- $\widetilde{H}(z)$ has an odd number of zeros and poles to the right side of any point in $(\xi, 1)$; therefore this interval always belongs to the FwFxLMS root locus.
- $\widetilde{H}(z)$ has an even number of zeros and poles to the right side of any point in $(0, \xi)$; therefore this interval does not belong to the FwFxLMS root locus.

From the above discussion, it can be deduced that $(\xi, 1)$ is the only interval on the positive real axis, which belongs to the FwFxLMS root locus. However, some intervals of the negative real axis may belong to the FwFxLMS root locus, depending on the order of the repeated zero at the origin and the location of the other zeros of $G(z)$. It is later shown that $(\xi, 1)$ is the most important part of the FwFxLMS root locus.

9.3.7 Breakaway Points

The FwFxLMS root locus does not necessarily have a breakaway point on the positive real axis inside the unit circle, unlike the FxLMS root locus. If the control parameter ξ is set to a value in the following interval, then there is no breakaway point on the real section of the root locus.

$$2 - x_B - 2\sqrt{1 - x_B} < \xi < 1 \tag{9.55}$$

Proof: here, it is desired to obtain a range of values for ξ for which the FwFxLMS root locus has no breakaway point on $(\xi, 1)$. Any breakaway point in the FwFxLMS root locus should satisfy the

breakaway point equation of

$$\widetilde{x}_B = \arg_z \left\{ \frac{\partial}{\partial z} \frac{1}{\widetilde{H}(z)} \right\} = 0 \tag{9.56}$$

On the other hand, differentiating Eq. (9.26) results in

$$\frac{\partial}{\partial z} \frac{1}{\widetilde{H}(z)} = \frac{z}{z-\xi} \times \left(\frac{\partial}{\partial z} \frac{1}{H(z)} \right) - \frac{\xi}{(z-\xi)^2} \times \frac{1}{H(z)} \tag{9.57}$$

From Eq. (8.12), it can be shown that

$$\frac{\partial}{\partial z} \frac{1}{H(z)} = \frac{z^{Q-2}}{G^2(z)} \left\{ (Qz - Q + 1) G(z) - \left(z^2 - z\right) \acute{G}(z) \right\} \tag{9.58}$$

Now, substituting Eqs. (8.12) and (9.58) into (9.57) results in

$$\frac{\partial}{\partial z} \frac{1}{\widetilde{H}(z)} = \frac{z^{Q-1}}{(z-\xi)^2 G^2(z)} \left\{ [(Qz - Q + 1)(z-\xi) - \xi(z-1)] G(z) - \left(z^2 - z\right)(z-\xi) \acute{G}(z) \right\} \tag{9.59}$$

Combining Eqs. (9.56) and (9.59) gives the following breakaway point equation.

$$\{(Q\widetilde{x}_B - Q + 1)(\widetilde{x}_B - \xi) - \xi(\widetilde{x}_B - 1)\} G(\widetilde{x}_B) - \left(\widetilde{x}_B^2 - \widetilde{x}_B\right)(\widetilde{x}_B - \xi) \acute{G}(\widetilde{x}_B) = 0 \tag{9.60}$$

Equivalently,

$$(Q\widetilde{x}_B - Q + 1)(\widetilde{x}_B - \xi) - \xi(\widetilde{x}_B - 1) - \left(\widetilde{x}_B^2 - \widetilde{x}_B\right)(\widetilde{x}_B - \xi) \frac{\acute{G}(\widetilde{x}_B)}{G(\widetilde{x}_B)} = 0 \tag{9.61}$$

If there is a breakaway point in the FwFxLMS root locus, it should be close to $z = 1$; therefore, the following assumptions can be made (similar to those made in Chapter 8 for the FxLMS root locus)

$$\widetilde{x}_B^2 - \widetilde{x}_B = (\widetilde{x}_B - 1)^2 + \widetilde{x}_B - 1 \approx \widetilde{x}_B - 1 \tag{9.62}$$

and

$$\frac{\acute{G}(\widetilde{x}_B)}{G(\widetilde{x}_B)} \approx \frac{\acute{G}(1)}{G(1)} \tag{9.63}$$

Using these two assumptions, Eq. (9.61) can be simplified to

$$(Q\widetilde{x}_B - Q + 1)(\widetilde{x}_B - \xi) - \xi(\widetilde{x}_B - 1) - (\widetilde{x}_B - 1)(\widetilde{x}_B - \xi) \frac{\acute{G}(1)}{G(1)} = 0 \tag{9.64}$$

Now, substituting Eq. (8.59) into (9.64) results in

$$(1 + D_{eq}) \widetilde{x}_B^2 - (2\xi + \xi D_{eq} + D_{eq}) \widetilde{x}_B + \xi(1 + D_{eq}) = 0 \tag{9.65}$$

which can be expressed as

$$\widetilde{x}_B^2 - \left(\xi + \frac{D_{eq} + \xi}{1 + D_{eq}} \right) \widetilde{x}_B + \xi = 0 \tag{9.66}$$

Since $D_{eq} \gg 1$ and $0 < \xi < 1$, this equation can be approximated by

$$\widetilde{x}_B^2 - \left(\xi + \frac{D_{eq}}{1 + D_{eq}}\right)\widetilde{x}_B + \xi = 0 \tag{9.67}$$

As can be seen, the FxLMS breakaway point x_B, as given in Eq. (8.47), appears in the breakaway point equation of the FwFxLMS root locus. Thus,

$$\widetilde{x}_B^2 - (\xi + x_B)\,\widetilde{x}_B + \xi = 0 \tag{9.68}$$

Note that in the above FwFxLMS breakaway point equation, $\widetilde{x}_B$ is the unknown variable and x_B is a known parameter. This quadratic equation (which is in form of $\widetilde{x}_B^2 + b\widetilde{x}_B + c$) has no real answer if its discriminant ($\triangle = b^2 - 4c$) is negative:

$$\begin{cases} b = & -(\xi + x_B) \\ c = & \xi \end{cases} \quad \Rightarrow \quad \triangle = (\xi + x_B)^2 - 4\xi$$

Thus, any value of ξ, for which there is no breakaway point on $(\xi, 1)$ in the FwFxLMS root locus, satisfies

$$(\xi + x_B)^2 - 4\xi < 0 \tag{9.69}$$

This inequality can be expanded as follows.

$$\begin{aligned} & \xi^2 + 2\,(x_B - 2)\,\xi + x_B^2 < 0 \\ \Rightarrow \quad & 2 - x_B - 2\sqrt{1 - x_B} < \xi < 2 - x_B + 2\sqrt{1 - x_B} \end{aligned} \tag{9.70}$$

It can be shown that for $x_B > 0$ the following inequality always holds.

$$2 - x_B + 2\sqrt{1 - x_B} > 1 \tag{9.71}$$

Using this result and considering $0 < \xi < 1$, Eq. (9.70) becomes

$$2 - x_B - 2\sqrt{1 - x_B} < \xi < 1 \tag{9.72}$$

Accordingly, if ξ satisfies the above inequality then the FwFxLMS root locus has no breakaway point on $(\xi, 1)$.

9.4 Properties of the FwFxLMS Root Locus

From the root locus rules, derived in the previous section, it can be shown that the FwFxLMS root locus branches have some typical trajectories in the z-plane. This section discussed these trajectories.

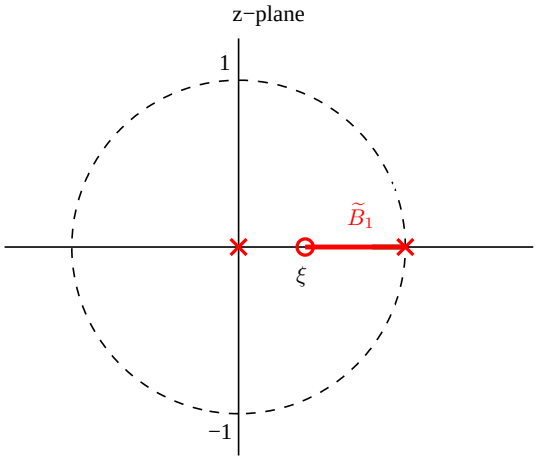

Figure 9.1: Typical trajectories of B_1 in FwFxLMS root locus

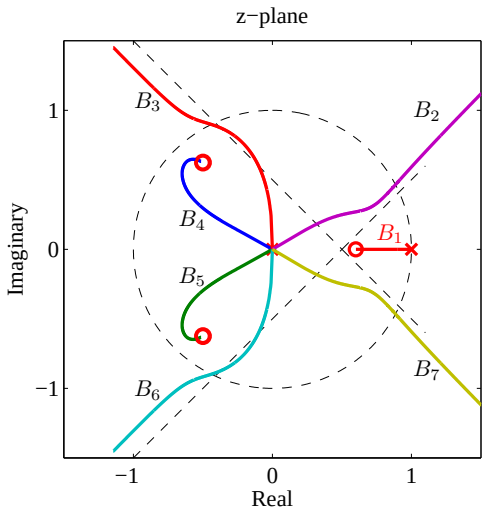

Figure 9.2: FwFxLMS root locus when $s_0 = s_1 = s_2 = 0$, $s_3 = s_4 = 1$ and $s_5 = 0.8$ and $\xi = 0.7$

9.4.1 Typical Trajectory of $\widetilde{B}_1$

As a typical property of the FwFxLMS root locus, $\widetilde{B}_1$ always starts at $z = 1$ and moves towards the origin on the real axis. If the control parameter ξ satisfies the inequality given in Eq. (9.70), then there is no breakaway point on the interval of $(\xi, 1)$. This causes $\widetilde{B}_1$ to continue its trajectory on the real axis until it reaches the end point at $z = \xi$. This typical trajectory is shown in Figure 9.1.

Figure 9.2 shows the FwFxLMS root locus for the example, described in Chapter 8, and when ξ is set to 0.7. As can be seen, there is no breakaway point on the trajectory of the dominant root (branch B_1) and, therefore, the interval of $(\xi, 1)$ is considered as the first branch of the root locus. (compared to the FxLMS root locus shown in Figure 8.1). This plot is obtained using numerical methods in MATLAB; however, the validity of all of the analytical rules, described in Section 9.3, can be seen in this plot.

9.4.2 Typical Trajectories of other branches

Other branches of the FwFxLMS root locus $\widetilde{B}_2, \widetilde{B}_4, \ldots,$ and $\widetilde{B}_Q$ start at $z = 0$ with individual departure angles and move towards the unit circle. They end at the zeros of $\widetilde{H}(z)$ or approach the asymptotes. According to Eq. (9.53), departure angles on these branches form the origin is independent of the parameters of the secondary path; however, they are dependant of the order of the secondary path.

9.4.3 Dominant Pole of FwFxLMS Adaptation Process

Based on the typical trajectories of the FwFxLMS root locus branches, described above, it is expected that the nearest root to the unit circle is located on $\widetilde{B}_1$. Therefore, this branch contains the dominant root of the FwFxLMS characteristic equation. This property is common in both of the FxLMS and FwFxLMS root loci. However, in the FxLMS root locus, B_1 detours towards the unit circle once reaching the breakaway point. Therefore, the maximum distance of the dominant root from the unit circle is equal to the distance of the breakaway point to $z = 1$. In the FwFxLMS root locus there is no breakaway point and, therefore, the root moving on $\widetilde{B}_1$ can get closer to the origin (until it reaches the branch end point at $z = \xi$). As a result, the dominant pole can be pushed towards the origin and, therefore, the dynamic of the FwFxLMS adaptation process becomes faster than that of the FxLMS.

9.5 Computer Simulation

This section verifies the validity and accuracy of the theoretical results, obtained in this chapter, by using computer simulation. Each curve is obtained by averaging over 100 simulation runs with independent noise sequences. In the simulation experiment, the impulse responses of the primary and secondary paths are similar to those used in Chapter 7. Also, the secondary path model is a perfect model and the acoustic noise is an stochastic white noise of power 1 ($\sigma_x^2 = 1$), generated by the computer.

In the first experiment, the FxLMS algorithm is used. The root locus of the adaptation process, performed by this algorithm, is plotted in Figure 9.3a. As can be seen, the branch containing the dominant root (B_1) returns towards the unit circle after reaching the breakaway point x_B. In the second experiment, the FwFxLMS algorithm with $\xi = 0.7$ is used. The root locus of the adaptation process, performed by this algorithm, is plotted in Figure 9.3b. As can be seen, the extra root of the FwFxLMS algorithm removes the breakaway point from the trajectory of the dominant root. In the third experiment, the FwFxLMS algorithm with $\xi = 0.5$ is used. The root locus of the adaptation process, performed by this algorithm, is plotted in Figure 9.3c. As can be seen, the extra root of the FwFxLMS algorithm removes the breakaway point from the trajectory of the dominant root and, also, this trajectory can come closer to the origin, compared to the second experiment. Therefore, it is expected that the dominant root of the FwFxLMS algorithm in the third experiment become closer to the origin, compared to the dominant root of the FwFxLMS algorithm in the second experiment. Also, it is expected that both the dominants roots of these two experiments to be closer to the origin than that of the first experiment. Therefore, the second experiment should be faster than the first experiment and the third experiment should be even faster than the second one.

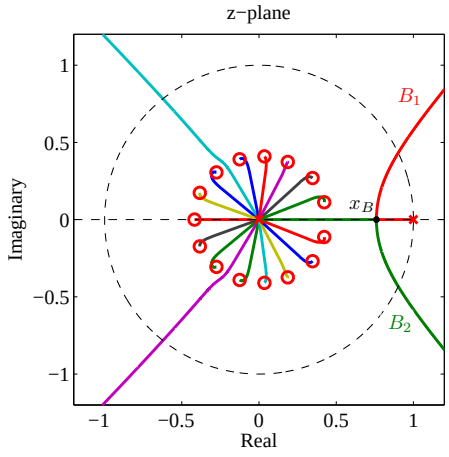

(a) FxLMS

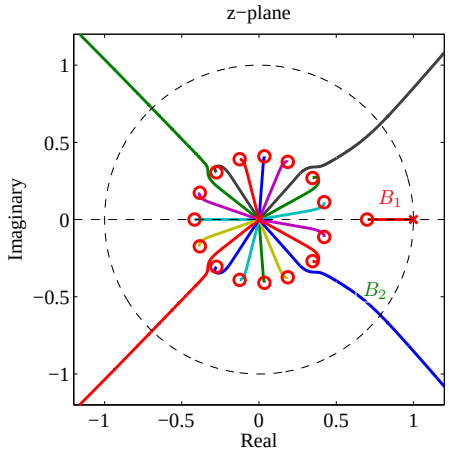

(b) FwFxLMS with $\xi = 0.7$

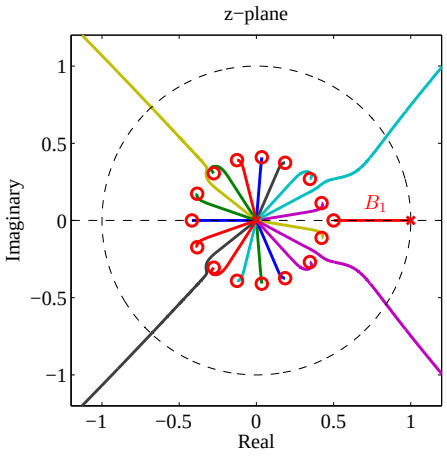

(c) FwFxLMS with $\xi = 0.5$

Figure 9.3: Root loci of the simulated FxLMS and FwFxLMS algorithms

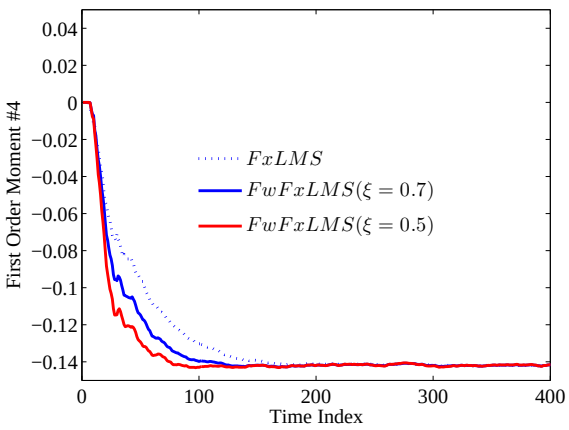

(a) Adaptive Weight #4

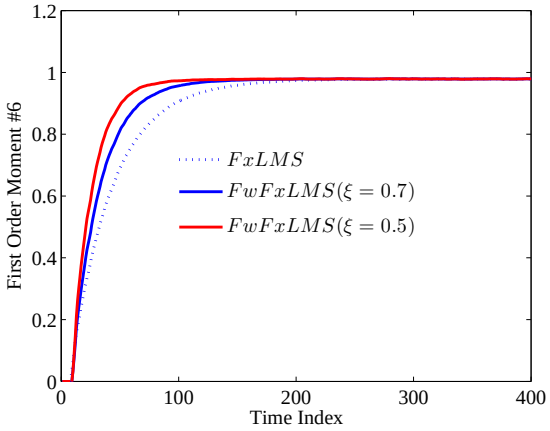

(b) Adaptive Weight # 6

Figure 9.4: Dynamic behaviours of first-order moments in FxLMS and FwFxLMS adaptation processes

Figure 9.4 shows dynamics of two different elements (4th and 6th elements) of the weight vector $\mathbf{w}(n)$ in the three experiments conducted above. Each curve is obtained by averaging over 100 independent data sets; consequently, these curves can be considers as the mean of the selected adaptive weights. Other elements of this vector also have the same behaviours. As expected, the adaptive weights converge to their steady-state levels faster in the third experiments, compared to the adaptive weights in the other two experiments. This issue can be also seen for other weights. Also, it can be seen that the steady-state levels of the weights are the same in all the experiments. This is in a good agreement with the theoretical results obtained in Section 9.1.3.

Figure 9.5 shows the MSE function in three experiments conducted above. As can be seen, the convergence speed of the MSE function directly related to the convergence speeds of the adaptive weights. According to the figure, this function has the same steady-state level in the FxLMS and the two FwFxLMS algorithms but this function converges to its steady-state level faster when the FwFxLMS is used. Also, by decreasing ξ in the FwFxLMS algorithm, the convergence speed of the MSE function is increased. This is in an excellent agreement with the theoretical results, obtained in this chapter.

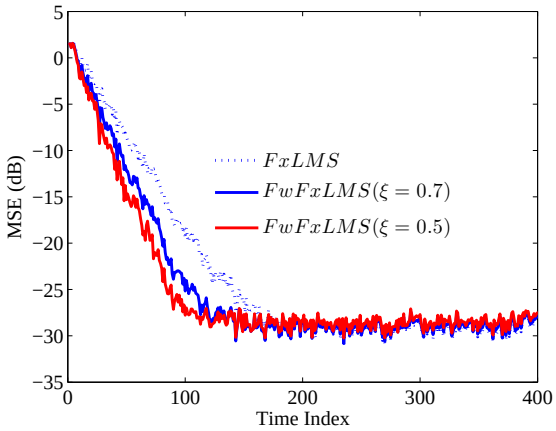

Figure 9.5: Dynamic behaviour of the MSE function in FxLMS and FwFxLMS adaptation processes

Chapter 10

Experimental Realisation

The experimental ANC setup, developed for and used in this research, has been designed based on a basic system, implemented in the University of Auckland Signal Processing Laboratory [70, 71]. This system is developed further for this research to implement a high performance ANC system with the ability of executing different ANC algorithms, e.g. FxLMS and FwFxLMS.

Section 10.1 introduces the developed experimental setup and its major components. In this section, two different FPGA designs which are separately developed for executing the FxLMS and FwFxLMS adaptation algorithms are described. Section 10.2 describes the methods applied for measurements and computations of basic parameters, which are required in numerical analysis of experimental results. Section 10.3 uses the obtained experimental results to validate the theoretical expressions derived in Chapters 3-6 for formulating behaviours of FxLMS-based ANC systems. Finally, Section 10.4 discusses the performance of the proposed ANC algorithm (FwFxLMS) in practise and compares it with the FxLMS algorithm.

10.1 Experimental Setup

Figure 10.1 shows the schematic diagram of the developed ANC setup. As can be seen, the ANC setup is developed to create a silence zone at the end of an acoustic duct. The length, width and height of this duct are $150cm$, $30cm$ and $25cm$, respectively. This duct is constructed from $1.8cm$ thick medium density fibre-board and its interior is carpeted. The major electro-acoustical hardware used in this setup are introduced below.

10.1.1 Microphones

Two similar AKG-D770 dynamic microphones are used in the experimental setup. The first microphone, which is used as the reference microphone, is placed at the beginning of the duct where the noise source is located. The output of this microphone can be considered as the reference signal $x\left(n\right)$. The second microphone, which is used as the error microphone, is placed at the end of the duct, where the desired silence zone is created. The output of this microphone can be considered as the error signal $e\left(n\right)$.

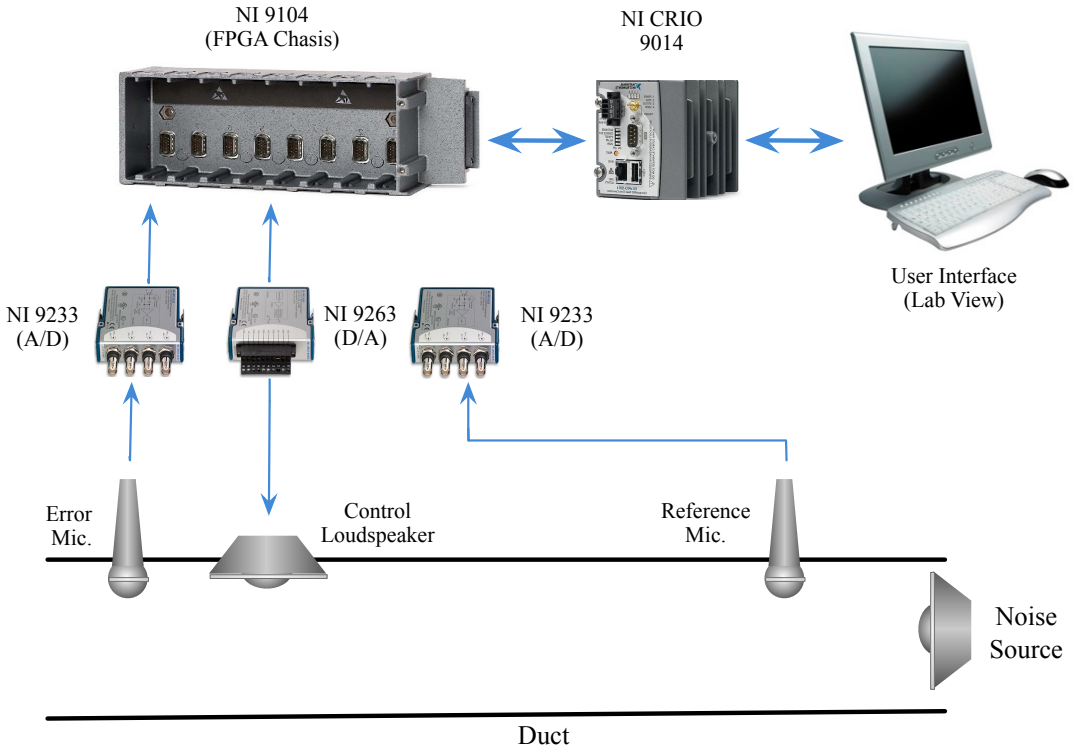

Figure 10.1: Schematic diagram of experimental ANC setup

10.1.2 Control Loudspeaker

The ANC setup includes a control loudspeaker to generate the anti-noise signal in the acoustic duct. This loudspeaker is driven by the control signal generated by the digital control system. It is important that the frequency response of the control loudspeaker is as flat as possible over the frequency range of the noise to be controlled. A Phonic SEp 207 powered loudspeaker with on-board 20W power amplifier is used as the control loudspeaker in this experimental setup.

10.1.3 Digital Electronic Control System

The major component of any ANC device is a real-time DSP controller, where the ANC algorithm is implemented. In our experimental ANC setup, a Compact RIO 9014 (cRIO 9014) which is an embedded real-time controller, made by National Instrument (NI), is used. The cRIO utilises an embedded Xilinx FPGA chassis with a 40MHz clock [72]. This chassis is connected to the reference and error microphones through two separate NI 9233 I/O modules, which are 24-bit analog to digital converters. Also, this chassis is connected to the control loudspeaker through a NI 9263 I/O, which is a 16-bit digital to analog converter. The connections between the cRIO, FPGA chassis, microphones and control loudspeaker are shown in Figure 10.1.

The combination of the FPGA chassis, real-time controller, and I/O modules creates a complete stand-alone embedded system. As can be seen in Figure 10.1, the only output module is connected to the 2nd channel of the FPGA chassis. Also, the two input modules are connected to the 3rd and 4th channels.

The FPGA circuitry in the chassis controls each I/O modules and passes data to the controllers through a local PCI bus using built-in communication functions. The FPGA design of the ANC algorithm can be developed by using the LabVIEW FPGA Module and compiled into a bit-stream file for download onto the cRIO, where the design is synthesised in the FPGA chip.

10.1.4 Real-Time Software

In this research, a general multi-threading structure for the implementation of real-time ANC algorithms (software) in cRIO is developed. Both the FxLMS algorithm and its novel alternative (FwFxLMS), can be implemented in this structure. FPGA designs for both of these algorithms are detailed below.

10.1.4.1 Multi-threading Structure for ANC

Using LabVIEW graphical programming environments, we can take full advantages of the multi-core processing power in the FPGA design of the experimental ANC setup. As shown in Figure 10.2, three loops execute in separate threads while abstracting the details of thread management away from the developer. In the following, these threads and their functions are introduced, separately.

10.1.4.2 Reading Thread

The first thread, called “reading thread”, reads data from the NI 9233 input modules, connected to the error and reference microphones. After reading data from input modules, they are filtered using a low-pass filter with the cut-off frequency of 1500 Hz and a high-pass filter with the cut-off frequency of 75 Hz. The obtained signals are labelled as “Reference” and “Error”. They are then stored in the cRIO memory. The FPGA design for the implementation of this thread is shown in Figure 10.2a .

10.1.4.3 Process Thread

The second and the most important thread, called “process thread”, is responsible for performing the ANC algorithm and computing the anti-noise signal in accordance with the reference and error signals. These two signals are continuously stored into cRIO memory by the reading thread, as described above. Once the anti-noise signal is computed, it is labelled as “Antinoise” and then it is stored in the cRIO memory. The structure of this thread is shown in Figure 10.2b. The detail of the FPGA designs for both the FxLMS and FwFxLMS algorithms are available in Appendix.

10.1.4.4 Writing Thread

The third thread, called “Writing Thread” is responsible for placing the anti-noise signal into the first channel of the NI 9263 output module, which directly drives the control loudspeaker. The anti-noise signal is continuously computed by the process thread so the writing thread can read it from the cRIO memory. The FPGA design of this thread is shown in Figure 10.2.

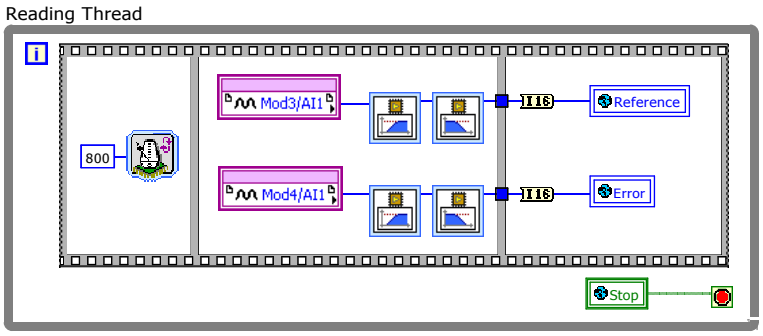

(a) FPGA implementation for the reading thread

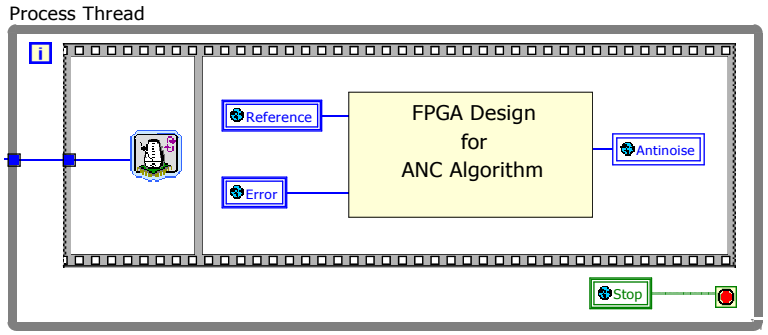

(b) FPGA implementation for the process thread

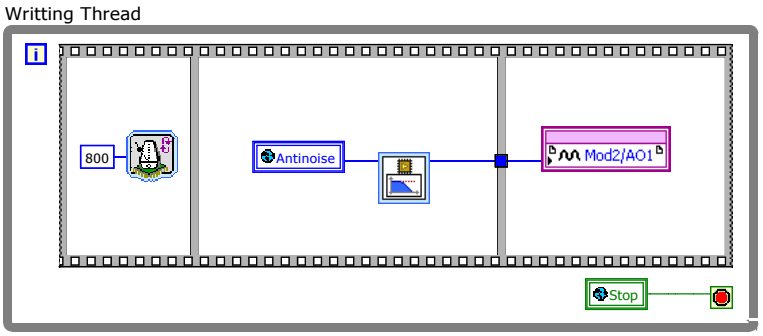

(c) FPGA implementation for the writing thread

Figure 10.2: A general multi-threading structure for FPGA design of ANC algorithms

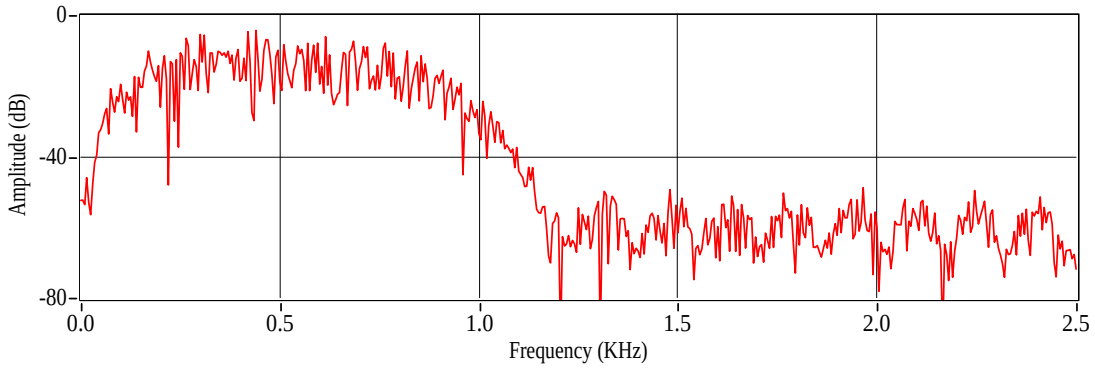

(a) minimum frequency=50 Hz, maximum frequency 1050 Hz

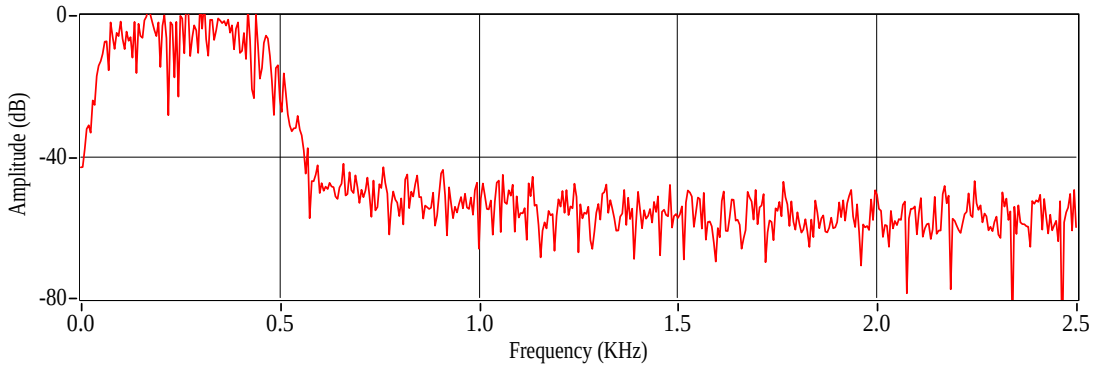

(b) minimum frequency=50 Hz, maximum frequency 550 Hz

Figure 10.3: Power spectrum of acoustic noise injected in acoustic duct

10.2 Measurement and Computation of Parameters

This section describes the methods applied for measurements and computations of basic parameters, required for the analysis of experimental results. Subsection 10.2.1 computes the parameters of the acoustic noise signals, injected into the acoustic duct. Subsection 10.2.2 explains how the minimal MSE level can be computed from the measured data. Subsection 10.2.3 explains how the actual secondary path and its models are identified. Also, this subsection computes $\|\mathbf{s}\|^2$ and D_{eq} for the actual secondary path and the perfectness ratios ρ_1, ρ_2 and ρ_3 for each secondary path model used in the experiments.

10.2.1 Acoustic Noise Parameters

In the experiments, reported below, two different acoustic noise signals are injected into the acoustic duct. For the generation of both of them, a white acoustic noise is used. This noise is then passed through two different band-pass filters. The outputs of the band-pass filters are stored into two separate files in WAVE format. These files can be played by using a computer and loudspeaker.

The first signal is obtained by passing the original white noise through a band-pass filter with the bandwidth of 1000 Hz, minimum frequency of 50 Hz and maximum frequency of 1050 Hz. The gain of this filter is adjusted such that the power of the reference signal is limited to $\sigma_x^2 \approx 6$ W. The power spectrum of the produced noise is shown in figure 10.3a. Since the operational sampling frequency of the ANC

system is set to 5554 Hz[1], the normalised band-width of this signal can be computed as depicted in Section 5.1.1:

$$B_w = \frac{1000}{\frac{1}{2} \times 5554} = 0.36 \tag{10.1}$$

The second signal is obtained by passing the original noise through a band-pass filter with the bandwidth of 500 Hz, minimum frequency of 50 Hz and maximum frequency of 550 Hz. Similar to the previous case, the gain of this filter is adjusted in such that the power of the obtained signal is limited to $\sigma_x^2 \approx 6$ W. The power spectrum of this noise is shown in figure 10.3b. For this acoustic noise, the normalised bandwidth B_w can be computed as

$$B_w = \frac{500}{\frac{1}{2} \times 5554} = 0.18 \tag{10.2}$$

The above values of B_w are used in Section 10.3 for the analysis of experimental results.

10.2.2 Minimal MSE Function

For the analysis of experimental results, it is essential to have an estimate value for the minimal MSE level, which can be interpreted as the minimum achievable residual acoustic noise power in the duct. Obviously, this parameter cannot be directly measured. However, we can estimate this parameter by using acoustic signals measured in the duct.

As mentioned in Subsection 10.1.1, the reference microphone measures the reference signal $x\,(n)$. Also, it is obvious that when the cancelling loudspeaker is not activated, the error microphone measures only the primary noise $d\,(n)$. Therefore, signals $x\,(n)$ and $d\,(n)$ are available in the experimental setup control system. These signals are then transferred to LabVIEW, where they can be stored into an ASCII text file. This file is used by a MATLAB function to compute J_o based on Eq. (2.23)[2]. Using this method, for the acoustic noise with the power spectrum, shown in Figure 10.3a, J_o can be found as

$$J_o = 0.0377\text{W} \tag{10.3}$$

This means that in the optimal case, an ANC system can reduce the power of this noise by about $10 \log \frac{J_o}{\sigma_x^2} = -22$ dB. Also, for the acoustic noise with the power spectrum, shown in Figure 10.3b, J_o can be found as

$$J_o = 0.0241\text{W} \tag{10.4}$$

Similarly, this value of J_o shows that in the optimal case, an ANC system can reduce this noise by about $10 \log \frac{J_o}{\sigma_x^2} = -24$ dB. The above estimate values for J_o are later used in Section 10.3 for the analysis of experimental results.

[1]The sampling frequency of the developed system is equal to the operating frequency of the while-loop in the process thread. The ratio of the operating frequencies of the reading and process threads while loops (in the FPGA design) should be an integer fraction otherwise the operating frequency of the system will vary over time. Based on this logic, the process thread while-loop frequency is set to 5554 Hz which is $\frac{1}{9}$ of the reading while-loop frequency ($50K^{\text{Sample}}/_{\text{s}}$) [70].

[2]The statistical expectation operator is estimated by averaging over 1024 consecutive samples of matrices, vectors or signals.

10.2.3 Secondary Path Parameters

Using the real-time secondary path identification system, integrated in the experimental setup, the secondary path impulse response in the acoustic duct can be estimated precisely. After estimating the impulse response, its coefficients are downloaded from the cRIO memory into LabVIEW, where they can be exported to an ASCII text file. This file is then used by a MATLAB function to compute the secondary path equivalent delay D_{eq}, as defined in Eq. (4.8). Also, this function computes $\|\mathbf{s}\|^2$, as the sum of squares of secondary path impulse response coefficients.

The impulse response, estimated by the experimental setup, is shown in Figure 10.4a. This figure is directly exported from LabVIEW. Using this impulse response and based on the steps described above, the parameters of the actual secondary path can be computed as follows.

$$D_{eq} = 42.39 \tag{10.5}$$

and

$$\|\mathbf{s}\|^2 = 0.4684 \tag{10.6}$$

The above values of D_{eq} and $\|\mathbf{s}\|^2$ are used in Sections 10.3 for the analysis of experimental results. Note that this impulse response can be considered as a nearly perfect secondary path model, as it is measured precisely and the actual ANC system operates with this secondary path.

Now, two imperfect secondary path models are generated. The first imperfect model ($\hat{\mathbf{s}}_1$) is measured when an extra noise source exists outside the acoustic duct. In this case, the noise generated by this source is not included in the identification algorithm; consequently, the impulse response, measured by the identification system, becomes noisy and deviates from the actual system ($\mathbf{s}$). Figure 10.4b shows the estimated impulse response in this condition. This impulse response is stored in an ASCII text file so that a MATLAB function can use it to compute its perfectness ratios by using Eqs. (6-13)-(6.15) as

$$\rho_1 = 1.1393 \tag{10.7}$$

$$\rho_2 = 0.9085 \tag{10.8}$$

$$\rho_3 = 1.0251 \tag{10.9}$$

The second model ($\hat{\mathbf{s}}_2$) is measured when the upper side of the duct is partially opened. In this case, the acoustic impedance of the duct secondary path is affected by the outside impedance and it is expected that the total impedance of the secondary path becomes lower. Figure 10.4c shows the impulse response measured in this condition. Similar to the previous case, this impulse response is stored in an ASCII text file so that a MATLAB function can use it to compute its perfectness ratios as

$$\rho_1 = 0.3597 \tag{10.10}$$

$$\rho_2 = 0.9153 \tag{10.11}$$

$$\rho_3 = 0.2009 \tag{10.12}$$

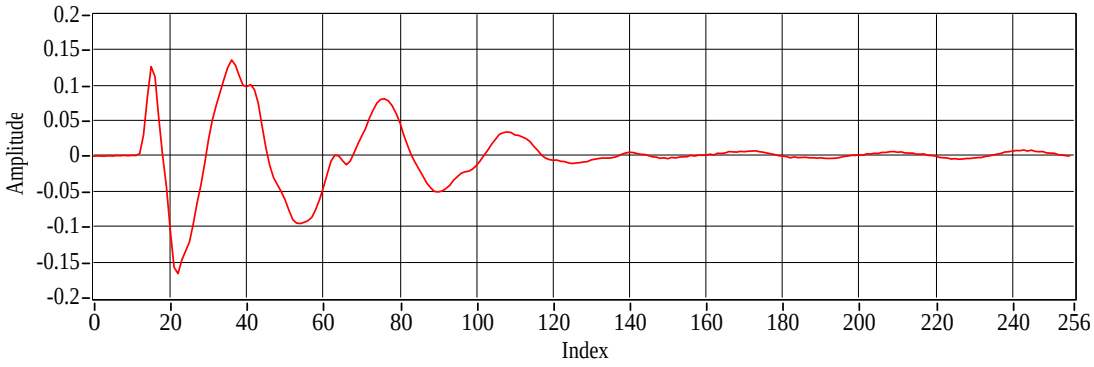

(a) Actual impulse response (**s**)

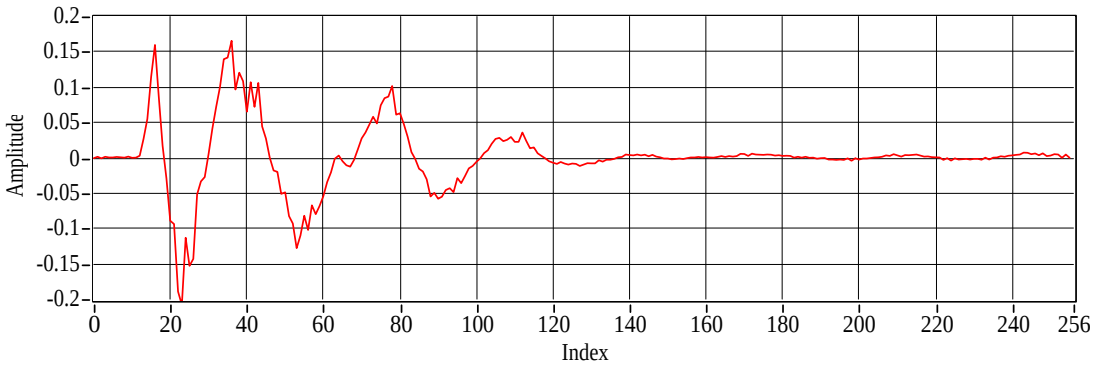

(b) Model 1 ($\hat{\mathbf{s}}_1$)

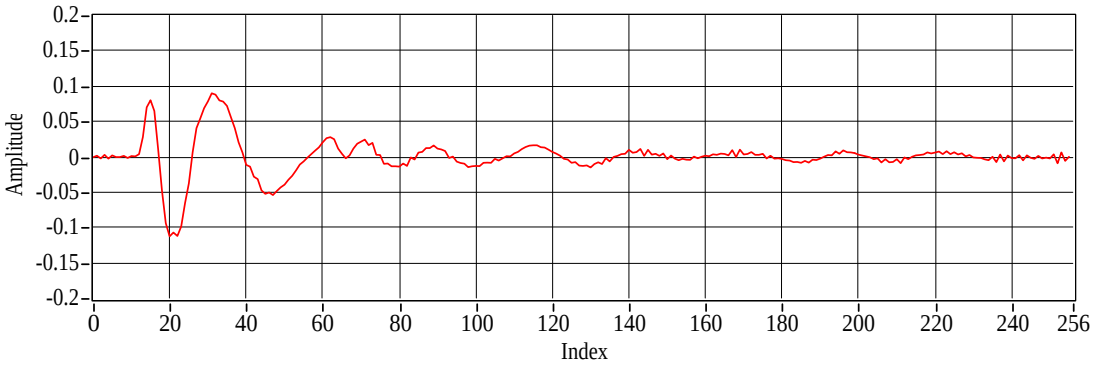

(c) Model 2 ($\hat{\mathbf{s}}_2$)

Figure 10.4: Actual secondary path impulse response and its imperfect models

Table 10.1: Values of basic parameters used in analysis of experimental results

	B_w	$J_o\,(\mathrm{W})$	ρ_1	ρ_2	ρ_3
Experimental Condition 1	0.36	0.0377	≈ 1	≈ 1	≈ 1
Experimental Condition 2	0.18	0.0241	≈ 1	≈ 1	≈ 1
Experimental Condition 3	0.36	0.0377	1.1393	0.9085	1.0251
Experimental Condition 4	0.18	0.0241	0.3597	0.9153	0.2009

10.3 Behaviours of Implemented ANC System

This section uses the developed experimental setup to show the practical validity of the theoretical results, derived in Chapters 3-6. The agreement between experimental and theoretical results are demonstrated by using several experiments, conducted in different conditions.

Experimental condition 1: in all the experiments conducted under this condition, the acoustic noise with the power of $\sigma_x^2 = 6$ W and band-width of $B_w = 0.36$ is injected into the duct. The power spectrum of this noise is shown in Figure 10.3a. For this acoustic noise, the minimal MSE level is given in Eq. (10.3) as $J_o = 0.0377$ W. In these experiments, the nearly perfect secondary path model, shown in Figure 10.4a, is uploaded into the cRIO memory. Accordingly, it is expected that all the perfectness ratios of this model are nearly equal to 1.

Experimental condition 2: in this condition, the acoustic noise with the power of $\sigma_x^2 = 6$ W and band-width of $B_w = 0.18$ is injected into the duct. The power spectrum of this noise is shown in Figure 10.3b. For this acoustic noise, the minimal MSE level is given in Eq. (10.4) as 0.0241 W. The secondary path model, uploaded into cRIO memory is remained unchanged. Therefore, it is still expected that all the perfectness ratios of the model are nearly equal to 1.

Experimental condition 3: in this condition, the acoustic noise, injected into the duct, is similar to the one used in the first experimental conditions; however, the secondary path model, shown in Figure 10.4b is uploaded in to the cRIO memory, instead of the nearly perfect model. As mentioned in Section 10.2.3, this model is identified when an external noise source is located close to the error microphone. Accordingly, this model is considered as an imperfect model. As shown in Eqs. (10.7)-(10.9), the perfectness ratios of this model are $\rho_1 = 1.1393$, $\rho_2 = 0.9085$ and $\rho_3 = 1.0251$.

Experimental condition 4: in all the experiments, conducted in this condition, the acoustic noise, injected into the duct, is similar to the one used in the second experimental conditions and the imperfect secondary path model, shown in Figure 10.4b is uploaded in to the cRIO memory. As shown in Eqs. (10.10)-(10.12) the perfectness ratios of this mode are $\rho_1 = 0.3597$, $\rho_2 = 0.9135$ and $\rho_3 = 0.2009$.

In the above mentioned conditions, several experiments with different values of the step-size are conducted. For each experiment, the output of the error microphone is monitored, recorded and analysed in the LabVIEW environment. The obtained results can be then compared with the theoretical results. For obtaining the theoretical results from the proposed expressions, appropriate values of B_w, J_o, ρ_1, ρ_2 and

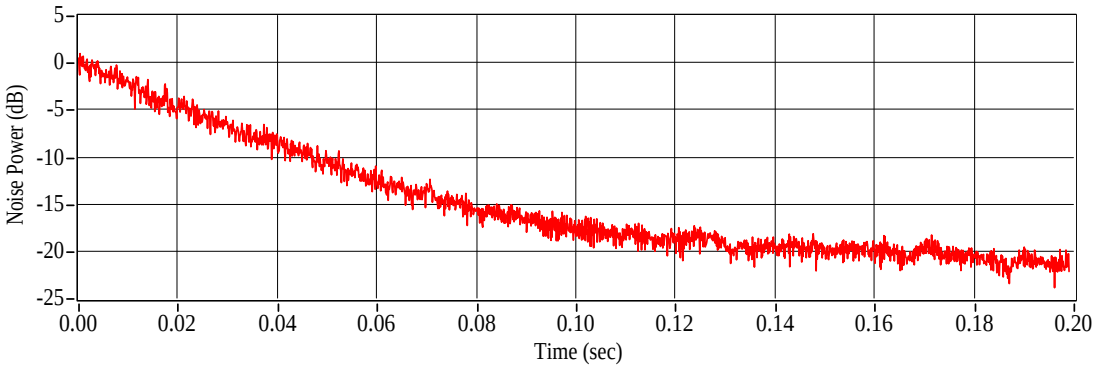

Figure 10.5: Variation of residual acoustic noise power in the implemented ANC system (under experimental condition 1)

ρ_3 should be used (these values are obtained in Section 10.2). For the sake of clarity, these values are collected in Table 10.1.

10.3.1 System Stability in Practise

Different experiments, conducted in the experimental condition 1, show that when $\mu < 1.300 \times 10^{-3}$, the implemented ANC system is always stable. For example, the residual acoustic noise power for the step size $\mu = 0.700 \times 10^{-3}$ is shown in Figure 10.5. This plot is directly exported from the LabVIEW environment, where the noise power is estimated by using recorded samples of the residual acoustic noise. Different experiments with different step-sizes show that when $1.300 \times 10^{-3} < \mu < 1.550 \times 10^{-3}$ the system starts diverging after a short time (becomes unstable); and when $\mu > 1.550 \times 10^{-3}$ the system starts diverging from the beginning. These observations are recorded in Table 10.2. According to this table, it can be concluded that a practical μ_{max} is located between 1.300×10^{-3} and 1.550×10^{-3}. However, it is not technically possible to estimate any specific value for μ_{max} from the experimental results. This is because of the experimental conditions uncertainties such as changing characteristics of the surrounding environment, non-stationary behaviours of the background noise and uncertainties associated with physical plants, control systems and measurement devices .

Now, by substituting the parameters, given in Table 10.1, into Eq. (5.23), the theoretical value of μ_{max} can be obtained as $\mu_{max} = 1.448 \times 10^{-3}$. It means that, in theory, for $\mu < 1.448 \times 10^{-3}$ the system always becomes stable and for $\mu < 1.448 \times 10^{-3}$, the algorithm always diverges. This result is in a good agreement with the experimental results described above.

Here, the minimum relative error between the practical and theoretical results can be obtained as the relative difference of the theoretical value of μ_{max} and the maximum step-size for which the ANC system is stable in practise (e.g. this value is 1.300×10^{-3} in the above experiment). Similarly, the maximum relative error can be obtained as the relative error between the theoretical value of μ_{max} and the minimum step-size for which the ANC system is always unstable in practise (e.g. this value is 1.550×10^{-3} in the above experiment). The obtained values of μ_{max} and the corresponding relative errors are recorded in Table 10.2.

The above experimental process can be repeated when the ANC setup operates in different experimental conditions (e.g. those described in Section 10.3). The obtained experimental results, along with the

Table 10.2: Comparison of experimental and theoretical values of step-size upper-bound

	Theory	maximum μ for stability in practise (μ_M)		minimum μ for instability in practise (μ_m)	
	μ_{max}	μ_M	$\frac{\mu_M - \mu_{max}}{\mu_{max}}\%$	μ_m	$\frac{\mu_m - \mu_{max}}{\mu_{max}}\%$
Experimental Conditions 1	1.448×10^{-3}	1.300×10^{-3}	-10.21%	$\mu > 1.550 \times 10^{-3}$	7.05%
Experimental Conditions 2	0.979×10^{-3}	0.850×10^{-3}	-13.16%	$\mu > 1.050 \times 10^{-3}$	-7.27%
Experimental Conditions 3	1.360×10^{-3}	1.200×10^{-3}	-11.78%	$\mu > 1.450 \times 10^{-3}$	-6.60%
Experimental Conditions 4	1.901×10^{-3}	1.700×10^{-3}	-10.58%	$\mu > 2.050 \times 10^{-3}$	-7.83%

theoretical results are collected in Table 10.2. Also, the relative error between the theoretical and experimental results are shown in this table. Note that, when the setup operates in the experimental condition 2, the theoretical value of μ_{max} should be computed by using Eq. (5.23) and when it operates in the experimental conditions 3 and 4, this value should be computed by using Eq. (6.26).

As can be seen in Table 10.1, the proposed theoretical formulation for μ_{max} can efficiently estimate this parameter with the relative error between -15% and 10%. The existence of this error can be justified because in theory it is not possible to consider the following issues.

1. Changing characteristics of the surrounding environment.
2. Non-stationary behaviours of the background noise.
3. Uncertainties associated with physical plants, control systems and measurement mechanisms.

Apart from this unavoidable error, the proposed formulation for μ_{max} is a very significant step towards matching available theoretical and experimental findings. This is because the commonly-used expression for μ_{max}, which was derived in [8, 48], can only apply to un-realistic cases with pure delay secondary paths, broad-band acoustic noise signals and perfect secondary path models. However, the proposed formulation can apply to a general case with an arbitrary secondary path, arbitrary acoustic noise bandwidth, and arbitrary secondary path model.

10.3.2 Steady-State Performance in Practise

In Chapters 4-6, different equations for evaluating the residual acoustic noise power in steady-state conditions (σ_e^2) are derived. Eq. (4.22) gives this quantity for an ideal case with a broad-band acoustic noise. Eq. (5.26) gives this quantity for a more realistic case with a band-limited acoustic noise. Also, Eq. (6.32) consider the secondary path model imperfectness in this quantity. In the following, the practical validity of these equations are investigated by using the developed experimental setup.

Initially, the implemented ANC system is activated in the experimental condition 1 and the step-size is set to a relatively small number (about 0.1 of its corresponding upper-bound). After a long time, when the system reaches its steady-state conditions, the power of the residual noise is computed in LabVIEW. Now, the step-size is incrementally increased and the system is re-started again. For each step-size, the above experiment is repeated and the steady-state power of the residual noise is measured. The measured data can be plotted as a function of the step-size, as shown in Figure 10.6a. For each step-size, the theoretical value of the steady-state residual acoustic noise can be also computed by using the closed-form expression given in Eq. (5.26) and the parameters given in Table 10.1. The results can be then plotted as another function of the step-size. This function is plotted by using a red line in Figure 10.6a. Also, the minimum attainable noise power (J_o) is shown in this figure .

For the other three experimental conditions, the same process can be repeated. The obtained experimental results are plotted in Figures 10.6b, 10.6c and 10.6d. Note that, when the system operates in the experimental condition 2, the theoretical results can be obtained by using Eq. (5.26) and when it operates in experimental conditions 3 and 4, the theoretical results can be obtained by using Eq. (6.32).

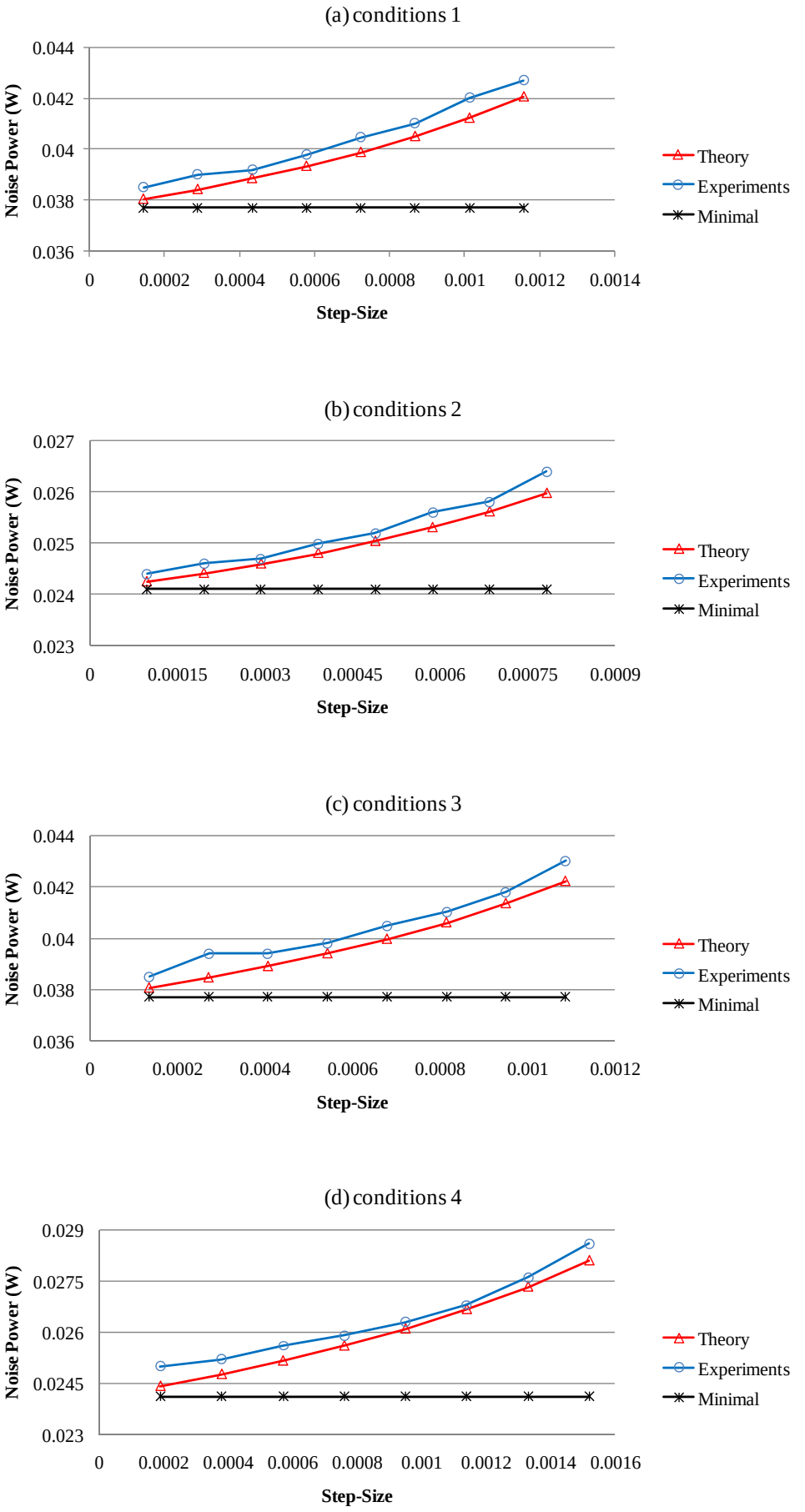

Figure 10.6: Steady-state residual acoustic noise power in the implemented ANC setup

As can be seen in plots of Figures 10.6, the theoretical and practical results are in a good agreement. The existence of the small offset between the experimental and theoretical results is due to the non-ideal experimental conditions. The agreement between the theoretical and experimental results, shown in Figure 10.6, confirms that the proposed formulations can effectively estimate the steady-state performance of practical FxLMS-based ANC systems.

10.3.3 Convergence Speed in Practise

In Chapters 4-6, closed-form expressions for the transient convergence speed measure of FxLMS-based ANC systems (ω) is derived. This parameter is expected to determine the convergence speed of these systems in different working conditions. Eq. (4.46) estimates this measure for an ideal case with a broadband acoustic noise. Eq. (5.30) estimates this measure for a more realistic case with a band-limited acoustic noise. Also, Eq. (6.39) consider the secondary path model imperfectness in this parameter. Herein, it is desired to investigate the practical validity of these equations. For this purpose, the transient convergence speed of the implemented ANC system should be evaluated by using available measurements. As shown in Chapter 7, the convergence speed measure ω can be interpreted as the slop of the residual noise power once the FxLMS algorithm starts operating (in transient conditions). Therefore, in order to estimate this slope in practise, the average speed at which the residual noise power reduces to -6 dB is measured. This speed can be evaluated by using the following formulation.

$$\omega \approx \frac{1.5071}{N_{6dB}} \frac{\mathrm{W}}{\mathrm{Sample}} \tag{10.13}$$

where 1.5071 is equivalent to -6 dB reduction in the acoustic power when the reference power is $\sigma_x^2 = 6$ W, and N_{6dB} is the time index at which the steady-state residual noise power is attenuated for 6 dB.

For each experiment with a particular value of the step-size, N_{6dB} can be measured in real-time and then it can be recorded in the LabVIEW environment. By using this measured value, ω can be evaluated from Eq. (10.13). This process can be repeated for different experimental conditions (e.g. those introduced in Section 10.3). The obtained results can be plotted as a function of the step-size, as shown in plots of Figure 10.7. Also, for each experiment, the theoretical value of ω can be computed by substituting corresponding parameters, given in Table 10.1, into Eqs. (5.30) or (6.39). For the first two experiments, in which a nearly perfect secondary path model is used, Eq. (5.30) should be used and for the last two experiments in which two different imperfect secondary path models are used, Eq. (6.39) should be used.

According to Figure 10.7, the theoretical results are in a good agreement with the experimental results. This agreement confirms the validity and accuracy of the proposed closed-form expressions for the transient convergence speed of FxLMS-based ANC systems.

Also, it can be seen in plots of Figure 10.7 that, in all experimental conditions, the implemented ANC system has its fastest convergence speed when the step-size is about half of its upper-bound. This observation is in an excellent agreement with the theoretical findings, given in Eqs. (4.48), (5.32) and (6.45).

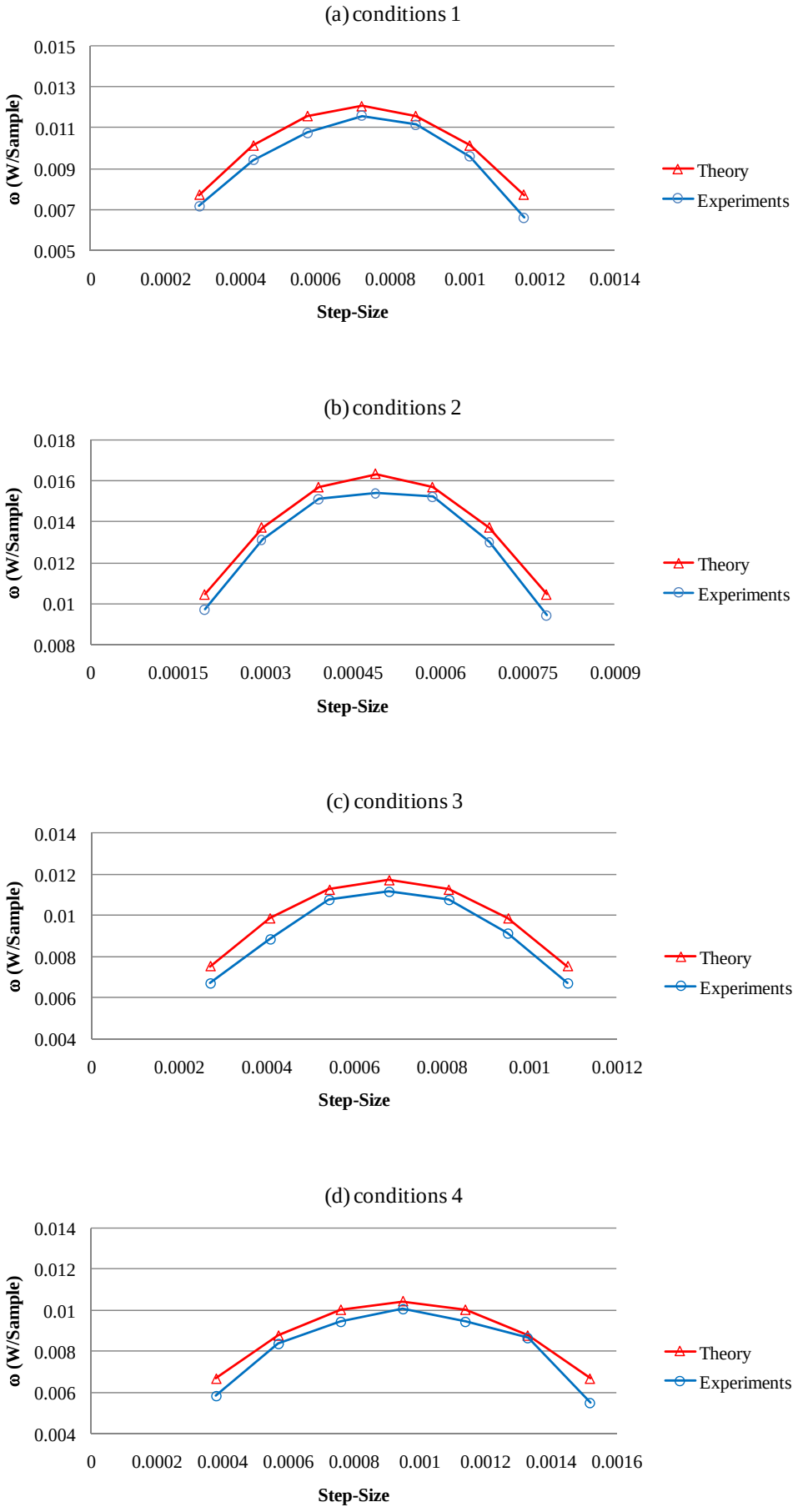

Figure 10.7: Transient convergence speed of the implemented ANC setup

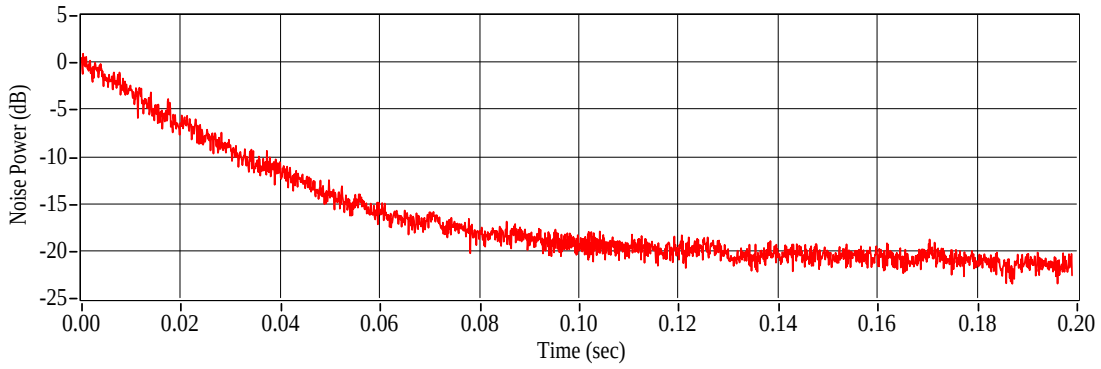

(a) $\xi = 0.9$

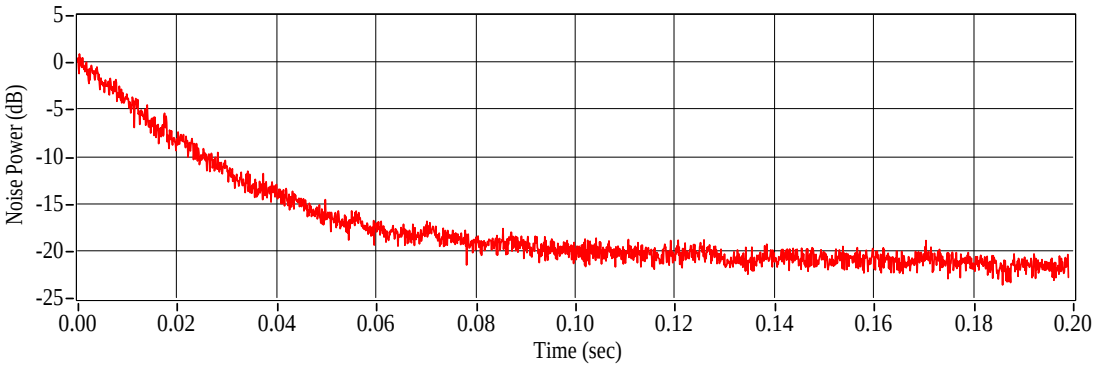

(b) $\xi = 0.7$

Figure 10.8: Residual acoustic noise power, obtained by using implemented FwFxLMS-based ANC system with $\mu = 0.700 \times 10^{-3}$ under first experimental conditions.

10.4 Experimental Results with FwFxLMS-Based ANC System

This section shows the efficiency of the FwFxLMS adaptation algorithm in practise. This algorithm is developed in Chapters 8 and 9, as one of the contributions of this thesis. For the practical verification of this algorithm, the FPGA design, described in Appendix, is implemented in the cRIO FPGA chassis. This design can be developed by the modification of the FPGA design for the FxLMS-based ANC system, described in Section 10.2. The experimental results, obtained from this new setup, can be compared with the results obtained from the implemented FxLMS-based ANC system.

As mentioned in Chapter 9, the steady-state performance of the FwFxLMS algorithm is similar to that of the FxLMS algorithm; however, we expect this algorithm to be faster than the FxLMS algorithm. Here, the acoustic noise with the power spectrum shown in Figure 10.3a, is injected into the duct. The residual acoustic noise is measured by the error microphone and it is then recorded in LabVIEW. Based on this recording, the residual acoustic noise power can be computed in LabVIEW .

As mentioned in Chapter 9, in the FwFxLMS algorithm the control parameter ξ should be set. The allowed range of ξ can be obtained by setting $D_{eq} = 42.39$ into Eqs. (8.47) and (9.55) as $0.72 < \xi < 1$. In the first experiment, the system is started with $\xi = 0.9$. Figure 10.8a, shows the variation of the acoustic noise power when $\mu = 0.700 \times 10^{-3}$ and $\xi = 0.9$. In this experiment, the value of the step-size and also the experimental condition are similar to the first experiment, described in Subsection 10.3.1.

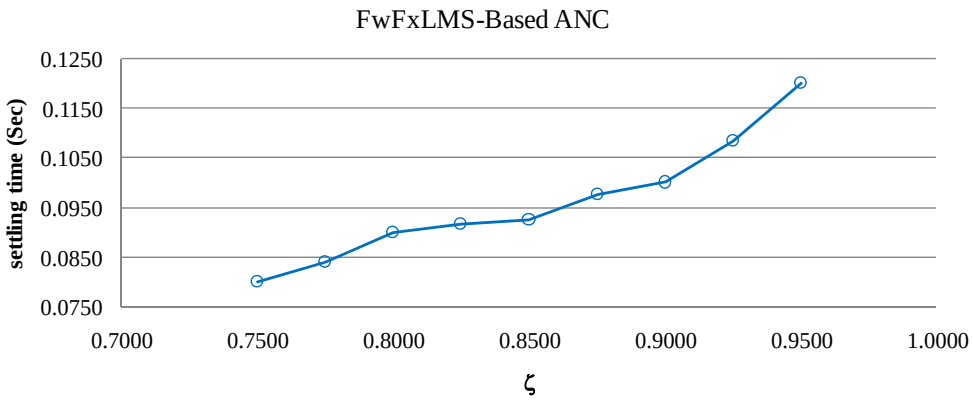

Figure 10.9: Influences of control parameter ξ on settling time of the implemented FwFxLMS-based ANC system

Therefore, the residual acoustic noise power, shown in Figure 10.5 can be used as a reference for the evaluation of the experimental results, obtained here.

Comparison of the two plots shown in Figures 10.5 and 10.8a, shows that when the implemented FxLMS-based ANC system is used, the residual noise power reaches its steady state level after about 0.12 seconds and when the implemented FwFxLMS-based ANC system is used this time reduces to about 0.10 seconds. Also, from these two figure it can be seen, that the steady-state performance of the two ANC systems are similar. Accordingly, the proposed ANC algorithm can efficiently improve the adaptation process dynamics in ANC systems, without changing its steady-state performance.

Now, ξ is set to a smaller number: $\xi = 0.75$. In this case, it is expected that the system becomes even faster, as described in Section 9.3. Figure 10.8b shows the variation of the residual acoustic noise power in this case. As can be seen in this figure, the system reaches its steady-state level in about 0.08 seconds; therefore, the attenuation is achieved faster, compared to the two previous cases.

The above experiment can be repeated for different values of ξ, located between 0.72 and 1. For each experiment, the time in which the system reaches its steady-state conditions can be recorded. The results can be then plotted with respect to ξ, as shown in Figure 10.9. As expected, this figure shows that by decreasing ξ, the implemented system dynamics become faster. This is in an excellent agreement with the theoretical results, discussed in Chapter 9 .

Chapter 11

Conclusions and Future Work

This chapter gives concluding remarks and highlights the major contributions of this thesis. It also presents directions for future research, based on the findings of this thesis.

11.1 Conclusions

The prime goal of this study has been a comprehensive theoretical analysis of FxLMS-based ANC systems in realistic conditions in which actual ANC systems work. This analysis has been performed based on two different approaches.

In the first approach, attention has been focused on the derivation of general closed-form expressions for parameters relevant to stability behaviours of ANC systems, such as the step-size upper-bound, steady-state performance, and convergence speed. These expressions have been derived based on a novel stochastic model for ANC systems.

In the second approach, attention has been focused on the dynamics of the FxLMS adaptation process in ANC systems. The root locus method has been found to be a a powerful tool for the analysis and control of ANC systems dynamics.

The main contributions of this thesis are summarised individually below.

11.1.1 Closed-form Expression for Step-Size Upper-bound

A relatively comprehensive expression for the upper-bound of the step-size, beyond which FxLMS-based ANC systems become unstable, has been derived in this thesis. This expression, given in Eq. (4.43), is in the form of the commonly-used one, previously derived by Elliott for pure delay secondary paths. However, instead of the physical time delay which appeared in Elliott's expression, a hypothetical parameter has appeared in the newly-derived expression. This novel parameter, which is called the secondary path equivalent delay in this thesis, can be computed for any arbitrary secondary path, unlike the secondary path time delay which is a physical parameter related to only pure delay secondary paths.

Also, influences of the acoustic noise band-width and secondary path modelling error on the step-size upper-bound have been investigated. It has been shown that these influences can be included in the closed-form expression, obtained for the step-size upper-bound. As an elegant result, the final expression for the step-size upper-bound, given in Eq. (6.26), can apply to realistic ANC systems with arbitrary secondary paths, arbitrary secondary path models, and band-limited acoustic noise signals.

11.1.2 Closed-form Expression for Steady-State Performance

A closed-form expression for the steady-state residual noise (power) level has been derived. Also, a closed-form expression for the misadjustment level, determining the relative distance between the actual and optimal steady-state noise levels, has been developed. Influences of the acoustic noise band-width and secondary path modelling error on these two expressions have been formulated. The final expression, given in Eq. (5.27) and (6.33), can apply to realistic ANC systems with arbitrary secondary paths, arbitrary secondary path models, and band-limited acoustic noise signals. It has been shown that an imperfect secondary path model does not necessarily cause the steady-state performance to be degraded. This is an interesting result which has been supported by simulation and experimental results in this thesis.

11.1.3 Closed-form Expression for Convergence Speed Measure

A novel measure for the evaluation of the convergence speed of the MSE function in FxLMS-based ANC systems has been introduced. A closed-form expression for this measure has been derived, considering a general secondary path. Influences of the acoustic noise band-width and secondary path modelling error on this measure have been investigated. By the analysis of this measure, it has been shown that increasing the noise band-width always causes the convergence speed of the system to be decreased. Also, it has been proved that an imperfect secondary path model does not necessarily causes the convergence speed to be degraded. However, it is impossible that an imperfect secondary path model causes both the steady-state performance and convergence speed of ANC systems to be improved.

Maximising the proposed convergence speed measure with respect to the step-size shows that the maximum convergence speed can be achieved when the step-size is set to the half of its upper-bound. The ratio of this step-size to its upper-bound (that is 0.5) is independent of the noise band-width and secondary path model. Therefore, no matter what the noise band-width is or what the secondary path model is, the maximum attainable convergence speed can be achieved by setting the step-size to half of its upper-bound.

11.1.4 Root Locus Plot of FxLMS Adaptation Process

A characteristic equation for the FxLMS adaptation process has been derived. Trajectories of the roots of this equation in the z-plane are determined as a function of step-size. As an interesting result, it has been found that the dominant root of this equation always moves on the first branch of the root locus. Also, it has been shown that there is always a breakaway point on this branch, limiting the dominant root

to become very close to the origin. Therefore, the location of this breakaway point is a limiting factor for the FxLMS adaptation process dynamics.

A closed-form expression for the location of the breakaway point in the FxLMS root locus has been derived. The secondary path equivalent delay has appeared in this expression. It was interesting to find that in both of the analyses performed in this thesis, the novel parameter of the secondary path equivalent delay has appeared. This is while the two analyses are completely independent; the first of which is based on the stochastic modelling of the MSE function and the second of which is based on the root locus analysis of the FxLMS adaptation process.

11.1.5 FwFxLMS Adaptation Algorithm

A mechanism for the localisation of the dominant root of the FxLMS characteristic equation, has been developed in this thesis. This mechanism can be considered as a novel ANC algorithm, called the FwFxLMS algorithm. It has been shown, that the FwFxLMS algorithm is able to remove the breakaway point from the FxLMS root locus, so the dominant root of the root locus can move closer to the origin in the z-plane. This means that the convergence speed of the adaptation process can become faster, compared to that of the original FxLMS algorithm. It has been mathematically proved that steady-state behaviours of the FwFxLMS algorithm is similar to that of the FxLMS; therefore this algorithm has no effect on the steady-state performance of active noise control.

11.1.6 Multi-threading Structure for Implementation of Real-Time ANC Algorithms

This thesis has developed and applied a general multi-threading structure for the implementation of different real-time ANC algorithms using LabVIEW FPGA Module. This structure partitions the ANC software into three loops which should be executed in separate threads while abstracting the details of thread management away from the developer. Both the traditional FxLMS algorithm and its novel alternative (FwFxLMS algorithm) have been implemented using this structure successfully.

11.2 Directions For Future Work

Active noise control is a multi-disciplinary research area with a huge number of modern applications. In this section the possible research work which can be conducted based on the contributions of this thesis are proposed.

11.2.1 Noise Colour Influences

In the analysis of stochastic adaptation algorithms, when it is desired to derive analytical expression for the parameters relevant to the adaptation process operation, it is usually acceptable to assume that the training data is a broad-band white stochastic signal so that its frequency spectrum is flat over the entire of frequency range. This thesis starts its analysis with this assumption and then extends it to a more

general case with band-limited white signals. This is because, even if the acoustic noise is white, its frequency spectrum cannot be flat over the entire frequency range in practise.

However, in some applications of active noise control, the acoustic noise is not white. In this case, influences of acoustic noise colours on the performance of the ANC algorithm should be studied. This research can be conducted based on the theoretical model, developed in Chapter 3 of this thesis. As mentioned in Chapter 3, this model can apply to any general acoustic noise. However, when we have intended to derive analytical results from this model in Chapters 4-6, we have had to simplify it by assuming a white acoustic noise (broad-band or band-limited). Removing the constraint caused by this simplifying assumption is another interesting area of research which can be focused on based on this thesis.

11.2.2 Intentional Misadjustment of Secondary Path Model

In Chapter 6, it has been shown that the secondary path modelling error does not necessarily cause the steady-state performance or convergence speed of FxLMS-based ANC systems to be degraded. However, this error cannot cause both of these parameters to be improved. In some applications of active noise control, the convergence speed of the adaptation algorithm is not an important issue. On the other hand, there are some other applications for which degrading steady-state performance is tolerable. Finding a mechanism for intentional misadjustment of the secondary path model in order to make a trade-off between the steady-state performance and convergence speed is another area of research, suggested by this thesis.

11.2.3 Other Applications

Applications of the FxLMS adaptation algorithm are not only limited to active control of acoustic noise. This algorithm can be used in a wide range of adaptive control applications such as adaptive echo cancellation, vibration control and adaptive inverse control. The theoretical results, contributed in this thesis, are derived based on the analysis of this algorithm in the active noise control framework and terminology. This analysis can be also performed for other applications and based on their relevant terminologies. However, the logic behind the analysis is the same as the logic used in this thesis.

Bibliography

[1] P. Leug, "Process of silencing sound oscillations," *U.S. Patent 2043416*, 1936.

[2] H. F. Olson and E. G. May, "Electronic sound absorber," *Journal of the Acoustical Society of America*, vol. 25, no. 4, pp. 829–829, 1953.

[3] H. F. Olson, "Electronic control of noise, vibration and reverberation," *Journal of the Acoustical Society of America*, vol. 28, pp. 966–972, 1956.

[4] L. G. Fogel, "Methods of improving intelligence under random noise interference," *U.S. Patent 2866848*, 1958.

[5] E. D. Simshauser and M. E. Hawley, "The noise canceling headset - an active ear defender," *Journal of the Acoustical Society of America*, vol. 27, pp. 207–217, 1955.

[6] B. Widrow, J. Glover, J. McCool, J. Kaunitz, C. Williams, R. Hearn, J. Zeidler, J. Eugene Dong, and R. Goodlin, "Adaptive noise cancelling: principles and applications," *Proceedings of the IEEE*, vol. 63, no. 12, pp. 1692–1716, Dec. 1975.

[7] S. M. Kuo and D. R. Morgan, *Active noise control systems: algorithms and DSP implementations*. New York, NY, USA: Wiley Interscience, 1996.

[8] S. J. Elliott, *Signal Processing for Active Control*. San Diego, CA.: Academic Press, 2001.

[9] D. Reynolds, *Engineering Principles of Acoustics: Noise and Vibration Control*. Boston, USA: Allyn and Bacon Inc., 1981.

[10] D. R. Morgan, "An analysis of multiple correlation cancellation loops with a filter in the auxiliary path," *IEEE International Conference on Acoustics, Speech, and Signal Processing*, pp. 457–461, Apr. 1980.

[11] B. Widrow, D. Shur, and S. Shaffer, "On adaptive inverse control," in *Proceeding of the 15th Asilomar Conference on Circuits, Systems and Computers*, Nov. 1981, pp. 185–189.

[12] J. C. Burgess, "Active adaptive sound control in a duct: computer simulation," *Journal of the Acoustical Society of America*, vol. 70, pp. 715–726, 1981.

[13] G. E. Warnaka, L. A. Poole, and J. Tichy, "Active acoustic attenuators," *U.S. Patent 4473906*, 1984.

[14] L. J. Eriksson, "Recursive algorithms for active noise control," *International Symposium of Active Control of Sound and Vibration*, pp. 137–146, 1991.

[15] B. Rafaely and S. Elliott, "H_2/H_∞ active control of sound in a headrest: design and implementation," *IEEE Transactions on Control Systems Technology*, vol. 7, no. 1, pp. 79–84, Jan. 1999.

[16] T. Meurers, S. Veres, and S. Elliot, "Frequency selective feedback for active noise control," *IEEE Control Systems Magazine*, vol. 22, no. 4, pp. 32–41, Aug. 2002.

[17] Y. Song, Y. Gong, and S. Kuo, "A robust hybrid feedback active noise cancellation headset," *IEEE Transactions on Speech and Audio Processing*, vol. 13, no. 4, pp. 607–617, Jul. 2005.

[18] I. Tabatabaei Ardekani and W. H. Abdulla, "Allpass filtered reference LMS algorithm for adaptive feedback active noise control," *Proceeding of 2009 Asia Pacific Signal and Information Processing Association Annual (APSIPA) Summit and Conference, Sapporo, Japan*, pp. 859–865, 2009.

[19] D. C. Swanson, "Active noise attenuation using a self-tuning regulator as the adaptive control algorithm," *Proceeding of Inter-Noise*, pp. 467–470, 1989.

[20] K. Zangi, "A new two-sensor active noise cancellation algorithm," *IEEE International Conference on Acoustics, Speech, and Signal Processing*, vol. 2, pp. 351 –354 vol.2, Apr. 1993.

[21] S. Elliott, I. M. Stothers, and P. A. Neslson, "A multiple error LMS algorithm and its applications to active control of sound and vibration," *IEEE Transactions on Acoustic, Speech and Signal Processing Processing*, vol. 35, pp. 1423–1434, 1987.

[22] M. Rupp and A. Sayed, "Two variants of the FxLMS algorithm," *IEEE ASSP Workshop on Applications of Signal Processing to Audio and Acoustics*, pp. 123 –126, Oct. 1995.

[23] ——, "Robust FxLMS algorithms with improved convergence performance," *IEEE Transactions on Speech and Audio Processing*, vol. 6, no. 1, pp. 78 –85, Jan. 1998.

[24] P. Davari and H. Hassanpour, "A variable step-size FxLMS algorithm for feedforward active noise control systems based on a new online secondary path modelling technique," *IEEE/ACS International Conference on Computer Systems and Applications*, pp. 74–81, Apr. 2008.

[25] N. Kunchakoori, A. Routray, and D. Das, "An energy function based fuzzy variable step size fxlms algorithm for active noise control," *IEEE Region 10 and the Third international Conference on Industrial and Information Systems*, pp. 1–7, Dec. 2008.

[26] A. Oppenheim, E. Weinstein, K. Zangi, M. Feder, and D. Gauger, "Single-sensor active noise cancellation," *IEEE Transactions on Speech and Audio Processing*, vol. 2, no. 2, pp. 285 –290, Apr. 1994.

[27] L. Eriksson, M. Allie, D. Melton, S. Popovich, and T. Laak, "Fully adaptive generalized recursive control system for active acoustic attenuation," *IEEE International Conference on Acoustics, Speech, and Signal Processing*, vol. 2, pp. II/253 –II/256 vol.2, Apr. 1994.

[28] A. Gonzalez, M. Ferrer, M. de Diego, and G. Pinero, "Fast filtered-x affine projection algorithm for active noise control," *IEEE Workshop on Applications of Signal Processing to Audio and Acoustics*, pp. 162–165, Oct. 2005.

[29] ——, "Fast filtered-x affine projection algorithm with efficient computation of coefficient update," *IEEE International Conference on Acoustics, Speech and Signal Processing*, vol. 5, p. V, May 2006.

[30] T. Walzman and M. Schwartz, "Automatic equalization using the discrete frequency domain," *IEEE Transactions on Information Theory*, vol. 19, no. 1, pp. 59 – 68, Jan. 1973.

[31] Q. Shen and A. Spanias, "Time and frequency domain x-block LMS algorithms for single channel active noise control," in *International Congress on Recent Developments in Air- and Structure-Borne Sound and Vibration*, 1992, pp. 353–360.

[32] K. M. Reichard and D. C. Swanson., "Frequency domain implementation of the filtered-x algorithm with online system identification," *Proceeding Recent Advances in Active Sound Vibration*, pp. 562–573, 1993.

[33] S. Kuo, M. Tahernezhadi, and L. Ji, "Frequency-domain periodic active noise control and equalization," *IEEE Transactions on Speech and Audio Processing*, vol. 5, no. 4, pp. 348–358, Jul. 1997.

[34] D. Morgan and J. Thi, "A delayless subband adaptive filter architecture," *IEEE Transactions on Signal Processing*, vol. 43, no. 8, pp. 1819–1830, Aug. 1995.

[35] S. J. Park, J. H. Yun, Y. C. Park, and D. H. Youn, "A delayless subband active noise control system for wideband noise control," *IEEE Transactions on Speech and Audio Processing, IEEE Transactions on*, vol. 9, no. 8, pp. 892–899, Nov. 2001.

[36] B. Siravara, N. Magotra, and P. Loizou, "A novel approach for single microphone active noise cancellation," *The 2002 45th Midwest Symposium on Circuits and Systems*, vol. 3, pp. III–469–III–472 vol.3, Aug. 2002.

[37] V. DeBrunner, L. DeBrunner, and L. Wang, "Sub-band adaptive filtering with delay compensation for active control," *IEEE Transactions on Signal Processing*, vol. 52, no. 10, pp. 2932–2941, Oct. 2004.

[38] I. Tabatabaei Ardekani and W. H. Abdulla, "A new subband algorithm for active attenuation of broadband noise," *Proceeding of 2009 International Symposium on Active Control of Sound and Vibration (ACTIVE), Ottawa, Canada*, Aug. 2009.

[39] S. Miyoshi and Y. Kajikawa, "Statistical-mechanics approach tothe filtered-x LMS algorithm," *Electronics Letters*, vol. 47, pp. 997–999, Aug. 2011.

[40] B. Widrow, J. McCool, M. Larimore, and J. Johnson, C.R., "Stationary and nonstationary learning characteristics of the lms adaptive filter," *IEEE Proceedings*, vol. 64, no. 8, pp. 1151–1162, Aug. 1976.

[41] H. Butterweck, "A wave theory of long adaptive filters," *IEEE Transactions on Circuits and Systems I: Fundamental Theory and Applications*, vol. 48, no. 6, pp. 739–747, Jun. 2001.

[42] L. Resende and J. Bermudez, "Statistical analysis of the FXLMS algorithm about the steady-state solution," *2006 International Telecommunications Symposium*, pp. 306–309, Sep. 2006.

[43] Y. Hinamoto and H. Sakai, "Analysis of the filter-X LMS algorithm and a related new algorithm for active control of multitonal noise," *IEEE Transaction on Audio, Speech, and Language Processing*, vol. 14, no. 1, pp. 123–130, Jan. 2006.

[44] S. Miyagi and H. Sakai, "Mean-square performance of the filtered-reference/ filtered-error LMS algorithm," *IEEE Transactions on Circuits and Systems I: Regular Papers*, vol. 52, no. 11, pp. 2454–2463, Nov. 2005.

[45] O. Tobias, J. Bermudez, and N. Bershad, "Mean weight behavior of the filtered-X LMS algorithm," *IEEE Transactions on Signal Processing*, vol. 48, no. 4, pp. 1061–1075, Apr. 2000.

[46] G. Long, F. Ling, and J. Proakis, "The LMS algorithm with delayed coefficient adaptation," *IEEE Transactions on Acoustics, Speech and Signal Processing*, vol. 37, no. 9, pp. 1397–1405, Sep. 1989.

[47] ——, "Corrections to the LMS algorithm with delayed coefficient adaptation'," *IEEE Transactions on Signal Processing*, vol. 40, no. 1, pp. 230–232, Jan. 1992.

[48] S. J. Elliott and P. A. Nelson, "Multiple-point equalization in a room using adaptive digital filters," *Journal of the Audio Engineering Society*, vol. 37, no. 11, pp. 899–907, Nov. 1989.

[49] E. Bjarnason, "Analysis of the filtered-x LMS algorithm," *IEEE Transactions on Speech and Audio Processing*, vol. 3, no. 6, pp. 504–514, Nov. 1995.

[50] L. Vicente and Masgrau, "Novel FxLMS convergence condition with deterministic reference," *IEEE Transactions on Signal Processing*, vol. 54, no. 10, pp. 3768–3774, Oct. 2006.

[51] Y. Takenouchi, H. Sizuhi, and A. Omoto, "Behavior of the practically implemented filtered reference LMS algorithm in an active noise control system," *Journal of Acoustical Science and Technology*, vol. 27, pp. 20–27, 2006.

[52] Y. Xiao, A. Ikuta, L. Ma, and K. Khorasani, "Stochastic Analysis of the FXLMS-Based Narrowband Active Noise Control System," *IEEE Transactions on Audio, Speech, and Language Processing*, vol. 16, no. 5, pp. 1000–1014, Jul. 2008.

[53] S. Snyder and C. Hansen, "The effect of transfer function estimation errors on the filtered-x LMS algorithm," *IEEE Transactions on Signal Processing*, vol. 42, no. 4, pp. 950–953, Apr. 1994.

[54] P. Lopes and M. Piedade, "The behavior of the modified FX-LMS algorithm with secondary path modeling errors," *IEEE Signal Processing Letters*, vol. 11, no. 2, pp. 148 – 151, Feb. 2004.

[55] L. Wang and W.-S. Gan, "Convergence analysis of narrowband active noise equalizer system under imperfect secondary path estimation," *IEEE Transactions on Audio, Speech, and Language Processing*, vol. 17, no. 4, pp. 566–571, May 2009.

[56] C. Boucher, S. Elliott, and P. Nelson, "Effect of errors in the plant model on the performance of algorithms for adaptive feedforward control," *IEE Proceedings of Radar and Signal Processing*, vol. 138, no. 4, pp. 313–319, Aug. 1991.

[57] L. J. Eriksson and M. C. Allie, "Use of random noise for on-line transducer modeling in an adaptive active attenuation system," *Journal of the Acoustical Society of America*, vol. 85, no. 2, pp. 797–802, Feb. 1989.

[58] M. Zhang, H. Lan, and W. Ser, "Cross-updated active noise control system with online secondary path modeling," *IEEE Transactions on Speech and Audio Processing*, vol. 9, no. 5, pp. 598 –602, Jul. 2001.

[59] M. T. Akhtar, M. Abe, and M. Kawamata, "A new structure for feedforward active noise control systems with improved online secondary path modeling," *IEEE Transactions on Speech and Audio Processing*, vol. 13, no. 5, pp. 1082–1088, Sep. 2005.

[60] M. Akhtar, M. Abe, and M. Kawamata, "A new variable step size lms algorithm-based method for improved online secondary path modeling in active noise control systems," *IEEE Transactions on Audio, Speech, and Language Processing*, vol. 14, no. 2, pp. 720–726, Mar. 2006.

[61] S. Haykin, *Adaptive Filter Theory*, 4th ed. Prentice Hall, 2002.

[62] W. A. Gardner, "Learning characteristics of stochastic gradient descent algorithm: A general study, analysis and critique," *Signal Processing*, vol. 6, pp. 113–133, 1984.

[63] B. Widrow and S. D. Stearns, *Adaptive Signal Processing*. Prentice Hall, 1985.

[64] A. H. Sayed, *Adaptive Filters*. Wiley Interscience, 2008.

[65] D. Thomson, "Spectrum estimation and harmonic analysis," *Proceedings of the IEEE*, vol. 70, no. 9, pp. 1055 – 1096, Sep. 1982.

[66] I. Tabatabaei Ardekani and W.H. Abdulla, "On the convergence of real-time active noise control systems," *Signal Processing*, vol. 91, no. 5, pp. 1262–1274, 2011.

[67] O. Bretscher, *Linear Algebra with Applications (3rd ed.),*. Prentice Hall, 2004.

[68] W. R. Evans, "Control system synthesis by root locus method," *Transactions of the American Institute of Electrical Engineers*, vol. 69, no. 1, pp. 66–69, Jan. 1950.

[69] R. C. Dorf and R. H. Bishop, *Modern Control Systems*. Upper saddle river, NJ, USA: Prentice Hall, 2005.

[70] M. C. McCallum and R. H. Farrand, "Can we kill ambient noise and enjoy quiet zones," BEng. Final Year Research Project, Department of Electrical & Computer Engineering, the University of Auckland, Tech. Rep., 2009.

[71] R. Huang and J. Ban, "Acoustic noise muting by antinoise maske," BEng. Final Year Research Project, Department of Electrical & Computer Engineering, the University of Auckland, Tech. Rep., 2010.

[72] *CompactRIO 9014 operating instructions*, National Instruments, 2007.

Appendix A

FPGA Designs

A.1 FPGA Design for FxLMS-Based ANC Systems

The FPGA design for the FxLMS-based ANC system, developed for this research, performs four consecutive tasks. Here, these tasks and their FPGA designs are detailed separately.

A.1.1 Task 1: constructing the reference vector

The first task constructs an addressable memory block from the reference signal. Other tasks can use this memory block as the reference vector $\mathbf{x}(n)$. Figure A.1 shows this memory block (shown by "Reference") and how the stored value of the reference signal is written in it. As seen in the figure , the length of the memory block (which is the length of the reference vector) is set to 256 ($L = 256$).

A.1.2 Task 2: computing the filtered reference vector

The second task is for computing the filtered reference vector $\mathbf{f}(n)$ using an available estimate model of the secondary path. The FPGA design for the secondary path identification system is developed in [70]. Figure A.2 shows the FPGA design for computing the filtered reference vector. As shown in this figure, this task uses the "Reference" memory block, constructed by Task 1. Also, it uses the "SP Model" memory block, which contains secondary path model parameters, estimated by the secondary path identification system. The values of the reference signal and secondary path model parameters are read from "SP Model" and "Reference" memory blocks and the filtered reference signal is computed from these values. Another addressable memory block, labelled as "Filtered x", is then constructed from the values of the filtered reference signal.

A.1.3 Task 3: updating weight vector

The third task is for updating the adaptive weight vector $\mathbf{w}(n)$ using the filtered reference vector, stored in the memory. The FPGA design, developed for the implementation of this task is shown in Figure A.3. The past values of the adaptive weights are read from an addressable memory block, shown by "Weights". After updating these weights by using the FxLMS algorithm, they are again stored in the same memory block. Obviously, this memory block should initiated when the ANC system starts operating.

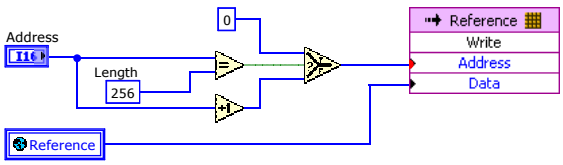

Figure A.1: FPGA design for task 1: constructing an addressable memory block of reference signal

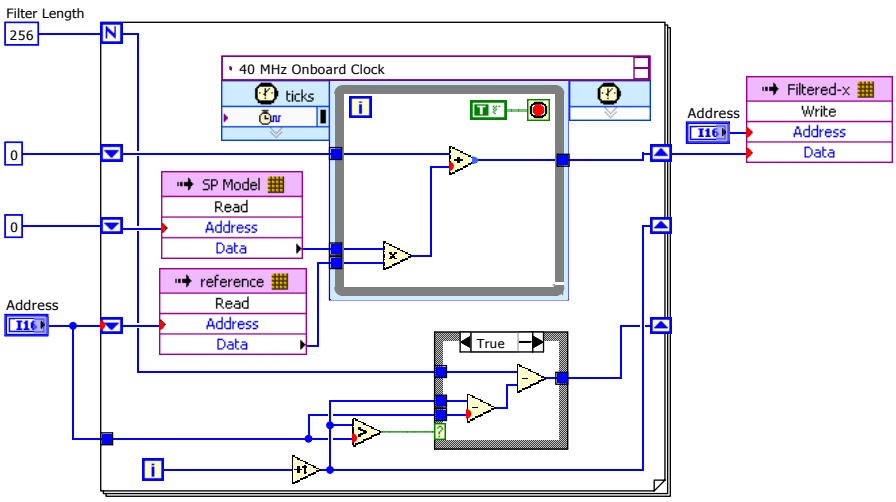

Figure A.2: FPGA design for task 2: filtering reference signal

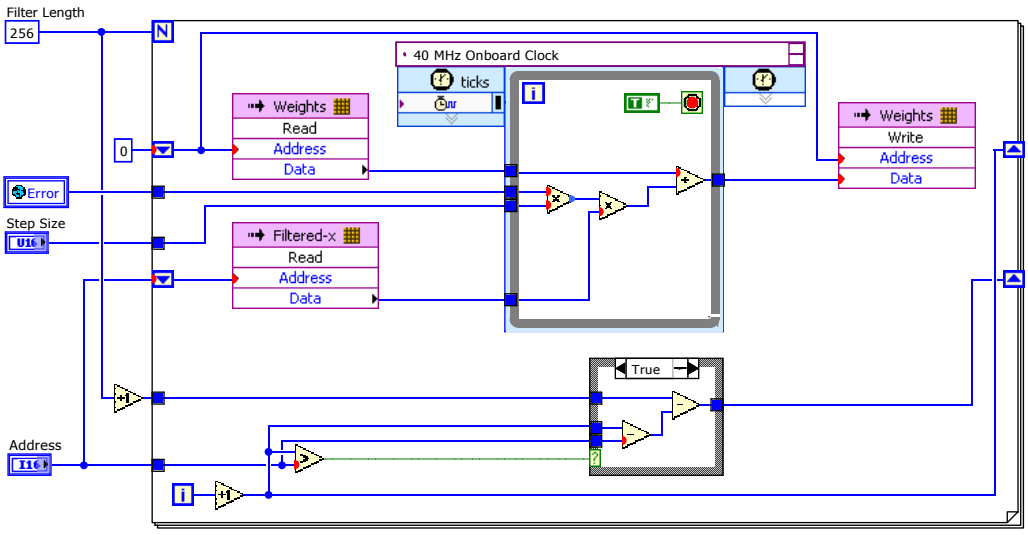

Figure A.3: FPGA design for task 3: FxLMS update equation

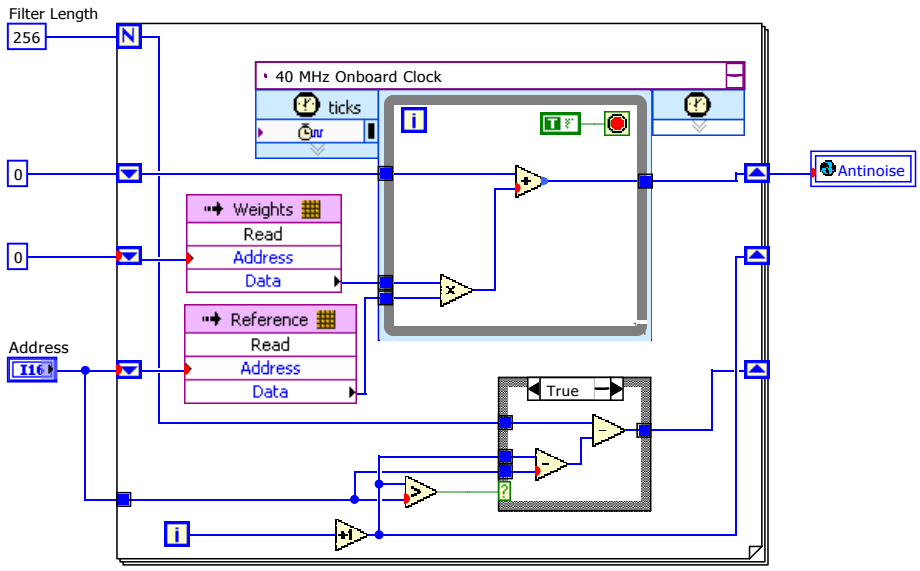

Figure A.4: FPGA design for task 4: computing anti-noise signal

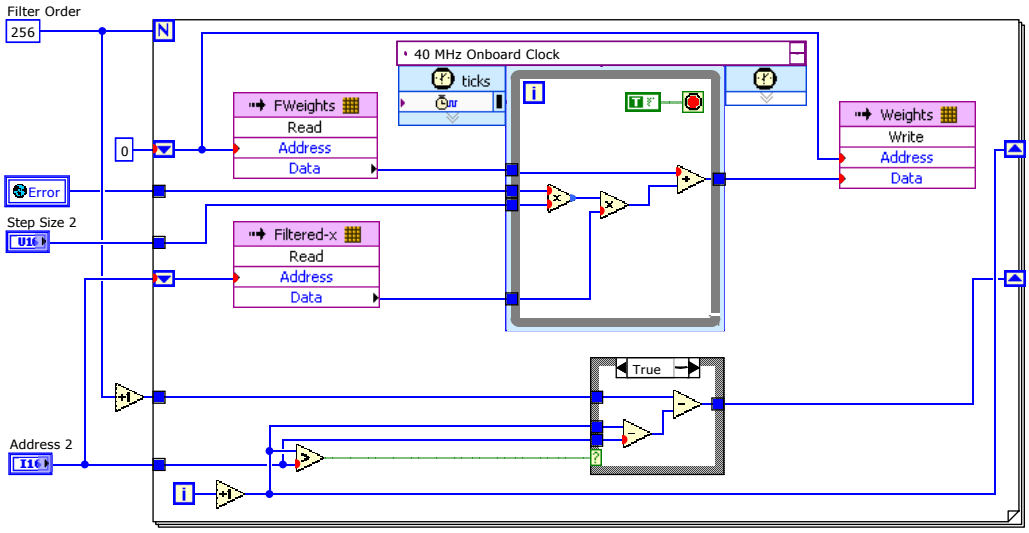

Figure A.5: FPGA design for task 3 in FwFxLMS ANC system

A.1.4 Task 4: computing anti-noise signal

The final task is for computing the anti-noise signal $y(n)$ from the data stored in the memory blocks. For this purpose, the values of the weights and reference signals can be read from addressable memory blocks "Reference" and "Weights". The anti-noise signal can be then computed from these values by using Eq. (2.1). The computed anti-noise signal is labelled as "Antinoise" and stored in the cRIO memory so that the writing thread can read it. The FPGA design for performing this task is shown in Figure A.4.

A.2 FPGA Design for FwFxLMS-Based ANC System

The main body of the FxLMS and FwFxLMS based ANC systems are the same. For implementing the FwFxLMS-based ANC system, all the FPGA designs (4 tasks) described above should be used; however, the FwFxLMS update equation should be used instead of the FxLMS update equation (task 3). The main difference in the two design is

that, in the new task the data stored in “FWeights” is used for updating the weight vector, instead of that stored in the “Weights”. Figure A.5 shows the FPGA design for the implementation of this task. “FWeights” is obtained by filtering the weight vector, stored in “Weights”.